ČESKÉ VYSOKÉ UČENÍ TECHNICKÉ V PRAZE

Fakulta jaderná a fyzikálně inženýrská

Katedra inženýrství pevných látek

Delayed recombination decay, thermal ionization and quantum tunneling in scintillating materials

HABILITAČNÍ PRÁCE
v oboru Aplikovaná fyzika

RNDr. Eva Mihóková, CSc.

Praha, březen 2018

Předmluva

Tato práce je komentovaným souborem publikací, které vznikaly přibližně od r. 2012 v rámci národní i mezinárodní spolupráce autorky při výzkumu optických vlastností a mechanizmu scintilace v pevnolátkových scintilačních materiálech ve formě monokrystalů, optických keramik i prášků. Jedná se o materiály, které jsou velice důležité pro detekci a monitorování ionizujícího záření, urychlených nabitých částic, i neutronů. Mají široké využití v celé škále aplikací, jejichž seznam se v posledních letech stále rozšiřuje. Jedná se zejména o moderní metody zobrazování i podpůrné terapie v medicíně, průmyslovou defektoskopii, bezpečnostní opatření ale i využití pro vědecké účely především ve fyzice vysokých energií.

Každá aplikace klade specifické nároky na vybrané charakteristické parametry scintilačního materiálu, které je žádoucí pro danou aplikaci cíleně optimalizovat. Optimalizace parametrů vyžaduje především detailní pochopení mechanizmu scintilace v konkrétním materiálu. To je možné pouze za součinnosti různých experimentálních technik a podpůrných teoretických studií umožňujících odhalit a studovat procesy degradující účinnost scintilátoru. Následně pak lze navrhovat a testovat způsoby jak tyto procesy potlačit, či alespoň minimalizovat.

Předkládaná práce obsahuje experimentální a teoretické studie, které byly umožněny díky finanční podpoře, získané v daném období v rámci několika projektů. Jedná se o projekt AV ČR v programu interní podpory projektů mezinárodní spolupráce : "Účinnost scintilátoru: kvantové efekty a zpožděná rekombinace" M100101212 (2012-2015), projekty Grantové agentury ČR: "Anorganické scintilátory: netradiční syntéza a rozměrově závislé charakteristiky" 13-09876S (2013-2016) a "Syntéza, charakterizace a uzpůsobování vlastností luminiscenčních nanokompozitů" 17-06479S (2017-2019), ve kterých byla autorka hlavní řešitelkou a dále několik dalších projektů Grantové agentury ČR a MŠMT KONTAKT, ve kterých byla autorka členkou řešitelského týmu.

Ráda bych poděkovala uvedeným grantovým agenturám za finanční prostředky, které prezentovaný výzkum umožnily. Děkuji také všem spolupracovníkům z oddělení Optických materiálů ve Fyzikálním ústavu AV ČR, v. v. i., kteří se významně podíleli na získávání velkého množství experimentálních dat a přípravě většiny zde komentovaných publikací, rovněž kolegům z KJCh ČVUT a University Milano-Bicocca v Itálii, kteří se rovněž podíleli na vzniku několika publikací. Velké poděkování patří prof. L. S. Schulmanovi z Clarkson University v USA za dlouholetou spolupráci, v rámci které vznikly teoretické interpretace a modely vycházející ze získaných experimentálních dat nejenom ve zde komentovaných publikacích ale i v pracích, které předcházeli prezentovanému období. Děkuji doc. L. Kalvodovi a prof. Z. Bryknarovi z KIPL ČVUT za to, že umožnili mé pedagogické působení na katedře a tím také sepsání této habilitační práce.

V Praze, 10.3. 2018 Eva Mihóková

Contents

1. Introduction

A scintillator is a material that converts absorbed ionizing energy of a high energy photon (X-ray or γ-ray), accelerated charged particle or neutron into a number of ultraviolet to visible (UV/VIS) photons. The scintillation detector consists of scintillating material coupled to a photodetector (photomultiplier tube or photodiode). The latter transforms created UV/VIS photons into an electrical pulse [1,2]. Suitable scintillating materials are found within the category of wide band-gap semiconductors or dieletrics.

Scintillation is the process of luminescence excited by ionizing radiation. The scintillation mechanism and efficiency criteria were already addressed in [3], with later refinement in [4]. The scintillation mechanism can be divided into three consecutive processes: *conversion, transport and luminescence*; see Fig. 1.

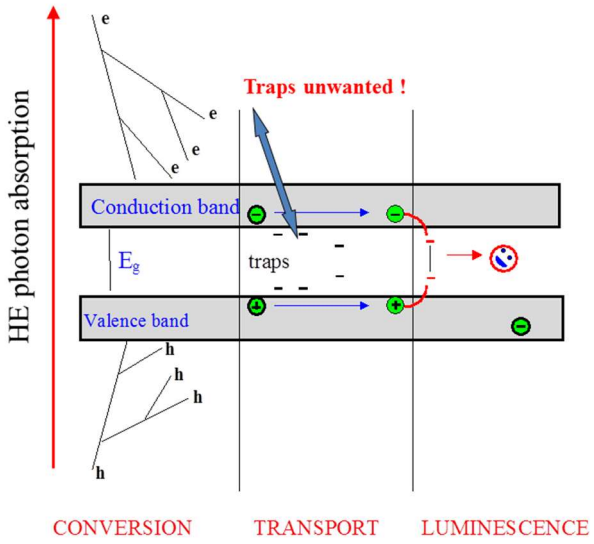

Fig. 1. Scheme of scintillation mechanism in a solid state crystalline material. After [2].

Depending on the particle energy, its initial multi-step interaction with the scintillator host lattice progresses predominantly *via* (i) the photoelectric effect (below ~100 keV), (ii) Compton scattering (within 200 – 8000 keV) and (iii) pair production above the latter limit. The hot electrons and deep holes that are created are gradually thermalized at the conduction and valence band edges, respectively. The conversion process typically lasts a few picoseconds; for details see [5,6,7]. In the transport process the separated electrons and holes migrate through the host lattice to reach the emission centers. During their migration charge carriers can be (repeatedly) trapped or even nonradiatively recombine at trapping levels ocurring in the host

band gap. Due to the trapping process the delivery of charge carriers to luminescent centers can be substantially delayed. Therefore the presence of localized energy states in the host band gap acting as trapping centers may considerably deteriorate scintillator performance. These states are formed by point defects, flaws, surfaces and interfaces that are strongly dependent on manufacturing technology [8]. During the final stage, the trapping and radiative recombination of the electron and hole at the luminescent center generates the desired luminescence.

Scintillating material research started soon after the discovery of X-rays by W. C. Roentgen in November 1895 [9]. Simple photographic film was found rather inefficient in X-rays registration which triggered the search for materials able to convert this new invisible radiation into a visible light in order to efficiently use sensitive photographic film-based detectors. $CaWO_4$ and ZnS-based powder phosphors soon became widely used for the detection of X-rays in combined phosphor-film detectors [10].

The first bulk single crystal scintillators, NaI:Tl and CsI:Tl, were introduced in the late 1940s [11,12] and even currently they are found in numerous applications. Since then a great number of other material systems have been reported [13]. NaI:Tl and CsI:Tl, first oxide-based $CdWO_4$ scintillator [14] and $Bi_4Ge_3O_{12}$ (BGO) [15] became widespread and are often used as "standards" to evaluate new materials under study.

Within the last two decades there is a vivid ongoing activity in the scintillator research field to meet the demands of variety of applications requiring the detection of ionizing radiation. An optimized $PbWO_4$ scintillator was developed in the 1990s for high energy physics [16,17]. A prominent field of interest focuses on medical and biomedical applications, such as imaging systems for medical diagnosis [18]. Particularly intriguing challenge is represented by an effort to push the limit of coincidence resolution time in the time-of-flight positron emission tomography [19] toward 10 ps [20]. Achieving that goal would significantly improve an effective sensitivity, provide better image quality, reduce the scan times, dose and costs and would eliminate the need for image reconstruction. On the other hand the task cannot be fulfilled with conventional scintillators and new approaches providing ultrafast scintillating materials need to be investigated [21,22]. Alternative research direction of scintillator applications in medicine focuses on their exploitation in medical therapy, such as X-ray induced photodynamic therapy (PDTX) [23]. Homeland security in various countries stimulates the search for materials of special composition for neutron detection [24].

New scintillating materials currently reported are predominantly based on the Ce^{3+} and Pr^{3+} activated materials, due to the short decay time (typically 10-60 ns) and high quantum efficiency of the $5d \rightarrow 4f$ radiative transitions of these centers at room temperature [25].

Due to different requirements of related applications and different preparation technologies employed scintillating materials are historically divided into two categories, namely phosphors and scintillators [26, 27]. Phosphors are those applied in the photon integrating (steady-state) detection mode, while scintillators are employed in the photon counting regime. Currently, the separation between phosphor (powders) and scintillator (bulk) materials is somewhat suppressed as some materials are used in both detection modes, in powder, bulk or other forms, depending on the application.

In the case of scintillators, *X (γ)*-ray photon counting consists of accumulating the generated light arriving soon after the initial conversion stage (cf. Fig.1) is accomplished, since the scintillator works as a high-energy photon counter. Significantly delayed light such as that due to trapping processes mentioned above cannot be technically exploited in the counting mode. The most important characteristics of scintillating materials are:

- *Scintillation efficiency*
- *Light yield*
- *Linearity of light response with the incident X(γ)-ray photon energy – energy resolution and nonproportionality*
- *X(γ)-ray stopping power*
- *Scintillation response in time*
- *Spectral matching between the scintillator and photo-detector*
- *Chemical and mechanical stability*
- *Radiation resistance*
- *Price*

The overall scintillation efficiency of *X* (*γ)*-ray-to-light conversion is determined both by intrinsic and extrinsic material characteristics. The number of UV/visible photons, N_{ph}, produced in the scintillation conversion per energy E of incoming *X (γ)*-ray photon can be expressed as [3,4]:

$$N_{ph} = \frac{E}{\beta E_g} \times SQ \quad , \tag{1}$$

where E_g represents the material band gap, S and Q are quantum efficiencies of the transport and luminescence stages respectively, and β is a phenomenological parameter which, for most materials, is typically between 2 and 3. The relative efficiency can then be obtained as:

$$\eta = \frac{\mathrm{E_{vis} N_{ph}}}{\mathrm{E}} \quad , \tag{2}$$

where E_{vis} is the energy of generated UV/VIS photons. The most efficient material currently known among phosphors and scintillators is ZnS:Ag with $\eta \sim 0.2$. More efficient materials could still be found within those with a narrow band gap below 3 eV.

The light yield (LY) of a scintillator is always inferior to the value given by formula (1) since it represents only a fraction of generated visible photons, namely those arriving to the photodetector within a certain time gate defined by the detection electronics (so called shaping time) after the high energy photon absorption. The values of shaping time are usually set between 100 ns and 10 μs. For detailed description of other scintillator characteristics, see, for example [25].

To control the luminescence and scintillation performance of activated solids, knowledge of the location of the activator's energy levels relative to the valence and conduction bands is absolutely crucial. To determine the energy separation between the activator‘s excited state and the host conduction band one can use the study of the processes of excited state ionization. In the second section we will mention experimental methods that allow study of these processes and focus on optical technique, relatively recently developed in our laboratory, that can be employed in that task.

A process that can significantly affect the dynamics of the luminescence center in various materials is tunneling between the luminescence center and a nearby defect, both quantum and thermally assisted. In the third section we will present our recent studies, both experimental and theoretical, finding quantum tunneling as a process participating in the loss of fast light in a variety of scintillating materials.

2. Delayed recombination decay and excited state thermal ionization

Conversion of excitation energy into mobile charges can occur as a result of photoionization or thermally stimulated ionization of the activator ions excited state. Studying these processes allows one to determine whether a given optical transition results in the release of charges and helps with the placement of the interacting energy levels within the band gap of the host. Photoionization and thermally stimulated ionization of impurity ions in ionic hosts can be studied via the "contact" method, namely classical photoconductivity measurements using blocking electrodes [28-41]. This method is limited to the study of bulk crystalline materials. "Contactless" methods, such as the microwave resonator cavity technique introduced in [42] and further exploited in [43-50], do not suffer from this restriction and can also be used for microcrystalline or nanocrystalline powders. Recently it was shown that measurements of

photoconductivity can in some cases be replaced by purely optical contactless techniques involving thermally stimulated luminescence (TSL) excitation spectroscopy [51-63] TSL after UV excitation [P1,P2] or *delayed recombination decay* measurements.

2.1. Principle and experimental implementation

The delayed radiative recombination at an activator center refers to the process in which the lowest excited state of an activator is selectively excited in its own absorption band. Following that an electron from the relaxed excited state is thermally promoted to the host conduction band. After some time, given mostly by trapping and detrapping processes (see Fig. 2) the electron returns to an ionized activator (not necessarily the same one) to radiatively recombine with the hole producing the luminescence photon. This photon is spectrally indistinguishable from that produced in an immediate (prompt) deexcitation of the activator. Thermally induced ionization of excited luminescence centers became the explanation of choice not only in the case of the Ce^{3+} center, but also in the case of Eu^{2+}, the excited state of which (5d) is of the same nature as that of Ce^{3+}; for a review see [64].

Given the variety of potential applications, this process has been widely studied on a time scale from minutes to hours as so called "persistent luminescence" in a number of oxide and nitride compounds in last two decades. For a review see [65,66] and references therein. In the *delayed recombination decay* technique presented below one follows a shorter time scale, microseconds to minutes, after the selective pulse excitation. Detailed monitoring of the intensity of delayed recombination as a function of temperature allows study of processes of thermal ionization of the activator's excited state.

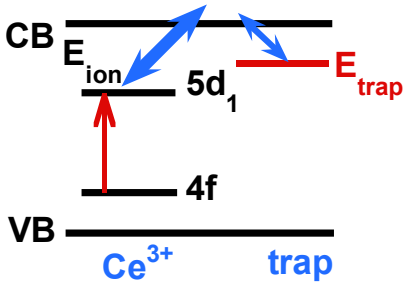

Fig. 2. Simple scheme of the processes of excited state ionization, electron trapping and detrapping in the Ce^{3+} center.

The contactless, purely optical method recently proved useful in testing thresholds of thermal ionization of emission centers in luminescent materials. It also allows the determination of the thermal ionization barier, E_{ion}, even if the procedure (see subsection 2.2) is more complex

compared to the method of measurement of TSL as a function of UV excitation temperature used in [P1,P2]. Nevertheless, the method has the virtue of being applicable to both bulk and powder materials.

The principle of the method was first described and implemented in [67]. When, after the photoluminescence (PL) excitation, the excited state of the luminescent center is thermally ionized, charge carriers that do not decay promptly can migrate through the conduction (or valence) band. During that process they can be trapped and therefore delayed in their recapture at the luminescent center (see Fig. 2). Escape from a trap is often thermally assisted and if the charge carrier reaches the luminescent center, its time spent in the trap will cause it to be part of the observed slow tail of the PL decay. Consequently, monitoring the temperature dependence of the slow tail of the PL decay, or the so called *delayed recombination decay*, supplies information about the thermal ionization of the activator's excited state. Experimental implementation of the method involves the following.

The delayed recombination signal is monitored by conventional equipment for measurements of slow PL decay on the micro-millisecond time scale. The sample is irradiated into the absorption band of an activator by an intense low-repetition-rate pulsed light source (e.g., 10 Hz). The luminescence decay is scanned until the arrival of the next excitation pulse. The system is set so that each excitation pulse (and corresponding measurement window opening) ocurrs immediately after the previous one so that unmonitored intervals between successive time windows are only due to the dead time of the electronics. The scheme of the measurement sequence is shown in Fig. 3. The accumulation time for each measurement is typically about 10 minutes. The decay is scaled within about 10-50 ms (light blue window in Fig. 3). The decay curve is then integrated after the background is subtracted and the first few channels (covering a time interval of about about 60 μs) that may contain the prompt nanosecond decay component are excluded. The integrated decay curve provides the overall intensity of delayed recombination processes at an activator. The measurement is performed at different temperatures starting from the highest one. From the plot of temperature dependence of the delayed recombination intensity the thermal ionization of the activator can be assessed (see the next subsection). The technique was recently used for luminescence centers in a variety of materials (see examples below) to provide more insight into the processes ocurring in the excited state of the luminescence center.

Ce-doped oxyorthosilicates Lu_2SiO_5 (LSO) and Y_2SiO_5 (YSO) became candidates for scintillator applications, particularly in the medical imaging field, more than 20 years ago [68]. The latest generation of scintillation detectors in Positron Emission Tomography (PET) uses

LSO:Ce and yttrium admixed LYSO:Ce especially after their optimization by divalent ion codoping and post-growth annealing, the mechanism of which has been recently clarified [69].

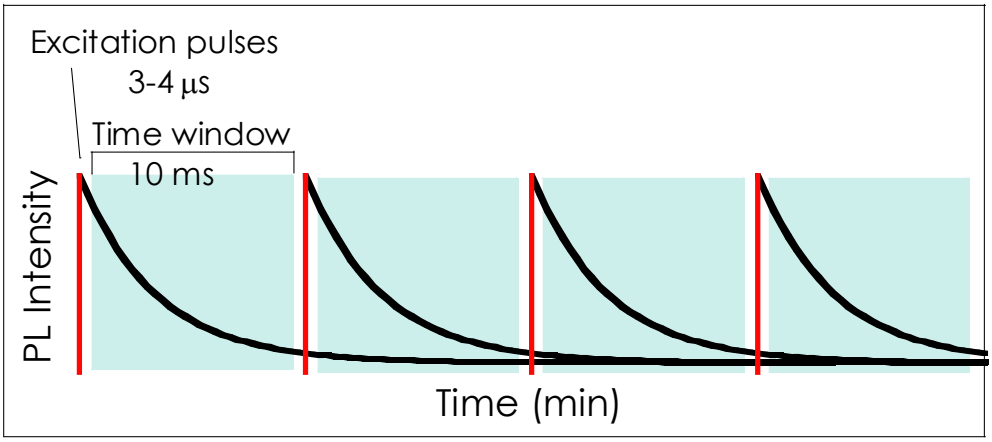

Fig. 3. The scheme of the delayed recombination measurement.

Temperature dependence of delayed recombination intensity related to Ce1 and Ce2 centers (due to two inequivalent positions of Lu or Y [70,71]) in these oxyorthosilicates with different compositions (see the legend in Fig. 4) was monitored. The graph displays an increase of the delayed recombination signal at the onset of thermal ionization of the Ce^{3+} excited state (Figs. 4 a,b). Correlated with the temperature dependence of nanosecond decay time this measurement helped to address the temperature stability of Ce1 and Ce2 centers as a function of Y concentration (from LSO to YSO). With increasing Y content both Ce1 and Ce2 centers become more stable against thermally induced ionization [P3].

Ce-doped gadolinium oxyorthosilicate GSO [72] has been used in oil-well logging due to the stability of its scintillation characteristics up to high temperatures [73]. It has monoclinic structure, with Gd^{3+} also occupying two inequivalent sites [74]. Mixed LGSO:Ce was dicovered to be an efficient, dense scintillator with high light yield, fast decay and weak afterglow [75-77]. Recent analysis [78] of the efficiency of these mixed crystals shows the general trend towards better efficiency of intermediate compositions compared to the limit compositions. The temperature dependence of delayed recombination intensity [P4] shows that the onset of the LGSO:Ce thermal ionization is shifted to slightly higher temperatures than that of LSO:Ce (around 200 K, cf. Fig. 4). In contrast to both, the onset of thermal ionization of GSO:Ce appears for both Ce centers around 400 K.

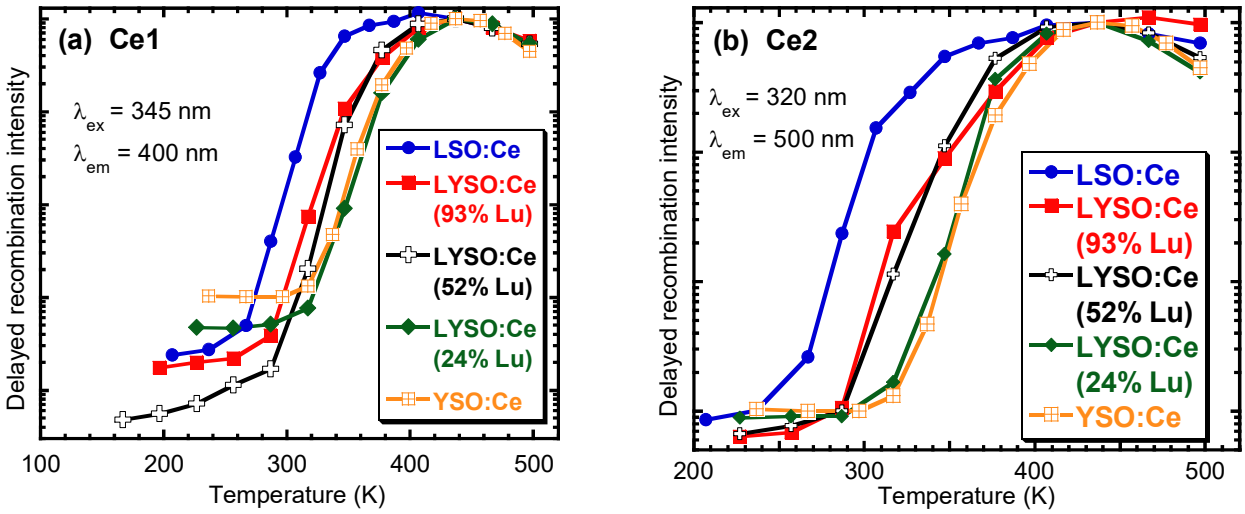

Fig. 4. Temperature dependence of normalized delayed recombination integrals of Ce1 (a) and Ce2 (b) centers for different hosts (composition given in the legend, see also [P3]).

In the nonstochiometric SHO ($Sr_{0.98}Hf_{1.02}O_{3.02}$) investigated for its efficient 334 nm emission, the steep increase of delayed recombination intensity above 400 K (see Fig. 5) is correlated with the onset of thermal quenching evidenced in the temperature dependence of decay times and emission intensities. Therefore, thermal ionization of the center was identified as one possible cause of the 334 nm band temperature quenching [79].

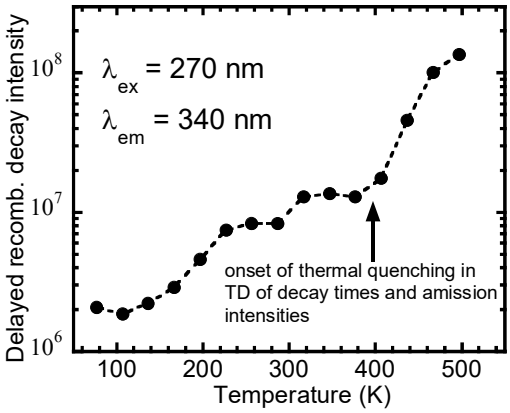

Fig. 5. Temperature dependence of the delayed recombination decay intensity of the 334 nm emission band of $Sr_{0.98}Hf_{1.02}O_{3.02}$ under excitation in the lowest energy absorption band of the center at 270 nm (see also [79]).

Optical characteristics of ternary sulfides having the general formula $ALnS_2$ (A=alkali metal, Ln-lanthanoid or Y) recently started to be investigated since the ternary sulfide host appears to be suitable for rare earth (RE) doping and such doped materials show prospective applications for X-ray and white LED phosphors [80,81,P5,P6]. The temperature dependence of the delayed recombination intensity in $KLuS_2:Eu^{2+}$ displayed in Fig. 6 helped to understand processes ocurring in the excited state of Eu^{2+} [P7].

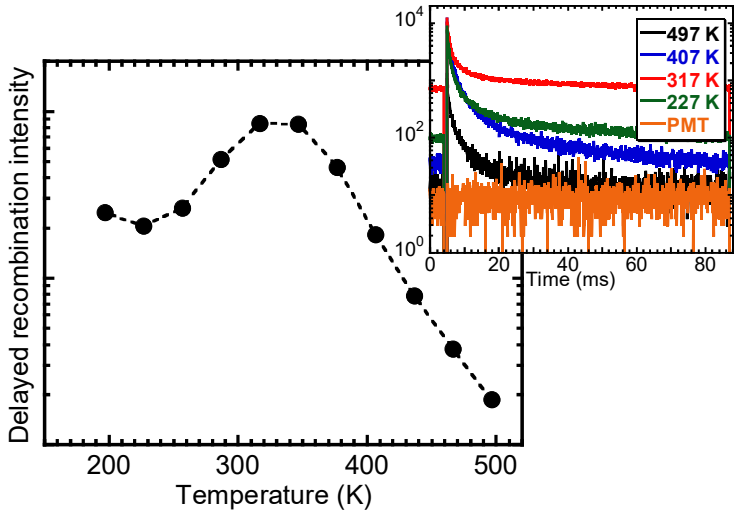

Fig. 6. Temperature dependence of delayed recombination intensity (ex = 395 nm, em = 520 nm) for $KLuS_2$:Eu (0.05%). In the inset, example of delayed recombination decays at temperatures indicated in the legend (see also [P7]).

2.2. The model of temperature dependence of delayed recombination decay intensity

The theoretical model considering the role of traps in shaping the temperature dependence of the delayed recombination intensity was first proposed for the case of discrete traps [P1] and then generalized for any trap distribution function [P8].

The intensity of delayed recombination light is proportional to the fraction of thermally ionized charge carriers $N_I(T)$ that can be expressed as:

$$N_I(T) = we^{-\frac{E_{ion}}{KT}} \quad , \tag{3}$$

where T is the excitation temperature, w is a dimensionless pre-exponential factor, E_{ion} is the thermal ionization energy (the energy separation between the excited state of the luminescent center and the bottom of the conduction band) and k is Boltzmann's constant. However, not all of the thermally ionized carriers will contribute to the overall delayed recombination signal. In particular, only those that get trapped and subsequently released from the traps (with a particular trap depth) whose detrapping time falls into the time interval of delayed recombination measurement will contribute (see above). In general, the number of traps with a certain trap depth can be determined from the distribution function of traps. Thus the intensity of delayed recombination decay can be expressed as:

$$I_{DR}(T) = we^{-\frac{E_{\text{ion}}}{kT}} \int_0^\infty dE\, p(E) \int_{t_b}^{t_e} dt\, \frac{1}{\tau(E)} e^{-\frac{t}{\tau(E)}} \quad , \tag{4}$$

where $p(E)$ is the distribution function of traps with trap depth E and $\tau(E)$ is the detrapping time of the trap with depth E. In this formula, $dt\ \frac{1}{\tau(E)} e^{-\frac{t}{\tau(E)}}$ is the probability that the charge carrier escapes from the trap of depth E, in the time interval $(t,t+dt)$. Thus if the time integration limits were from 0 to ∞ in Eq.(4), then the time integral would yield unity, since each trapped charge carrier eventually escapes. Performing the time integral one obtains

$$I_{DR} = we^{-\frac{E_{\text{ion}}}{kT}} \int_0^\infty dE\ p(E) \left[e^{-\frac{t_b}{\tau(E)}} - e^{-\frac{t_e}{\tau(E)}} \right] \ . \tag{5}$$

The time integral gives the function in square brackets, which is a kind of response function. Given that there is a charge carrier in the trap at time zero, it gives the probability of its escape from the trap in the time interval (t_b, t_e), where t_b and t_e are times corresponding to the beginning and end of the delayed-recombination-decay signal recording, respectively. The detrapping time is expected to have the form [82]:

$$\tau(E) = s^{-1} e^{\frac{E}{kT}} \ , \tag{6}$$

where s is a frequency factor characterizing the number of attempts per unit time that a charge carrier would make to escape from the trap. Formula (4) is general, valid in any class of materials characterized by a trap distribution function $p(E)$. In the case of discrete traps, as in the crystalline hosts considered in [P1], formula (4) reduces to:

$$I_{DR}(T) = we^{-\frac{E_{\text{ion}}}{kT}} \sum_{k=1}^{n} A_k \left[e^{-\frac{t_b}{\tau(E_k)}} - e^{-\frac{t_e}{\tau(E_k)}} \right] , \tag{7}$$

with A_k being the amplitude of the trap with depth E_k and n the number of traps of various kinds participating in the process. The amplitude A_k is proportional to the number of traps of the same kind contributing to the delayed recombination signal.

One should keep in mind that formula (7) does not take into account the fact, that the PL efficiency of the luminescence center can vary with temperature. Therefore, before applying formula (7), experimental data $I_{DR}(T)$ must be corrected for the temperature quenching of the luminescence center. The correction factor can be determined from the measurement of the temperature dependence of the PL steady state intensity (as was done for example in [83]). Should the luminescence center not be quenched, the PL intensity as a function of temperature would remain constant. The number of parameters entering formula (7) is relatively high, however, most of them namely the trap depths E and frequency factors s (related to detrapping times by (6)), can be determined from an independent experiment using the TSL technique.

The model just descriebed was tested on a Pr^{3+} doped $Lu_2Si_2O_7$ (LPS) single crystal [P1]. The delayed recombination intensity was monitored after Xe-flashlamp excitation in the $4f \rightarrow 5d_1$ absorption band (240 nm) of Pr^{3+}. Monitoring was performed by the multichannel scaling method scanning the decay for about 10 ms. The accumulation time for each measurement was about 10 minutes. The measurements were performed at various temperatures in the range 197-497 K. The decay curves were integrated in the whole time range (10.3 ms). The integral values obtained were corrected for the temperature dependence of the PL efficiency of the Pr^{3+} $5d_1 \rightarrow 4f$ emission measured in the steady-state mode. The resulting data as a function of temperature are given as the solid circles in Fig. 7. Before applying the model (7) to the data the parameters of traps entering the formula (7) needed to be determined. By wavelength resolved measurements both below and above room temperature the traps displaying the $5d_1 \rightarrow 4f$ emission of Pr^{3+} were identified. Their corresponding parameters were evaluated by the *initial rise* method [82] applied after suitable partial cleaning procedures of the glow curves. In [P9] it was shown that all TSL peaks follow the first order recombination kinetics. Under that circumstance the frequency factor s associated with each particular trap can be calculated from the formula relating s, the heating rate β (0.1 K/s) and the temperature maximum of the TSL peak T_m [82]:

$$\beta E/kT_m^2 = s \times e^{-E/kT_m}. \quad (8)$$

The detrapping time of the trap τ is determined from (6). Having determined the trap parameters, formula (7) could be fit to experimental data. To reduce the remaining number of free parameters (amplitudes A_k and thermal ionization energy E_{ion}), only TSL peaks displaying relatively high intensity were considered. The best fit to the data is represented by the solid line in Fig. 7. It yielded the value of thermal ionization energy 0.54 eV. The value is consistent with that obtained using the alternative technique of measurement of TSL as a function of UV excitation temperature also reported in [P1].

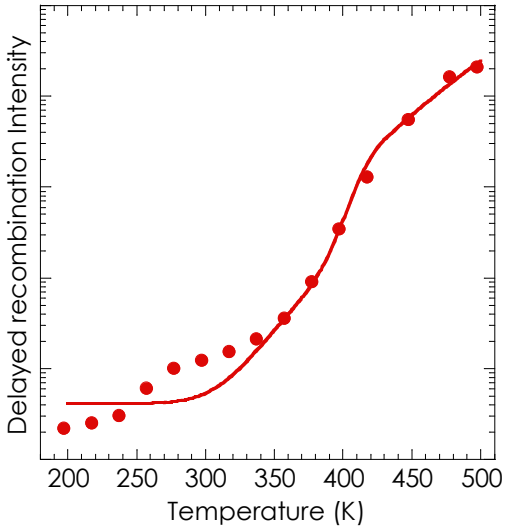

Fig. 7. Temperature dependence of the delayed recombination light emitted by LPS:0.5mol%Pr integrated in the time range 10μs-10.3 ms. The solid circles are experimental data, the line is the numerical fit of formula (7) to the data with E_{ion} = 0.54 eV (see also [P1]).

The validity of the model as well as its applicability to powder materials was tested on Ce^{3+}-doped SHO microcrystalline powder. The thermal ionization energy of Ce^{3+} excited state in this material was determined.

The delayed recombination decay of SHO:Ce^{3+} was measured under microsecond xenon flashlamp excitation in the temperature range 170-500 K. At each temperature the sample was excited by 200 nm light (host lattice excitation). Excitation in the host instead of excitation into the 4*f*-5d_1 absorption band of the Ce^{3+} was chosen due to the fact, that PL intensity under host excitation (200 nm) is less affected by experimental distortions connected with the powder form of the sample (a detailed explanation is given in [P8]). The decay of the emitted light was recorded in a 0-5 ms time window. The entire measurement, with repetitive excitation and signal accumulation, lasted 10 minutes. Each data point in Fig. 8 was obtained by integrating the recorded signal in a 10 μs-5 ms time interval. The data were corrected for the temperature quenching of Ce^{3+} 5d_1→4*f* emission measured in the steady-state mode. Trapping states of SHO:Ce^{3+} were studied and their characteristic parameters were determined [P8] by the *initial rise* technique. Formula (7) was fit to the experimental data.

A satisfactory fit of the delayed recombination data in the considered temperature interval (see the solid line in Fig. 8) was obtained by taking into account the role of two traps. Consideration of other traps with weak amplitude does not change the quality of the fit. The best fit of delayed recombination data considering the role of two traps provides an ionization energy value 0.25±0.02 eV. This value is consistent with that found from the study of TSL after UV excitation also reported in [P2].

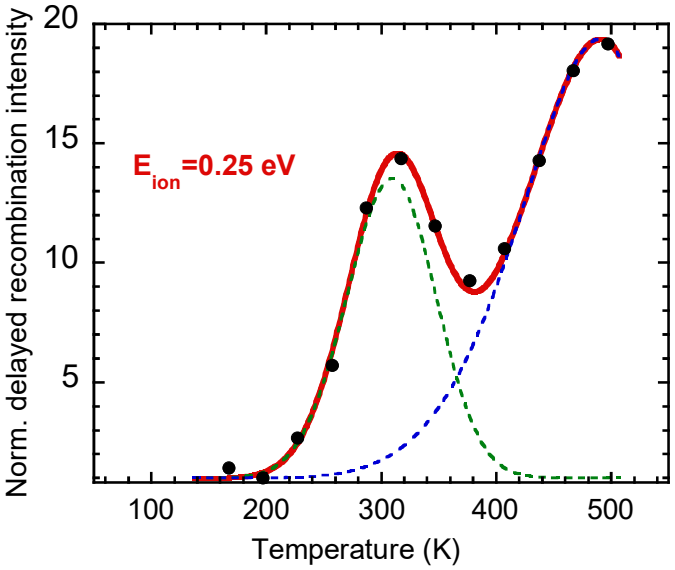

Fig. 8. Normalized (to minimum) delayed recombination intensity of $SrHfO_3:Ce^{3+}$as a function of temperature. Solid circles are experimental data. Solid line is the fit of Eq. (6) to the data, dashed lines are contributions of each single trap to the overall signal. The parameters used in the fit are: A_1 = 1; E_1 = 0.18 eV; $s_1 = 1.2 \times 10^8$ s^{-1}; A_2 = 0.02; E_2 = 0.45 eV; $s_2 = 2.4 \times 10^9$ s^{-1}; E_{ion} = 0.25 eV(see also [P8]).

Recently the model was also applied for YAG:Eu powder [P10]. The delayed recombination decay of YAG:Eu was measured under microsecond xenon flashlamp excitation from 77 to 740 K. At each temperature the sample was excited by 370 nm light. The decay of the emitted light was recorded in a 0-5 ms time window. The entire measurement with repetitive excitation and signal accumulation lasted 10 minutes. Each data point (solid circles in Fig. 9) was obtained by integrating the recorded signal in a time interval of 10 μs to 5 ms and corrected for thermal quenching of the Eu^{2+} emission center.

Some trap parameters entering formula (7) were determined by TSL analysis. A satisfactory fit of the temperature dependence of delayed recombination intensity (solid line in Fig. 9) was obtained by consideration of the role of three traps and ionization energy of about 0.17 eV.

Compared to the method of TSL after UV excitation used in [P1,P2], the above approach to determine the ionization energy is certainly more complicated, since it requires more complex experiments and careful data analysis. However, unlike the TSL method after UV excitation requiring the presence of traps in the material that are stable in a conveniently wide temperature range [P2], it does not impose any specific requirements on trap characteristics. Therefore, for those materials in which stable traps are absent in a convenient temperature region, it still offers a feasible way to determine the thermal ionization energy by means of optical spectroscopy.

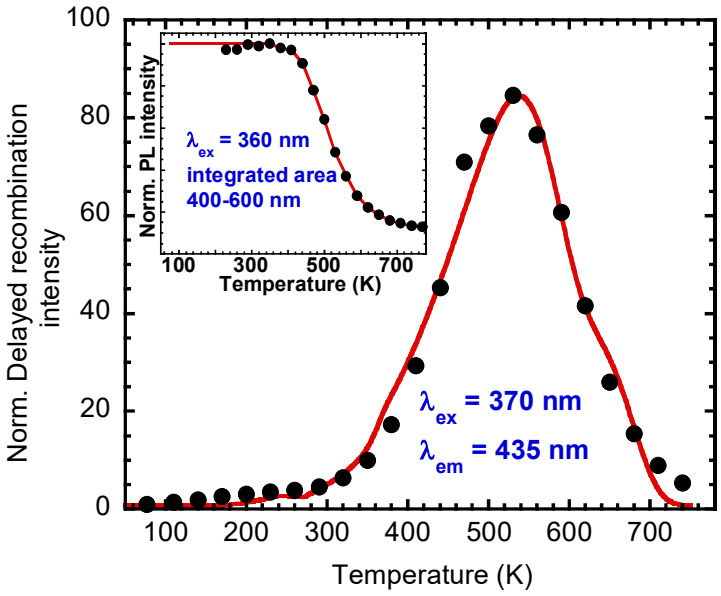

Fig. 9. Delayed recombination decay intensity as a function of temperature. Solid circles are experimental data corrected for the reduction of the Eu^{2+} emission center efficiency with temperature. Solid curve is the fit of function (6) (in the text) to the data. The parameters of the fit are: A_1 = 1; E_1 = 0.25 eV; s_1 = 1× 10^{10} s^{-1}; A_2 = 0.25; E_2 = 0.82 eV; s_2 = 1.5 × 10^{12} s^{-1}; A_3 = 0.08; E_2 = 1.2 eV; s_3 = 1 × 10^{14} s^{-1}; E_{ion} = 0.17 eV. In the inset normalized PL intensity of the Eu^{2+} emission as a function of temperature (see also [P10]).

3. Delayed recombination decay and tunneling between the luminescence centers and trapping states

Tunneling can significantly affect the dynamics of luminescence center excited states and, as such, also affects the performance of luminescent materials. Its effectiveness strongly depends on the distance between the luminescence center and the trap. However, spatial correlation (aggregation) of emission centers and charge carrier traps seems to be a rather frequent event in luminescent materials [84]. Tunneling has already been considered in the description of luminescence decay in various materials some time ago [85-88]. There is a body of literature on materials used in TSL and optically stimulated luminescence (OSL) dating, in which the anomalous fading associated with quantum tunneling is frequently observed [89-102]. Tunneling, both quantum and thermally assisted was systematically applied to explain more recently studied photo-, radio- and thermo luminescence characteristics in various doped oxide phosphors and scintillators [83,103-108]. Delayed recombination decay measurement, presented in the previous section as an effective tool to study the thermally induced ionization of the luminescence center, appears to be suitable to detect the presence of quantum tunneling as well.

3.1. Low temperature delayed recombination decay and quantum tunneling

The low temperature limit of delayed recombination decay intensity given by formula (7) is zero. Therefore at low enough temperatures one would not expect to obtain a detectable delayed recombination signal due to thermal ionization of the luminescence center. As addressed in [P8], this is not the case. There are examples of well detected signals of delayed recombination decay at temperatures where thermal ionization of the luminescence center is not expected. Also, the successful fit in Figs. 7-9 involves an additive constant in formula (7) covering the low temperature region. This presence of a low temperature signal not covered by formula (7) suggests that besides the temperature dependent contribution, there is a temperature independent contribution to the delayed recombination signal that *is not* due to thermal ionization of the luminescence center. There must be another mechanism at work, evidently a kind of sub-gap process which does not involve the conduction band of the host. Considering what was addressed above, a good candidate to explain such a phenomenon appears to be quantum tunneling between the recombination center and a nearby trap.

The idea of quantum tunneling being the culprit for a low temperature contribution to delayed recombination decay has been pursued both experimentally and theoretically. The first experimental support was obtained by measurements of delayed recombination decay of an LPS:Pr^{3+} crystal in the temperature range 8-217 K [P11]. Low temperature data presented in Fig. 10 confirm, that a significant, detectable delayed recombination signal survives down to 8 K, where undoubtedly there cannot be any contribution from thermal ionization. Furthermore, within the observed interval 8–217 K this delayed signal can, to a good approximation, be considered constant. In particular the slight variation is to be compared to the intensity changes of several orders of magnitude in the interval 200–500 K (cf. Fig. 10). In other words, a steady, non-thermal, level has been reached. These characteristics support the hypothesis that the low temperature contribution to delayed recombination signal is due to quantum tunneling.

More extensive experimental support was obtained in later studies. Delayed recombination intensity in several complex oxide scintillating crystals [P12] was investigated in the temperature range from 8 to 230 K. Selected crystals had different lattice structures, were grown by different techniques and doped with different activators, either Ce^{3+} or Pr^{3+}, mostly used in fast scintillating materials. In all the materials studied the intensity of the delayed recombination intensity was practically constant up to at least 120 K. Such temperature independence of the delayed recombination intensity correlates well with the temperature independence of quantum tunneling between the activator and nearby trap(s). The only

exception represented multicomponent garnet $Gd_3Ga_3Al_2O_{12}$:Ce, (GGAG:Ce), a novel, more complex, ultra efficient single crystal scintillator [109-113]. In this material more complex behavior of the signal was observed and remains to be understood (see the next subsection).

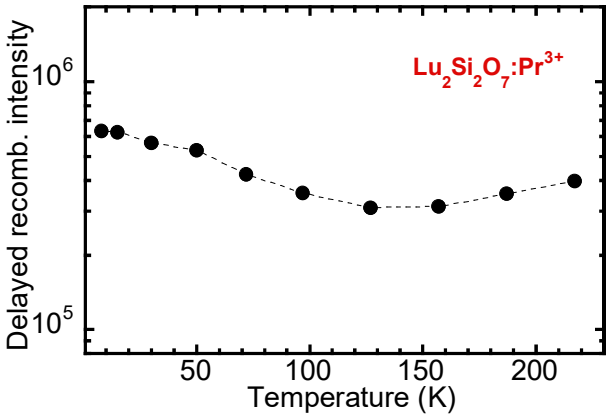

Fig. 10.Temperature dependence of the delayed recombination intensity of LPS:Pr^{3+} emission; λ_{exc} = 240 nm, λ_{em} = 305 nm. Luminescence decay was integrated in the range from 50 μs to 600 s. (The dashed line is only to guide the eye, see also [P11]).

Fig. 11a displays the delayed recombination intensity of $Y_2SiO_5:Pr^{3+}$ measured under UV excitation into the 4*f*→5*d* transition of the Pr ion within the 8-230 K temperature interval. As addressed above, a practically constant signal is observed in the whole temperature range. Fig. 11b shows an example of delayed recombination decay at 8K. The decay is perfectly approximated by the single exponential function indicated in the figure. This result represents a nice example of a host and an activator where there is quantum tunneling between *single* traps (or traps of one kind) and activators ocurring at a constant distance in all the ensemble of trap-activator pairs. For other materials studied the decay was more complex, similar to that presented below in Fig. 12b, indicating either (i) participation of more than one kind of a trap, (ii) single traps with different neighborhoods, i.e. traps differently perturbed, or (iii) single traps with different distances from activators.

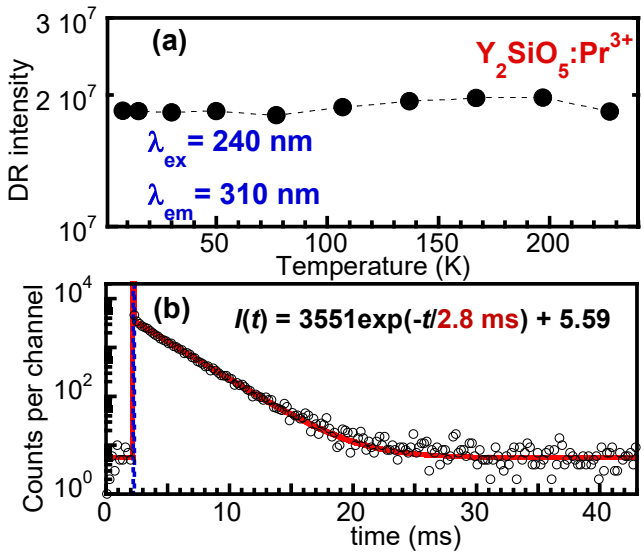

Fig. 11. In (a) is shown delayed recombination intensity of $Y_2SiO_5:Pr^{3+}$as a function of temperature. Excitation and emission wavelengths are displayed in the figure. In (b) is shown delayed recombination decay at 8 K. Empty circles are experimental data, solid line is the fit of function I(t), given in the figure, to the data (see also P12]).

Temperature dependence of delayed recombination decay intensity in a variety of scintillating Ce^{3+} and Pr^{3+} –doped simple garnets was studied in [P13]. We examined various forms of garnets, in particular Czochralski grown single crystals, LPE thin film and a nanopowder prepared by a radiation synthesis. These materials are considered to have significant potential in the family of fast and high light yield oxide scintillators. We monitored simple garnets in the broad temperature region 8-500 K. Compared to the silicates [P12], tunneling in garnets involves deeper trap(s). This follows from the position of the activator's excited state with respect to the conduction band. For example, the $5d_1$ state of Ce^{3+} in $Y_3Al_5O_{12}$ is situated about 1.2 eV below the conduction band [114], while that of Pr^{3+} in $Lu_2Si_2O_7$ is about 0.5 eV [P1] and that of Ce^{3+} in Lu_2SiO_5 is about 0.45 eV [39]. For all samples studied we obtained consistent results showing practically constant delayed recombination intensity within the entire temperature range 8-500 K, see an example in Fig. 12a. Such results confirm first, the presence of quantum tunneling between the activator and nearby traps and second, the absence of thermal ionization of the activator's excited state well above room temperature.

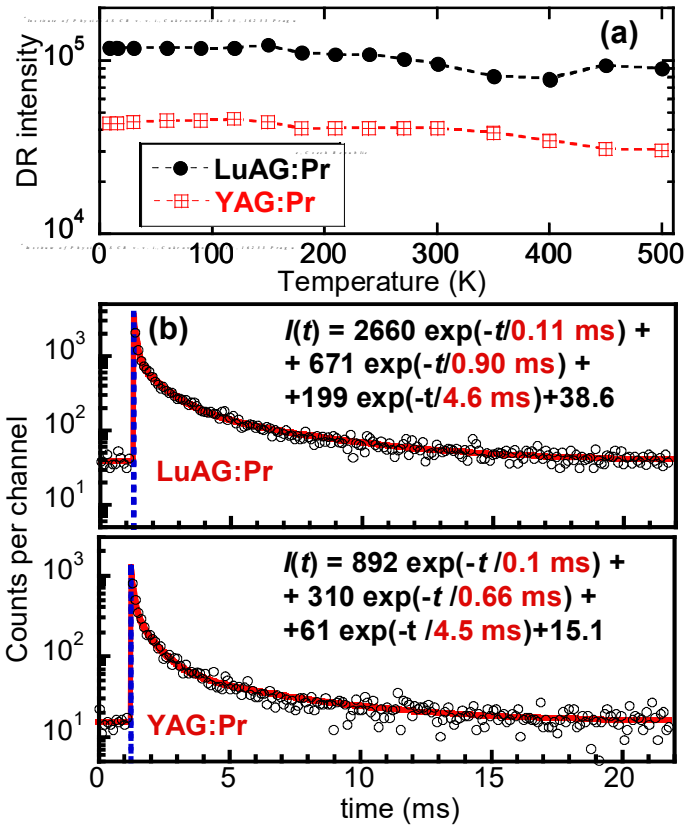

Fig. 12. In (a) is shown delayed recombination intensity of LuAG:Pr^{3+} (λ_{ex}=285 nm, λ_{em}=310 nm) and YAG: Pr^{3+} (λ_{ex}=285 nm, λ_{em}=325 nm) single crystals as a function of temperature. In (b) are shown delayed recombination decays at 8 K. Empty circles are experimental data, solid line is the fit of function I(t), given in the figure, to the data. See also [P13].

3.2. Models of quantum tunneling between the trap and recombination center

To address theoretically, whether quantum effects could be responsible for the observed low temperature delayed recombination, a simple one-dimensional model has been set up [P11]. A scenario of the underlying process is reflected by the scheme in Fig. 13a. The electron tunnels from the activator into a nearby trap. In principle the trap energy can be somewhat higher or lower than that of the excited activator state. However, it is considered more likely that it be lower. For long-term processes energy conservation would prevent the trapping, a problem that can be avoided for lower energies through non-radiative decay. Once in the trap, the electron can tunnel back. This—in principle—time dependent process, was handled using time-independent wave functions, in particular by establishing the extent to which the idealized trap

eigenstate spreads into the activator region. The one-dimensional model is of the form $H=p^2/2m + V(x)$, with m the electron mass and $V(x)$ a potential:

$$V(x) = -\beta\delta(x) - V_0\,\theta(\ell - |x|) - \alpha\delta(x - \ell - \lambda), \tag{9}$$

with V_0, α, β, λ being positive constants. The form of potential together with the definition of the parameters is shown in Figure 13b. The parameters determine the trap energy, the ground and excited states of the activator and the distance between trap and activator. These values are picked so that the trap energy is a bit lower than that of the excited state of the activator and the energy separation between the activator's ground state and first excited state approximate that known for Ce^{3+} or Pr^{3+} ions in oxide hosts. The distance is varied and is on the scale of a few Angstroms, reflecting the dimensions in the relevant substances.

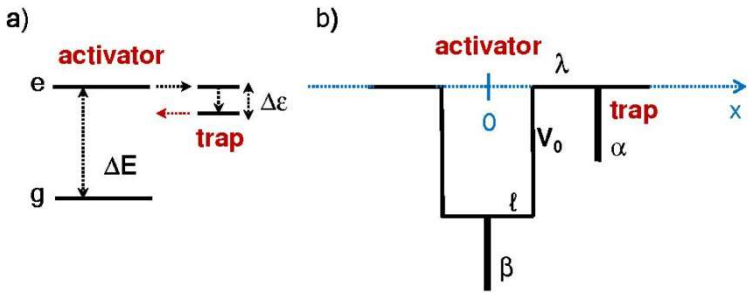

Fig. 13. (a) Simple scheme for a tunneling process between the activator, with the ground state g and excited state e, and the trap located nearby. The energy separation between the ground and excited state of the activator is ΔE while that of the excited state of the activator and the trap state is Δε. (b) The one-dimensional potential used in numerical calculations (see the text). The activator is placed at the origin (0) and V_0,ℓ, λ are the depth and half-width of the square as well as the strength of delta function representing the region of attraction of the activator, while α is the strength of delta function representing the region of attraction of the trap; λ+ ℓ is thus the distance of the trap from the center of the activator. See also [P11].

However, independent of the form of potential, the one-dimensional model exaggerates the tunneling effect because all amplitude from the trap must go either left or right. In three dimensions the wave function tends to spread reducing the likelihood of returning to the activator. Partly the effect is compensated by the use of a geometrical factor (below), but a more accurate calculation would demand full dimensionality.

The amplitude of the electron 'in the trap' that enters the region of the activator must satisfy selection rules, which in one dimension requires a parity change. Therefore, the quantity that is calculated is the probability of finding the trap electron actually in the activator region and having its parity opposite to that of the ground state. The odd parity portion of this piece of wave function ψ_T (trap wave function) will allow a transition to the activator ground state with

the emission of a photon. It is assumed that since the energy of the trap state is not very different from that of the excited state, transition amplitudes should be about the same. Within the ion, the odd portion of ψ_T should resemble the odd portion of the activator's wave function. As a consequence, the reduction R in decay rate should be simply the norm of the odd component of ψ_T, namely

$$R = \int_{\text{region of ion}} \left| \frac{1}{2} \left(\psi_T(x) - \psi_T(-x) \right) \right|^2 dx \tag{10}$$

The quantity R is further multiplied by a geometrical factor G that accounts for the use of a one dimensional model in a three-dimensional situation. The simplest way to deal with this is to imagine that the activator is actually 3-dimensional and spherically symmetric. Then one can calculate the solid angle subtended by the activator as seen from the center of the trap. The ratio of this to all solid angles is then taken. This ratio, G, is

$$G = \frac{\pi \ell^2}{4\pi(\ell + \lambda)^2} \tag{11}$$

Finally, the three dimensional probability is multiplied by the usual prompt decay rate Γ_0 to get an effective decay rate Γ for the electron from the trap. The use of this rate is justified by the fact that the trap energy is not much below that of the excited state of the activator, so that electromagnetic transition matrix elements should be about the same:

$$\Gamma = G \times R \times \Gamma_0 \tag{12}$$

The time-independent Schrödinger equation is solved numerically by discretizing on the line. Fig. 14 presents the wave functions for the parameters given in the caption. For those values the energies are ΔE =3 eV and $\Delta\varepsilon$ =70 meV. The reduction in the decay rate is about 3×10^{-6}. This reduction implies a lifetime on the order of 10 ms (provided that the prompt lifetime is on the order of tens of ns, typical of Ce^{3+} and Pr^{3+} in oxide hosts). This delayed lifetime extends the usual lifetime by six orders of magnitude. These results give theoretical support for the hypothesis that quantum tunneling is responsible for low temperature delayed recombination decay.

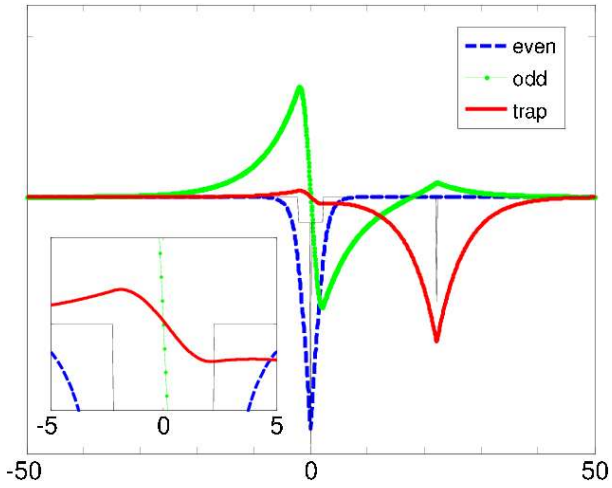

Fig. 14. Wave functions. A rescaled version of the potential is also shown. The solid (red) is the trap wave function, the dashed (blue) the even state (activator's ground state) and the dotted (green), the odd (activator's excited state). In the inset is the detail of the trap wave function in the region of the activator. The parameter values are: λ=20Å, ℓ=2.2 Å, β=3.9 eV, α=1.6 eV and V_0=2.5 eV (see also [P11]).

To allow a more stringent test of the tunneling hypothesis we set up a two dimensional model [P14]. Both the trap and the 'activator' are taken to be isotropic, Gaussian wells. Specifically, the potential has the following form:

$$V(\rho,z) = -\alpha e^{-(\rho^2+z^2)/r_A^2} + \beta/2\,(\rho^2 + z^2) - \gamma e^{-(\rho^2+(z-\lambda)^2)/r_T^2} \quad , \qquad (13)$$

where ρ is the 2D polar coordinate (along the line connecting the centers of the trap and activator) and z the orthogonal coordinate whose origin is the activator. The quantities α and γ are the depths of the activator and trap potential wells, respectively, β models the centrifugal potential and r_A and r_T are effective activator and trap radii, respectively.

Solution of the Schrödinger equation was achieved using the program 'WavePacket' [115]. Since both activator and trap were symmetric about the line connecting their centers, there was azimuthal symmetry and we sought only eigenstates having that symmetry. In Fig. 15 we present an example of the trap wave function obtained from our numerical calculation. The right hand panel illustrates the presence of the trap wave function in the activator region.

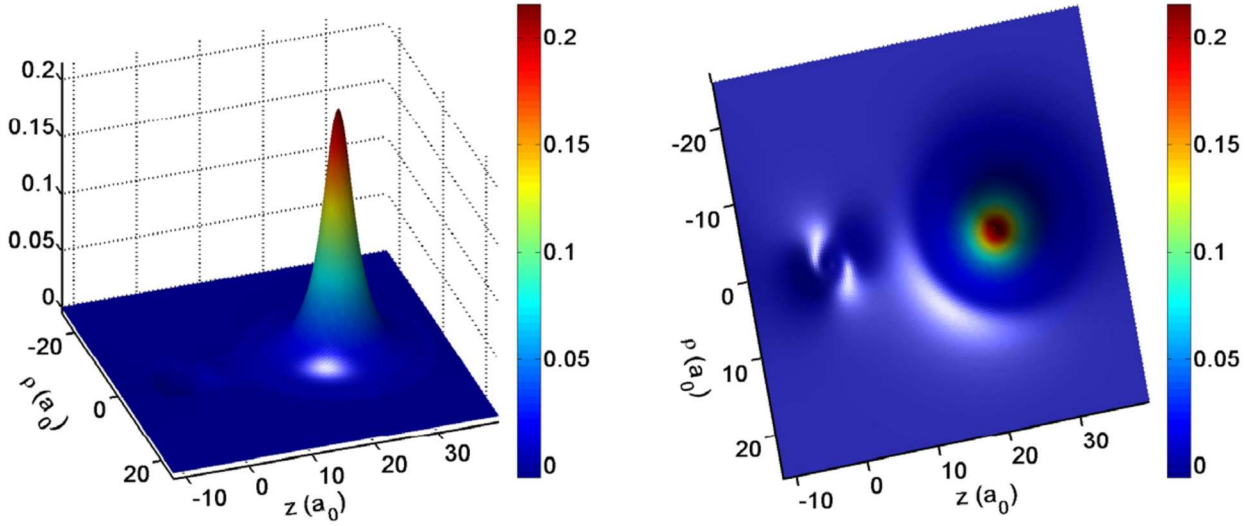

Fig. 15. Example of a calculated trap wave function shown from two different perspectives. The trap-activator distance λ is 23 Bohr radii (about 12 Å). The view in the second panel better displays the portion of the wave function in the area of the activator. The small asymmetry that can be seen as white spots on the dark background is an artifact of the solution method (see also [P14]).

We developed analytical estimates of reduced decay rate Γ (trap decay rate) compared to the prompt activator's decay rate Γ_0. The reduction R is due to the quantum tunneling process:

$$\Gamma = R \times \Gamma_0 \tag{14}$$

We focused on three states. First there is the ground state of the activator, which we call 'ψ_G'. Then there is its excited state, ψ_E. And finally there is the trap state, ψ_T. The prompt rate is $\Gamma_0 \sim |\langle \psi_E | r | \psi_G \rangle|^2$. To estimate the dropoff of the wave function we take the trap to be an attractive point potential. In three dimensions the wave function is $\sqrt{\kappa/2\pi}\exp(-\kappa r)/r$, where r is the distance from the trap center and $\kappa = -2mE_T/\hbar$. (This is normalized to square-integral unity.) Because in the region of the activator the ψ_T resembles ψ_E, the only reduction in decay rate would come from the smaller amplitude associated with the trap state:

$$R = \frac{\eta \int_{activator} \left| \sqrt{\frac{\kappa}{2\pi}} \frac{\exp(-\kappa r)}{r} \right|^2 d^3 r_{activator}}{\langle \psi_T | \psi_T \rangle} \quad , \tag{15}$$

where η=2-3 is the correction factor. Taking an estimate for the integral in (13), R was approximated as:

$$R = \eta \frac{2}{3} \left(\frac{a}{\lambda}\right)^2 (\kappa a) \exp -2\kappa\lambda \ , \tag{16}$$

where a is the activator radius and λ is acivator-trap center-to-center distance; for more details see [P14].

The formulas developed in [P14], in particular equation (14), can be used to determine trap properties. The first example can be $Y_2SiO_5:Pr^{3+}$, whose decay curve is shown in Fig. 11b. There is a single exponential with time constant (inverse decay rate) of 2.8 ms. The prompt decay for this scintillator has a lifetime of 18 ns [67]. Thus the reduction factor is 8.2×10^{-6}. The best estimate for the trap binding energy is the energy separation of the activator excited state from the conduction band, which was estimated to be 0.4 eV [67]. Finally, for the radius of the Pr^{3+} ion we use the value 1.13Å [116]. Using these values together with analytical estimates of R plotted as a function of λ, the trap-activator distance λ turns out to be about 13 Å.

A second example is $Lu_2Si_2O_7:Pr^{3+}$ (LPS:Pr) whose delayed recombination decay was measured in [P12] and approximated by two exponentials with lifetimes 0.13 and 1.6 ms. The lifetime for prompt decay is 19 ns [117]. This gives reduction factors of 1.5×10^{-4} and 1.3×10^{-5}, respectively. As above, the best guess for the trap binding energy is that of the activator excited state. With that assumption the binding energy is roughly the same for both of them. The location of the Pr^{3+} excited state below the conduction band was determined to be [P1] 0.54 eV. For the short lifetime and for plausible values of η we have an activator trap distance value of about 6-8 Å. For the longer lifetime we get the distance of about 10-11 Å.

As observed earlier, for quantum tunneling to occur there should be a trap whose energy is nearly resonant with the excited state of the activator. For Pr^{3+} in LPS:Pr the excited state energy separation from the conduction band is 0.54±0.05 eV [P1]. There is independent evidence that such a trap with nearly resonant energy is indeed present. Thermally stimulated measurements (TSL) were performed in LPS:Pr to determine the trap parameters [P9]. The trap depth 0.51±0.01 eVassociated with the TSL peak at 211 K is within experimental error in excellent agreement with the separation of the Pr^{3+} excited state from the conduction band. Combined information on LPS:Pr material properties confirm that the observed delay in the decay of LPS:Pr is most likely due to quantum tunneling between the trap associated with the 211 K peak and the Pr^{3+} activator. Our calculation shows that this trap is located at distances of about 8 and 11 Å.

The trap is most likely an oxygen vacancy. The mean distance of Lu-O in LPS:Pr is about 2.23Å [118] which makes the closer trap a vacancy located at the third or fourth nearest oxygen site with respect to the Pr ion. Since there is no need for charge compensation when substituting

Pr^{3+} for Lu^{3+} or Y^{3+} (above), the vacancy is not necessarily expected to be located at the closest oxygen sites.

3.3. Local changes of the host band structure due to the impurity

There are experimental observations that could be explained by considering local changes in the conduction or valence bands. In Baran et al. [119] the authors deal with electron states in crystals and explain the luminescence spectra of β-Ca_2SiO_4:Eu^{2+}, Eu^{3+}. They have the interesting suggestion that in the neighborhood of an impurity there is a bend in the conduction band; namely in that region there are fewer electron states and they are of higher energy.

As another example, consider irregularities that have been seen in the low temperature dependence of scintillator delayed recombination signals. For many substances this signal is approximately temperature independent as described in the previous subsection. However, there is at least one important case that does not fit this picture. The intense peak in the delayed recombination signal in Ce^{3+}-doped $Gd_3Ga_3Al_2O_{12}$:Ce, (GGAG:Ce) [P12], at around 100K (cf. Fig. 16) has not been satisfactorily explained. But if the conduction band does bend near the Ce^{3+} impurity things can change dramatically. The Ce^{3+} ion and the nearby resonant trap could then have different energy separations from the conduction band and unlike the Ce^{3+} excited state, the trap can be very shallow. The temperature independent quantum tunneling between Ce^{3+} and the trap would be accompanied by the transfer of excitation energy from the shallow trap to Ce^{3+} via the conduction band at very low temperatures. The latter temperature dependent process would produce the observed bump in the delayed recombination signal.

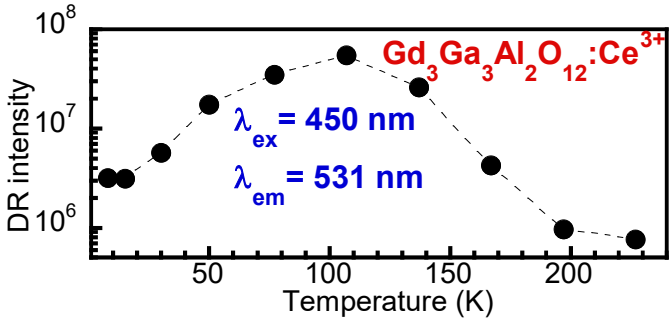

Fig. 16. Delayed recombination decay intensity of GGAG:Ce3+ as a function of temperature. Excitation and emission wavelengths are displayed in the figure (see also [P12]).

We have explored this idea of the conduction band bending using the simplest of one-dimensional models, the Kronig–Penney model with δ-functions [P15]. A great deal of work

along these lines has already been done, since impurities play an important role in almost-periodic systems. Early literature that employs the Kronig–Penney model includes Refs. [120,121] and many others. For photonic crystals, where the one-dimensional feature can be directly relevant, the Kronig–Penney model has also provided a framework [122,123]. The emphasis in these works has been on the impurity state itself or on transmission properties. In many cases the techniques are similar, however, our primary concern is electronic states that respond to a single impurity. This seems close to the work of Baran et al. [119].

Without an impurity and in a simple form, the Kronig–Penney model has Hamiltonian

$$H_0 = \frac{p^2}{2m} + \lambda \sum_{n=0}^{N-1} \delta(x - na) \quad , \tag{17}$$

where a is the lattice spacing, N the number of cells, m the mass, and λ the strength of the potential. We take λ to be negative, mimicking the attraction experienced by electrons at atomic locations. For the electronic case we insist (as is usual in these models) that the state ψ at $x = Na$ differ from that at $x = 0$ *only* by a phase, that phase being Nka with k the wave vector entering the Bloch theorem. Coefficients of the wave function ψ at the site $i+1$ with respect to the site i are determined by the transfer matrix $M_{i \to i+1}$.

We assume that impurity is at site L with $1 \leq L \leq N$. We do *not* seek a value for the impurity level—as some of the articles cited earlier do. Rather we assume it is there and its associated defect provides a force—different from the usual—on nearby electrons, i.e. in cell-L there is an additional positive, constant, repulsive potential throughout the interval $La < x < (L+1)a$. To provide a framework for solution we further assume that this situation repeats, so that, as for the system without impurities, we require that the associated full transfer matrix M_{all} has eigenvalues of magnitude unity. This condition sets allowed energies (bands) and forbiden gaps.

The spectrum of M_{all} is displayed in Fig. 17. The red dots are the eigenvalues of M_{all}; when they have magnitude one indefinite ring propagation is possible. Superimposed on this image are green dots at height 1.04, which are located at energy values for which magnitude 1 eigenvalues exist for $V=0$. These would be the bands (and in their absence, the gaps) without the impurity. To make clear that many energy values *within* the non-defect bands are also eliminated we have put a pair of black dots displaced by 0.02 from 1 for each eigenvalue of M_{all} that is *not* of magnitude 1. In principle this can also be seen from the red dots at small magnitude values. A number of observations can be made from this image. First, many states that were formerly ($V=0$) in the conduction band no longer appear there. Moreover, the first conduction

band has increased its energy. It is to the right of the beginning of the V=0 band confirming the "bend in the band", as suggested in [119]. That there is little or no increase for the next band is to be expected since the energies are larger and the potential may be expected to have less influence.

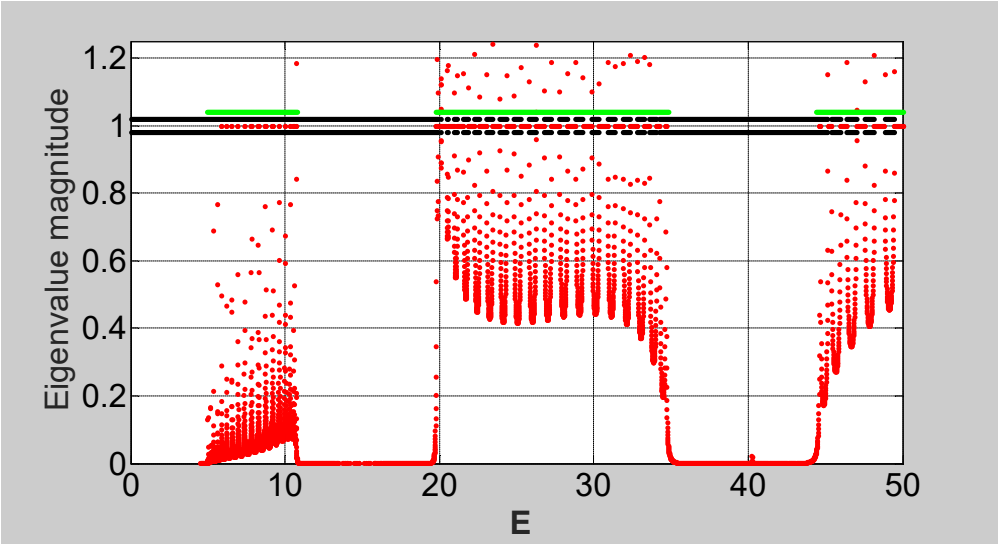

Fig. 17. Absolute values of eigenvalues M_{all} are shown as red points (some of which are excluded because of a cutoff in the axes). In addition, when an eigenvalue does not have magnitude 1, a pair of black dots are displayed at 1 ±0.02. Finally to better judge the effect of the impurity, the normal, i.e., V=0, energy band is shown in green at a height of1.04 (although these are magnitude unity eigenvalues of M_{all}).Parameter values: λ =−10, a =1, V=15, N=20, L =9. The energy, E, in this figure is roughly twice the actual energy in eV (see also [P15]).

What we found exploring the model above is that a lone defect has a profound effect on the eigenstates, and besides shifting the location of the gap it can also change the nature of the eigenfunctions throughout the crystal. For more details, see [P15].

4. General discussion and conclusion

An increasing number of applications of luminescent and scintillating materials in many fields of modern life imposes requirements on their performance. To meet the application-specific demands there is a continuous search for either new materials or ways to improve existing ones. This task can only be handled by intense study of material characteristics and understanding the underlying mechanism of luminescence as well as processes affecting light production. An indispensable tool that helps throughout are methods of optical spectroscopy. They can, in particular, effectively monitor the excited state of the luminescence center which has a crucial role in assessing the phosphor or scintillating material performance. Routine use of classical

methods can be supplemented by novel techniques employing standard instruments in a specific inventive way.

We have addressed experimental implementation and application of the delayed recombination decay technique. This technique can be used to study electron transfer processes in solids and allow determination of the position of the impurity excited state within the host‘s forbidden gap. There are other methods available, briefly referred to. The strengths and weaknesses of each of these techniques determines its suitability for each particular case. Photoconductivity using blocking electrodes can only be used for crystal bulk materials. It also has limited sensitivity. The microwave resonator cavity technique has a sensitivity even lower, however it is suitable also for powder materials. Furthermore, it allows studying the dynamics of electron transfer processes. This is a unique feature among all other techniques mentioned. On the other hand the technique involves a relatively complex and demanding experiment. TSL methods are purely optical, have very high sensitivity, are applicable to both crystalline and powder materials and can be relatively easily implemented. In the case of TSL excitation spectroscopy, when not automated, it may become very laborious and time consuming. The method exploiting TSL as a function of UV illumination temperature requires the presence of traps in the material that are stable in a conveniently wide temperature range.The delayed recombination technique combining TSL and PL measurements, involves relatively complicated analysis, however it does not impose any requirements on trap properties and is suitable for both crystalline and powder materials. We presented its application to several currently investigated materials.

Another virtue of delayed recombination decay technique is the possibility to assess the presence of quantum tunneling between the luminescent center and nearby trap(s). Delayed recombination decay data combined with data from independent experiments together with developed analytical estimates can get handle on the trap-activator distances. In this context the technique helps to understand the origin of temperature independent losses of fast scintillation light in scintillating materials. Since such losses do not seem to be infrequent, it is of high importance that they be addressed and studied, for the ultimate goal would be to prevent them.

5. List of commented author's selection of publications

[P1] M. Fasoli, A. Vedda, E. Mihóková and M. Nikl, "Optical methods for the evaluation of the thermal ionization barrier of lanthanide excited states in luminescent materials," *Phys. Rev. B* **85**, 085127 (1-8) (2012); see pp. 33-40.

[P2] E. Mihóková, V. Jarý, M. Fasoli, A. Lauria, F. Moretti, M. Nikl and A. Vedda, "Trapping states and excited state ionization of the Ce^{3+} activator in the $SrHfO_3$ host," *Chem. Phys. Letters* **556**, 89-93 (2013); see pp. 41-45.

[P3] V. Jarý, M. Nikl, E. Mihóková, J. A. Mareš, P. Průša, P. Horodyský, W. Chewpraditkul and A. Beitlerová, "Influence of yttrium Content on the Ce1 and Ce2 Luminescence Characteristics in $(Lu_{1-x}Y_x)_2SiO_5$ Single Crystals," *IEEE Trans. Nucl. Science* **59**, 2079-2084 (2012); see p. 46-51.

[P4] V. Jarý, E. Mihóková, J. A. Mareš, A. Beitlerová, D. Kurtsev, O. Sidletskiy, and M. Nikl, "Comparison of the scintillation and luminescence properties of the $(Lu_{1-x}Gd_x)_2SiO_5$:Ce single crystal scintillators," *J. Phys. D Appl. Phys.* **47**, 365304 (2014); see pp. 52-59.

[P5] V. Jarý, L. Havlák, J. Bárta, E. Mihóková, and M. Nikl, "Luminescence and structural properties of $RbGdS_2$ compounds doped by rare earth elements," *Opt. Mater.* **35** 1226-1229 (2013); see pp. 60-63.

[P6] V. Jarý, L. Havlák, J. Bárta, E. Mihóková, and M. Nikl, "Optical and structural properties of RE^{3+}-doped $KLnS_2$ compounds," *IEEE Trans. Nucl. Science* **61**, 385-389 (2014). See pp. 64-68.

[P7] V. Jarý, L. Havlák, J. Bárta, E. Mihóková, and M. Nikl, "Optical properties of Eu^{2+} - doped $KLuS_2$ phosphor," *Chem. Phys. Lett.* **574**, 61-65 (2013); see pp. 69-74.

[P8] E. Mihóková, V. Jarý, L. S. Schulman, M. Nikl, "Delayed recombination and excited state ionization of the Ce^{3+} activator in the $SrHfO_3$ host," *Phys. Stat. Sol. RRL* **7**, 228-231 (2013); see pp. 75-78.

[P9] E. Mihóková, M. Fasoli, F. Moretti, M. Nikl, V. Jarý, G. Ren, A. Vedda, "Defect states in Pr^{3+} doped lutetium pyrosilicate," *Opt. Mater.,* **34**, 872-877 (2012); see pp. 79-84.

[P10] E. Mihóková, V. Babin, V. Jarý, L. Havlák, M. Buryi, M. Nikl, "Defect states and temperature stability of Eu^{2+}center in Eu-doped yttrium aluminum garnet," *J. Lumin.,* **190**, 309-313 (2017); see pp. 85-89.

[P11] E. Mihóková, L. S. Schulman, V. Jarý, Z. Dočekalová, and M. Nikl, "Quantum tunneling and low temperature delayed recombination in scintillating materials," *Chem. Phys. Lett.* **377**, 66-69 (2013); see pp. 90-93.

[P12] E. Mihóková, V. Jarý, L. S. Schulman and M. Nikl, "Low temperature delayed recombination decay in complex oxide scintillating crystals," *IEEE Trans. Nucl. Sci.* **61**, 257-261 (2014); see pp. 94-98.

[P13] E. Mihóková, V. Babin, K. Bartosiewics, L. S. Schulman, V. Čuba, M. Kučera and M. Nikl, "Low temperature delayed recombination decay in scintillating garnets," *Opt. Mater.* **40**, 127-131 (2015); see pp. 99-103.

[P14] E. Mihóková and L. S. Schulman, "Low temperature delayed recombination and trap tunneling," *J. Phys.: Condens. Matter* **27**, 075501 (1-8) (2015); see pp. 104-111.

[P15] E. Mihóková and L. S. Schulman, "Energy bands and gaps near an impurity," *Phys. Lett. A* **380**, 3430-3433 (2016); see pp. 112-115.

References

[1] G. F. Knoll in *Radiation Detection and Measurement* (Wiley, New York 2000).

[2] M. Nikl, Meas. Sci. Technol. **17**, R37-R54 (2006).

[3] D. J. Robbins, *J. Electrochem. Soc.* **127**, 2694 (1980).

[4] A. Lempicki, A. J. Wojtowicz, E. Berman, *Nucl. Instrum. Methods Phys. Res., Sect. A* ***333***, 304 (1993).

[5] J. Q. Grim, Q. Li, K. B. Ucer, A. Burger, G. A. Bizarri, W. W. Moses, R. T. Williams, *Phys. Status Solidi A* **209**, 2421 (2012).

[6] P. A. Rodnyi, P. Dorenbos, C. W. E. van Eijk, *Phys. Status Solidi B* **187**, 15 (1995).

[7] A. N. Vasil'ev, *Nucl. Instrum. Methods Phys. Res., Sect. B* **107**, 165 (1996).

[8] J. A. Shepherd, S. M. Gruner, M. W. Tate, M. Tecotzky, *Opt. Eng.* **36**, 3212 (1997).

[9] W. C. Röntgen, *Science* **3**, 227 (1896).

[10] A. W. Fuchs, *Image* **9**, 4 (1960).

[11] R. Hofstadter, *Phys. Rev.* **75**, 796 (1949).

[12] W. van Sciver, R. Hofstadter, *Phys. Rev.* **84**, 1062 (1951).

[13] M. J. Weber, *J. Lumin.* **100**, 35 (2002).

[14] R. H. Gilette, *Rev. Sci. Instrum.* **21**, 294 (1950).

[15] M. J. Weber, R. R. Monchamp, *J. Appl. Phys.* **44**, 5495 (1973).

[16] A. A. Annenkov, M. V. Korzhik, P. Lecoq, *Nucl. Instrum. Methods Phys. Res., Sect.* **490**, 30 (2002).

[17] M. Nikl, Phys.Status Solidi (a) **178**, 595 (2000).

[18] C. W. E. van Eijk, *Phys. Med. Biol.* **47**, R85 (2002).

[19] T. Jones, D. Townsend, *J. Med. Imag.* **4**, 011013 (2017).

[20] P. Lecoq, *Trans. Rad. Plasma Med. Sci*. **1**, 473 (2017).

[21] H. Burešová, L. Procházková, R.M. Turtos, V. Jarý, E. Mihóková, A. Beitlerová, R. Pjatkan, S. Gundacker, E. Auffray, P. Lecoq, M. Nikl, V. Čuba, *Opt. Express* **24,** 15289 (2016).

[22] S. E. Derenzo, E. Bourret-Courshesne, G. Bizarri, A. Canning, *Nucl. Instr. Meth. Phys. Research A* **805**, 36 (2016).

[23] P. Retif, S. Pinel, M. Toussaint, C. Frochot, R. Chouikrat, T. Bastogne, M. Barberi-Heyob, *Theranostics* **5**, 1030 (2015).

[24] R. C. Runkle, A. Bernstein, P. E. Vanier, *J. Appl. Phys.* **108**, 111101 (2010).

[25] M. Nikl, A. Vedda, V. V. Laguta, in *Springer Handbook of Crystal Growth* (Eds: G. Dhanaraj, K. Byrappa, V. Prasad, M. Dudley) Springer, Heidelberg, GE, pp. 1663-1700 (2010).

[26] L. H. Brixner, *Mater. Chem. Phys*. **16**, 253 (1987).

[27] M. Ishii, M. Kobayashi, *Prog. Cryst. Growth Charact. Mater.* **23**, 245 (1992).

[28] C. Pedrini, D. S. Mc Clure and C. H. Anderson, *J. Chem. Phys.* **70**, 4959(1979).

[29] C. Pedrini, F. Rogemond and D. S. McClure, *J. Appl. Phys.* **59**, 1196 (1986).

[30] C. H. Anderson and Z. J. Kiss, *Bull. Am. Phys. Soc.* **9**, 87 (1964).

[31] P. M. Heyman, *Appl. Phys. Lett.* **14**, 81–4 (1969).

[32] C. H. Anderson, Rare earth ions in cubic sites in: *Crystals With The Fluorite Structure* (Oxford: Clarendon) (1974).

[33] C. Pedrini, P. O. Pagost, C. Madej and D. S. Mc Clure, *J. Phys. France* **42**, 323 (1981).

[34] C. Pedrini, F. Gaume-Mahn and D. S. McClure, Photoconductivity due to autoionisation of divalent rare earth impurities in crystals having the fluorite structure, in *The Rare-Earth in Modern Science and Technology* (New York: Plenum Press) (1982).
[35] D. S. McClure and C. Pedrini, *Phys. Rev.* B **32**, 8465 (1985).
[36] W. M. Yen, M. Raukas, S. A. Basun, W. van Schaik and U. Happek U, *J. Lumin.* **69**, 287 (1996).
[37] W. Yen, *J. Lumin.* **83–84**, 399 (1999).
[38] E. van der Kolk, J. T. M. de Haas, A. J. Bos,C. W. E. van Eijk and P. Dorenbos, *J. Appl. Phys.* **101**, 83703 (2007).
[39] E. van der Kolk, S. A. Basun, G. F. Imbusch and W. M. Yen, *Appl. Phys. Lett.* **83**, 1740 (2003).
[40] E. van der Kolk, P. Dorenbos, J. T. M. de Haas and C. W. E. van Eijk, *Phys. Rev.* B **71**, 045121 (2005).
[41] J. Ueda, S. Tanabe and T. Nakanishi, *J. Appl. Phys.* **110**, 053102 (2011).
[42] M.-F. Joubert, S. A. Kazanskii , Y. Guyot, J.-C. Gâcon, J. Y. Rivoire and C. Pedrini, *Opt. Mater.* **24**, 137 (2003).
[43] M.-F. Joubert, S. A. Kazanskii, Y. Guyot, J.-C. Gacon and C. Pedrini, *Phys. Rev.* B **69**, 165217 (2004).
[44] C. Pedrini, M.-F. Joubert and D. S. McClure, *J. Lumin.* **125**, 230 (2007).
[45] H. Loudyi, Y. Guyot, S. A. Kazanskii, J.-C. Gacon, B. Moine, C. Pedrini and M.-F. Joubert, *Phys. Rev.* B **78**, 045111 (2008).
[46] M.-F. Joubert, S. A. Kazanskii, Y. Guyot, H. Loudyi, J.-C. Gacon and C. Pedrini, *Opt. Mater.* **28**, 35 (2006).
[47] H. Loudyi, Y. Guyot, J.-C. Gacon, C. Pedrini and M.-F. Joubert, *Opt. Mater.* **30**, 26 (2007).
[48] H. Loudyi, Y. Guyot, J.-C. Gacon, C. Pedrini and M.-F. Joubert, *J. Lumin.* **127**, 171 (2007).
[49] H. Loudyi, Y. Guyot, S. A. Kazanskii, J.-C. Gacon, B. Moine, C. Pedrini and M.-F. Joubert, *Phys. Rev.* B **78**, 045111 (2008).
[50] L. Nurtdinova, V. Semashko, Y. Guyot, S. Korableva, M.-F. Joubert and A. Nizamutdinov, *Opt. Mater.* **33**, 1530 (2011).
[51] H. Arbell and H. Halperin, *Phys. Rev.***117**, 45 (1960).
[52] N. Kristianpoller and M. Israeli, *Phys. Rev.* B **2**, 2175 (1970).
[53] N. Kristianpoller, *Solid State Commun.* **48**, 621 (1983).
[54] P. Dorenbos, C. W. E. van Eijk, A. J. J. Bos and C. L. Melcher, *J. Phys.: Condens. Matter* **6**, 4167 (1994).
[55] P. Dorenbos, A. J. J. Bos and C. W. E. van Eijk, *J. Phys.: Condens. Matter* **14**, L99 (2002).
[56] V. Murk, M. Nikl, E. Mihokova and K. Nitsch, *J. Phys.: Condens. Matter.* **9**, 249 (1997).
[57] A. Krasnikov, M. Nikl and S. Zazubovich, *Phys. Status Solidi (b)* **243**, 1727 (2006).
[58] J. Fleniken, J. Wang, J. Grimm, M. J. Weber and U. Happek, *J. Lumin.* **94–95**, 465 (2001).
[59] J. Grimm, J. Fleniken, K. W. Kraemer, D. Biner, U. Happek and H. U. Guedel, *J. Lumin.* **122–123**, 325 (2007).
[60] O. Arellano-Tanori, R. Melendrez, M. Pedroza-Montero, B. Castaneda, V. Chernov, W. M. Yen and M. Barboza-Flores, *J. Lumin.* **128**, 173 (2008).
[61] A. J. J. Bos, R. M. van Duijvenvoorde, E. van der Kolk, W. Drozdowski and P. Dorenbos, *J. Lumin.* **131**, 1465 (2011).
[62] F. You, A. J. J. Bos, Q. Shi, H. Shihua and P. Dorenbos, *Phys. Rev.* B **85**, 115101 (2012).
[63] T. Maldiney *et al. Nat. Mater.* **13**, 418 (2014).
[64] P. Dorenbos, *J. Phys. Cond. Matter* **17**, 8103 (2005).

[65] J. Holsa J, T. Laamanen, M. Lastusaari, M. Malkamaki, P. Novak, *J. Lumin.* **129**, 1606 (2009).
[66] P. F. Smet, J. Botterman, K. Van den Eeckhout, K. Korthout, D. Poelman, *Opt. Mater.* **36**, 1913 (2014).
[67] J. Pejchal, M. Nikl, E. Mihóková, J. A. Mareš, A. Yoshikawa, H. Ogino, K. M. Schillemat, A. Krasnikov, A. Vedda, K. Nejezchleb and V. Múčka, *J. Phys. D: Appl. Phys.* **42,** 055117 (2009).
[68] H. Suzuki, T. A. Tombrello, C. L. Melcher and J. S. Schweitzer, *Nucl. Instrum. Methods Phys. Res. A* **320**, 263 (1992).
[69] S. Blahuta, A. Bessiere, B. Viana, P. Dorenbos, V. Ouspenski, *IEEE Trans. Nucl. Science* **60**, 3134 (2013).
[70] T. Gustafsson, M. Klintenberg, S. E. Derenzo, M. J. Weber, and J. O. Thomas, *Acta Crystallogr. Sect. C* **57**, 668 (2001).
[71] N. Y. Leonyuk, E. L. Belokoneva, G. Bocelli, L. Righi, E. V. Shvanskii, R. V. Henrykhson, N. V. Kulman, and D. E. Kozhbakhteeva, *J. Cryst. Growth* **205**, 361 (1999).
[72] K. Takagi K and T. Fukuzawa, *Appl. Phys. Lett.***42**, 43 (1983).
[73] S. Makino and H. Yokota, *Nucl. Instr. Methods Phys. Res. A* **548**, 446 (2005).
[74] J. Felsche, The crystal chemistry of the rare-earth silicates in: Rare Earth *Structure and Bonding* **13**, (Springer: Berlin Heidelberg) 99-197 (1973).
[75] G. B. Loutts, A. I. Zagumennyi, S. V. Lavrishchev, Yu. D. Zavartsev, and P. A. Studenikin *J. Cryst. Growth* **174**, 331 (1997).
[76] T. Usui, H. Yamamoto, S. Shimizu, N. Shimura, Y. Kurata, and H. Ishibashi, *Proc. IEEE Nuclear Science Symp. Conf. Rec.* **N24-006** 1412 (2007).
[77] O. Sidletskyi, V. Bondar, B. Grinyov, D. Kurtsev, V. Baumer, K. Belikov, K. Katrunov, N. Starzhinsky, O. Tarasenko, V. Tarasov, and O. Zelenskaya, *J. Cryst. Growth* **312**, 601 (2010).
[78] A. Gektin, A. Belsky, and A. Vasil'ev, *IEEE Trans. Nucl. Sci.* **61**, 262 (2014).
[79] M. Nikl, P. Bohacek, B. Trunda, V. Jary, P.Fabeni, V. Studnicka, R. Kucerkova, A. Beitlerova, *Opt. Mater.* **34**, 433 (2011).
[80] L. Havlak, V. Jary, M. Nikl, P. Bohacek, J. Barta, *Acta Mater.***59**, 6219 (2011).
[81] V. Jarý, L. Havlák, J. Bárta, and M. Nikl, *Phys. Stat. Solidi RRL* **6**, 95 (2012).
[82] S. W. S. Mc Keever, in *Thermoluminescence in Solids*, Cambridge University press: Cambridge (1985).
[83] A. Vedda, M. Nikl, M. Fasoli, E. Mihóková, J. Pejchal, M. Dušek, G. Ren, C. R. Stanek, K. J. McClellan and D. D. Byler, *Phys. Rev. B* **78**, 195123 (2008).
[84] F. Clabau, X. Rocquefelte, T. Le Mercier, P. Deniard, S. Jobic, and M.-H. Whangbo, *Chem. Mater*. **18**, 3212 (2006).
[85] C. J. Delbecq, Y. Toyozawa, and P. H. Yuster, *Phys. Rev. B* **9**, 4497 (1974).
[86] M. Tachyia and A. Mozumder, *Chem. Phys. Lett.***28**, 87 (1974).
[87] M. Tachyia and A. Mozumder, *Chem. Phys. Lett.***34**, 77 (1975).
[88] P. Avouris and T. N. Morgan, *J. Chem. Phys.***74**, 4347 (1981).
[89] R. Visocekas, T. Ceva, C. Marti, F. Leffaucheux, M. C. Robert, *Phys. Stat. Sol. (a)* **35**, **(**1976).
[90] R. Visocekas, *Nucl. Tracks Radiat. Meas.* **10**, 521 (1985).
[91] R. Visocekas, A. A. Spooner, A. Zink, P. Blanc, *Rad. Measurements* **23**, 377 (1994).
[92] R. Visocekas, A. Zink, *Rad. Eff. Def. Sol.* **134**, 265 (1995).
[93] A. Zink, R. Visocekas, A. J. J. Bos, *Rad. Measurements* **24**, 513 (1995).
[94] R. Visocekas, V. Tale, A. Zink, I. A. Tale, *Rad. Measurements* **29**, 427 (1998).
[95] R. Visocekas, *Rad. Measurements* **32**, 499 (2000).
[96] D. J. Huntley, M. Lamothe, *Can. J. Earth Sci.* **38**, 1093 (2001).

[97] R. Visocekas, *Radiation Protection Dosimetry* **100**, 45 (2002).
[98] M. Auclair, M. Lamothe, S. Huot, *Radiat. Meas.***37**, 487 (2003).
[99] N. C. Tsirliganis, G. S. Polymeris, G. Kitis, V. Pagonis, *J. Lumin.***126**, 303 (2007).
[100] D. J. Huntley, *J. Phys. Condens. Matter* **18**, 1359 (2006).
[101] P. Morthekai, M. Jain, A. S. Murray, K. J. Thomsen, L. Bøtter-Jenses, *Rad. Measurements* **43**, 67 (2008).
[102] I. K. Sfampa, G. S. Polymeris, N. C. Tsirliganis, V. Pagonis, G. Kitis, *Nucl. Instr. Meth. Phys. Res. B* **320**, 57 (2014).
[103] A. Vedda, M. Martini, F. Meinardi, J. Chval, M. Dusek, J. A. Mares, E. Mihokova, M. Nikl, *Phys. Rev.* B **61**, 8081 (2000).
[104] M. Nikl, E. Mihokova, J. Pejchal, A. Vedda, M. Fasoli, I. Fontana, V. V. Laguta, V. Babin, K. Nejezchleb, A. Yoshikawa, H. Ogino, G. and Ren, *IEEE Trans. Nucl. Science* **55**, 1035 (2008).
[105] E. Mihóková, M. Fasoli, A. Lauria, F. Moretti, M. Nikl, V. Jarý, R. Kučerková, and A. Vedda *Opt. Mater.* **34** 228 (2011).
[106] E. Mihóková, K. Vávrů, P. Horodyský, W. Chewpraditkul, V. Jarý, and M. Nikl, *IEEE Trans. Nucl. Science* **59**, 2085 (2012).
[107] E. Dell'Orto, M. Fasoli, G. Ren, A. Vedda, *J. Phys. Chem. C* **117**, 20201 (2013).
[108] A. Dobrowolska, A. J. J. Bos, P. Dorenbos, *J. Phys. D: Appl. Phys*. **47**, 335301 (2014).
[109 K. Kamada , T. Yanagida , T. Endo , K. Tsutumi , Y. Fujimoto, A. Fukabori, A. Yoshikawa, J. Pejchal and M. Nikl , *Crystal Growth & Design* **11**, 4484 (2011).
[110] J. M. Ogiegło, A. Katelnikovas, A. Zych, T. Jüstel, A. Meijerink, and C. R. Ronda, *J. Phys. Chemistry A* **117,** 2479 (2013).
[111] J. Ueda, K. Aishima, S. Tanabe, *Optical Materials* **35**, 1952 (2013).
[112] P. Dorenbos, *J. Lumin.* **134**, 310 (2013).
[113] Y. Wu, G. Ren, *Optical Materials* **35**, 2146 (2013).
[114] D. S. Hamilton, S. K. Gayen, G. J. Pogatshnik, R. D. Ghen, and W. J. Miniscalco, *Phys. Rev. B* **39**, 8807 (1989).
[115] Lorenz U and Schmidt B 2009 WavePacket-simulations in quantum dynamics (http://sourceforge.net/projects/ wavepacket)
[116] R. D. Shannon, *Acta Cryst.* A **32**, 751 (1976).
[117] M. Nikl, G. Ren, D. Ding, E. Mihóková, V. Jarý and H. Feng, *Chem. Phys. Lett.* **493**, 72 (2010).
[118] F. Soetebier and W. Urland, *Z. Kristallogr. NCS* **217**, 22 (2002).
[119] A. Baran, J. Barzowska, M. Grinberg, S. Mahlik, K. Szczodrowski, Y. Zorenko, *Opt. Mater.* **35**, 2107 (2013).
[120] M. Stęślicka, S. Sengupta, *Physica* **54**, 402 (1971).
[121] Z. A. Kasamanyan, *Sov. Phys. JETP* **34**, 648 (1972), in Russian: *Ž. Èksp. Teor. Fiz*. **61**, 1215 (1971).
[122] G. A. Luna-Acosta, H. Schanze, U. Kuhl, H.-J. Stöckmann, *New J. Phys*. **10**, 043005 (2008).
[123] G. A. Luna-Acosta, N. M. Makarov, U. Kuhl, H.-J. Stöckmann, *Phys. Rev. B* **80**, 115112 (2009).

PHYSICAL REVIEW B **85**, 085127 (2012)

Optical methods for the evaluation of the thermal ionization barrier of lanthanide excited states in luminescent materials

M. Fasoli,[1,*] A. Vedda,[1] E. Mihóková,[2] and M. Nikl[2]

[1]*Dipartimento di Scienza dei Materiali, Università di Milano-Bicocca, via Cozzi, 53, 20125 Milano, Italy*

[2]*Institute of Physics, Academy of Sciences of the Czech Republic, v. v. i., Cukrovarnická 10, 16253 Prague, Czech Republic*

(Received 16 November 2011; revised manuscript received 9 January 2012; published 27 February 2012)

We improve a recently proposed approach for the evaluation of the thermal ionization barrier of the lanthanide excited states in luminescent materials by taking into account the effect of traps and their decay time temperature dependence. We present two distinct methods, and we apply them to the case of $Lu_2Si_2O_7$:Pr. To this purpose, wavelength resolved thermally stimulated luminescence and photoluminescence time decay measurements extending up to the ms time scale have been performed. In the frame of the first method, the thermal ionization barrier of the Pr^{3+} $5d_1$ excited state has been evaluated by studying the progressive filling of traps during illumination by ultraviolet light within the $4f$-$5d_1$ absorption band of Pr^{3+} at different temperatures. The thermal ionization barrier turned out to be 0.54 ± 0.05 eV. In the second approach this parameter has been calculated by a numerical reconstruction of the temperature dependence of the $5d_1$-$4f$ delayed recombination decay integral in two different time windows ([53.3 μs − 10.3 ms] and [53.3 μs − 600 s]) with the sum of contributions from different traps whose parameters have been investigated by thermally stimulated luminescence (TSL). The results obtained are in agreement with those found using the trap-filling method. The advantages and limits of both approaches have been critically exposed, in order to discuss the possibility of their extensive employment for the determination of the ionization barrier of a rare earth ion excited-state level in an insulating host.

DOI: 10.1103/PhysRevB.85.085127 PACS number(s): 78.60.Kn, 78.70.Ps, 78.55.Hx, 61.72.−y

I. INTRODUCTION

Given the extensive use of rare earth (RE) ions as luminescence centers in phosphors and scintillators, determining the position of their ground and excited states level within the band gap of the host matrix is of crucial importance for the design and applications of these materials. Based on experimental values of charge transfer and $4f$-$5d$ transition energies of RE^{2+} ions, a model has been developed which provides their positions within the bandgap of an insulating host.[1] This model was extended to RE^{3+} ions as well with position uncertainities up to 0.5 eV[1] and later refined with the help of intervalence charge transfer transitions.[2] Different experimental techniques and methods have been insofar proposed and employed to determine particular transition energies, among these are optical absorption (OA), photoluminescence excitation (PLE),[3] thermally stimulated luminescence (TSL),[4,5] the microwave resonant cavity technique,[6] photoconductivity (PC),[7] and ultraviolet photoemission spectroscopy.[8] PC in particular is a useful technique for determining how close to the conduction band (CB) the excited state of the luminescent ion is. When the energy difference is small enough, thermal ionization of an electron from the lanthanide excited state to the CB can occur even at room temperature (RT). As a consequence of this phenomenon the optical properties of the material can be adversely affected showing a luminescence quenching and a reduced light yield. Unfortunately, PC measurements can be performed only on bulk samples thus preventing the use of this technique on powder phosphors.

In this work we propose two different, purely optical, experimental methods for the evaluation of the thermal ionization barrier of the excited level of a luminescent center. Both these methods can be applied also on powder samples and rely on the effect of localized traps evidenced by TSL measurements.

In the presence of deep traps, which can be filled upon light illumination when thermal ionization of the RE ion excited level occurs, the thermal ionization barrier can be evaluated by monitoring the TSL intensity as a function of the illumination temperature. This method, which will be described first, involves only TSL measurements; it is relatively simple, but it requires the possibility to exploit traps stable in a conveniently wide temperature range.

The second method that will be described involves the parallel use of TSL and photoluminescence (PL) decay measurements. In a few recent works dealing with Ce^{3+}- and Pr^{3+}-doped orthosilicates,[9,10] a new experimental approach was proposed, relying on purely optical techniques for the evaluation of the ionization barrier of the $5d_1$ level of Ce^{3+} (Pr^{3+}) governing the escape of the electron to the CB. When measuring the PL decay of Ce^{3+} (Pr^{3+}) at low temperature, the typical decay time of the $5d$-$4f$ transition, a few tens of ns, is observed. As temperature increases, however, thermal ionization of the $5d_1$ level may become effective. Such a process leads to PL decay-time shortening because of the onset of a second escape path, and it leaves an electron in the CB. The electron that escaped to the CB can thus be temporarily trapped in a localized defect and released at a later time, leading to a delayed radiative recombination process. By measuring the temperature dependence of the delayed recombination intensity, the authors calculate the ionization barrier of Ce^{3+} (Pr^{3+}) $5d_1$ excited state.

The delayed recombination intensity, however, is affected by the probability of captured electrons being released from the traps. Since this probability is temperature dependent, it can modulate the delayed recombination intensity and has to be taken into account for a reliable evaluation of the ionization barrier. We propose a mathematical model, relying on experimental TSL and PL data, which evaluates

the contribution of TSL traps to the delayed recombination as a function of temperature.

In this paper we apply both methods mentioned to Praseodymium-doped Lutetium pyrosilicate, $Lu_2Si_2O_7$ (LPS:Pr), calculating the ionization barrier of the Pr^{3+} $5d_1$ excited state. LPS is an efficient inorganic scintillator, which shows particularly promising performance for medical application such as positron emission tomography.[11,12]

We will present our results discussing the potentiality of the approaches together with the assumptions made and with the conditions for their fruitful application.

II. EXPERIMENTAL CONDITIONS

The LPS:Pr^{3+} single crystal considered in this work was grown in SIC CAS, Shanghai, China by the Czochralski method using an Ir crucible.[13] The Pr^{3+} concentration in the melt was 0.5 at.%. For the measurements a plate of about $7 \times 7 \times 1$ mm was cut from the top of the parent boule with Ø20 $\times$ 40 mm and polished to an optical grade. TSL measurements in the 10–310 K range were performed after x-ray irradiation at 10 K by a Philips 2274 x-ray tube operated at 20 kVp. The TSL apparatus consisted of a high-sensitivity spectrometer measuring the TSL intensity as a function of both the temperature and wavelength. The detection system was a monochromator TRIAX 180 Jobin-Yvon coupled to a charge-coupled-device detector Jobin-Yvon Spectrum One 3000 operating in the 190–1100 nm interval. The spectral resolution was about 5 nm. The TSL emission spectra were corrected for the spectral efficiency of the detection system. A 0.1 K/s heating rate was adopted.

TSL measurements were performed also after x-ray irradiation at RT. In this second case the measurements were obtained irradiating by a Machlett OEG 50 x-ray tube operated at 20 kV, and they were performed from RT up to 770 K with a linear heating rate of 1 K/s using two different apparatuses. The first apparatus used was a homemade high-sensitivity TSL spectrometer measuring the TSL intensity as a function of both temperature and emission wavelength; the detector was a double stage microchannel plate followed by a 512 diode array; the dispersive element was a 140 line/mm holographic grating, the detection range being 200–800 nm. The spectral resolution was approximately 15 nm. In the second TSL apparatus the total emitted light was detected as a function of temperature by photon counting using an EMI 9635 QB photomultiplier tube. In some cases, TSL glow curves were corrected for the temperature dependence of the $5d_1$-$4f$ radiative transition of Pr^{3+}.

PL measurements were performed by a custom-made 5000 M Horiba Jobin Yvon spectrofluorometer. PL-delayed recombination decays were excited by a microsecond xenon flashlamp and measured using the multichannel scaling method. An Oxford Instruments liquid nitrogen bath optical cryostat allowed the temperature regulation from about 190 to 500 K.

The decay fits were obtained by the least-square sum fitting procedure (SpectraSolve software package, Ames Photonics, Inc.) after performing the convolution of the considered function with the instrumental response. The PL-delayed recombination intensity was measured after integration in a time window between 10 μs and 10 min.

III. RESULTS AND DISCUSSION

A. Method I (TSL)

The idea on which this method is based is quite straightforward: if a sample is exposed to optical radiation exciting selectively the luminescent centers, a fraction of the excited ions can be thermally ionized, and the electrons can become delocalized and migrate through the CB. For an electron situated in the excited state of a luminescent center, the probability $p(T)$ of being promoted to the CB is given by the expression

$$p(T) = e^{-\frac{E_{\text{th}}}{k_B T}}, \tag{1}$$

where k_b is the Boltzmann's constant, T is the absolute temperature of the sample, and E_{th} is the thermal ionization barrier. The ionized electrons can either recombine with a hole at a luminescent center or get trapped at localized defects. The probability of the release of an electron from the trap depends on both the temperature and characteristics of the trap itself. For some traps such a probability is not negligible and thus the electrons will be only temporarily trapped before returning to the CB. If we assume (i) that the fraction of thermally ionized electrons that is captured by a selected trap depends on neither temperature in a given temperature range nor light power (linearity of the trap response), and (ii) that the trap is stable (i.e., the electron release probability is negligible), then the intensity of the TSL peak related to that trap will be proportional to $p(T)$. Therefore, the fraction of thermally ionized electrons can be easily evaluated by means of the TSL technique. Then, by photoexciting the luminescent centers holding the sample at a given temperature, we can then evaluate, from expression (1), the thermal ionization barrier E_{th}.

The sample was mounted on a holder whose temperature was controlled by a Peltier cell within the range 283–353 K. Once the temperature was stable, the sample was exposed to 240 nm (band pass = 5 nm) light for 5 minutes, exciting the $4f$-$5d_1$ transition of Pr^{3+} ions. The sample was then set to RT, and a TSL measurement was carried out from RT to 773 K. The glow curves obtained are reported in Fig. 1. At least three TSL peaks are detected from 350 to 650 K, while the signal above 650 K is due to deeper traps which are not fully emptied during subsequent TSL measurements.

The response linearity of the TSL signal was verified by TSL measurements obtained after x-ray irradiations at doses which gave rise to TSL intensities comparable to those obtained following light illumination (Fig. 1). It turned out that the signal between 430 and 490 K (related to the main TSL peak) displays a good linearity, while higher temperature peaks are supra-linear. Although, in principle, supra-linear peaks could also be employed provided that the correction for their response is performed, obviously in this case we preferred to exploit the main peak at 460 K. The integrals obtained from the glow curves of Fig. 1 from 430 to 490 K after subtracting the background signal are reported in the Arrhenius plot shown in Fig. 2. From the slope of the plot, the

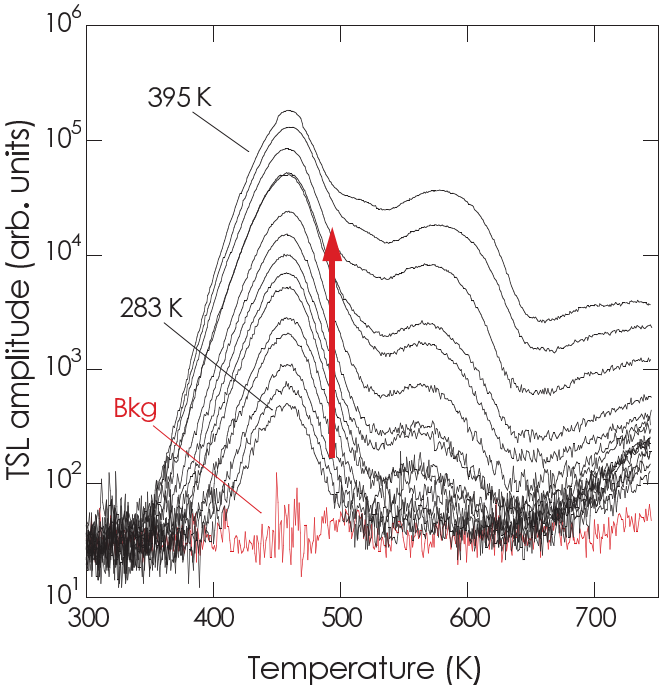

FIG. 1. (Color online) TSL glow curves of LPS:0.5mol%Pr after light illumination (240 nm, 630 μW/cm^2) at different temperatures. The arrow indicates temperature increasing.

thermal ionization barrier E_{th} value was obtained, and it turned out to be 0.54 $\pm$ 0.05 eV. Finally, TSL measurements after excitation at different wavelengths (from 225 to 255 nm) were also performed. Since the shape of the TSL excitation spectrum so obtained was consistent with the optical 4f-5d absorption

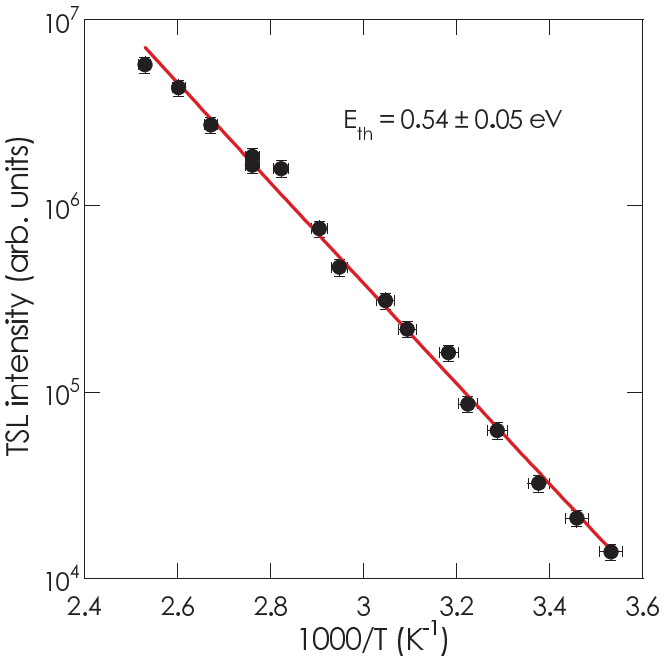

FIG. 2. (Color online) Arrhenius plot of the integrals obtained from the glow curves of Fig. 1 from 430 and 490 K after subtracting the background signal.

bands of Pr^{3+}, we can confirm that really the thermal ionization starts from the $5d_1$ Pr^{3+} excited level.

We observe that the main condition for application of this method is that the filling of traps from the excited state really involves the CB and no direct thermally assisted center-to-trap transitions occur. However in the latter case we would rather expect the filling of one specific trap. In our work we observed a variety of peaks following illumination, characterized by different thermal depths (see Table I of the next section); therefore, we believe that transition to CB is the most probably occurring mechanism.

B. Method II (PL/TSL)

In this approach we consider the temperature dependence of the luminescence center PL decay profile. When no ionization occurs, the intensity of the light emitted after the excitation pulse shows the decay profile characteristic of the luminescence center (faster if more recombination paths are present). In the case of Pr^{3+} 5d-4f transition, for example, the decay time is in the order of a few tens of ns. If, on the other hand, a significant fraction of electrons gets thermally ionized, then delayed recombination can occur, giving rise to slower components in the decay curve.

As we already observed in Method I, after the excitation pulse, the fraction of excited centers that is thermally ionized is given by expression (1). Some of these ionized electrons will recombine immediately at the luminescence center with no delay so that it is not possible to discriminate between their emission and the one due to the prompt relaxation of photo-excited centers. A fraction of the ionized electrons, however, is temporarily trapped by localized defects. Such electrons, as a consequence, will undergo a delayed recombination at the luminescence centers. Thus this delayed recombination light holds the information about the thermally ionized electrons; analyzing with an appropriate model the temperature dependence of its intensity, we can extract the value of the thermal ionization barrier E_{th}. Similarly to what was explained for Method I, also in this case we assume that no direct thermally assisted center-to-trap transitions occur.

Being the delayed recombination light due to the effect of localized traps, let us first consider in our model, for simplicity, the case in which only one kind of trap is present. After the excitation pulse, the decay time profile of the delayed recombination light is governed by the decay time $\tau(T)$ of the traps, which are supplying the electrons to the luminescence centers. The emitted light intensity as a function of time, at temperature T, is given by the expression

$$I(t;T) = I_{0;T} e^{-\frac{t}{\tau(T)}}, \tag{2}$$

where $I_{0;T}$ is a constant proportional to the number of trapped electrons and $\tau(T)$ is the decay time of the traps that can be obtained from

$$\tau(T) = s^{-1} e^{\frac{E}{k_B T}}, \tag{3}$$

where E is the thermal depth of the trap and s is its frequency factor. Now let us assume that our detection system can integrate the light emitted within the time window $[t_1, t_2]$ after the excitation pulse. We remark that, since we are interested only in the delayed recombination light, it is important that

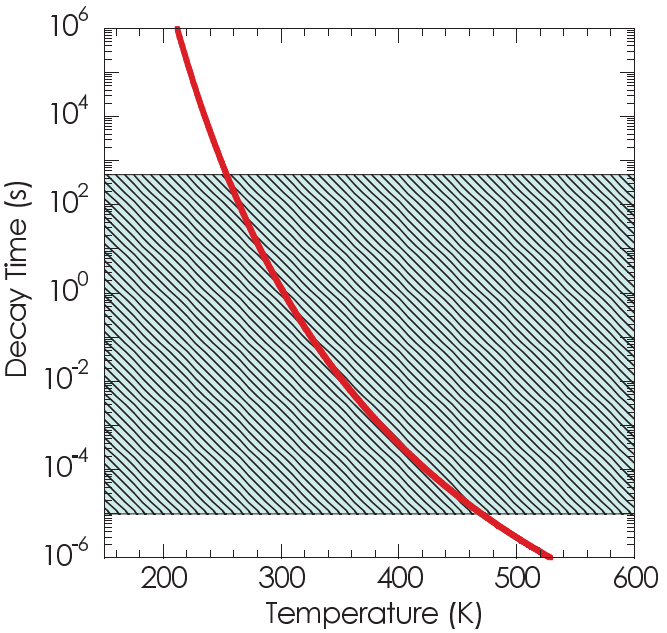

FIG. 3. (Color online) Temperature dependence of the decay time of a trap with depth $E = 0.84$ eV and a frequency factor $s = 1 \cdot 10^{14}$ s^{-1}. The dashed area indicates the time window $[t_1, t_2] = [10\ \mu s, 600\ s]$.

the lower limit t_1 of the time window is high enough to avoid the prompt emission from being detected by our system. The delayed recombination intensity value $A_{DR}(T)$ that we obtain at temperature T is then given by

$$A_{DR}(T) = \int_{t_1}^{t_2} I(t;T)dt = I_{0;T}\tau(T)\left(e^{-\frac{t_1}{\tau(T)}} - e^{-\frac{t_2}{\tau(T)}}\right). \quad (4)$$

If we integrate expression (2) from 0 to ∞ we obtain the total delayed recombination light, that is

$$A^{\infty}_{DR}(T) = \int_{0}^{\infty} I(t;T)dt = I_{0;T}\tau(T). \quad (5)$$

This means that the fraction of the total delayed recombination light that is emitted within the time window $[t_1, t_2]$ and collected by the detection system is

$$\frac{A_{DR}(T)}{A^{\infty}_{DR}(T)} = \left(e^{-\frac{t_1}{\tau(T)}} - e^{-\frac{t_2}{\tau(T)}}\right). \quad (6)$$

As a realistic numerical example, let's consider a trap with a thermal depth $E = 0.84$ eV, a frequency factor $s = 1 \cdot 10^{14}$ s^{-1}, and a detection system integrating in the time window $[t_1, t_2] = [10\ \mu s, 600\ s]$. The trap decay time can be calculated from expression (3), and its temperature dependence is plotted in Fig. 3. The shaded area indicates the region within the detection system time window, and it evidences that the trap decay time falls within the time window when the temperature is between approximately 250 K and 470 K.

Due to the strong temperature dependence of the trap decay time $\tau(T)$, the ratio in expression (6) is consequently also affected by temperature; this dependence is shown in Fig. 4.

From the plot it is evident that the ratio $A_{DR}/A^{\infty}{}_{DR}$ is close to 0 at any temperature except for the same temperature range in which the trap decay time falls within the time window $[t_1, t_2]$. The physical meaning of this curve is straightforward.

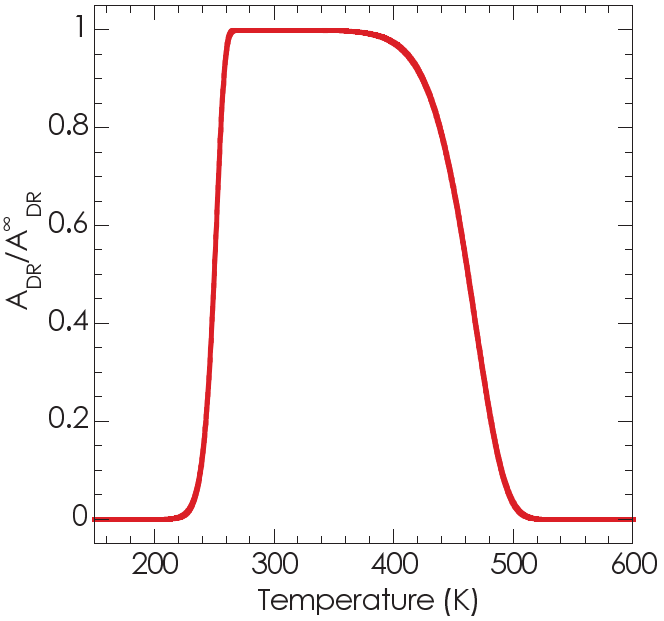

FIG. 4. (Color online) Temperature dependence of the fraction of delayed recombination light related to a trap with $E = 0.84$ eV and a frequency factor $s = 1 \cdot 10^{14}$ s^{-1} emitted in the time window $[t_1, t_2] = [10\ \mu s, 600\ s]$.

At high temperature (above 500 K), the trap decay time is so short that, after the excitation pulse, most of the trapped electrons are released (and recombine) in a time shorter than t_1 and cannot be detected. To the opposite limit, at any temperature lower than 250 K, the trap decay time is extremely long so that most of the delayed recombination light is emitted at longer times than t_2. Only for intermediate temperatures a significant fraction of the light is detected. Following all these considerations, the intensity $I(T)$ of the delayed recombination light emitted in the time window $[t_1, t_2]$ is given by

$$I(T) = const \cdot e^{-\frac{E_{th}}{k_B T}}\left(e^{-\frac{t_1}{\tau(T)}} - e^{-\frac{t_2}{\tau(T)}}\right). \quad (7)$$

If we now extend the model to the case in which several trap species are involved, we need to sum the contribution of each trap to the delayed recombination light,

$$I(T) = const \cdot e^{-\frac{E_{th}}{k_B T}} \cdot \sum_i A_i\left(e^{-\frac{t_1}{\tau_i(T)}} - e^{-\frac{t_2}{\tau_i(T)}}\right), \quad (8)$$

where the index i runs through the different type of traps, and the constants A_i account for the different filling of the traps due to their different electron-capture probability. The temperature dependence of the decay time of each trap $\tau_i(T)$ can be calculated from experimental data obtained from TSL measurements. In fact the initial rise technique[14] allows the evaluation of the thermal depth energy E_i of a trap and, if its recombination is of first order kinetics, also of its frequency factor s_i. The decay time of the trap at temperature T is then obtained from expression (3).

According to the model, the experimental procedure required to evaluate the thermal ionization barrier E_{th} can be summarized in three steps.

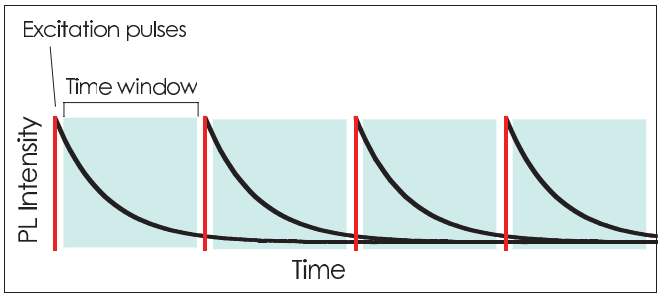

FIG. 5. (Color online) Sketch of the delayed recombination measurement.

(1) Measurement of the delayed recombination light intensity $I(T)$ integrating within the time window $[t_1, t_2]$ for a set of different temperatures T.

(2) Evaluation of the decay $\tau(T)$ for each trap from the trap energy depth E and its frequency factor s obtained from TSL analysis.

(3) Numerical fit of expression (8) to obtain the value of the desired parameter E_{th}.

Let's now apply the method to the case of LPS:Pr.

1. Step 1

The delayed recombination light intensity was monitored using conventional equipment for PL decay time measurements. The sample was excited in the $4f$-$5d_1$ absorption band (240 nm) of Pr^{3+} by a Xenon flashlamp (with a pulse width of about 3–4 μs and flash rate of approximately 10^2 Hz). The emission monochromator was set to 305 nm, close to the maximum of the $5d_1$-$4f$ emission. The detection was performed with the multichannel scaling method scanning the decay for approximately 10 ms. The system was set so that each excitation pulse (and corresponding measurement window opening) occurred immediately after the previous one so that nonmonitored intervals between successive time windows were due only to the dead time of the electronics (less than 100 μs). The measurement sequence is sketched in Fig. 5. The accumulation time for each measurement was 10 minutes. The measurement was performed at different temperatures in the range 197–497 K starting from the highest temperature.

In Fig. 6 some of the decay curves obtained are shown. It is important to notice that the time scale considered is several orders of magnitude longer than the characteristic decay time of the $5d_1$-$4f$ transition of Pr^{3+} (10 ms compared to tens of ns). A single channel covers 10.667 μs so that, apart from the first 4–5 channels containing the excitation pulse, all of the detected light is due to delayed recombination. We remark that the apparent increase of the background level (clearly visible in the channels before the excitation pulse) is due to delayed recombination light emitted at times longer than 10 ms and excited by previous pulses. The slow tails of the decays stack together increasing the background signal (see Fig. 5). As expected, this phenomenon is particularly evident for measurements performed at higher temperature where the thermal ionization of the excited level of Pr^{3+} is more effective. For the evaluation of the delayed recombination light we proceeded as follows. We first removed the first 4–5 channels containing the excitation pulse and the prompt

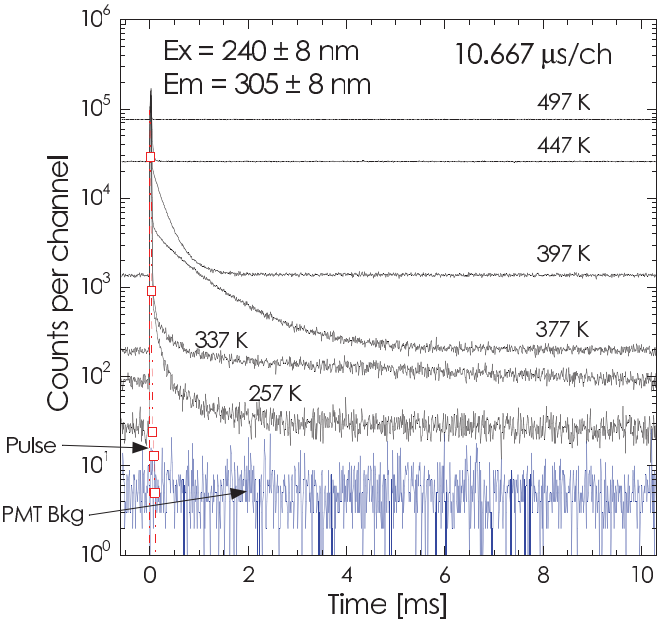

FIG. 6. (Color online) Delayed recombination curves performed on LPS:0.5mol%Pr at different temperatures under excitation of the $4f$-$5d_1$ transition of Pr^{3+} and monitoring the $5d_1$-$4f$ emission. The signal was accumulated for 600 s.

recombination light. Then we subtracted the background level detected in the channels before the pulse, and we integrated the curve in the whole time range (Fig. 7, grey area). The value obtained corresponds to an integration of the signal in the time window [53 μs, 10.3 ms]. As a second option for the integration we subtracted the true photomultiplier background level integrating the signal marked by the dashed area in Fig. 7. This integration is approximately equivalent to collecting the delayed recombination light emitted during

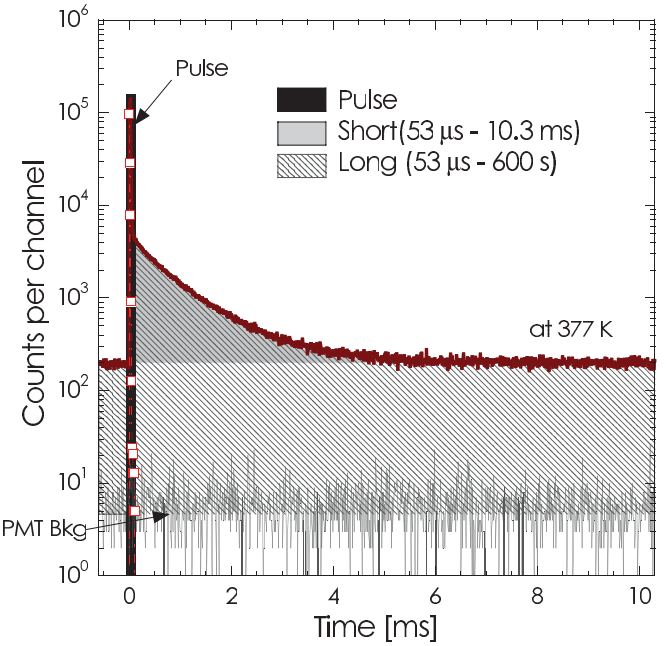

FIG. 7. (Color online) Example of the evaluation of the delayed recombination light emitted in two different time integration ranges.

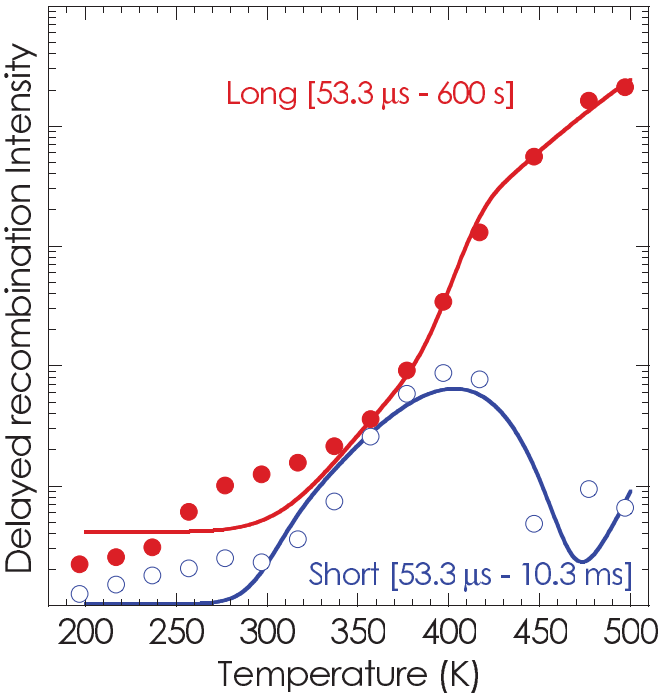

FIG. 8. (Color online) Temperature dependence of the delayed recombination light emitted by LPS:0.5mol%Pr in two different time integration ranges. The lines are numerical fits according to Eq. (8) with $E_{th} = 0.42$ eV for the short integration range and $E_{th} = 0.54$ eV for the long integration range. In the fits, we associated a statistical error to the data.

the whole measurement and corresponds to a time window [53 μs, 600 s]. However, we are aware that this latter integration tends to underestimate the contribution of the slower decay components since the excitation pulses occurring toward the end of the measurements can contribute only to the fast components. Conversely, the short integration window is not affected by this problem, but data show a lower reliability due to the critical evaluation of the integral.

We will refer to the two different time integrations in the ranges [53 μs, 10.3 ms] and [53 μs, 600 s] as the "short" and "long" time windows, respectively. The intensity of the delayed recombination light emitted within both the short and long time window is reported as a function of temperature in Fig. 8. These curves were corrected for the temperature dependence of the PL efficiency of the Pr^{3+} $5d_1$-$4f$ emission measured in steady-state mode.

2. Step 2

We employed wavelength-resolved TSL measurements to identify which traps display emission in the $5d_1$-$4f$ transition of Pr^{3+}, which was selected for the PL-delayed recombination measurements. Figures 9–11 display the measurements performed both above (Figs. 9 and 10) and below (Fig. 11) RT. Above RT, we could compare the TSL patterns obtained after both light illumination and x-ray irradiation (Figs. 9 and 10, respectively): in the $5d_1$-$4f$ emission region up to 400 nm, we observed the same TSL peaks at 460 and 515 K (see Fig. 1) with different relative intensities. The emission of the highest T-peak in the 600 K region is centered at

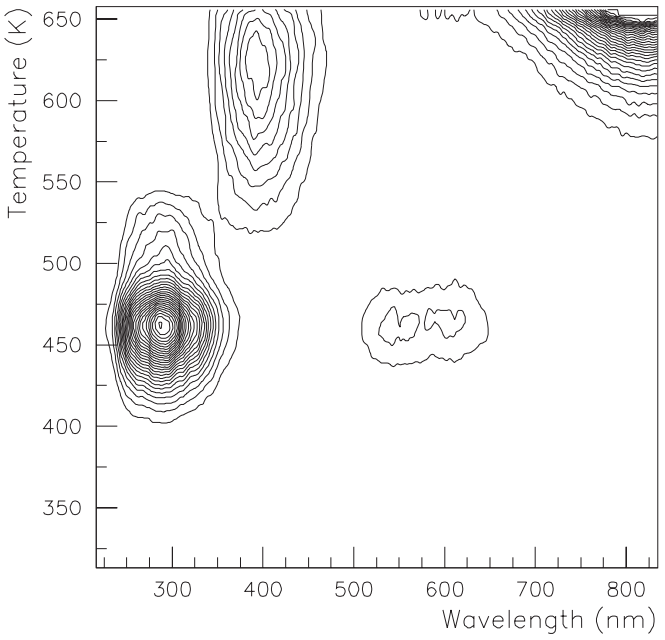

FIG. 9. Wavelength-resolved TSL measurements performed on LPS:0.5mol%Pr after RT 240 nm light irradiation.

400 nm; such emission is no longer due to Pr^{3+}, while it could be related to a defect. Therefore such a peak should not be considered in the numerical fit of expression (8) to be performed in Step 3. Analogous considerations can be made for the low T measurement: the only peaks emitting in the $5d_1$-$4f$ transition of Pr^{3+} are those at 77, 211, and 267 K.

We therefore evaluated the parameters of six traps responsible for peaks at 77, 211, 267, 334, 460, and 515 K by the "initial rise" method applied after suitable partial cleaning procedures of the glow curves coupled to numerical peak reconstruction

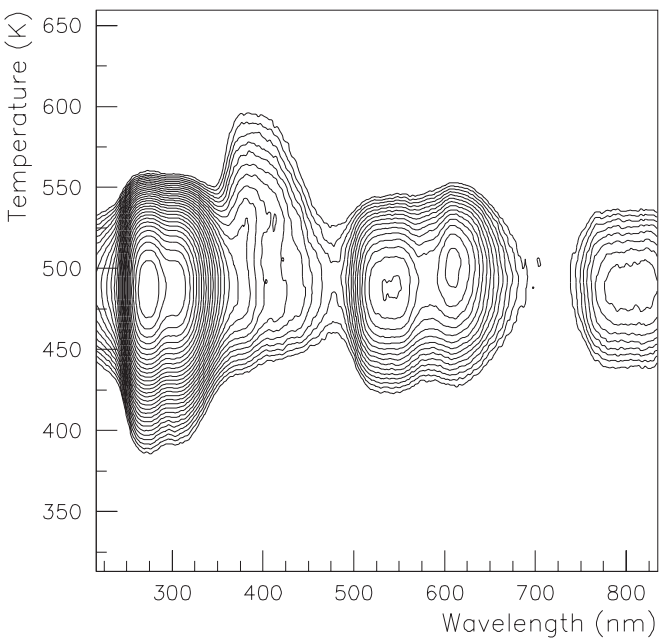

FIG. 10. Wavelength-resolved TSL measurements performed on LPS:0.5mol%Pr after RT x-ray irradiation.

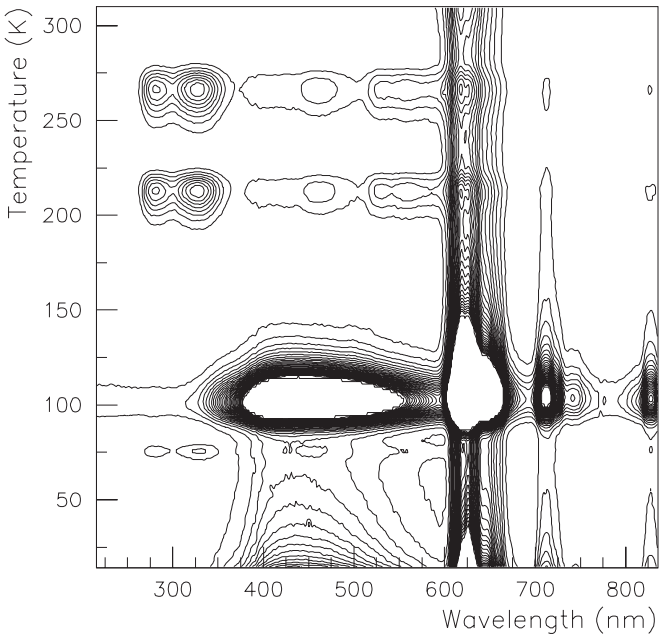

FIG. 11. Wavelength-resolved TSL measurements performed on LPS:0.5mol%Pr after x-ray irradiation at 10 K.

technique.[14] The results are reported in Table I. The data are similar to those reported in Ref. 15. In that paper only one broad peak could be evidenced in the 480 K region. In this case, using light illumination, we could identify two distinct peaks at 460 and 515 K.

3. Step 3

The delayed recombination curves were fit according to Eq. (8). The decay times of each trap entering in the equation were calculated from the values of T_m and E using expression (3), where s given by

$$s = \frac{\beta E}{k_B T_m^2} e^{\frac{E}{k_B T_m}}. \quad (9)$$

Equation (9) is valid in the framework of first-order recombination kinetics, which the involved TSL peaks were shown to obey to in Ref. 15. In order to reduce the number of parameters, we chose to consider only four TSL peaks that displayed a relative higher intensity, namely those at 77, 211, 267, and 460 K.

We chose to use the following fit approach. The parameters E and T_m were fixed to the experimental values obtained from TSL. The amplitudes A_i and the ionization energy E_{th} were considered free parameters. In this case we experienced a substantial difficulty of obtaining fit convergence because of the high number of parameters. Therefore we moved to a semistatistical approach using *Mathematica 8.0* software: the starting values of E_{th} and of the amplitudes A_i were generated randomly and kept fixed during each fit session. As many as 10^4 sessions were performed. Selected examples of the fits are reported in Fig. 8. The values of E_{th} minimizing χ^2 were 0.42 eV and 0.54 eV for the short and the long time windows, respectively. The values obtained are consistent with those evaluated with the first method. However, we underline that the evaluation of trap parameters by TSL analysis should be carried on in an optimal way in order to obtain a reliable result. Indeed, we succeeded to reconstruct very well low T TSL peaks with the parameters obtained, while not fully satisfactory results were found for peaks above 400 K.

With respect to Method I, this second approach is certainly more complicated, since it requires more complex experiments and delicate data analyses. However, for those materials in which stable traps are absent in a convenient temperature range, it could be the only practicable route. Besides the proposed application perspectives, we believe that such a model satisfactorily shows the relationship between trapping centers, TSL-glow curves, and delayed recombination processes revealing the complicated dynamics of carrier trapping, detrapping, and recombination as a function of temperature,

TABLE I. Parameters of TSL peaks recombining in the $5d_1$-$4f$ transition of Pr^{3+}. The error for E is $\pm 10\%$.

LPS:Pr	T_m (K)	E (eV)
LT	77 ± 2	0.19
	211 ± 2	0.53
	267 ± 2	0.80
HT	334 ± 2	0.80
	460 ± 7	1.27
	515 ± 7	1.10

IV. CONCLUSIONS

Two methods for the evaluation of the thermal ionization energy, E_{th}, of an excited state level of a RE ion in an insulating host have been described. In both cases the role of defects acting as carrier traps has been exploited. The investigation has been focused on LPS:Pr scintillator as an example.

One approach involves only TSL measurements following ultraviolet irradiation with light belonging to the excitation spectrum of the $4f$-$5d_1$ level at several temperatures. As it has been described, the method is relatively simple and allows a reliable evaluation of E_{th}, provided that some necessary properties of the traps employed are verified, like thermal stability in the temperature range considered and TSL emission linearity versus their filling by carriers.

The second approach consists of considering the tight correlation between delayed recombination decay related to the $5d_1$-$4f$ transition and defects acting as carrier traps delaying their radiative recombination. In this paper we have proposed the feasibility of a numerical reconstruction of the temperature dependence of the slow components' intensity with the sum of contributions from different traps investigated by TSL, in two different time windows.

This represents a clear and quantitative evidence of such correlation, which was proposed until now mainly in a qualitative way. Moreover, we have shown that such numerical reconstruction also allows the determination of the thermal ionization energy that can be considered as a free parameter of the fit. At variance with the first method, in this case no specific requirements for the characteristics of traps are needed. However, due to the complexity of the fit, the use of this approach requires a very careful preventive investigation of traps parameters by TSL methods. Future tests of such a

method on other materials and its comparison with different techniques will allow one to further verify its reliability.

ACKNOWLEDGMENTS

The financial support of the Italian CARIPLO Foundation project "Energy transfer and trapping processes in nanostructured scintillator materials" (2008–2011) of the Czech Academy of Sciences GAAV project KAN300100802 and of the MSMT KONTAKT project ME10084 are gratefully acknowledged. The authors are thankful to G. Ren from Shanghai Institute of Ceramics for providing the crystals for this study.

*mauro.fasoli@mater.unimib.it

[1]P. Dorenbos, J. Phys. Condens. Matter **15**, 575 (2003).
[2]P. Dorenbos, A. H. Krumpel, E. van der Kolk, P. Boutinaud, M. Bettinelli, and E. Cavalli, Opt. Mater. **32**, 1681 (2010).
[3]N. R. J. Poolton, A. J. J. Bos, G. O. Jones, and P. Dorenbos, J. Phys. Condens. Matter **22**, 185403 (2010).
[4]P. Dorenbos and A. J. J. Bos, Radiat. Meas. **43**, 139 (2008).
[5]J. Fleniken, J. Wang, J. Grimm, M. J. Weber, and U. Happek, J. Lumin. **94–95**, 465 (2001).
[6]H. Loudyi, Y. Guyot, S. A. Kazanskii, J.-C. Gâcon, B. Moine, C. Pédrini, and M.-F. Joubert, Phys. Rev. B **78**, 045111 (2008).
[7]U. Happek, S. A. Basun, J. Choi, J. K. Krebs, and M. Raukas, J. Alloys Compd. **303–304**, 198 (2000).
[8]C. W. Thiel, H. Cruguel, H. Wu, Y. Sun, G. J. Lapeyre, R. L. Cone, R. W. Equall, and R. M. Macfarlane, Phys. Rev. B **64**, 085107 (2001).
[9]J. Pejchal, M. Nikl, E. Mihokova, A. Novoselov, A. Yoshikawa, and R. T. Williams, J. Lumin. **129**, 1857 (2009).
[10]H. Feng, V. Jary, E. Mihokova, D. Ding, M. Nikl, G. Ren, H. Li, S. Pan, A. Beitlerova, and R. Kucerkova, J. Appl. Phys. **108**, 033519 (2010).
[11]D. Pauwels, N. Lemasson, B. Viana, A. Kahn-Harari, E. V. D. van Loef, P. Dorenbos, and C. W. E. van Eijk, IEEE Trans. Nucl. Sci. **47**, 1787 (2000).
[12]L. Pidol, B. Viana, A. Kahn-Harrari, A. Bessiere, and P. Dorenbos, Nucl. Instrum. Methods Phys. Res. A **537**, 125 (2005).
[13]H. Y. Li, L. S. Qin, S. Lu, and G. H. Ren, J. Inorg. Mater. **21**, 527 (2006).
[14]S. W. S. McKeever, *Thermoluminescence of Solids* (Cambridge University Press, Cambridge 1985).
[15]E. Mihóková, M. Fasoli, F. Moretti, M. Nikl, V. Jarý, G. Ren, and A. Vedda, Opt. Mater **34**, 872 (2012).

Chemical Physics Letters 556 (2013) 89–93

Contents lists available at SciVerse ScienceDirect

Chemical Physics Letters

journal homepage: www.elsevier.com/locate/cplett

Trapping states and excited state ionization of the Ce^{3+} activator in the $SrHfO_3$ host

E. Mihóková [a,*], V. Jarý [a], M. Fasoli [b], A. Lauria [b,1], F. Moretti [b,2], M. Nikl [a], A. Vedda [b]

[a] Institute of Physics, AS CR v.v.i., Cukrovarnická 10, 16253 Prague, Czech Republic
[b] Dip. di Scienza dei Materiali, Università di Milano-Bicocca, via Cozzi 53, 20125 Milano, Italy

ARTICLE INFO

Article history:
Received 15 November 2012
In final form 18 November 2012
Available online 27 November 2012

ABSTRACT

We study trapping states of Ce^{3+}-doped $SrHfO_3$ by thermally stimulated luminescence in a wide temperature range (10–730 K). We determine characteristic parameters of the traps by the initial rise technique. We also determine the energy of thermal ionization of the excited state of Ce^{3+} in $SrHfO_3$ host by purely optical method based on the study of UV illumination-induced thermoluminescence. The method provides a value of the thermal ionization energy of about 0.25 eV.

1. Introduction

Ce^{3+}-doped $SrHfO_3$ (SHO) has attracted recent interest as a scintillating material due to its high density (7.56 g/cm^3) and high effective atomic number. Because of its high melting point (T_m > 2400 °C) the material is not available as a single crystal and therefore is currently being investigated in the form of nanocrystals [1,2] or ceramics obtained from crystalline powders prepared by solid-state synthesis [3]. Alternative techniques for the preparation of Ce-doped SHO powders are the sol–gel route [4,5] or acetate–citrate combustion [6,7].

Fast photoluminescence (PL) and scintillation response of SHO:Ce^{3+} are ensured by the allowed $5d_1 \rightarrow 4f$ transition of the Ce^{3+} ion. The PL and scintillation room temperature (RT) decay times previously reported were 36 and 42 ns, respectively [2,3]. More recent studies [6] performed in powder samples prepared by two different preparation techniques found PL decay time values of about 15 ns. Not only is this value significantly different from that reported in [2], but it is also the shortest decay time observed for a Ce^{3+} activator in any known scintillating host. The surprisingly short RT decay time indicates the possibility of temperature quenching or ionization of the luminescent center, undesired phenomena degrading scintillator performance. A recent study [8] devoted to this issue indeed confirmed thermal ionization of the excited state of the Ce^{3+} center in the SHO host. The evidence is provided by several observations: (i) shortening of the prompt nanosecond PL decay time with increasing temperature, (ii) observation of delayed recombination decay at the Ce^{3+} center after its UV excitation, and (iii) detection of the thermally stimulated luminescence (TSL) signal after UV excitation at RT.

The energy of thermal ionization of the excited state of a luminescent center in a host is an important characteristic affecting the figure of merit of a scintillating material. It is usually experimentally determined by photoconductivity measurements. The conventional photoconductivity technique is applicable only to materials in the form of crystals. For materials in powder form one has to look for 'contactless' alternatives. The microwave resonator technique for the study of photoconductivity in rare-earth-doped dielectric crystals [9] was for the first time used for powder samples in [10]. Another possibility is given by the recently described optical experimental method involving the study of temperature dependence of the TSL signal obtained after UV illumination [11].

In this Letter we study trapping states of SHO:Ce^{3+} in a wide temperature range (10–730 K). We determine characteristics of the traps by the initial rise technique. We also study the thermal ionization of the Ce^{3+} excited state in the SHO host in a greater detail. We aim to determine the ionization energy of the luminescence center by an approach introduced in [11]. It is based on the study of the temperature dependence of the TSL glow curve observed after UV excitation of the Ce^{3+} center.

2. Experimental details

Ce^{3+} doped SHO samples were prepared by acetate and citrate combustion. The preparation technique is described elsewhere [6,7]. Dopant concentration was 0.1 mol%. The final sintering temperature was 1150 °C.

Wavelength resolved thermally stimulated luminescence (TSL) measurements in the 10–310 K temperature range were performed with a heating rate of 0.1 K/s after irradiation at 10 K. The detection system featured a CCD detector (Jobin-Yvon Spectrum One 3000) coupled to a monochromator (Jobin-Yvon Triax 180) with 100 grooves/mm grating operating in the range 200–1100 nm.

* Corresponding author. Fax: +420 2 312 3184.
E-mail address: mihokova@fzu.cz (E. Mihóková).
[1] Present address: Department of Materials, ETH Zurich, Wolfgang Pauli Strasse, 10, HCI F 506, 8093 Zurich, Switzerland.
[2] Present address: LPCML, Université Claude Bernard Lyon 1, Bâtiment Alfred Kastler, 10 rue Ada Byron, 69622 Villeurbanne cedex, France.

0009-2614/$ - see front matter © 2012 Elsevier B.V. All rights reserved.
http://dx.doi.org/10.1016/j.cplett.2012.11.039

TSL glow curves above RT were measured after irradiation at RT from 293 up to 730 K using a linear heating rate of 1 K/s. The emitted light was detected in photon counting mode by a photomultiplier (EMI 9635QB). X-ray irradiation was realized with Philips 2274 and Machlett OEG50 tubes operating at 20 and 30 kV for irradiations at 10 K and RT, respectively. UV illumination at 310 nm was performed by exploiting the beam of a Perkin Elmer Lambda 950 spectrometer. The temperature of the sample during UV illumination was controlled by a Peltier cell (20.9W 2.2 APE-127-08-15).

Photoluminescence (PL) measurements were performed by a custom made 5000M Horiba Jobin Yvon spectrofluorometer. Excitation by the deuterium steady-state lamp was used for the emission spectra measurements. An Oxford Instruments liquid nitrogen bath optical cryostat allowed temperature regulation from about 150 to 500 K.

Steady-state PL excitation spectra in the UV–VUV region were measured at the Superlumi station in DESY using the detector in the standard 'integral' as well as 'fast component' and 'slow component' regimes with 'all times', '0–5 ns' and '150–190 ns' time gates, respectively (time-0 refers to the excitation pulse arrival).

3. Results and discussion

3.1. Study of the trapping states by TSL

The TSL glow curve of SHO:Ce^{3+} after irradiation at 10 K (Figure 1) features well resolved TSL peaks at about 80, 100, 205, 230, 255 and 290 K. No shifts of the temperature positions of the peak maxima were observed by varying the irradiation dose by about two orders of magnitude. Therefore it may be concluded that these peaks follow first order recombination kinetics [12]. The contour plot displayed in Figure 2 shows the presence of a prominent emission due to Ce^{3+} ion at around 400 nm [6,13] accompanied by a weak defect emission at higher wavelength.

To evaluate the depths of the traps associated with the observed TSL peaks we used the *initial rise* technique (including partial cleaning of the glow curve) [12]. For each TSL peak we performed from two to three partial cleanings of the curve and corresponding initial rise evaluations. The amplitude of initial part of the glow peak can be approximated by an exponential function:

$$\mathrm{Amp}(T) = b + we^{-\frac{E}{kT}}, \quad (1)$$

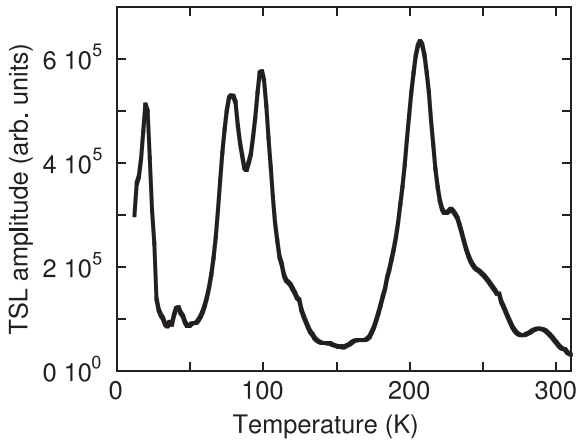

Figure 1. TSL glow curve of SHO:Ce^{3+} plotted as a function of temperature after X-ray irradiation at 10 K. The signal was obtained after integration of the wavelength resolved measurement in the 300–700 nm range.

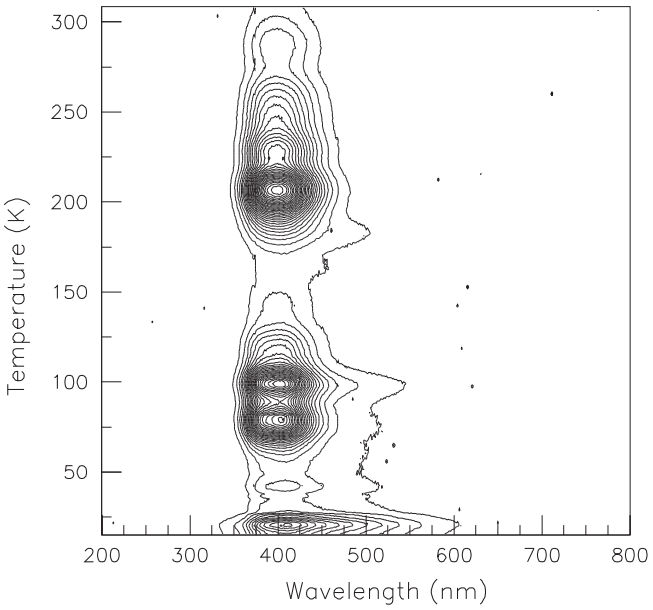

Figure 2. Wavelength resolved TSL measurements performed on SHO:Ce^{3+} after X-ray irradiation at 10 K.

where b is a constant, E is the trap depth, w is a pre-exponential factor, k is the Boltzmann's constant and T is the absolute temperature. The frequency factors associated with traps whose TSL peaks follow the first order recombination kinetics can be calculated from the formula relating the frequency factor s, the heating rate β and the temperature maximum of the TSL peak T_m:

$$\beta E/kT_m^2 = s \times e^{-\frac{E}{kT_m}} \quad (2)$$

The lifetime of the trap τ at the temperature T can be calculated as:

$$\tau = s \times e^{\frac{E}{kT}} \quad (3)$$

The average value of the trap depths, frequency factors corresponding to the first order recombination kinetics and RT lifetimes are listed in Table 1. Considering an error of about 1 K in the determination of the position of the TSL peak maximum, only the order of magnitude of the frequency factor can be estimated.

The TSL glow curve of SHO:Ce^{3+} after irradiation at RT (see the inset of Figure 3) features the TSL peaks at about 320, 413, 473 and 583 K. It should be pointed out that due to variation in the heating rate (1 K above RT versus 0.1 K below RT) the TSL peaks at 320 K (the inset of Figure 3) and 290 K (Figure 1) most probably corre-

Table 1
Trap parameters obtained by initial rise technique and consideration of the first order recombination kinetics.

T_m (K)	E (eV)	s (s^{-1})	τ (s) at RT
Irr. at 10 K			
78	0.12 ± 0.01	$\sim 10^{6}$	$\sim 10^{-6}$
100	0.19 ± 0.01	$\sim 10^{8}$	$\sim 10^{-5}$
205	0.48 ± 0.01	$\sim 10^{10}$	$\sim 10^{-2}$
230	0.46 ± 0.01	$\sim 10^{8}$	~ 1
255	0.60 ± 0.01	$\sim 10^{10}$	~ 1
290	0.76 ± 0.01	$\sim 10^{11}$	$\sim 10^{2}$
Irr. at RT			
320	0.9 ± 0.1	$\sim 10^{13}$	$\sim 10^{2}$
413	0.97 ± 0.01	$\sim 10^{10}$	$\sim 10^{6}$
473	1.15 ± 0.04	$\sim 10^{11}$	$\sim 10^{9}$
583	1.60 ± 0.04	$\sim 10^{12}$	$\sim 10^{15}$

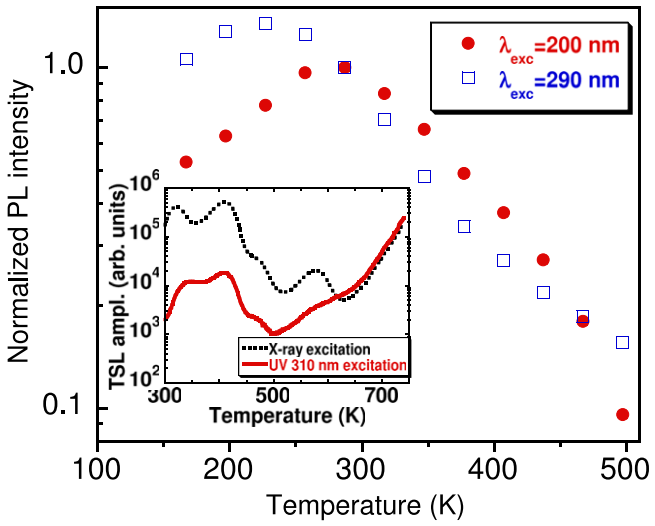

Figure 3. Temperature dependence of the normalized (at RT) PL intensity of $SrHfO_3:Ce^{3+}$. The PL emission spectra excited at 200 nm (solid circles) and 290 nm (empty squares) were integrated in the range 350–540 nm of the 5d–4f Ce^{3+} emission. In the inset are reported TSL glow curves of $SrHfO_3:Ce^{3+}$ after X-ray irradiation as well as UV illumination (310 nm, 35 min) at RT. The high temperature monotonic increase of the signal corresponds to black body emission.

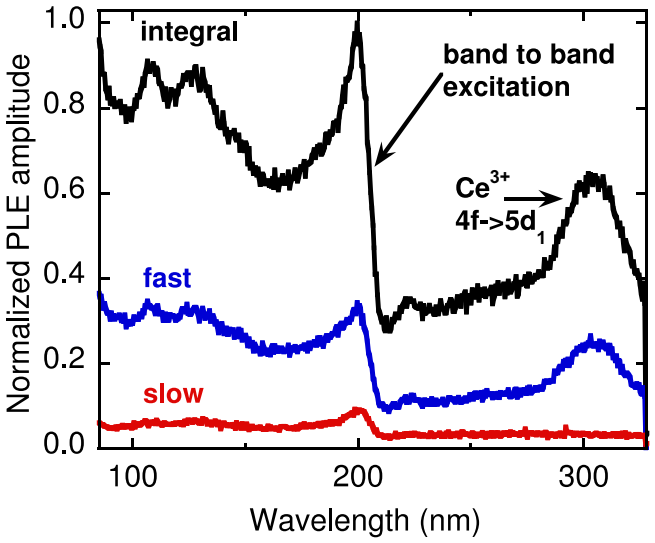

Figure 4. Normalized PL excitation spectra of $SrHfO_3:Ce^{3+}$ at RT with λ_{em} = 380 nm. The curves indicated in the figure correspond to measurements performed in various detector regimes:integral, fast component and slow component (cf. Section 2).

spond to the same trap. Variation of the irradiation dose by about two orders of magnitude confirmed that TSL peaks above RT also follow the first order recombination kinetics. Corresponding TSL spectra [8] similarly to those below RT confirmed the predominant presence of the Ce^{3+} recombination center emitting around 400 nm. To evaluate the characteristic parameters of the traps associated with TSL peaks an analogous procedure described above was applied. For quantitative analysis, however, the TSL glow curves above RT had to be corrected for the temperature quenching of the Ce^{3+} recombination center, as was done, for example, in [14]. The details on the correction procedure are given below. Corresponding trap depths, frequency factors and RT lifetimes are listed in Table 1.

3.2. Correction for the temperature quenching of the Ce^{3+} emission center

The correction curve for Ce^{3+} emission quenching can be obtained from the temperature dependence of the steady-state PL intensity. In Figure 3 we present the PL intensity of the Ce^{3+} emission band measured under excitation in both the host lattice (200 nm) and the Ce^{3+} absorption band (290 nm). We find the data obtained for the excitation at 200 nm more suitable for determination of the correction since they are less affected by possible distortions due to following reasons.

First and most important, there is a larger energy separation between excitation and emission light, i.e., less of a problem with light scattering. The data obtained for the 290 nm excitation (cf. Figure 3) show a less steep decrease above 400 K due to the contribution of the scattered excitation light which distorts the true shape of the curve. This problem does not occur in emission spectra for the host lattice 200 nm excitation.

Second, the temperature change has a weaker effect on the absorption profile. Unlike the case of an optically thick bulk crystal, the outgoing PL light in powder is collected only from several outer grain layers of the sample due to scattering losses on powder grains. As a result, the portion of the incident light contributing to the measured PL amplitude critically depends on the amplitude of absorbance. It is extremely difficult to experimentally quantify the scattering losses. On the other hand, the temperature change of absorbance amplitude can be significant, also due to effects like temperature exchange of absorption strengths for 4f–$5d_1$ and 4f–$5d_2$ transitions of Ce^{3+} as shown in Ce^{3+}-doped $Y_3Al_5O_{12}$ (YAG) crystal [15]. The change in absorbance of 4f–$5d_1$ transition of Ce^{3+} in YAG:Ce between 300 and 500 K becomes more than 25% [16]. A much smaller effect of absorbance amplitude is expected under excitation at the absorption edge of the host when the excitation light is fully absorbed within only a thin layer (several μm) of the powder. On the other hand, in this case the distortion of the temperature dependence of the PL intensity could occur due to the energy losses in the process of transfer between the host and the Ce^{3+} center. Nevertheless, PLE spectra of $SHO:Ce^{3+}$ measured in the VUV region [13] showed rather efficient energy transfer between the SHO host and the Ce^{3+} ion. PLE spectra at RT (see Figure 4) show in great detail that the transfer of excitation from the host to the Ce^{3+} luminescence ion is not only efficient but also fast. This is because the contribution of the slow component (time gate 150–190 ns) to the PLE peak at 200 nm is substantially weaker compared to that of the fast component (time gate 0–5 ns), at least from RT above.

The PL intensity under the 200 nm excitation features a monotonic decrease from RT down to low temperatures (cf. Figure 3). The observation might be due to decreasing efficiency of the energy transfer between the host and the Ce^{3+} center with decreasing temperature. This is feasible considering that the Ce^{3+} excitation is competing with the excitation of the self-trapped exciton or some other state [13] that is quenched (thermally disintegrated) with increasing temperature. Consequently, for the purpose of defining the correction curve (due to the intracenter Ce^{3+} temperature quenching) the PL intensity from RT down to low temperatures was considered constant.

3.3. Study of ionization of the Ce^{3+} excited state by TSL

Detection of the TSL signal in the material after the PL excitation of the luminescence center indicates that the carriers were thermally promoted into the conduction or valence bands. In the case of the Ce^{3+} luminescence center in the SHO host the PL excitation would involve a direct 4f → $5d_1$ transition of Ce^{3+} located around 300 nm. Electrons migrate in the conduction band and can be trapped by point defects. When they are released and finally deliv-

ered to the luminescence center, their radiative recombination produces the TSL light. The TSL intensity after the PL excitation of the luminescence center will be proportional to the fraction of carriers N_I that thermally ionizes and enters the conduction band:

$$N_I(T) = we^{-\frac{E_{ion}}{kT}}, \quad (4)$$

where T is the excitation temperature, w is a pre-exponential factor, E_{ion} is the thermal ionization energy (the energy separation between the excited state of the luminescent center and the bottom of the conduction band) and k is Boltzmann's constant. Eq. (4) is a reasonable approximation when retrapping to Ce^{3+} is either not significant or temperature independent, and one does not consider possible intrinsic temperature dependence of E_{ion}. When this holds, from the study of the temperature dependence of the TSL intensity excited by the UV light one can, in principle, estimate the ionization energy E_{ion}.

Based on this concept we pursue determination of the ionization energy of the Ce^{3+} center in the SHO host. Then we studied the excitation temperature dependence of UV excited TSL glow curves.

The sample was illuminated at the defined temperature by UV light (310 nm) corresponding to the Ce^{3+} $4f \rightarrow 5d_1$ absorption band. After illumination it was cooled (or heated) to RT and the TSL glow curve in the 293–730 K temperature interval was recorded.

TSL glow curves obtained after both X-ray and UV (310 nm) irradiations of the SHO:Ce^{3+} sample at RT (the inset of Figure 3) were already presented in [8]. The observed TSL peaks have been associated with electron traps and Ce^{3+} as also mentioned above was identified as the single TSL-active recombination center.

The TSL glow curves obtained for a sequence of illumination temperatures are displayed in Figure 5a,b. Here we present only the temperature region (where the TSL signal is not masked by black body radiation) that was used in a subsequent analysis. One can see that starting from the highest illumination temperature, 347 K, the TSL glow curves become less intense as the illumination temperature progressively decreases. This observation nicely correlates with the expected decreasing probability of the center thermal ionization according to formula (4). Note that from illumination temperature 347 K down to 313 K we only observe one dominant TSL peak at about 410 K. As the illumination temperature decreases, a TSL peak at about 330 K appears. Its intensity increases with decreasing illumination temperature. From 272 K to the lowest illumination temperatures it becomes consistently more intense relative to that of the 410 K peak. The temperature evolution of these two peaks reflects their partial or even full (for the 330 K peak) thermal decay above certain illumination temperatures.

To exclude possible effects of signal saturation we checked that the measured glow curves fall into the linear regime of the TSL signal dependence on the irradiation dose. The results in the inset of Figure 6 demonstrate that up to about six times the TSL intensity presented in Figure 5a,b, the dependence on the dose is indeed linear.

For subsequent attempts to determine the ionization energy of the Ce^{3+} center from the TSL data, those with fully or partially decayed TSL peaks are not directly applicable. For simplicity, we decided to take into consideration only the data obtained in the range of illumination temperatures where the TSL signal is reasonably intense and both TSL peaks are sufficiently stable. Alternatively, all glow curves could have been considered, integrating the signal only in the temperature range unaffected by thermal decay.

The TSL intensity corresponding to a specific illumination temperature was obtained by integration of the TSL glow curve in the range 300–470 K. Arrhenius plot of TSL intensity as a function of

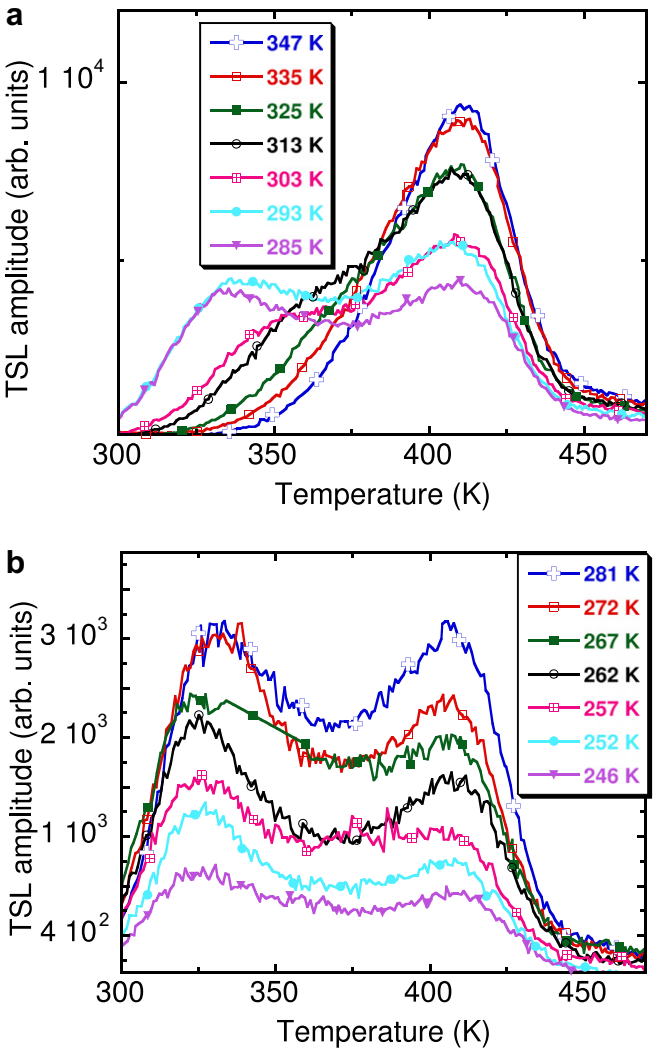

Figure 5. Both (a) and (b) show the influence of temperature variation on the TSL glow curves of $SrHfO_3$:Ce^{3+} after UV illumination at 310 nm for 35 min. The illumination temperature is reported in the legend.

illumination temperature T_{ill} is presented in Figure 6. Due to the reasons discussed above the TSL intensity from intermediate to high T_{ill} (solid squares) does not manifest behavior consistent with formula (4). In contrast, the TSL intensity obtained for T_{ill} in the region from 246 to 293 K (solid circles) manifests a monotonic increase. We fit formula (4) to the data in this region of illumination temperatures. We point out that only relative changes in TSL intensity affect the slope of the line, and thus the value of E_{ion}. These relative changes are, however, unaffected by possible temperature quenching of the Ce^{3+} luminescence center and therefore TSL glow curves need not be corrected for this phenomenon. The value obtained for E_{ion} from the fit is 0.24 ± 0.01 eV. Since we controlled illumination temperature with a precision of about ±1 K, the final estimated value of ionization energy is 0.24 ± 0.02 eV. We note that the method might also be affected by an extensive shift of the host absorption edge in the temperature interval involved in the fit. We measured excitation spectra of the Ce^{3+} emission band and estimated the shift of absorption edge within 250–310 K to be about 0.02 eV. The value falls within the estimated error of the determined ionization energy.

It is worth pointing out that the value of about 0.25 eV is rather close to the value of barrier quenching, 0.3 eV, obtained from the temperature dependence of PL decay time [8]. As pointed out in

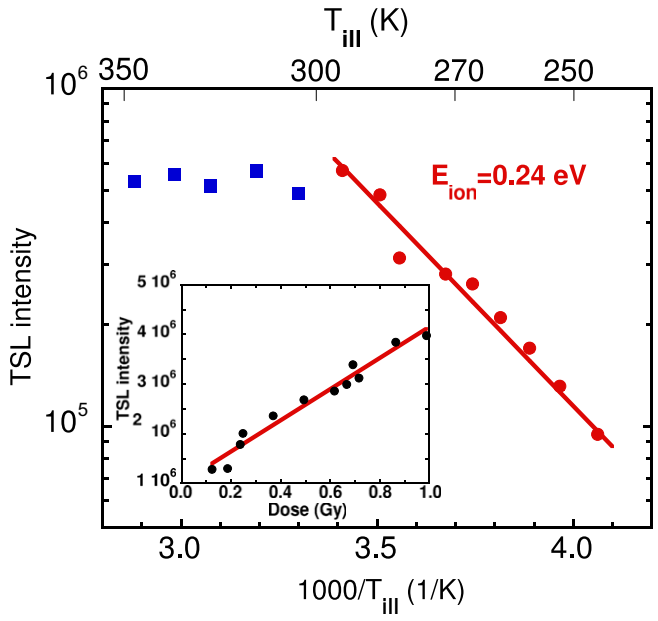

Figure 6. TSL intensity of SHO:Ce^{3+} as a function of illumination temperature. Solid squares and solid circles are obtained by integration of the TSL glow curves in the region 300–470 K. The solid line is the fit of formula (1) in the text to the data represented by the solid circles. In the inset is shown the TSL intensity of SHO:Ce^{3+} as a function of X-ray irradiation dose. The solid circles were obtained by integrating the TSL signal between 300 and 470 K. The solid line is the linear fit to these data.

[8], the temperature shortening of the PL decay time can have two sources, namely classical thermal quenching and thermal ionization of the luminescence center excited state. Similar temperature dependencies of PL intensity and PL decay time [8] suggested that a classical thermal quenching causes the PL decay time shortening. The current study, resulting in a thermal ionization energy being about 0.25 eV, shows that both processes operate with similar barrier energies.

4. Conclusion

In the present Letter we studied trapping states in SHO:Ce^{3+} by TSL technique in a wide temperature range (10–730 K). We determined the characteristic parameters of traps associated with observed TSL peaks. We also determined the energy of thermal ionization of the excited state of the Ce^{3+} ion in a SHO host by a purely optical method that yielded a value of the thermal ionization energy of about 0.25 eV.

The method is based on the dependence of the TSL intensity induced by the UV light on the illumination temperature. If the TSL signal is sufficiently strong, one can extract the ionization energy from a simple analysis of such an experiment. An additional advantage of this method is that the analysis does not require the correction of experimental data for the temperature quenching of the TSL-active luminescence center.

The method, first introduced and tested for a $Lu_2Si_2O_7$:Pr^{3+} crystal [11], has now been applied for a microcrystalline powder of $SrHfO_3$. Its applicability not only for crystal but also powder materials, while encouraging with respect to the development of methods for studying thermal ionization processes in scintillators, does not eliminate larger issues that might arise in all cases, such as the possible temperature dependence of the ionization energy itself.

Acknowledgments

This Letter was supported by the CARIPLO Foundation project ‘Energy transfer and trapping phenomena in nano-structured scintillator materials’, Czech GA AV KAN300100802 and M100101212 projects and II-20100033 EC project of DESY Hamburg.

References

[1] Y.M. Ji et al., J. Cryst. Growth 280 (2005) 93.
[2] H. Retot, A. Bessiere, A. Kahn-Harari, B. Viana, Opt. Mater. 30 (2008) 1109.
[3] E.V. Van Loef et al., IEEE Trans. Nucl. Sci. 54 (2007) 741.
[4] M. Villanueva-Ibanez, C. Le Luyer, S. Parola, O. Marty, J. Mugnier, J. Sol–Gel Sci. Technol. 31 (2004) 277.
[5] M. Villanueva-Ibanez, C. Le Luyer, S. Parola, C. Dujardin, J. Mugnier, Opt. Mater. 27 (2005) 1541.
[6] E. Mihóková et al., IEEE Trans. Nucl. Sci. 57 (2010) 1245.
[7] A. Lauria, N. Chiodini, E. Mihóková, F. Moretti, A. Nale, M. Nikl, A. Vedda, Opt. Mater. 32 (2010) 1356.
[8] V. Jarý, E. Mihóková, M. Nikl, P. Boháček, A. Lauria, A. Vedda, Opt. Mater. 33 (2010) 149.
[9] M.F. Joubert, S.A. Kazanski, Y. Guyot, J.C. G?con, C. Pedrini, Phys. Rev. B 69 (2004) 165217.
[10] H. Loudyi, Y. Guyot, J.C. G?con, C. Pedrini, M.F. Joubert, J. Lumin. 127 (2007) 171.
[11] M. Fasoli, A. Vedda, E. Mihóková, M. Nikl, Phys. Rev. B 85 (2012) 085127.
[12] S.W.S. Mc Keever, Thermoluminescence of Solids, Cambridge University Press, Cambridge, 1985.
[13] E. Mihóková et al., Phys. Rev. B 82 (2010) 165115.
[14] A. Vedda et al., Phys. Rev. B 78 (2008) 195123.
[15] D.J. Robbins, J. Electrochem. Soc. 126 (1979) 1550.
[16] M. Nikl, unpublished results.

Influence of yttrium Content on the Ce1 and Ce2 Luminescence Characteristics in $(Lu_{1-x}Y_x)_2SiO_5 : Ce$ Single Crystals

V. Jarý, M. Nikl, E. Mihóková, J. A. Mareš, P. Průša, P. Horodyský, W. Chewpraditkul, and A. Beitlerová

***Abstract*—We investigate the luminescence and scintillation characteristics of highly efficient cerium-doped scintillators, lutetium-(yttrium) orthosilicate ($Lu_{2(1-x)}Y_{2x}SiO_5 : Ce$, $x = 0 - 1$). The radioluminescence, photoluminescence excitation (PLE) and emission (PL) spectra of the Ce1, Ce2 centres as well as the decay curves and their temperature dependences are measured in the 80–500 K range. Light yield values are provided as well. The influence of yttrium concentration on the Ce1, Ce2 luminescence characteristics is demonstrated. With increasing yttrium content the onset of the Ce1 and Ce2 decay time decrease as well as the Ce1, Ce2 delayed recombination integrals increase shift to higher temperatures. The $5d_1$ thermally induced excited-state ionization of both Ce1 and Ce2 centres is confirmed and studied by purely optical methods.**

***Index Terms*—Oxide compounds, photoluminescence, scintillation detectors.**

I. Introduction

CERIUM doped lutetium oxosilicate ($Lu_2(SiO_4)O$ —LSO) single crystals' luminescence and scintillation properties were reported in literature in the first half of 90's of 20th century [1], [2] and due to favorable combination of high density, effective atomic number and fast Ce^{3+} emission in the violet range of the spectrum, LSO soon became the material of choice for advanced medical imaging by PET scanners.

As there are two lutetium sites in the monoclinic, C2/c LSO structure [3], [4], two Ce^{3+} centres are created with seven (Ce1–the larger one) and six (Ce2) oxygen ligands. Their luminescence characteristics can be well resolved at 10 K [1], [2] and it was stated that Ce2 centre is badly resolved and eventually quenched above some 100 K [2]. Employing the EPR technique it was revealed that only of about 5% of Ce^{3+} occupies the Ce2 site in LSO:Ce [5]. A significant scintillation afterglow at room temperature soon appeared to be a major problem in the initial period of this crystal investigation and anti-correlation between thermoluminescence (TSL) intensity and light output was discovered. After annealing in different atmospheres it was shown that the oxygen vacancies might play the role of possible traps responsible for the afterglow effect [6] which was confirmed in a later study [7]. Furthermore, tunnelling mechanism between the oxygen vacancy-related electron trap and Ce^{3+} recombination centre was proposed to explain an unusual independence of trap depth on the TSL peak position in a wide temperature range above RT [8].

Considerable improvement in the crystal perfection and uniformity of scintillation features of LSO:Ce were reported in 2003 when the major part of 400 tested samples showed the uncorrected light yield within 300–450% of that of BGO [9]. An intrinsic disadvantage of the Ce^{3+} -doped LSO, however, is given by a partial ionization of the $5d_1$ excited state of Ce^{3+} around RT, which was revealed by photoconductivity [10] and microwave [11], [12] studies.

The yttrium admixed $(Lu_{1-x}Y_x)_2(SiO_4)O : Ce$ was reported several years later by the different groups [13]–[16] and immediately a discussion connected to difference in the scintillation mechanism with respect to LSO:Ce arose. Recent study has found a great similarity in vibrational characteristics of LSO, LYSO and YSO structures by methods of the Raman spectroscopy. Moreover, C2/c space group symmetry was confirmed in all of them [17]. Very recently, a systematic study of temperature dependences (TD) of nanosecond decay times, delayed recombination decays and emission intensities in LYSO:Ce was carried on in which careful separation of the Ce1 and Ce2 characteristics was performed [18]. At odds with data reported in [2], it was found that Ce2 centre is not quenched up to 350 K at least, but becomes rather thermally ionized around room temperature, similarly to what was found in the case of Ce1 centre [10].

YSO:Ce $(Y_2(SiO_4)O : Ce)$ single crystals were studied comparatively less [19]–[22] since having lower density excludes them from application in PET imaging. Powder YSO:Ce, on the other hand, is a commercial, widely studied and used phosphor. However, luminescence characteristics of the single crystal and powder YSO:Ce cannot be precisely compared as the latter crystallizes in a slightly different structure and different material defectness can be expected as well [23], [24].

Manuscript received November 07, 2011; revised January 23, 2012; accepted February 26, 2012. Date of publication April 19, 2012; date of current version October 09, 2012. This work was supported in part by GAAV KAN 300100802, MSM 6840770040 "Application of radionuclides and ionizing radiation" and in part by the KMUTT Grant under NRU Projects.

V. Jarý and P. Průša are with the Faculty of Nuclear Sciences and Physical Engineering, Czech Technical University in Prague, Prague 162 53 , Czech Republic (e-mail: jary@fzu.cz; petr.prusa@fjfi.cvut.cz).

M. Nikl, E. Mihóková, J. A. Mareš, and A. Beitlerová are with the Institute of Physics, ASCR, Prague 162 53, Czech Republic (e-mail: nikl@fzu.cz; mihokova@fzu.cz; amares@fzu.cz; beitler@fzu.cz).

P. Horodyský is with Crytur, Ltd., 51101 Turnov, Czech Republic (e-mail: horodysky@crytur.cz).

W. Chewpraditkul is with Department of Physics, KMUTT, Bangkok 10140, Thailand (e-mail: weerapong.che@kmutt.ac.th).

Color versions of one or more of the figures in this paper are available online at http://ieeexplore.ieee.org.

Digital Object Identifier 10.1109/TNS.2012.2190940

Both LSO:Ce and YSO:Ce single crystals co-doped with Ca^{2+} have been recently investigated [25], [26] and improvement in their scintillation characteristics, namely afterglow suppression and scintillation decay acceleration, were claimed. However, the Ca^{2+} role has not been convincingly explained so far to our best knowledge. In both YSO and LSO powdered and nano-crystal samples the EPR investigation showed the presence of the F^{+} centre (a single electron in an oxygen vacancy) the EPR temperature dependence of which matches well the dominant TSL peak within 360–400 K [27].

The lattice parameters increase when Y content gets higher in the LYSO solid solution crystal [4], [17] which may have profound influence on the relative occupancy of the Ce1 and Ce2 centres. It has also been demonstrated in the Pr-doped LSO and YSO single crystals that Pr^{3+} $5d_1$ excited state in the latter host persists to significantly higher temperatures against the quenching and thermally induced ionization [28] and similar behaviour can be therefore expected for the $5d_1$ level of the Ce^{3+} due to their similar positioning with respect to the bottom of conduction band [29]. It is interesting to note, however, that in LSO host somewhat different ionization barriers were reported for Ce^{3+} (450 meV in [10]) and Pr^{3+} (280 meV in [28]) and this aspect needs further study.

In this paper we report the luminescence characteristics and their temperature dependencies with respect to the influence of yttrium/lutetium content ratio in $(Lu_xY_{1-x})_2SiO_5:Ce$ single crystal set, $x = 0-1$. RT excitation and emission spectra of YSO:Ce and LSO:Ce are shown in order to compare the separation of the spectral features of the Ce1 and Ce2 centres. Nanosecond decay times and delayed recombination decay integral for both the Ce1 and Ce2 centres are evaluated within 77–500 K. We show that stability of the $5d_1$ state of the Ce^{3+} against thermally induced ionization increases with the addition of yttrium into LSO host lattice and large effect is observed especially in the case of the Ce2 centre.

II. Experimental Setup

Single crystals of $L_{0.24}Y_{0.76}SO:Ce$ (0.2 m %—will be referred as LYSO:Ce (24% Lu) in the text), $L_{0.52}Y_{0.48}SO:Ce$ (0.2 m %—LYSO:Ce (52% Lu)) and YSO:Ce (0.2 m %) were grown using Czochralski method from the Ir crucible in argon atmosphere in CRYTUR, Ltd. in Czech Republic, LSO:Ce (0.2 m %) in Shanghai Institute of Ceramics (SIC), China, and $L_{0.93}Y_{0.07}SO:Ce$ (0.1 m %—LYSO:Ce (93% Lu)) was purchased from Proteus, Ltd., USA. The fact that the samples come from different producers causes some uncertainty as raw materials purity, crystal growth conditions, eventual co-doping or unintentional impurities may vary from one crystal to another and these factors may possibly influence the results which will be discussed in the text below. The polished plates of $7 \times 7 \times 1$ mm were used for the luminescence experiments.

Photoluminescence spectra, decay and afterglow curves were measured by the custom made spectrofluorometer 5000 M, Horiba Jobin Yvon using the steady state deuterium lamp (photoluminescence excitation and emission spectra), X-ray tube (afterglow curves) and microsecond xenon or nanosecond hydrogen pulsed flashlamps (delayed recombination and prompted decay curves, respectively) as the excitation sources. The experimental set-up for light yield measurement consists of an HPMT (hybrid photomultiplier) (model DEP PPO 475B), an ORTEC NIM model 672 spectroscopy amplifier, and a multichannel buffer in PC. This set-up works in pulse-height mode [30]. ^{137}Cs (661.6 keV) gama-ray source was used for scintillaton response excitation. Shaping time of amplifier was set to 1 μs. Photelectron yield was obtained by gausian fit of the peak. Afterwards, light yield was calculated by multiplying by HPMT photocathode quantum efficiency, using known emission spectra. Measurements of the characteristics within 77–500 K were performed using the liquid nitrogen bath optical cryostat (Oxford Instruments). Single grating monochromators and photon counting photomultiplier based detectors were used in the optical part of the set-up. Spectra were corrected for instrumental effects and a convolution procedure was applied to the decay curves to determine true decay times (SpectraSolve software package, Ames Photonics).

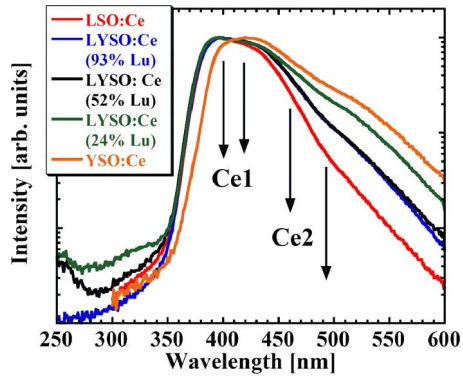

Fig. 1. RT Normalized emission spectra under X-ray excitation of L(Y)SO:Ce with different Lu concentration (see the legend). Positions of Ce1 and Ce2 emission subbands are marked by arrows [18].

III. Results and Discussion

Gaussian decomposition of $LYSO:Ce^{3+}$ -related PL spectra and the Ce1, Ce2 emission subbands ascription have been published recently [18]. RT X-ray excited emission spectra (X-ray tube, W anode, $U = 40$ kV, $I = 15$ mA) of L(Y)SO:Ce with different lutetium concentration are displayed in Fig. 1.

Fig. 1 demonstrates that with decreasing Lu concentration (going from LSO to YSO host) the Ce2 emission becomes relatively more intense. Adding just 7% of Y into pure LSO changes the intensity of Ce2 significantly. Temperature dependence of radioluminescence spectra was studied in [31].

RT absorption spectra of YSO:Ce, LYSO:Ce (52% Lu) and LSO:Ce are shown in Fig. 2. The absorption bands in the 200–380 nm spectral region are attributed to the fully-allowed $4f-5d_x$ transition of the Ce^{3+}. It is worth noting that the position of $4f-5d_1$ band at 360 nm is independent of lutetium content which points to the similar crystal field conditions in LSO, LYSO and YSO hosts. The onset of the orthosilicate band edge at 190 nm can be noted as well in all the presented spectra.

RT normalized excitation and emission spectra of LSO:Ce (a) and YSO:Ce (b) for different excitation and emission wave-

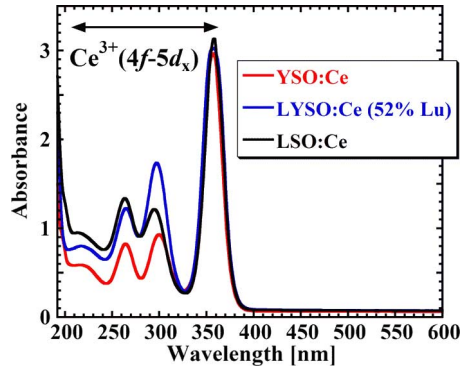

Fig. 2. RT Absorption spectra of L(Y)SO:Ce with different Lu concentration (see the legend).

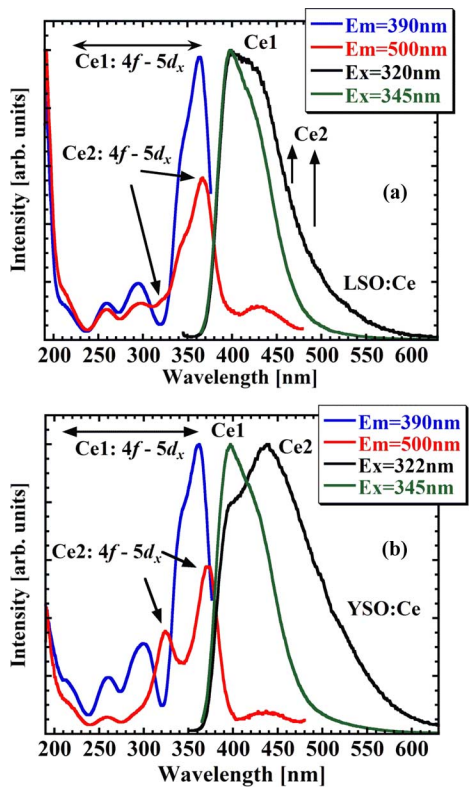

Fig. 3. RT normalized excitation and emission spectra of LSO:Ce (a) and YSO:Ce (b); excitation and emission wavelengths are displayed in the legend.

lengths are presented in Fig. 3. The wavelengths were chosen in order to separate the Ce1 and Ce2 spectral characteristics up to a maximum extent and to compare such separation for pure LSO:Ce (a) and YSO:Ce (b). In the excitation spectrum of LSO:Ce (a) and YSO:Ce (b) measured for the 390 nm emission only the transitions related to Ce1 centre are present. On the contrary, in the excitation spectrum of LSO:Ce (a) and YSO:Ce (b) recorded for the 500 nm emission the mixture of Ce1 and Ce2-related characteristics is inevitable due to the emission bands overlap and re-absorption of Ce1 emission by the Ce2 absorption bands. Nevertheless, the $4f - 5d_1$ and $4f - 5d_2$ transitions of Ce2 at 372 nm and 324 nm, respectively, are clearly visible in the emission spectra taken for the 500 nm emission even at RT, for both LSO:Ce (a) and YSO:Ce (b), and their positions coincide with those determined in LSO [2] and LYSO

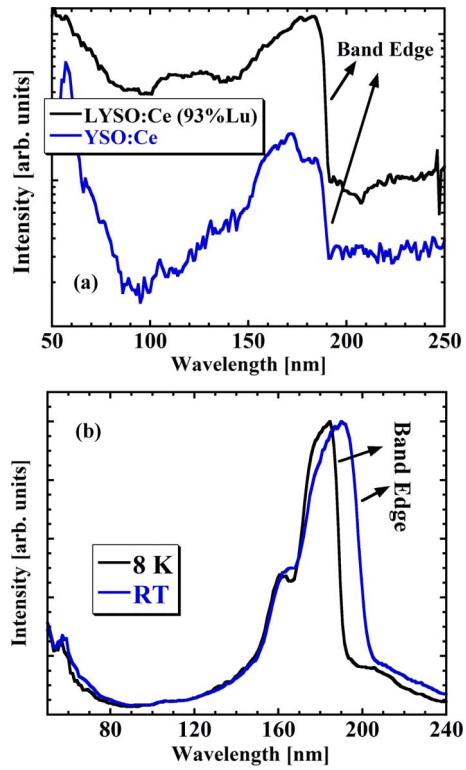

Fig. 4. Excitation spectra measured using synchrotron radiation; (a) YSO:Ce and LYSO:Ce (93% Lu), $Em = 300$ nm , RT; (b) LYSO:Ce (93% Lu), $Em = 400$ nm at 8 K and RT.

[18] hosts at lower temperatures. It also points to comparatively higher Ce2 concentration in YSO host as a resolution of Ce2 excitation features in LSO is significantly worse (see Fig. 3(a)) compared to YSO. In other words, with decreasing Lu content the Ce2 emission becomes more intense (consistently with X-ray excited emission spectra (see Fig. 1)). Similar experiment was carried out for the mixture LYSO:Ce crystals studied in this work (figures not included) and it was confirmed that the separation of the spectral features of the Ce1 and Ce2 centres is found to be somewhere in-between those of LSO:Ce and YSO:Ce. In accordance with the absorption spectra (see Fig. 2), the onset of the orthosilicate band edge at 190 nm can be seen in all excitation spectra (see Fig. 3(a), (b)).

The synchrotron radiation induced excitation spectra monitoring the position of the orthosilicate band edge are given in Fig. 4. The (a) part of the figure shows the spectra for YSO:Ce and LYSO:Ce (93% Lu) at 8 K for the 300 nm emission (in the region of host emission) and it can be seen that the band edge position at 190 nm is not affected by the different host composition. It means that similar crystal field conditions must be present in those hosts (consistent with absorption spectra features). The (b) part of the Fig. 4 reveals the magnitude of temperature evolution i.e. the shift in the band edge position of LYSO:Ce (93% Lu) by circa 20 nm between 8 K and RT monitored by through the Ce^{3+} emission band at 400 nm.

Ce1 (a) and Ce2-related (b) ns decay times (in the units of the radiative lifetime) temperature dependences for different hosts are displayed in Fig. 5. The excitation wavelengths used for the decay measurements are 345 nm for Ce1 and 320 nm for Ce2

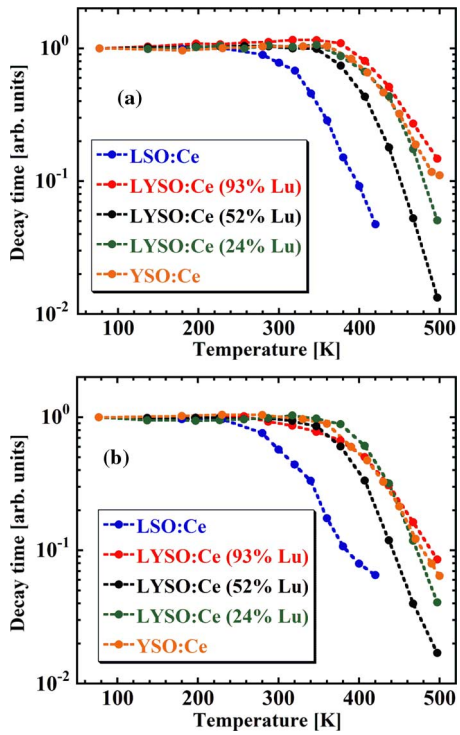

Fig. 5. Nanosecond decay time temperature dependence of Ce1 (a) and Ce2 (b) centres for different hosts (composition given in the legend), in the multiplication of the radiative lifetime at the lowest temperatures.

while the emission ones are 400 nm for Ce1 and 500 for Ce2. Low temperature (77 K) radiative lifetimes reach values as follows: LSO: $\mathrm{Ce1} = 35.9$ ns , $\mathrm{Ce2} = 55.7$ ns ; YSO : $\mathrm{Ce1} = 33.9$ ns $\mathrm{Ce2} = 55.4$ ns ; LYSO:Ce (93% Lu): $\mathrm{Ce1} = 29.8$ ns , $\mathrm{Ce2} = 47.9$ ns ; LYSO:Ce (52% Lu): $\mathrm{Ce1} = 32.3$ ns , $\mathrm{Ce2} = 48.7$ ns and LYSO:Ce (24% Lu): $\mathrm{Ce1} = 35.5$ ns , $\mathrm{Ce2} = 49.0$ ns . It can be clearly seen that with increasing Y concentration (from LSO to YSO host) the nanosecond decay time for both Ce1 and Ce2 centres begins to shorten at higher temperatures. Both centres in YSO host are stable at least till 360 K while the RT nanosecond decay time of Ce2 in LSO host is about 30% of its radiative decay time at low temperature. The commercial sample of LYSO:Ce containing 93% Lu, however, tends to disobey this rule, especially for the Ce1 centre since its decay time temperature dependence points out to higher thermal stability. Such discrepancy points to a possibility of technological modifications, e.g. the mentioned Ca^{2+} co-doping, which further improves the scintillation characteristics and is not disclosed by the producer. Such hypothesis is supported by an unexpectedly high light yield (see Table I). Further analysis is necessary in order to explain the described inconsistency. For the details concerning ns decay curves shape see [31].

Table I presents the light yield (in phot/MeV) of the studied samples as a function of the lutetium content. As the crystals are not grown by the same producer it is not possible to draw straightforward conclusions between the composition and light yield value, but we note that the highest light yield is achieved in Lu93% crystal which shows the enhanced stability of $\mathrm{Ce}_{\mathrm{Lu1}}$ centre mentioned above.

TABLE I
LIGHT YIELD AS A FUNCTION OF Y CONTENT

Sample	*Light Yield (phot/MeV)*
LSO:Ce	12300 ± 500
LYSO:Ce (93% Lu)	30000 ± 1200
LYSO:Ce (52% Lu)	19500 ± 800
LYSO:Ce (24% Lu)	21800 ± 900
YSO:Ce	18800 ± 800

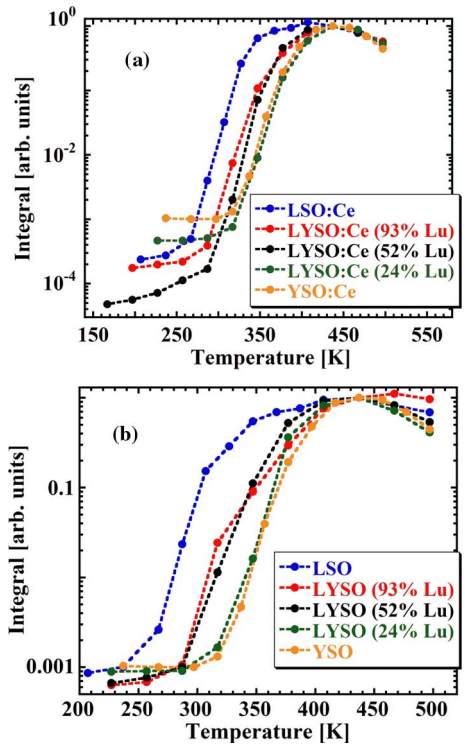

Fig. 6. Temperature dependence of normalized delayed recombination integrals of Ce1 (a) and Ce2 (b) centres for different hosts (composition given in the legend).

To investigate further the origin of Ce^{3+} ns decay time shortening observed the innovative method of measuring the TD of intensity of the delayed radiative recombination was employed [32]. In this experiment the excitation/emission wavelength is set the same as in the nanosecond decay measurement, but time window is set up to a few tens of milliseconds. The excitation is accomplished by a low frequency (10–30 Hz) intense microsecond xenon flashlamp and the driving software ensures that the next excitation flash comes right after the time window is closed, i.e. the dead-times between the windows are minimized. Temperature dependence of the decay curve integral can with an excelent sensitivity indicate the escape of electron from $5d_1$ state to conduction band and its later return resulting in the delayed radiative recombination.

Fig. 6 illustrates the temperature dependence of delayed recombination integrals related to Ce1 (a) and Ce2 (b) for different hosts (compositions are displayed in the legend). Before integrating the curves the highest points (containing prompt ns luminescence) were omitted, for details see [31]. In agreement with ns decay time temperature dependence, with increasing Y

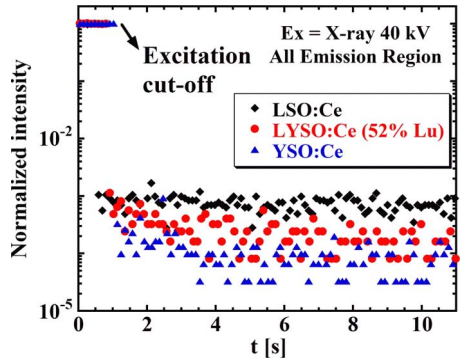

Fig. 7: Normalized RT afterglow curves for LSO:Ce, LYSO:Ce (52% Lu) and YSO:Ce; excited by X-ray (40 kV), all emission region.

concentration (from LSO to YSO host) both Ce1 and Ce2 centres are more stable against ionization process. While both Ce1 and Ce2 centres in YSO are not affected by thermal ionization at RT, Ce2 centre in LSO is already severely ionized at this temperature. The integrals at low temperature reach the constant non-zero value. This points out that there are some athermal proccesses causing the delayed radiative recombination and this aspect needs further study.

In order to compare the afterglow effect and its dependence on the L(Y)SO:Ce composition (see the legend) the afterglow curves were measured—see Fig. 7. The sample was continuously irradiated by X-ray source (40 kV) for several tens of seconds and then the excitation was shut-down. The spectrally unresolved emission was monitored along this process in the 11 s time window. Keeping the experimental conditions the same it is possible to quantitatively compare different samples. Apparently, with increasing Lu amount in the sample the afterglow becomes more significant. There is one order of magnitude difference in the intensity ratio before/few seconds after the X-ray cutting-off for LSO and YSO systems. The afterglow phenomenon in LSO:Ce is related to the presence of TSL glow curve peak at about 70 °C [33]. Admixture of yttrium shifts the position of this peak to higher temperature [34]. Consistently, the thermally induced escape of electron from relative trap slows down, afterglow process slows down as well and the amplitude of afterglow signal decreases.

IV. Conclusion

There are two different Ce^{3+} emission centres (namely Ce1, Ce2) formed in the $(Lu_{1-x}Y_x)_2(SiO_4)O : Ce$, $x = 0 - 1$, single crystals as a result of two different lutetium (respective yttrium) sites in orthosilicate structure. Radioluminescence, photoluminescence and excitation spectra as well as both prompt and delayed kinetics curves were measured in a broad temperature region in order to investigate the influence of yttrium concentration on the Ce1 and Ce2 luminescence characteristics and their temperature dependences. Spectral characteristics of Ce1 and Ce2 can be resolved and excitation bands can be assigned to the Ce1 and Ce2 $4f - 5d_{1,2}$ transitions in both LSO and YSO even at room temperature. With increasing yttrium content the Ce2 emission becomes more intense in radioluminescence spectra, the onset of the Ce1 and Ce2 decay time decrease shifts to higher temperatures and both the Ce1 and Ce2 centres become more stable against thermally-induced ionization of their excited $5d_1$ states. Afterglow curves revealed that with increasing Lu amount in the sample the afterglow becomes more significant. Light yield measurement showed the LYSO:Ce (93%) sample reaches the highest value of 30000 ph/MeV.

References

[1] H. Suzuki, T. A. Tombrello, C. L. Melcher, and J. S. Schweizer, "UV and gamma-ray excited luminescence of cerium-doped rare earth oxyorthosilicates," *Nucl. Instrum. Methods Phys. Res., Sect. A*, vol. 320, p. 263, 1992.

[2] H. Suzuki, T. A. Tombrello, C. L. Melcher, and J. S. Schweitzer, "Light emmission mechanism of $Lu_2(SiO_4)O : Ce$," *IEEE Trans. Nucl. Sci.*, vol. 40, no. 4, pp. 380–383, Aug. 1993.

[3] T. Gustafsson, M. Klintenberg, S. E. Derenzo, M. J. Weber, and J. O. Thomas, "Lu_2SiO_5 by single-crystal X-ray and neutron diffraction," *Acta Crystallogr., Sect. C*, vol. 57, p. 668, 2001.

[4] N. Y. Leonyuk, E. L. Belokoneva, G. Bocelli, L. Righi, E. V. Shvanskii, R. V. Henrykhson, N. V. Kulman, and D. E. Kozhbakhteeva, "High-temperature crystallization and X-ray characterization of Y_2SiO_5, $Y_2Si_2O_7$ and $LaBSiO_5$," *J. Cryst. Growth*, vol. 205, p. 36, 1999.

[5] L. Pidol, O. Guillot-Noël, A. Kahn-Harari, B. Viana, D. Pelenc, and D. Gourier, "EPR study of Ce^{3+} ions in lutetium silicate scintillators $Lu_2Si_2O_7$ and Lu_2SiO_5," *J. Phys. Chem. Solids*, vol. 67, p. 643, 2006.

[6] R. Visser, C. L. Melcher, J. S. Schweitzer, H. Suzuki, and T. A. Tombrello, "Photostimulated luminescence and thermoluminescence of LSO scintillators," *IEEE Trans.Nucl. Sci.*, vol. 41, no. 4, pp. 689–693, Aug. 1994.

[7] D. W. Cooke, B. L. Bennett, R. E. Muenchausen, K. J. McClellan, J. M. Roper, and M. T. Whittaker, "Intrinsic trapping sites in rare-earth and yttrium oxyorthosilicates," *J. Appl. Phys.*, vol. 86, p. 5308, 1999.

[8] A. Vedda, M. Nikl, M. Fasoli, E. Mihokova, J. Pejchal, M. Dusek, G. Ren, C. R. Stanek, K. J. McClellan, and D. D. Byler, "Thermally stimulated tunneling in rare-earth-doped oxyorthosilicates," *Phys. Rev. B: Condens. Matter*, vol. 78, p. 195123, 2008.

[9] C. L. Melcher, M. A. Spurrier, L. Eriksson, M. Eriksson, M. Schmand, G. Givens, R. Terry, T. Homant, and R. Nutt, "Advances in the scintillation performance of LSO:Ce single crystals," *IEEE Trans. Nucl. Sci.*, vol. 50, no. 4, pp. 762–766, Aug. 2003.

[10] E. van der Kolk, S. A. Basun, G. F. Imbusch, and W. M. Yen, "Temperature dependent spectroscopic studies of the electron delocalization dynamics of excited Ce ions in the wide band gap insulator, Lu_2SiO_5," *Appl. Phys. Lett.*, vol. 83, p. 1740, 2003.

[11] M. F. Joubert, S. A. Kazanskii, Y. Guyot, J. C. Gacon, and C. Pedrini, "Microwave study of photoconductivity induced by laser pulses in rare-earth-doped dielectric crystals," *Phys. Rev. B: Condens. Matter*, vol. 69, p. 165217, 2004.

[12] H. Loudyi, Y. Guyot, J. C. Gacon, C. Pedrini, and M. F. Joubert, "Understanding the scintillation separation of the spectral features of the CeLu1 and CeLu2 centres of cerium-doped LSO, LYSO, YSO and LPS crystals from microwave study of photoconductivity and trapping," *Opt. Mater.*, vol. 30, p. 26, 2007.

[13] D. W. Cooke, K. J. McClellan, B. L. Bennett, J. M. Roper, M. T. Whittaker, R. E. Muenchausen, and R. C. Sze, "Crystal growth and optical characterization of cerium-doped $Lu_{1.8}Y_{0.2}SiO_5$," *J. Appl. Phys.*, vol. 88, p. 7360, 2000.

[14] C. M. Pepin, P. Berard, A. L. Perrot, C. Pepin, D. Houde, R. Lecomte, C. L. Melcher, and H. Dautet, "Properties of LYSO and recent LSO scintillators for phoswich PET detectors," *IEEE Trans. Nucl. Sci.*, vol. 51, no. 3, pp. 789–795, Jun. 2004.

[15] L. Pidol, B. Viana, A. Kahn-Harari, A. Galtayries, A. Bessiere, and P. Dorenbos, "Optical properties and energy levels of Ce^{3+} in lutetium pyrosilicate scintillator crystal," *J. Appl. Phys.*, vol. 95, p. 7731, 2004.

[16] L. S. Qin, H. Y. Li, S. Lu, D. Z. Ding, and G. H. Ren, "Growth and characteristics of LYSO $(Lu_{2(1-x-y)}Y_{2-x}SiO_5 : Ce_y)$ scintillation crystals," *J. Cryst. Growth*, vol. 281, p. 518, 2005.

[17] D. Chiriu, N. Faedda, A. G. Lehmann, P. C. Ricci, A. Anedda, S. Desgreniers, and E. Fortin, "Structural characterization of $Lu_{1.8}Y_{0.2}SiO_5$ crystals," *Phys. Rev. B: Condens. Matter*, vol. 76, p. 054112, 2007.

[18] H. Feng, V. Jary, E. Mihokova, D. Ding, M. Nikl, G. Ren, H. Li, S. Pan, A. Beitlerova, and R. Kucerkova, "Temperature dependence of luminescence characteristics of $Lu_{2(1-x)}Y_{2x}SiO_5 : Ce^{3+}$ scintillator grown by the Czochralski method," *J. Appl. Phys.*, vol. 108, p. 033519, 2010.

[19] A. R. Kulesskii, A. M. Korovkin, A. V. Kruzhalov, A. M. Korovkin, A. V. Kruzhalov, L. V. Viktorov, and B. V. Shul'gin, "Radioluminescence and scintillation properties of yttrium and rare-earth silicates," *Zh. Prikl. Spektrosk.*, vol. 48, p. 650, 1988.

[20] B. V. Shulgin, A. R. Kulesskii, A. M. Korovkin, V. L. Petrov, and S. V. Podurovski, "Spectra and kinetics of pulsed cathodoluminescence of $Y_2SiO_5 - Tb$, Ce," *Opt. Spectrosc. (USSR)*, vol. 68, p. 491, 1990.

[21] M. Balcerzyk, M. Moszynski, M. Kapusta, D. Wolski, J. Pawelke, and C. L. Melcher, "YSO, LSO, GSO and LGSO. A study of energy resolution and nonproportionality," *IEEE Trans. Nucl. Sci.*, vol. 47, no. 4, pp. 1319–1323, Aug. 2000.

[22] W. Drozdowski, A. J. Wojtowicz, D. Wiśniewski, P. Szupryczyński, S. Janus, J. L. Lefaucheur, and Z. Gou, "VUV spectroscopy and low temperature thermoluminescence of LSO:Ce and YSO:Ce," *J. Alloys Compd.*, vol. 380, pp. 146–150, 2004.

[23] S. H. Shin, D. Y. Jeon, and K. S. Suh, "Emission band shift of the cathodoluminescence of $Y_2SiO_5 : Ce$ phosphor affected by its activator concentration," *Jpn. J. Appl. Phys.*, vol. 40, p. 4715, 2001.

[24] D. W. Cooke, J. K. Lee, B. L. Bennett, J. R. Groves, L. G. Jacobsohn, E. A. McKigney, R. E. Muenchausen, M. Nastasi, K. E. Sickafus, M. Tang, and J. A. Valdez, "Luminescent properties and reduced dimensional behavior of hydrothermally prepared $Y_2SiO_5 : Ce$ nanophosphors," *Appl. Phys. Lett.*, vol. 88, p. 103108, 2006.

[25] M. A. Spurrier, P. Szupryczynski, K. Yang, A. A. Carey, and C. L. Melcher, "Effects of Ca^2+ Co-doping on the scintillation properties of LSO:Ce," *IEEE Trans. Nucl. Sci.*, vol. 55, no. 3, pp. 1178–1182, Jun. 2008.

[26] H. E. Rothfuss, C. L. Melcher, L. A. Eriksson, and M. A. S. Koschan, "The effect of Ca^{2+} codoping on shallow traps in YSO:Ce scintillators," *IEEE Trans. Nucl. Sci.*, vol. 56, no. 3, pp. 958–961, Jun. 2009.

[27] D. W. Cooke, M. W. Blair, J. F. Smith, B. L. Bennett, L. G. Jacobsohn, E. A. McKigney, and R. E. Muenchausen, "EPR and luminescence of F^+ centres in bulk and nanophosphor oxyorthosilicates," *IEEE Trans. Nucl.Sci.*, vol. 55, no. 3, pp. 1118–1122, Jun. 2008.

[28] J. Pejchal, M. Nikl, E. Mihokova, A. Novoselov, A. Yoshikawa, and R. T. Williams, "Temperature dependence of the Pr^{3+} luminescence in LSO and YSO hosts," *J. Lumin.*, vol. 129, p. 1857, 2009.

[29] P. Dorenbos, "Systematic behaviour in trivalent lanthanide charge transfer energies," *J. Phys.: Condens. Matter*, vol. 15, p. 8417, 2003.

[30] J. A. Mares, A. Beitlerova, M. Nikl, N. Solovieva, K. Nitsch, M. Kucera, M. Kubova, V. Gorbenko, and Y. Zorenko, "Scintillation and optical properties of YAG:Ce films grown by liquid phase epitaxy," *Radiat. Meas.*, vol. 42, p. 533, 2007.

[31] V. Jarý, M. Nikl, G. Ren, P. Horodysky, G. P. Pazzi, and R. Kucerkova, "Influence of yttrium content on the Ce_{Lu1} and Ce_{Lu2} luminescence characteristics in $(Lu_{1-x}Yx)_2SiO_5 : Ce$ single crystals," *Opt. Mater.*, 2011, 10.1016/j.optmat.2011.04.034.

[32] J. Pejchal, M. Nikl, E. Mihóková, J. A. Mareš, A. Yoshikawa, H. Ogino, K. M. Schillemat, A. Krasnikov, A. Vedda, K. Nejezchleb, and V. Múčka, " Pr^{3+} -doped complex oxide single crystal scintillators," *J. Phys. D: Appl. Phys.*, vol. 42, p. 055117, 2009.

[33] P. Dorenbos, C. W. E. van Eijk, A. J. J. Bos, and C. L. Melcher, "Afterglow and thermoluminescence properties of $Lu_2SiO_5 : Ce$ scintillation crystals," *J. Phys.: Condens. Matter*, vol. 6, pp. 4167–4180, 1994.

[34] E. Mihóková, K. Vávrý, P. Horodyský, W. Chewpraditkul, V. Jarý, and M. Nikl, "Thermally stimulated luminescence in Ce-doped yttrium oxyorthosilicate," in *11th Int. Conf. Inorganic Scintillators Their Appl. SCINT*, Science Campus Justus-Liebig-Univ. Giessen, Germany, Sep. 2011.

IOP Publishing Journal of Physics D: Applied Physics
J. Phys. D: Appl. Phys. **47** (2014) 365304 (8pp) doi:10.1088/0022-3727/47/36/365304

Comparison of the scintillation and luminescence properties of the $(Lu_{1-x}Gd_x)_2SiO_5$:Ce single crystal scintillators

V Jarý[1], E Mihóková[1], J A Mareš[1], A Beitlerová[1], D Kurtsev[2], O Sidletskiy[2] and M Nikl[1]

[1] Institute of Physics AS CR, Na Slovance 2, CZ-18221 Prague 8, Czech Republic
[2] Institute for Scintillation Materials NAS of Ukraine, 60 Lenin Avenue, 61001 Kharkiv, Ukraine

E-mail: jary@fzu.cz

Received 28 April 2014, revised 3 July 2014
Accepted for publication 15 July 2014
Published 21 August 2014

Abstract

We provide a systematic comparison of the scintillation and luminescence properties, including emission mechanisms, of the highly efficient cerium-doped scintillators lutetium-(gadolinium) orthosilicates $Lu_2(SiO_4)O$ (LSO), $(Lu_{1-x}Gd_x)_2(SiO)_4O$(LGSO) and $Gd_2(SiO_4)O$ (GSO). Determined characteristics manifest an advantage of LGSO:Ce with respect to both LSO:Ce and GSO:Ce for scintillator applications around room temperature. This is thanks to combined fast decay (faster than both limit compositions) high light yield, similar to that of LSO:Ce (twice higher than GSO:Ce) and low afterglow, similar to that of GSO:Ce (almost two orders of magnitude lower than LSO:Ce). High temperature applications do not, however, seem to be a suitable option for LGSO:Ce due to evidenced thermal ionization of both Ce1 and Ce2 centres above room temperature.

Keywords: rare-earth (oxy)orthosilicate, Ce^{3+}-doping, scintillator, excited state dynamics, luminiscence, light yield, afterglow

(Some figures may appear in colour only in the online journal)

1. Introduction

Most of the rare-earth (RE) oxyorthosilicates, $(RE)_2(SiO_4)O$ have been successfully grown in a single crystal form by the Czochralski technique [1]. Among these, $Gd_2(SiO_4)O$ (GSO), $Y_2(SiO_4)O$ (YSO) and $Lu_2(SiO_4)O$ (LSO) have no absorption lines in the visible spectral region and thus have been examined as potential single crystal scintillators by doping with cerium [2]. Because of their high density and effective atomic number, reasonably high scintillation emission intensities and fast scintillation decay times, they all show good potential as gamma-ray detectors. Ce-doped gadolinium oxyorthosilicate (GSO:Ce) was described by Takagi and Fukazawa [3] in 1983 and subsequently studied by others [4–6]. Technology of the growth of large crystals was developed [7, 8] and GSO:Ce found its application in oil-well logging due to stability of its scintillation characteristics up to high temperatures [9]. On the other hand the LSO:Ce and yttrium-admixed LYSO:Ce are used in the latest generation of scintillation detectors in positron emission tomographs (PET) especially after their optimization by divalent ion codoping and post-growth annealing, the mechanism of which has been recently clarified [10].

In pioneering studies the fact that the Ce^{3+} activator ion can occupy two different crystallographically independent sites in $(RE)_2(SiO_4)O$ has not been considered in the light emission mechanism. Felsche [11] shows that $Gd_2(SiO_4)O$ has the monoclinic structure of space group P2 1/c. The Gd^{3+} ions occupy two distinct sites. One site is surrounded by 7 oxygen ligands while the other is surrounded by 9 oxygen ligands. The fact that the Ce^{3+} ions occupy two independent sites and experience two different crystal fields is reflected in the

experimental results and plays a key role in supporting the two-activation-centre model proposed in [2]. An effect of Y content on luminescence characteristics of two Ce emission centres in mixed LYSO:Ce crystals has been studied in more detail in [12].

LGSO:Ce was discovered as an efficient, dense scintillator with a high light yield, fast decay and weak afterglow described in [13–15] and the phenomenon of light yield improvement for such mixed crystal was demonstrated in [16]. LGSO may possess monoclinic P21/c or C2/c structures depending on the Lu/Gd ratio in the host [17]. Recent analysis of the mixed scintillation crystal efficiency [18] shows the general trend towards a better efficiency of intermediate compositions compared to the limit components. The description of these phenomena in terms of e–h separation and thermalization processes points to the key role of the lattice structure and phonon spectra.

At the same time, there are additional reserves for the crystal performance improvement by the optimization of activator state, point defects structure, and concentration. In Ce-doped orthosilicates, the annealing procedure was described for GSO:Ce [19], LYSO:Ce [20], and $Lu_{0.4}Gd_{1.6}SiO_5$:Ce [21]. For GSO:Ce, annealing in vacuum at 1500 °C leads to an improvement of the light output, the energy resolution and the radiation hardness [19]. On the contrary, an improvement of the light yield and energy resolution in LGSO:Ce was reported by annealing in oxygen-deficient atmosphere at temperatures $800 \leqslant T < T_m - 550$ (T_m—the melting temperature of the crystal [21]). The study of optimization of the LGSO:Ce scintillation parameters by the heat treatment is reported in [22]. Three main parameters of the heat treatment (atmosphere composition, temperature, and duration of annealing) were considered, showing improvement in energy resolution, but no significant effect on light yield.

In this work, the optical and luminescence characteristics of GSO:Ce and LGSO:Ce single crystals, including their temperature dependencies, are studied and compared to those of LSO:Ce. Excitation and emission spectra of GSO:Ce and LGSO:Ce recorded at 77 K are shown in order to compare the separation of the spectral features of the Ce1 and Ce2 centres. Nanosecond decay times and delayed recombination decay integral for both the Ce1 and Ce2 centres are evaluated within 77–500 K focused on the presence of the excited state ionization processes. Temperature dependence of nanosecond decay times is approximated by the phenomenological model to evaluate the energy barrier of the quenching process. The application potential of materials is discussed. Besides detailed physical description of the mixed LGSO:Ce scintillator, this work emphasizes the difference in physical phenomena and their practical consequences in the case of admixing Gadolinium in the LSO host with respect to the Yttrium admixture, earlier described in LSO-LYSO-YSO material system [12].

2. Samples

A single crystal of $Lu_2(SiO_4)O$:Ce (LSO:Ce) was grown by the Czochralski method from a Ir crucible in an argon atmosphere in the Shanghai Institute of Ceramics (SIC), China [23]. $Lu_{1.1}Gd_{0.9}SiO_5$:Ce crystal with the monoclinic C2/c structure (the same as in LSO:Ce) was grown using a similar growth procedure by the Czochralski method in the Institute for Scintillation Materials, Ukraine [16]. The Ce concentration in LGSO:Ce crystal was 0.3 at.% with respect to the lanthanide cation content. The sample of commercial GSO:Ce was kindly provided by Dr. H. Ishibashi from Hitachi Chemical Co., Japan. The dimensions of samples used for measurements were $6 \times 8 \times 1$ mm, $10 \times 5 \times 1$ mm and $6 \times 6 \times 1$ mm for LSO:Ce, LGSO:Ce and GSO:Ce, respectively.

3. Experimental setup

Absorption spectra were measured using the UV/Vis Spectrophotometer Shimadzu UV-1601. Radioluminescence (RL), photoluminescence excitation (PLE) and emission (PL) spectra, decay and afterglow curves were measured by the model 5000 Mspectrofluorometer, Horiba Jobin Yvon. The detection part of the set-up involved a single grating monochromator with the grating blazing wavelength at 500 nm and the photon counting detector TBX-04. Various excitation sources were used depending on the type of measurement: the steady state deuterium lamp Heraus Gmbh, Germany(PL and PLE spectra), the x-ray tube Seifert Gmbh, Germany (RL spectra and afterglow curves), the microsecond xenon pulsed flash lamp (delayed recombination decay over millisecond time scale) or nanosecond nanoLED (prompt nanosecond decay over sub microsecond time scale)pulsed light sources. The last two pulse excitation sources are also produced by Horiba Jobin Yvon. Measured spectra were corrected for the spectral dependence of excitation energy (PLE) and spectral dependence of detection sensitivity (PL). A convolution procedure was applied to the decay curves to determine true decay times (SpectraSolve software package, Ames Photonics). The experimental set-up for the light yield (LY) measurement consisted of the hybrid photomultiplier (model PPO 475B, DEP company, The Netherlands), spectroscopy amplifier (NIM model 672, ORTEC) with the shaping time of 2 μs, and a multichannel buffer in PC [24]. Scintillation response was excited by the ^{137}Cs (662 keV) gamma-ray radioisotope source. The Gaussian-approximated photopeak in the pulse-height spectra was used to determine the photoelectron yield. The light yield was calculated from the photoelectron yield employing the spectral dependence of quantum efficiency of the above specified photomultiplier (provided by the manufacturer) and corrected emission spectra of the studied crystals—typical error of the measurement is ±3%, for more details see [25]. Measurements of the optical characteristics within the 77–500 K temperature range were performed using the liquid nitrogen bath optical cryostat (Optistat, Oxford Instruments).

4. Results and discussion

There are two different Ce^{3+} emission centres (namely Ce1, Ce2) formed in the $(Lu_{1-x}Gd_x)_2(SiO_4)O$:Ce, x ϵ (0,1), single crystals resulting from two different lutetium (gadolinium)

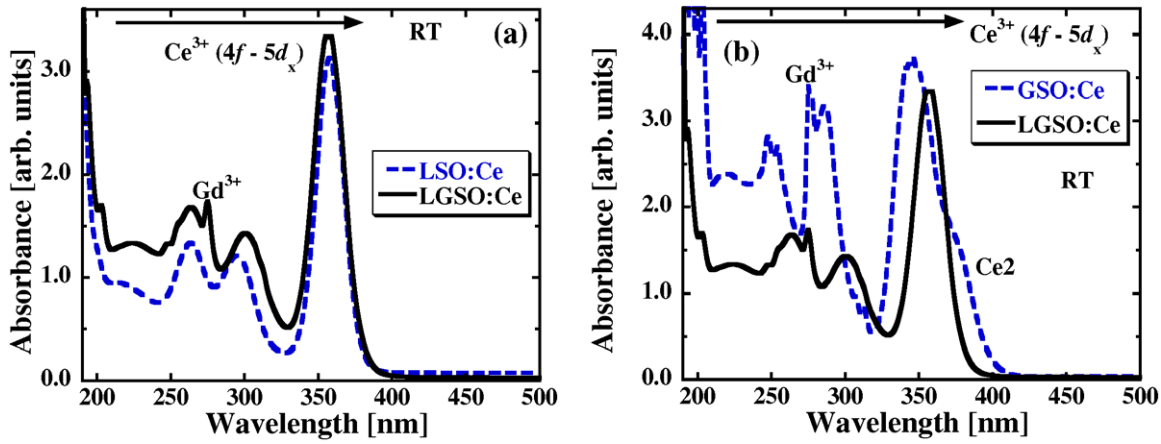

Figure 1. RT Absorption spectra of: (*a*) LSO:Ce (blue dashed line) and LGSO:Ce (black solid line); (*b*) GSO:Ce (blue dashed line) and LGSO:Ce (black solid line).

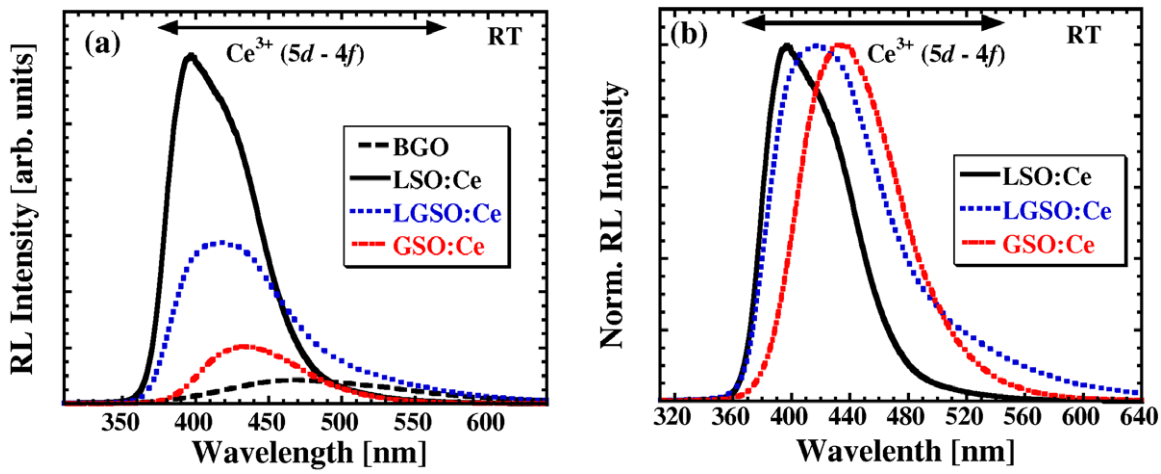

Figure 2. RT emission spectra of LSO:Ce (black solid line), LGSO:Ce (blue dotted line), GSO:Ce (red dash-and-dotted line) and BGO (black dashed line) under the x-ray (40 kV, 15 mA) excitation for an (*a*) absolute and (*b*) normalized comparison.

sites in the monoclinic orthosilicate structure. To identify and characterize both these centres we used procedures similar to those applied in [12].

Room temperature (RT) absorption spectra of LSO:Ce, LGSO:Ce and GSO:Ce are shown in figures 1(*a*) and (*b*). The absorption bands in the 200–400 nm spectral region are attributed to the fully-allowed $4f$–$5d_x$ transitions of the Ce^{3+} activator in those silicate hosts. It is worth noting that the positions of the $4f$–$5d_1$ bands of Ce^{3+} in LSO:Ce and LGSO:Ce are independent of gadolinium content as their structure is the same, while distinct deviations are observed in GSO:Ce due to its different crystal structure. In the gadolinium containing samples, typical Gd^{3+} absorption lines around 275 nm due to the ${}^8S_{7/2} - {}^6I_x$ $4f$–$4f$ transitions can be seen. The onset of the orthosilicate band edge at around 190 nm can be noticed as well in all presented spectra.

RT x-ray (40 kV, 15 mA) excited emission spectra of LSO:Ce, LGSO:Ce and GSO:Ce are displayed in figure 2(*a*). The spectrum of the $Bi_4Ge_3O_{12}$(BGO) single crystal is plotted as a reference for comparison of the absolute emission intensity. The emission arising from the fully allowed $5d$–$4f$ transition of the Ce^{3+} ion peaks at 396 nm, 417 nm and 434 nm in LSO, LGSO and GSO hosts, respectively. Corresponding RL intensities reach about 760%, 490% and 140% of that of BGO (RL intensity was obtained by integrating corrected RL spectrum in the energy and radiant flux coordinates). Within studied orthosilicates the lowest intensity of the Ce^{3+} emission in the GSO host might be due to the fact that Ce2 centre in the GSO host is significantly quenched at RT ([2] and discussed below). Figure 2(*b*) demonstrates the evolution of both the emission position and emission band shape with increasing Gd concentration (going from pure LSO to pure GSO host). Since the Ce2 emission is situated in the low energy part of the spectrum [2], due to the most intense shoulder of LGSO:Ce in this part of the RL spectrum (see figure 2(*a*)), one may expect that Ce2 emission under RT x-ray excitation is the most intense in the LGSO host. More discussion and determination of Ce1 and Ce2 locations will follow.

Unlike RL measurement, the LY measurement collects only the fast light component produced by a material [24]. The measured LY of GSO:Ce and LGSO:Ce shows values of 10 000 and 19 000 ph MeV^{-1}, respectively. Light yield measurements of LSO:Ce has shown the LY value around 20 000 ph MeV^{-1} [25]. Similar LY value in contrast to almost twice lower RL intensity (see figure 2(*a*)) of LGSO:Ce with respect to LSO:Ce,

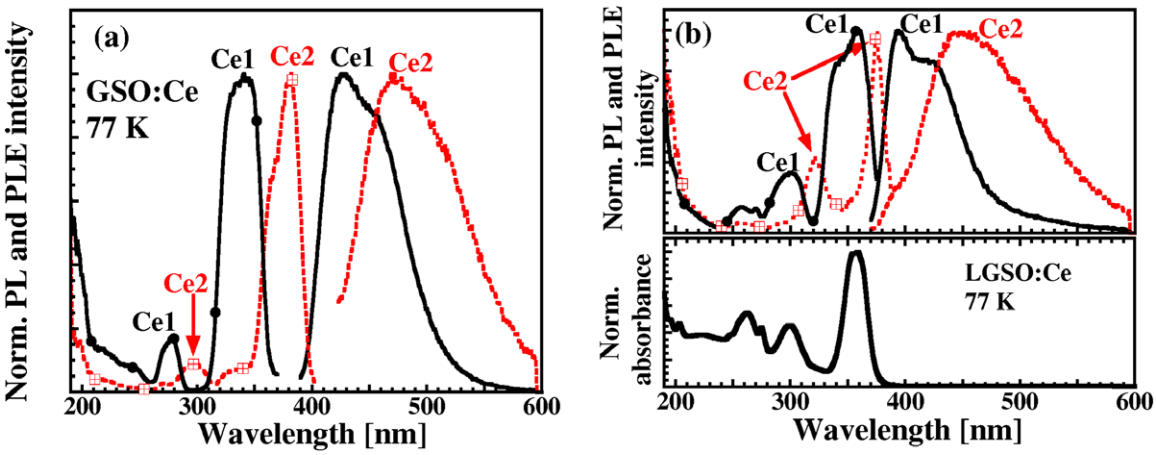

Figure 3. Normalized photoluminescence excitation and emission spectra. Position of Ce1 and Ce2 transitions are designated. In (*a*) GSO:Ce at 77 K, for Ce1 and Ce2 transitions $\lambda_{ex} = 340$ nm, $\lambda_{em} = 405$ nm and $\lambda_{ex} = 390$ nm, $\lambda_{em} = 520$ nm, respectively. In (*b*) LGSO:Ce at 77 K. In the upper panel, for Ce1 and Ce2 transitions $\lambda_{ex} = 340$ nm, $\lambda_{em} = 390$ nm and $\lambda_{ex} = 320$ nm, $\lambda_{em} = 520$ nm, respectively. In the lower panel, normalized absorption spectrum of LGSO:Ce.

Table 1. Peak wavelengths and decay time parameters related to the Ce1 and Ce2 centres in LSO:Ce [12, 26], LGSO:Ce and GSO:Ce at three temperatures of 77 K, RT and 497 K.

	$\lambda_{abs,max}$ (nm)	λ_{ex} (nm)[a]	λ_{em} (nm)[a]	77 K decay (ns)	RT decay (ns)	497 K decay (ns)
LSO:Ce1	356 (RT [25])	347	400	35,85	28,00	1,7 (420 K)
LSO:Ce2		320	500	55,69	31,87	3,64 (420 K)
LGSO:Ce1	358 (77 K)	339	405	30,05	23,36	0,39
LGSO:Ce2	375 (77 K)	389	520	63,46	43,18	0,71
GSO:Ce1	340 (77 K)	340	405	27,00	25,05	8,17
GSO:Ce2	381 (77 K)	389	520	43,17	6,63	0,45 (377 K)

[a] λ_{ex} and λ_{em} are chosen to achieve a maximum separation of the Ce1 and Ce2 characteristics.

points to the fact, that LGSO produces much smaller portion of slow light (more evidence provided below). Such a feature makes it more advantageous in fast scintillator applications as well as those requiring a low afterglow level. However, with respect to GSO:Ce, LY of LGSO:Ce is only about twice higher while its corresponding RL overall intensity is more than three times higher (see figure 2(*a*)). This observation indicates that some slow decay components in LGSO:Ce do exist as well (see below).

Normalized photoluminescence excitation and emission spectra of GSO:Ce and LGSO:Ce recorded at 77 K are presented in figures 3(*a*) and the upper panel of (*b*), respectively, for various excitation and emission wavelengths. Those wavelengths were chosen in order to separate the parts of the spectra due to the Ce1 and Ce2 emissions in a similar way that is used for LSO:Ce and YSO:Ce in [12]. Peak positions are displayed in a simple scheme in figure 2. They are also listed in the summarizing table 1. Comparing absorption (see figure 1(*b*)), and PLE spectra (see figure 3(*a*)), one can assign the low-energy part (at around 370–400 nm) of the GSO:Ce absorption spectra to the Ce2 centre. From the excitation and emission maxima, the Stokes shift for the Ce1 centre can be estimated, giving the values 750 meV and 320 meV for GSO:Ce and LGSO:Ce, respectively. To complete the optical study, the absorption spectrum of LGSO:Ce was recorded at 77 K, see figure 3(*b*). It is dominated by the $4f$–$5d_x$ transitions of the Ce^{3+} in the 210–380 nm spectral range, those of Ce1 in particular. The band positions reasonably coincide with those in the PLE spectrum. However, the broadening of the $4f$–$5d^1$ excitation band at the high energy side (for the 390 nm emission) in LGSO:Ce at 357 nm, while compared to the absorption spectrum, remains unclear and needs further investigation. In accordance with the absorption spectra in figure 1, the onset of the orthosilicate band edge at 190 nm can be seen in all excitation spectra (see figures 3(*a*) and (*b*)), more intensely at RT since at lower temperature the band edge of orthosilicate host is high-energy shifted [12].

To roughly estimate the contribution of the Ce1 and Ce2 centres to the overall scintillation emission in GSO:Ce at low temperature, both RL and PL (for 340 nm and 390 nm excitations) spectra were recorded at 77 K, see figure 5. The PL spectra were summed up (Ce1 + Ce2 curve in figure 4) and their intensity ratio was varied to fit the RL spectral shape. In this way, one can estimate Ce1 and Ce2 emission contributions to the overall spectrum being 70% and 30%, respectively. Consequently, it seems unlikely that quenching of the Ce2 centre in GSO at RT would be the only cause of its lower light yield and RL integral intensity.

Ce1 (a) and Ce2 related (b) ns decay time (in the units of the radiative lifetime, see table 1 for $T = 77$ K) temperature dependences for different hosts are displayed in figure 6. Temperature stability of LSO:Ce has already been discussed

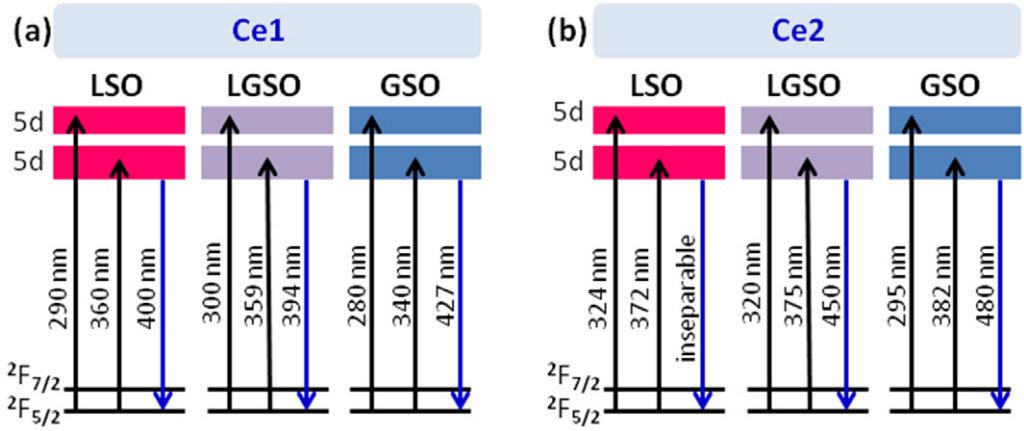

Figure 4. Simple scheme displaying transitions in Ce1 and Ce2 centres observed in PL and PLE spectra presented in figure 3. Data for the LSO host are taken from [12] and shown for completeness.

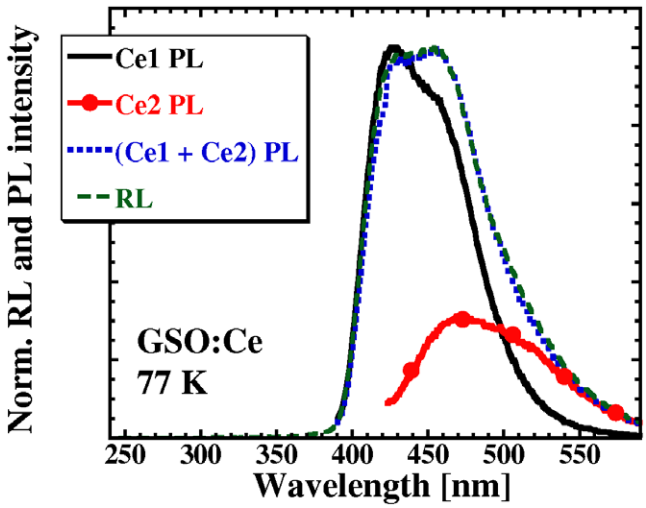

Figure 5. Normalized RL (x-ray excitation 40 kV, 15 mA) and PL ($\lambda_{ex} = 340$ nm, $\lambda_{em} = 390$ nm) spectra of the GSO:Ce recorded at 77 K. The sum of Ce1 and Ce2 emission spectra is practically coinciding with the RL spectrum.

and compared to LYSO:Ce and YSO:Ce in [12]. Concerning the Ce1 centre, GSO:Ce is the most stable with respect to the ns decay time shortening (caused by thermal quenching and/or thermally induced ionization of the Ce^{3+} excited state —see below) as its decay time at 497 K still reaches 30% of its radiative lifetime value. Unlike GSO:Ce, both LSO:Ce and LGSO:Ce decay times sharply decrease above RT. The onset of this mentioned shortening for the Ce1 centre is at 280 K (LSO:Ce), 290 K (LGSO:Ce) and 350 K (GSO:Ce). In contrast, Ce2 centre in GSO is very thermally unstable and its decay time at RT reaches only 15% of its low temperature value, as already published in [2]. The onset of ns decay time shortening for the Ce2 centre is then at 200 K (GSO:Ce), 260 K (LGSO:Ce) and 280 K (LSO:Ce).

As an example, decay curves related to the Ce^{3+} $5d$–$4f$ transitions for the Ce1 and Ce2 centres in LSO, LGSO, and GSO hosts recorded at RT are shown in figures 7(*a*) and (*b*). In LSO:Ce, an exponential prompt ns decay is evident up to a time of about 200 ns for both the Ce1 and Ce2 centres. However, one also observes a significant contribution of slower light, having its origin in the delayed recombination due to the $5d^1$ state thermally induced ionization. It has been proposed [27] that this delayed recombination is due to a thermally stimulated tunneling process between the Ce recombination centre and a nearby trap, but the temperature dependence of photoconductivity reported under selective photoexcitation into the $5d_x$ absorption bands also evidences the promotion of electrons into the conduction band [28]. More details will be provided below. Interestingly, significantly less slow light is found in both LGSO:Ce and GSO:Ce which means that ns decay time shortening, especially for the Ce2 centre in GSO, is not caused by thermally induced ionization of the excited state but rather by the classical thermal quenching process. LGSO:Ce ns decay time shortening around RT is most probably affected by both processes as temperature dependence of the ns decay time is not governed by a single barrier process. Some tunneling-driven recombination processes can participate as well. More experimental work will therefore have to be carried out to fully understand such behaviour.

In the standard Mott–Seitz model of thermal quenching based on the configuration coordinate diagram [29] an excited state of a luminescence centre can decay *via* spontaneous radiative transitions, phonon-assisted vibronic transitions or nonradiative transitions. When the phonon-assisted transitions are negligible and more than one nonradiative quenching channel participate in the decay process, the decay rate can be expressed as:

$$(\tau_{\text{observed}})^{-1} = (\tau_{\text{radiative}})^{-1} + \sum K_{\text{xi}}.\exp\left(-E_{\text{xi}}/kT\right), \qquad (1)$$

where τ_{observed}, $\tau_{\text{radiative}}$, K_{xi}, E_{xi}, k, and T represent the PL decay time measured at temperature T, the low temperature limit of the reciprocal PL decay time $k = 1/\tau$ (see table 1), frequency factor of the i-th quenching channel, i-th energy barrier height, Boltzmann constant and absolute temperature, respectively. The parameters of the best fit of equation (1) to experimental data are listed in table 2.

All dependences connected to LSO and GSO can be fit by a single quenching channel model ($i = 1$ in equation (1) giving rise to parameters K_x, E_x which are listed in table 2.

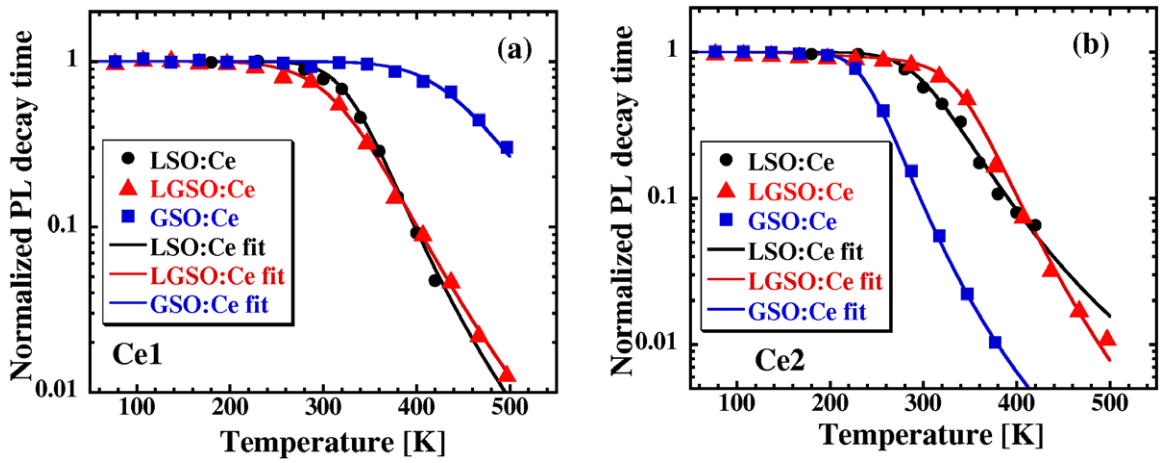

Figure 6. Nanosecond decay time temperature dependence of the Ce1 (*a*) and Ce2 (*b*) centres for LSO (black full circles), LGSO (red full triangles), GSO (blue full squares), in the units of the radiative lifetime at the lowest temperatures (for the values, see table 1; $T = 77$ K); λ_{ex} and λ_{em} tabulated in table 1. Fits of the data by the model described in the text are provided by solid lines.

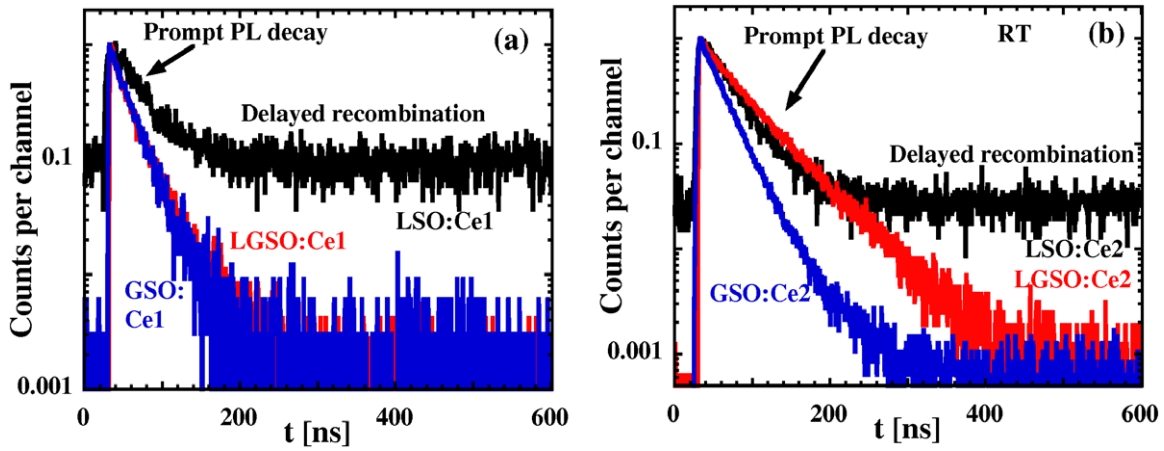

Figure 7. RT PL decay curves related to the Ce^{3+} $5d$–$4f$ transitions for the Ce1 (*a*) and Ce2 (*b*) centres in LSO (black solid line), LGSO (red solid line) and GSO (blue solid line) hosts; λ_{ex} and λ_{em} tabulated in table 1.

Table 2. Parameters of the best fits connected to the Ce1, Ce2 ns decay time temperature dependence (using the equation (1) to fit the experimental data). The parameters uncertainty corresponding to the range within which a satisfactory fit is obtained is about 5% for E_{xi} and an order of magnitude for K_{xi}.

	k_{rad} [s^{-1}]	K_{xi} [s^{-1}]	E_{xi} [meV]
LSO:Ce1	2.97×10^7	5.2×10^{13}	420
LSO:Ce2	1.80×10^7	1.2×10^{12}	300
LGSO:Ce1	3.33×10^7	3.0×10^{10}	200
		4.0×10^{13}	420
LGSO:Ce2	1.58×10^7	2.5×10^7	60
		1.0×10^{14}	470
GSO:Ce1	3.70×10^7	3.5×10^{12}	450
GSO:Ce2	2.32×10^7	1.2×10^{13}	280

Energy barriers are connected to either thermal quenching of the luminescence or thermally induced ionization of the excited state, which is discussed in connection to figures 6, 7 and 8. Dependences of LGSO, on the other hand, had to be approximated by a two channel model ($i = 1, 2$ in equation (1)), the best parameters of which are again listed in table 2. The origin of two different quenching processes is discussed below.

To better understand the origin of the temperature quenching of the Ce^{3+} decay times, the innovative method of measuring the temperature dependence of intensity of the delayed radiative recombination was employed [30]. In this experiment excitation/emission wavelength is set the same as in the nanosecond decay measurement, but the time window is set up to a few tens of milliseconds. The excitation is accomplished by a low frequency (10–30 Hz) intense microsecond xenon flash lamp and the driving software ensures that the next excitation flash comes right after the time window is closed, i.e. the dead-times between the time windows are minimized. Temperature dependence of the decay curve integral can, with an excellent sensitivity, indicate the escape of an electron from the $5d_1$ state to the conduction band and its later return resulting in the delayed radiative recombination.

Figure 8 illustrates the temperature dependence of delayed recombination integrals related to Ce1 and Ce2 centres for different hosts. Before integrating the decay curves the highest points (containing prompt ns luminescence) were omitted, for details see [12, 30].

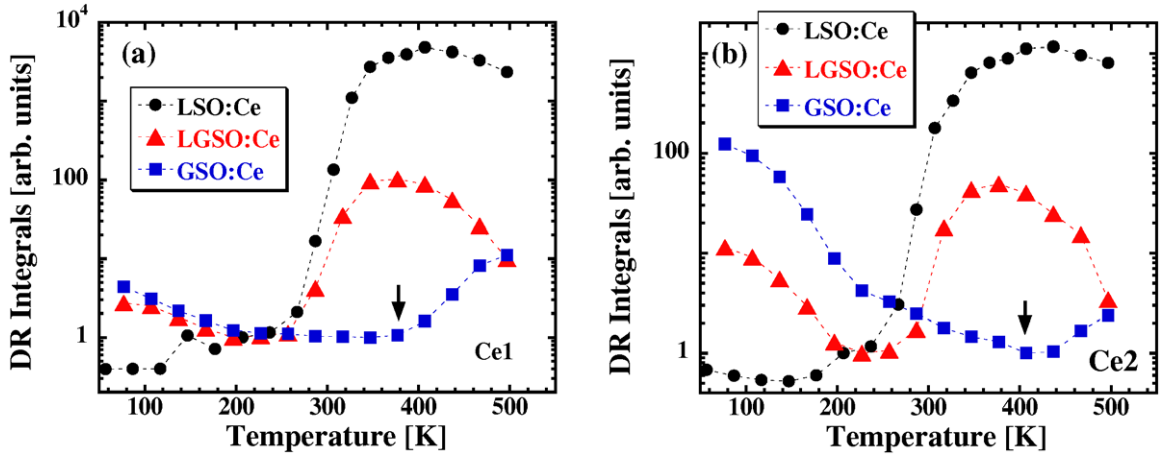

Figure 8. Temperature dependence of normalized delayed recombination (DR) integrals of the Ce1 (*a*) and Ce2 (*b*) centres for LSO (black full circles), LGSO (red full triangles), GSO (blue full squares). The arrows show the onset of the thermally induced ionization of the $5d^1$ state; λ_{ex} and λ_{em} tabulated in table 1.

As already shown in [12], both cerium centres in LSO become ionized below RT, with the onset at around 200 K, which is in a good agreement with the ns decay curve behaviour at RT. A similar observation can be made for the LGSO host but the onset of the ionization is shifted to slightly higher temperatures which results in a lower background value (with respect to LSO:Ce) in the ns decay curves at RT in figure 6. Moreover there is another process, characterized by the second set of fit parameters in table 2, shaping the dependence at lower temperatures which we assign to a kind of tunnelling process, based on the similarity with LSO:Ce [27]. It is also worth noting that the electron transport between the trap and the Ce^{3+} centre can be affected by different environments with varying relative content of Gd and Lu. Disorder in the mixed crystal components distribution and clusterization should modify the edges of the conduction and valence bands [16] thus affecting the energy gap between the $Ce^{3+}5d^1$ level and the bottom of the conduction band. Decrease of the delayed recombination integrals above 400 K in LSO:Ce and LGSO:Ce can be due to shaping of their temperature dependence by the presence of traps due to the dependence of detrapping times on temperature and finite time of the delayed recombination decay measurement [31, 32]. In contrast, GSO:Ce exhibits dramatically different behaviour, for both Ce1 and Ce2 centres. The delayed recombination integral decreases from the lowest temperatures up to some 400 K which means that the ns decay time shortening in this temperature region is not due to ionization of the Ce^{3+} excited state but rather due to classical thermal quenching of luminescence, as already discussed above. The onset of ionization for GSO:Ce1, Ce2 is then at around 400 K, as also indicated by arrows in figure 7.

We also note that delayed recombination integrals show a non-zero value even at the lowest temperatures, which has been explained by quantum tunnelling between the luminescence centre and a nearby defect state [33]. The increase of the signal at the lowest temperatures is difficult to explain and better understanding of the delayed recombination behavior would require an independent study of characteristics of the traps involved in the delayed recombination process [31].

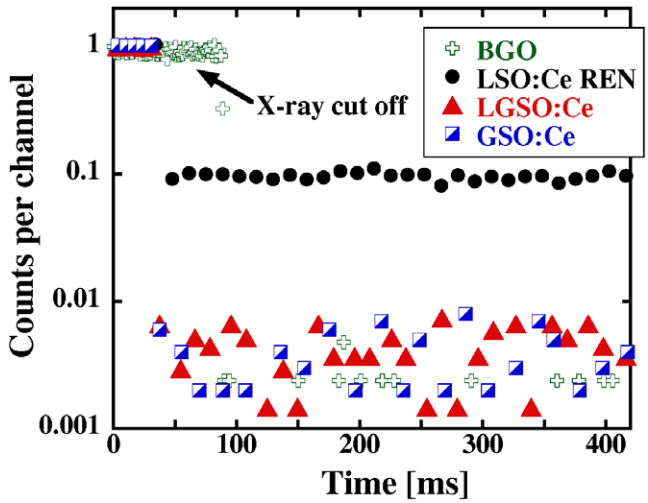

Figure 9. Normalized RT afterglow curves for LSO:Ce, LGSO:Ce, GSO:Ce and the standard BGO crystal excited by x-ray (40 kV), all emission regions.

In order to compare the afterglow effect and its dependence on the L(G)SO:Ce composition the afterglow curves were measured (see figure 9). A sample was continuously irradiated by the x-ray source (40 kV) for several tens of seconds and then the excitation was cut-off. The spectrally unresolved emission intensity was monitored along this process in the 0.5 s time window. Keeping the experimental conditions the same, it is possible to quantitatively compare different samples. Apparently, with increasing Gd amount in the sample the afterglow becomes less significant as the average signal level after the x-ray switching-off is 0.096, 0.0021, 0.0013 for LSO:Ce, LGSO:Ce and GSO:Ce, respectively. The afterglow of the last two crystals falls into the same level as that of the standard BGO crystal (also shown in figure 9 for comparison) known altogether as the material with an extremely low afterglow [34, 35]. Relatively low afterglow of LGSO:Ce is in a good agreement with the ns decay curve shape in figure 7 which is lacking the delayed recombination component. It means that Ce centres in the LGSO at RT are not noticeably ionized. GSO, on the other hand, is not ionized

at all at RT and its lower integral RL intensity (compared to LSO and LGSO) is due to thermal quenching of Ce2 and some other efficiency loss in the scintillation mechanism as discussed above.

5. Conclusions

Radioluminescence, photoluminescence emission and excitation spectra as well as both the prompt and delayed decay kinetics of LSO:Ce, LGSO:Ce and GSO:Ce were measured in a broad temperature region in order to investigate the influence of the gadolinium concentration on the Ce1 and Ce2 luminescence characteristics and their temperature dependencies. The positions of the Ce^{3+} absorption bands at RT are almost independent of the gadolinium content in LSO:Ce and LGSO:Ce having the same crystal structure while there are distinct deviations observed in GSO:Ce having a different crystal structure. With increasing gadolinium concentration (going from LSO to GSO) the emission maximum is shifting to lower energies. Spectral characteristics of the Ce1 and Ce2 can be well resolved and excitation bands can be assigned to the Ce1 and Ce2 $4f$–$5d_{1,2}$ transitions in all the studied hosts. A phenomenological model is employed to describe the Ce^{3+} excited state dynamics and explain the nanosecond decay time's reduction with increasing temperature. It is demonstrated that LSO:Ce nanosecond decay time shortening, for both the Ce1 and Ce2 centres, is dominantly caused by thermally-assisted excited state ionization with the onset below 200 K. Such ionization leads to delayed light production which worsens the afterglow and affects the nanosecond decay time characteristics. GSO:Ce, on the other hand, suffers predominantly from a thermal quenching which causes nanosecond decay time shortening of the Ce1 and Ce2 centres above 360 K and 200 K, respectively. Lower overall emission intensity of RL spectra at RT and a lower light yield of GSO:Ce compared to other orthosilicates can only partly be explained by thermal quenching of the Ce2 centre. LGSO:Ce behavior lies in-between LSO:Ce and GSO:Ce somewhat closer to the former due to the same structure. The shape of the nanosecond decay time temperature dependence of LGSO:Ce implies a more complicated emission mechanism, which possibly includes a kind of tunneling process. Early ionization of both the Ce1 and Ce2 centres above RT discourage the LGSO:Ce usage in high temperature applications. Afterglow curves revealed that in both the LGSO:Ce and GSO:Ce samples the afterglow intensity is considerably reduced compared to that of LSO:Ce. As a result of these characteristics, the comparative advantage of LGSO:Ce with respect to LSO:Ce and GSO:Ce appears mainly around RT.

Acknowledgments

Support from the Czech Science Foundation project P204/12/0805 is gratefully acknowledged. Authors are grateful to H. Ishibashi from Hitachi Chemical Co. for providing the GSO:Ce sample.

References

[1] Anan'eva G V, Korovkin A M, Merkulyaeva T I, Morozova A M, Petrov M V, Savinova I R, Startsev V R and Feofilov P P 1981 *Izv. Akad. Nauk SSSR, Neorg. Mater.* **17** 1037
[2] Suzuki H, Tombrello T A, Melcher C L and Schweitzer J S 1992 *Nucl. Instrum. Meth.* A **320** 263
[3] Takagi K and Fukazawa T 1983 *Appl. Phys. Lett.* **42** 43
[4] Sekita M, Miyazawa Y, Akahane T and Chiba T J. 1989 *Appl. Phys.* **66** 373
[5] Melcher C L, Schweitzer J S, Utsu T and Akiyama S 1990 *IEEE Trans. Nucl. Sci.* **NS-37** 161
[6] Kobayashi M and Ishii M 1991 *Nucl. Instr. Method* B **61** 491
[7] Utsu T and Akiyama S J 1991 *Cryst. Growth* **109** 385
[8] Kurashige K *et al* 2004 *IEEE Trans. Nucl. Sci.* **51** 742
[9] Makino A and Yokota H 2005 *Nucl. Instrum. Meth.* A **548** 446
[10] Blahuta A, Bessiere A, Viana B, Dorenbos P and Ouspenski V 2013 *IEEE. Trans. Nucl. Sci.* **60** 3134
[11] Felsche J 1973 *Structure and Bonding* vol 13, ed Dunitz *et al* (Berlin: Springer) p 99
[12] Jary V, Nikl M, Mihokova E, Mares J A, Prusa P, Horodysky P, Beitlerova A and Chewpraditkul W 2012 *IEEE Trans. Nucl. Sci.* **59** 2079
[13] Loutts G B, Zagumenni A I, Lavrishichev S V, Zavartsev Y D and Studenikin P A 1997 *J. Cryst. Growth* **174** 331
[14] Usui T, Shimizu S, Shimura N, Kurashige K, Kurata Y, Ishibashi H and Yamamoto H 2006 *IEEE Nucl. Sci. Symp. Conf. Rec.* **2** 1166
[15] Sidletskiy O *et al* 2010 *J. Cryst. Growth* **312** 601
[16] Sidletskiy O *et al* 2012 *Cryst. Growth Des* **12** 4411
[17] Sidletskiy O *et al* 2009 *Crystallogr. Rep.* **54** 1256
[18] Gektin A, Belsky A and Vasil'ev A 2014 *IEEE Trans. Nucl. Sci.* **61** 262
[19] Bondar V G, Grinyov B V, Katrunov K A, Lisetski L N, Nagornaya L L, Ryzhikov V D, Spasov V G, Starzhinskiy N G and Tamulaitis G 2005 *Nucl. Instrum. Meth.* A **537** 215
[20] Chai B 2007 US Patent No. 766845 B1
[21] Usui T, Shimura N, Kurata Y and Kurashige K 2006 US Patent No. 0266277 A1
[22] Kurtsev D, Sidletskiy O, Neicheva S, Bondar V, Zelenskaya O, Tarasov V, Biatov M and Gektin A 2014 *Mater. Res. Bull.* **52** 25
[23] Ren G, Qin L, Li H and Lu S 2006 *Cryst. Res. Technol.* **41** 163
[24] Mares J A and D'Ambrosio C 2007 *Opt. Matter* **30** 22
[25] Mares J A, Nikl M, Mihokova E, Beitlerova A, Vedda A and D'Ambrosio C 2008 *IEEE Trans. Nucl. Sci.* **55** 1142
[26] Kamenskikh I A *et al* 1995 *Radiat. Eff. Defects solids* **135** 391
[27] Vedda A *et al* 2008 *Phys. Rev.* B **78** 195123
[28] van der Kolk E, Basun S A, Imbush G F and Yen W M 2003 *Appl. Phys. Lett.* **83** 1740
[29] di Bartolo B 1968 *Optical Interaction in Solids* (New York: Wiley)
[30] Pejchal J *et al* 2009 *J. Phys. D: Appl. Phys.* **42** 055117
[31] Fasoli M, Vedda A, Mihokova E and Nikl M 2012 *Phys. Rev.* B **85** 085127
[32] Mihokova E, Nikl M, Schulman L S and Jary V 2013 *Phys. Status Solidi RRL* **7** 228
[33] Mihokova E, Schulman L S, Nikl M, Docekalova Z and Jary V 2013 *Chem. Phys. Lett.* **578** 66
[34] Oi T, Takagi K and Fukazawa T 1980 *Appl. Phys. Lett.* **36** 278
[35] Moszynski M, Gresset C, Vacher J and Odru R 1981 *Nucl. Instrum. Methods* **188** 403

Optical Materials 35 (2013) 1226–1229

Contents lists available at SciVerse ScienceDirect

Optical Materials

journal homepage: www.elsevier.com/locate/optmat

Luminescence and structural properties of $RbGdS_2$ compounds doped by rare earth elements

V. Jarý [a,*], L. Havlák [a], J. Bárta [b], E. Mihóková [a], M. Nikl [a]

[a] Institute of Physics, Academy of Sciences of the Czech Republic, Na Slovance 1999/2, Praha 8 18221, Czech Republic
[b] Faculty of Nuclear Sciences and Physical Engineering, Czech Technical University in Prague, Brehova 7, Praha 1 11519, Czech Republic

ARTICLE INFO

Article history:
Received 20 September 2012
Received in revised form 3 January 2013
Accepted 19 January 2013
Available online 7 March 2013

Keywords:
Luminescence
X-ray diffraction
Crystal structure
Optical materials
Ternary sulfides
Rare earths doping

ABSTRACT

Rare earth elements (Pr, Ce) doped ternary sulfides of formula $RbGd_{1-x}RE_xS_2$ were synthesized in the form of crystalline hexagonal platelets by chemical reaction under the flow of hydrogen sulfide. The X-ray powder diffraction detected only a single crystalline phase of rhombohedral lattice system. Optical properties of studied systems are investigated by methods of time-resolved luminescence spectroscopy. Thermal stability of the Pr^{3+} emission is demonstrated. Application potential in the white light-emitting diode solid state lighting or X-ray phosphors is discussed.

1. Introduction

We have recently started to investigate the scintillation and luminescence properties of the unexplored family of rare earth (RE)-doped ternary sulfides $RbLaS_2$, $RbLuS_2$, which show prospective applications for X-ray and white LED phosphors [1,2]. Rare-earth ternary sulfides of general formula $MLnS_2$, where M = alkali metal and Ln = rare earth metal, mostly adopt α-$NaFeO_2$ rhombohedral structure (space group $R\bar{3}m$, no. 166), featuring alternating layers of MS_6 and LnS_6 regular octahedra [3,4]. In the rhombohedrally-centered hexagonal unit cell, Ln^{3+} ions occupy 3(b) Wyckoff sites (0,0,0); M^+ ions reside in 3(a) sites (0,0,1/2) and sulfur in 6(c) sites (0,0,z). The parameter $z \sim 0.23$ depends on the size of Ln^{3+} ion [5]. In this paper we study optical properties of the $RbGdS_2$ host doped with Ce and Pr ions. We aim to better understand the mechanisms of scintillation and luminescence of such a ternary sulfide system as well as a correlation between chemical composition and the observed characteristics. In addition to luminescence spectra and decay characteristics, concentration and temperature dependences of emission features as well as phenomenological model of Ce^{3+} excited state dynamics are also addressed.

2. Experimental setup

$RbGdS_2$:Pr and $RbGdS_2$:Ce crystals were prepared in an electric resistance furnace by the reaction of H_2S with a mixture of Gd_2O_3:CeO_2 or Gd_2O_3:Pr_6O_{11} and excess of Rb_2CO_3 [1]. The reaction temperature reached 1000 °C and the hydrogen sulfide flow was applied for 90 min. Further details are reported in [1].

Phase identification, purity assessment and determination of lattice constants of the prepared materials were investigated by X-ray powder diffraction (XRPD) using Ni-filtered Cu $K\alpha_{1,2}$ radiation and modified, computer-controlled HZG-3 goniometer. X-ray fluorescence (XRF) analyzer Niton XL3t 900 was employed to investigate the doping efficiency of Pr into the prepared solid phase. Due to spectral interference, Pr Lα (5.034 keV) and integral of Gd Lβ_1 through Gd Lβ_4 (6.713–7.034 keV) fluorescent lines were used for the XRF analysis. Micrographs of the prepared platelets were recorded using DN 45 TH 4 TV light microscope (Lambda Praha Ltd.), equipped with CCD camera and RCH-Condenser (Relief Contrast after Hostounský).

Absorption spectra were measured using UV/VIS Spectrophotometer Shimadzu UV-1601. Photoluminescence spectra and decay curves were measured by the custom made Spectrofluorometer 5000 M, Horiba Jobin Yvon, using the steady state deuterium lamp (photoluminescence excitation spectra (PLE) in the 200–500 nm spectral region and emission spectra (PL) in 200–800 nm spectra), X-ray tube (radioluminescence (RL) spectra in 200–800 nm) and

* Corresponding author. Tel.: +420 724539175.
E-mail address: jary@fzu.cz (V. Jarý).

0925-3467/$ - see front matter © 2013 Elsevier B.V. All rights reserved.
http://dx.doi.org/10.1016/j.optmat.2013.01.028

microsecond xenon and nanosecond hydrogen pulsed flashlamps (PL decay curves) as the excitation sources. Spectra were corrected for instrumental effects and a convolution procedure was applied to the decay curves to determine true decay times (SpectraSolve software package, Ames Photonics). Room-temperature (RT) luminescence properties of $RbGdS_2$:RE crystalline platelets were studied without powdering of the samples. The Oxford Instruments liquid nitrogen bath cryostat and Janis Instruments closed cycle refrigerator were used to control the sample temperature in the temperature regions 300–500 K and 8–300 K, respectively.

3. Results and discussion

According to the measured XRPD patterns, the prepared material contained rhombohedral crystalline phase without any presence of Gd_2O_2S oxy-sulfide phase, which can be present in the case of inappropriately selected reaction conditions similarly to $RbLuS_2$ [2]. Strongly preferred orientation observed in Fig. 1 as enhanced intensity of some diffraction lines, most notably those of (003) family, could not be eliminated even by thorough grinding of the sample. Positions of the diffraction lines were determined by fitting of the respective peaks with Gaussian doublets (due to $K\alpha_{1,2}$), yielding the set of calculated d_{hkl} values with assessed uncertainties according to the Bragg equation and $u(2\theta) \approx 0.01°$:

$$2 \cdot d_{hkl} \cdot \sin\theta_{hkl} = n \cdot \lambda \quad (1)$$

The diffraction peaks at 10.5° and 21° are caused by the partially filtered Cu Kβ spectral line in the incident X-ray radiation and correspond to Cu Kα lines at 11.62° and 23.36°. The lattice constants a and c were then determined by weighted linear regression (WLR) of d_{hkl} (weight:$[u(d_{hkl})]^{-2}$) using the expression for hexagonal lattice system:

$$\frac{1}{d_{hkl}^2} = \left(\frac{h^2 + hk + k^2}{a^2}\right) + \frac{l^2}{c^2} \quad (2)$$

For undoped $RbGdS_2$ samples, the obtained values $a = 0.4095(2)$ nm, $c = 2.2862(4)$ nm are significantly lower than the values reported in PDF #86-0699 [5], $a = 0.4110(1)$ nm, $c = 2.2900(7)$ nm. In an earlier work [3], lower values of $a = 0.4098$ nm, $c = 2.2880$ nm, comparable to our results, were reported. The lattice constant a slightly increases with increasing amount of Pr dopant (Fig. 1, inset), whereas lattice constant c remains essentially constant. This observation is consistent with the fact that both terminal compounds ($RbGdS_2$ and $RbPrS_2$) have an identical lattice constant c and only differ in the lattice constant a [5]. Therefore, $RbGdS_2$:Pr compound most probably forms a solid solution, with pronounced structural effects only in the high-doping area. Due to the fact that no impurities were detected using XRF and the measured intensity of Pr analytical line linearly

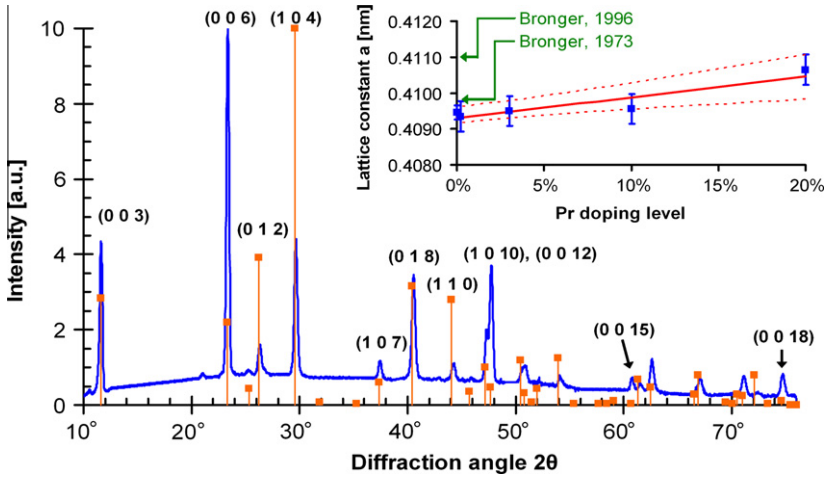

Fig. 1. Diffraction pattern of the pure $RbGdS_2$ sample, compared to PDF #86-0699 record (vertical lines). In the inset: evolution of lattice parameter a with Pr content. Squares are experimental data, solid line is the weighted linear regression (WLR), dashed line is the WLR confidence interval (98%).

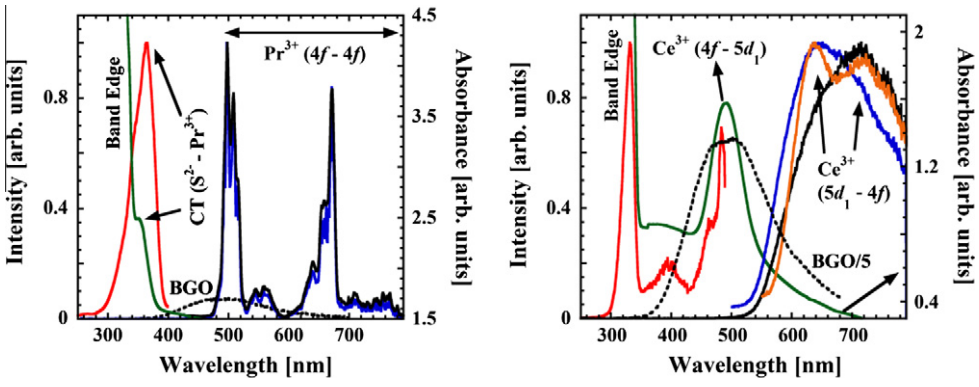

Fig. 2. RT absorption (green solid line), RL (black solid line), PL (blue solid line), PLE (red solid line) and 77 K PL ($\lambda_{ex} = 483$ nm – orange solid line) spectra of (a) $RbGdS_2$:Pr ($\lambda_{ex} = 362$ nm and $\lambda_{em} = 498$ nm) and (b) $RbGdS_2$:Ce ($\lambda_{ex} = 483$ nm and $\lambda_{em} = 715$ nm); RL spectra of BGO (black dashed line) for comparison (in (b) intensity divided by 5 for better clarity). (For interpretation of the references to color in this figure legend, the reader is referred to the web version of this article.)

increases with Pr content, the preparation method used seems to be very promising with respect to both structural and chemical purity of the formed material.

RT absorption, RL, PLE (λ_{em} = 498 nm) and PL (λ_{ex} = 362 nm) spectra of Pr^{3+}-doped $RbGdS_2$ (Pr 1%) are presented in Fig. 2a. Both absorption and PLE spectra feature the $RbGdS_2$ band edge situated at about 332 nm (low energy shifted with respect to 324 nm and for $RbLaS_2$ [1] 307 nm and for $RbLuS_2$ [2]) and another band at 365 nm ascribed to the CT transition S^{2-}–Pr^{3+}, which is, for applications, more suitable (low energy shifted) than in the $RbLaS_2$:Pr (350 nm [1]) and $RbLuS_2$:Pr (355 nm[2]). Described CT transition represents a completely new way of efficient excitation in the near UV region. PL and RL spectra coincide and exhibit characteristic well-resolved and intense Pr^{3+} 4*f*–4*f* emission lines within the 480–750 nm spectral region. RL intensity is almost 10 times higher than that of powder $Bi_4Ge_3O_{12}$ (BGO) standard scintillator. Decay curve related to the $^3P_0$–$^3H_4$ transition of Pr^{3+} (λ_{ex} = 362 nm, λ_{em} = 498 nm) is single exponential with decay time of 62 μs which is in a good agreement with the expected value of partially relaxed parity-forbidden 4*f*–4*f* Pr^{3+} transitions.

RT absorption, RL, PL (λ_{ex} = 483 nm) and PLE (λ_{em} = 715 nm) spectra of Ce^{3+}-doped $RbGdS_2$ (Ce 1%) are displayed in Fig. 2b. Both absorption and PLE spectra consist of the $RbGdS_2$ band edge at about 330 nm, the band of unknown (possibly host) origin at 395 nm, and the peak of the Ce^{3+} 4*f*–5d_1 transition at about 490 nm. Emission spectra, both excited by X-ray and 483 nm radiation, feature one broad band with maximum at 650 nm (for VIS excitation) and 715 nm (under X-ray excitation) whose origin is in the Ce^{3+} 5*d*–4*f* transition. Such a low-energy shifted Ce^{3+} emission, with respect to the oxide hosts, can be explained by a strong crystalline field and enhanced covalent bonding in this complex-sulfide matrix. Low energy shift of the RL spectrum compared to that of PL is observed and typically occurs for 5*d*–4*f* luminescence transition of Ce^{3+}or Pr^{3+} when there is a non-negligible concentration of somewhat perturbed sites of these ions in the lattice [6]. The intensity of X-ray excited emission spectrum is about 1/3 of that of powder BGO standard. It is more intense than in $RbLaS_2$:Ce 162 (only 18% of BGO [1]), but less intense than in $RbLuS_2$:Ce (180% of BGO [2]) which points to inversely proportional relation between Ce^{3+} RL intensity and RE^{3+} radius ($r_{La} > r_{Gd} > r_{Lu}$]. Thus, both the intensity and position of Ce^{3+} emission in $RbLnS_2$ strongly depend on Ln^{3+} size [1,2]. The decay curve related to the Ce^{3+} 5*d*–4*f* emission (λ_{ex} = 490 nm, λ_{em} = 640 nm) is double exponential, dominated by the component having the decay time of 2.2 ns. Such fast decay, the presence of slower component and low emission intensity (compared to BGO), all point to the fact that in this host, already at RT, the Ce^{3+} emission is either strongly quenched or the Ce^{3+} 5d_1 excited state is significantly ionized.

To demonstrate the real possibility of using $RbGdS_2$:Pr for white LED phosphors, the temperature stability of the Pr^{3+} emission was investigated between 20 °C and 200 °C, results shown in Fig. 3. Temperature dependences of emission spectra integrals and decay times of two samples of $RbGdS_2$:Pr with different Pr content (0.05% and 3%) were measured from RT up to 200 °C. Decay time values are reduced to 50% (for both samples) and emission spectra integrals (integrated in the 450–680 nm range – see Fig. 2a) are reduced to 30% (0.05% sample) and 25% (3% sample) of their RT value. Observed reduction can also be influenced by the temperature dependence of the transition dipole operator itself. Observed dependences make the material usable for applications at higher temperatures (e.g. white LED phosphor). Even for the $RbGdS_2$ compound doped by 3% of Pr, there are no indications of the concentration quenching. In comparison with $SrGa_2S_4$ [7], where the smallest Ga–Ga distance is d = 3.052 Å, $RbGdS_2$, having the smallest Gd–Gd distance d = 4.110 Å, offers a higher level of doping, before the energy transfer (concentration quenching) and cross-relaxation processes

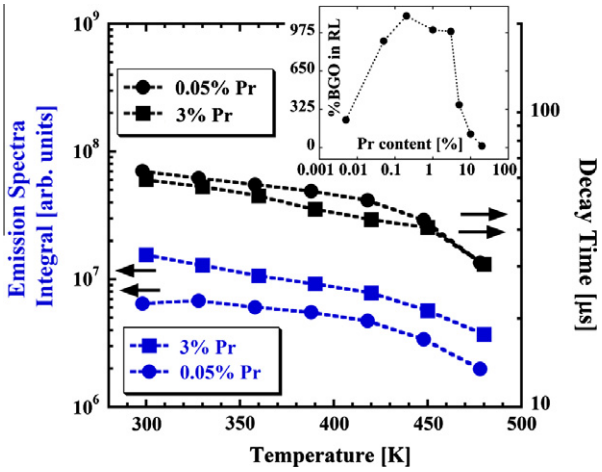

Fig. 3. Temperature dependences of the Pr^{3+} emission spectra integrals (λ_{ex} = 362 nm) for 3% sample (blue full squares) and 0.05% sample (blue full circles) and of decay times of the Pr^{3+} $^3P_0$–$^3H_4$ transition (ex = 362 nm, em = 498 nm) for 3% sample (black full squares) and 0.05% sample (black full circles); RL intensity as a function of Pr content in $RbGdS_2$:Pr in the inset. (For interpretation of the references to color in this figure legend, the reader is referred to the web version of this article.)

occur. The probabilities of those phenomena between two such sites are proportional to $1/d^6$. The intensity of $RbGdS_2$:Pr emission under X-ray excitation as a function of Pr content was studied in the broad concentration range (0.005–20% mol), results are shown in the inset of Fig. 3. Starting from low Pr concentration, the 0.005% sample still shows 230% of BGÓs intensity. The maximum of 1150% of BGO is reached for the 0.2% sample and for heavily doped sample (20% of Pr), RL intensity reaches only about 10% of BGO, probably due to severe concentration quenching. For future research and potential application purposes the interval of concentrations 0.1–3% appears to be the most suitable.

In order to better understand the observed behavior of the Ce^{3+} emission, the low temperature PLE (for 640 nm emission) and PL (under 485 nm excitation – Fig. 2b) spectra together with the temperature dependence of the decay times were recorded. PLE spectrum exhibits the same features as that at RT (Fig. 2b). However, there is a typical high-energy shift in the band edge position between 330 nm at RT and 320 nm at 77 K. PL spectrum measured

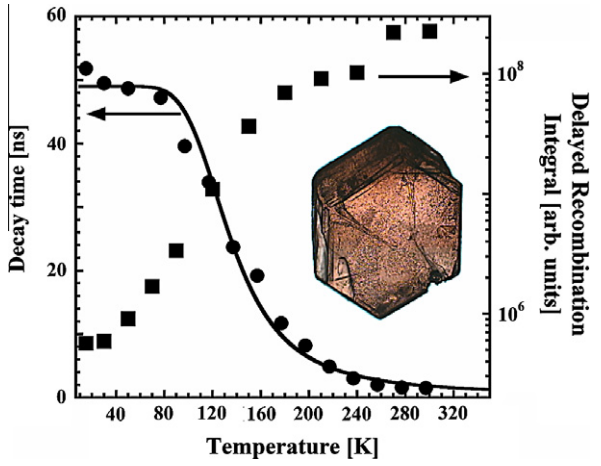

Fig. 4. Temperature dependence of the ns decay time (λ_{ex} = 490 nm, λ_{em} = 640 nm) of $RbGdS_2$:Ce (full circles), fit of the ns decay times by phenomenological model (solid line), temperature dependence of the delayed recombination integrals (λ_{ex} = 490 nm and λ_{em} = 640 nm) of $RbGdS_2$:Ce (full squares); light microscope micrograph of the Ce^{3+}-doped $RbGdS_2$ crystal (magnification 300×) in the inset.

at 77 K shows the characteristic well-resolved doublet of Ce^{3+} ground state ($^2F_{5/2}$ at 639 nm and $^2F_{7/2}$ at 722 nm). The energy separation, ~1700 cm^{-1}, matches the value of about 2000 cm^{-1} known from many other hosts. With increasing temperature the doublet becomes unresolved due to ground state levels thermalization. The measured temperature dependence of the ns decay times (λ_{ex} = 490 nm, λ_{em} = 640 nm) and its fit considering standard barrier quenching as well as the temperature dependence of delayed recombination integrals (for details concerning the method, see [8]) related to Ce^{3+} 5*d*–4*f* transition (λ_{ex} = 490 nm, λ_{em} = 640 nm) in $RbGdS_2$:Ce are displayed in Fig. 4. The data concerning ns decay time can be approximated by a simple equation:

$$(\tau_{observed})^{-1} = (\tau_{radiative})^{-1} + K_x \exp(-E_x/kT) \quad (3)$$

where $\tau_{observed}$, $\tau_{radiative}$, K_x, E_x, k, and T represent the PL decay time measured at temperature T, the low temperature limit of the PL decay time (52.5 ns), frequency factor, quenching barrier height, Boltzmann constant and absolute temperature, respectively [9]. The parameters of the best fit of Eq. (3) to experimental data are $K_x = 8.10^9\ s^{-1}$ and E_x = 70 meV. Correlation between the increase of the delayed recombination integrals and the decrease of ns decay times with increasing temperature indicates that the Ce^{3+} emission center becomes ionized. More specifically, electron is thermally promoted from the $5d_1$ excited state to the conduction band of $RbGdS_2$ from where it can return at later times and radiatively recombine with the hole, giving rise to the delayed recombination luminescence. A more detailed explanation of the delayed recombination integral behavior requires an independent study of characteristics of the traps involved in the delayed recombination process [10].

4. Conclusion

In this study we present the RE^{3+}-doped (RE = Ce and Pr) $RbGdS_2$ single crystalline materials as novel, potentially interesting white LED and X-ray phosphors. We prepared the single crystal samples about 0.1 mm thick with a cross-section area up to a few square mm, consisting of the single, $RbGdS_2$ phase. The absorption and PLE spectra show the $RbGdS_2$ band edge at 330 nm, Ce^{3+} 4*f*–5d_1 absorption band at 483 nm and CT S^{2-}–Pr^{3+} band at 365 nm. The charge transfer transition offers a completely new way of efficient excitation in the near UV region, which could be exploited in white LED phosphors. X-ray excitation provides the characteristic Pr^{3+} 4*f*–4*f* line emissions within the 480–750 nm region (reaching 1150% of BGO standard) and broad Ce^{3+} emission band in the red spectral region (reaching 30% of BGO). RT decay times of the 498 nm (Pr^{3+}) emission line and Ce^{3+} emission band are about 62 μs and 2.2 ns, respectively. The Ce^{3+} center is strongly ionized at room temperature. Phenomenological model describing the Ce^{3+} excited state dynamics provides the value of thermal ionization energy barrier of 70 meV. Thermal stability of Pr^{3+} emission is confirmed. Elevated effective atomic number (Z_{eff} = 52), efficient energy transfer from the host and lower band gap, relative to oxide-based materials, are intrinsic advantages of the RE^{3+}-doped $RbGdS_2$ with respect to most of existing X-ray phosphors. Dependence of luminescence characteristics on Ln^{3+} cation in $RbLnS_2$ host is found. All studied samples show very reasonable long-term stability.

Acknowledgement

The financial support of the TACR Project TA01011017 is gratefully acknowledged.

References

[1] L. Havlak, M. Nikl, J. Barta, V. Jary, P. Bohacek, Acta Materialia 59 (2011) 6219–6227.
[2] V. Jary, L. Havlak, J. Barta, M. Nikl, Phys. Status Solidi Rapid Res. Lett. 6 (2012) 95–97.
[3] W. Bronger, R. Elter, E. Maus, T. Schmitt, Rev. Chim. Miner. 10 (1973) 147.
[4] W. Bronger, W. Bruggemann, M. von der Ahe, D. Schmitz, J. Alloys Compd. 200 (1993) 205.
[5] W. Bronger, J. Eyck, K. Kruse, D. Schmitz, Eur. J. Sol. State Inorg. 33 (1996) 213.
[6] C. Pedrini, B. Moine, J.C. Gacon, B. Jacquier, J. Phys. Cond. Matter 4 (1992) 5461.
[7] Z. Xinmin, W. Hao, Z. Heping, S. Qiang, J. Rare Earth 25 (6) (2007) 701–705.
[8] J. Pejchal, M. Nikl, E. Mihokova, J.A. Mareš, A. Yoshikawa, H. Ogino, K.M. Schillemat, A. Krasnikov, A. Vedda, K. Nejezchleb, V. Mucka, J. Phys. D: Appl. Phys. 42 (2009) 055117.
[9] M. Nikl, G. Ren, D. Ding, E. Mihokova, V. Jary, H. Feng, Chem. Phys. Lett. 493 (2010) 72–75.
[10] M. Fasoli, A. Vedda, E. Mihokova, M. Nikl, Phys. Rev. B 85 (2012) 085127.

Optical and Structural Properties of RE^{3+}-Doped $KLnS_2$ Compounds

V. Jarý, L. Havlák, J. Bárta, E. Mihóková, and M. Nikl

***Abstract*—Rare-earth ($RE = Sm$, Pr, Tb, Tm) doped ternary sulfides having the general formula $KLn_{0.995}RE_{0.005}S_2$ ($Ln =$ La, Gd, Lu) and undoped $KLnS_2$ were synthesized in the form of crystalline hexagonal platelets by a chemical reaction in an electric resistance furnace under the flow of hydrogen sulfide. X-ray powder diffraction confirmed only a single phase of the rhombohedral lattice system (space group R-3 m). Time-resolved luminescence spectroscopy was employed to investigate radioluminescence, photoluminescence, decay kinetics and absorption spectra. The $KLnS_2$ band edge at 300–330 nm was found and characteristic Pr^{3+}, Sm^{3+}, Tb^{3+} and Tm^{3+} $4f - 4f$ emission lines in the visible spectral range were observed. The charge transfer transitions in the Pr^{3+}- and Sm^{3+}-related excitation spectra in the range 330–370 nm are described and the eficient energy transfer from the host to the emission centers is revealed. We discuss the potential for application of these materials in white LED solid-state lighting and X-ray phosphors.**

***Index Terms*—Luminescence, scintillator, sulfides, white LED.**

I. Introduction

HEAVY and efficient scintillation materials for X-ray and gamma-ray detection as well as the white light-emitting diode solid state lighting materials are under development and new groups of materials can be considered for applications in high energy physics, medical screening, industrial defectoscopy, homeland security and others. Optical properties of RE^{3+}-doped sulfides ($RE = Sm$, Pr, Tb, Tm) are rather scarcely reported in the literature. Corresponding work is mostly focusing on the binary compounds in a powder form.

RL and PL spectra and concentration dependence of BaS:Sm are reported in [1]. Europium and samarium doped CaS thin films (CaS:Eu,Sm) with different thickness were prepared by the pulsed laser deposition technique in [2]. Europium and samarium co-doped strontium sulfide infrared up-conversion phosphor was synthesized via calcining the precursor [3]. Its up-conversion emission spectrum is a continuous broadband spectrum with one peak at 599 nm resulting from the transitions of $Eu^{2+}5d(^2T_{2g}) \rightarrow 4f(^8S_{11/2})$. Thermally stimulated luminescence of alkaline earth sulfide phosphors (CaS, SrS, and BaS) doped with rare earth ions (Sm and Ce) was investigated in [4]. Photoluminescence of ZnS:Sm phosphor prepared in a reductive atmosphere is reported in [5]. Rare-earth ternary complexes $Tb_{1-x}Eu_x(m\text{-}NBA)_3Phen$ (X = 1, 0.25, 0.5, 0.75, 1.0) were synthesized and characterized in [6]. It was found that luminescence of Eu^{3+} complex was enhanced by co-doping with Tb^{3+}. Optical absorption and PL spectra of (CdZn)S;$CdCl_2$:Tb films prepared by chemical deposition method on glass substrates are investigated in [7]. Excitation mechanism of luminescence centers in nanostructured ZnS:Tb thin-film electroluminescent device is discussed in [8]. Synthesis and luminescence properties of sulfidic photoluminescent materials activated by Ce^{3+} and Tb^{3+} are reported in [9]. They are described as green photoluminescence materials with persistence of about 5 minutes. The luminescence properties of ZnS:Tb,P are examined in [10] to investigate the possibility of applying donor (D)-acceptor (A) pair emission in ZnS crystals to electroluminescence (EL) device. Zinc sulfide thin films doped with trivalent rare earths (cerium, europium, terbium, thulium) grown by the atomic layer epitaxy (ALE) method are investigated in [11]. The synthesized SrS:Pr phosphor featuring white luminiscence is introduced in [12]. Ba_2ZnS_3:Pr phosphors, emitting white to green light, synthesized by the double-crucible method, are described in [13]. The photoluminescence of $Ca_4Ga_2S_7$:Pr^{3+} is studied in [14]. Electroluminescence of Pr ions in ZnS thin films is mentioned in [15]. Room-temperature visible luminescence from Pr^{3+} ions embedded in germanium sulfide glass hosts is reported in [16]. Infrared luminescence of thulium doped CdS:Tm,Cu phosphors, which have been calcined in a sulphur atmosphere, is found in [17].

Rare-earth-doped $RbLnS_2$ ($Ln = La, Gd, Lu$) ternary sulfide compounds, in the form of crystalline hexagonal platelets, have been examined by our group recently as an interesting family of materials [18]–[20] whose intrinsic advantages and properties are listed in detail in the pioneer work [18]. Potassium rare-earth sulfides of general formula $KLnS_2$ (where $Ln = La - Lu$) crystallize in a rhombohedral lattice of α-$NaFeO_2$ structure type (space group $\bar{R}3m$, [21]); however, the hexagonal setting of the rhombohedral lattice is more common in literature. These sulfides contain alternating layers of KS_6 and LnS_6 edge-sharing, trigonally-distorted octahedra stacked along the [1] vector in the hexagonal setting. The Ln lattice site with D_{3d} point symmetry can easily accommodate any trivalent rare-earth ion due to its favorable size, identical structure type of all $KLnS_2$ compounds

Manuscript received May 17, 2013; revised July 17, 2013; accepted July 26, 2013. Date of publication September 05, 2013; date of current version February 06, 2014. This work was supported in part by Czech TACR TA01011017 and Czech GACR 13-09876S projects.

V. Jarý, L. Havlák, E. Mihóková, and M. Nikl are with the Institute of Physics, ASCR, 162 53 Prague 6, Czech Republic (e-mail: jary@fzu.cz; havlak@fzu.cz; mihokova@fzu.cz; nikl@fzu.cz).

J. Bárta is with the Faculty of Nuclear Sciences and Physical Engineering, Czech Technical University, Prague 11519, Czech Republic (e-mail: jenceslav@gmail.com).

Color versions of one or more of the figures in this paper are available online at http://ieeexplore.ieee.org.

Digital Object Identifier 10.1109/TNS.2013.2277606

and also due to isovalent substitution with no charge compensation required. $KLnS_2$ density calculated from the diffraction data [21] and known value of formula units in the cell ($Z = 3$ in hexagonal setting) approximately linearly increases with atomic number: 3.50 g cm^{-3} ($KLaS_2$), 4.13 g cm^{-3} ($KGdS_2$), 4.71 g cm^{-3} ($KLuS_2$). The effective atomic number, a very important parameter for scintillating solid materials, also increases from 49.7 ($KLaS_2$) through 56.5 ($KGdS_2$) up to 63.3 ($KLuS_2$), which is comparable to a widely used $Lu_3Al_5O_{12}$ scintillator (62.9).

Recently, Eu^{2+}-doped $KLuS_2$ was considered as an interesting phosphor incl. the white LED light source in [22]. In this work we continue the study of emission features of other rare-earth dopants (Sm^{3+}, Pr^{3+}, Tb^{3+} and Tm^{3+}) in $KLnS_2$ matrix that, to our best knowledge, have not been so far reported in the literature.

II. Experimental Details

$KLnS_2$ crystals (Ln = La, Gd, Lu), both RE^{3+}-doped (RE = Sm, Pr, Tb, Tm) and undoped, were prepared in an electric resistance furnace by the reaction of H_2S with a mixture of 5N Ln_2O_3, 0.5% RE_xO_y (4N Sm_2O_3, 5N Pr_6O_{11}, 3N Tb_2O_3, 3N Tm_2O_3) and excess of 4N7 K_2CO_3. The reaction temperature reached 1000°C and the hydrogen sulfide flow was applied for 90 minutes. Further details are reported in [18]. Phase identification, purity assessment and determination of lattice constants of the prepared materials were investigated by X-ray powder diffraction (XRPD) using Ni-filtered Cu-$K_{\alpha 1,2}$ radiation and modified, computer-controlled HZG-3 goniometer.

Absorption spectra were measured using UV/VIS Spectrophotometer Shimadzu UV-1601. Photoluminescence (PL) spectra and decay curves were measured by the custom made Spectrofluorometer 5000 M, Horiba Jobin Yvon, using the steady state deuterium lamp (photoluminescence excitation (PLE) and emission (PL) spectra in the 190 – 500 nm and 200 – 800 nm spectral regions, respectively), Seifert X-ray tube (radioluminescence (RL) spectra within 200 – 800 nm), microsecond xenon-filled lamp and nanosecond pulsed LED diodes (PL decay curves) as the excitation sources. Spectra were corrected for instrumental effects and a convolution procedure was applied to the decay curves to determine true decay times (SpectraSolve software package, Ames Photonics). Room-temperature (RT) luminescence properties of $KLnS_2$:RE crystalline platelets were studied without powdering the samples.

III. Results and Discussion

To our best knowledge, no records of studied $KLnS_2$ phases exist in the ICDD PDF-2 database; therefore, the diffraction data measured in this paper could not be correlated with diffraction line intensities and only their positions can be calculated from the reported unit cell dimensions [21].

All the studied samples contained only a single phase with rhombohedral lattice system, possibly with prominent preferred orientation of the crystals even despite thorough grinding. No additional phases such as hexagonal oxysulfides Ln_2O_2S were detected in the samples. The measured positions

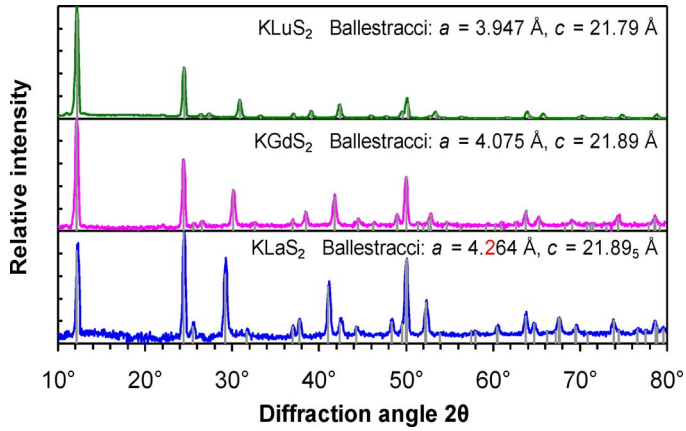

Fig. 1. Diffraction patterns of typical $KLnS_2$ samples with calculated positions of diffraction lines indicated by solid vertical lines with arbitrary height; structural reference: [21].

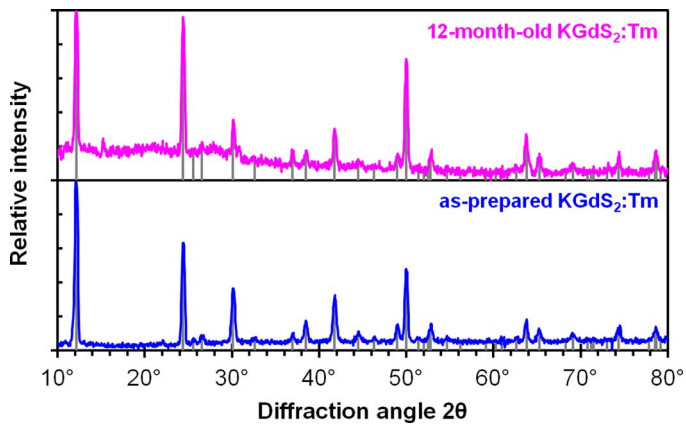

Fig. 2. Measured diffraction patterns of $KGdS_2$:Tm sample indicating long-term stability at ambient conditions; structural reference: [21].

of R-3m allowed diffraction lines (Fig. 1) corresponded very well to the unit cell dimensions determined by Ballestracci [21] with the exception of $KLaS_2$ (reported values $a = 4.464$ Å, $c = 21.895$ Å). The ratio c/a reported for $KLaS_2$ is very close to the critical value of $\sqrt{24}$, implying it should be pseudo-cubic; however, in the original paper [21], the parameter a is most probably misprinted and should be probably 4.264 Å according to other data reported in the paper. The diffraction pattern of $KLaS_2$ sample measured in this paper confirms the value of $a \sim 4.255(9)$ Å. Sometimes, slight variations in unit cell dimensions were observed among the samples, most probably due to the different size of rare-earth ions doped into the host structure.

The long-term stability of these new phosphors at room-temperature conditions in the presence of air can be illustrated by Fig. 2. The diffraction pattern of a freshly-prepared $KGdS_2$:Tm sample is identical to the diffraction pattern of the same sample after 12 months. No presence of Gd_2O_2S phase or other impurities was detected by X-ray diffraction; for comparison, $CsLnS_2$ phosphors clearly degrade at room temperature in the presence of air [23].

The RT X-ray excited luminescence spectra (X-ray tube, W cathode, $U = 40$ kV, $I = 15$ mA) of $KLnS_2$ (Ln = La, Gd,

Lu) doped with trivalent Sm, Pr, Tb, Tm (all of the 0.5% dopant concentration) as well as that of the undoped samples are displayed in Fig. 3(a-e). Their intensities are compared to that of powdered $Bi_4Ge_3O_{12}$ (BGO) standard scintillator. RL spectra of Sm^{3+}, Pr^{3+} and Tb^{3+}-doped $KLaS_2$, $KGdS_2$ and $KLuS_2$ are dominated by well-resolved and very intense $4f-4f$ emission lines within the 540 – 750 nm (Sm^{3+}), 480 – 800 nm (Pr^{3+}), and 340 – 800 nm (Tb^{3+}) spectral regions. The main emission lines of Pr^{3+} ($^3P_0 - {}^3H_4$ transition at 498 nm), Sm^{3+} ($^4G_{5/2} - {}^6H_{5/2}$ transition at 566 nm) and Tb^{3+} ($^5D_4 - {}^7F_5$ transition at 548 nm) are significantly more intensive than the emission of BGO (40 × for Sm^{3+} in $KGdS_2$, 25 × for Pr^{3+} in $KGdS_2$, 23 × for Tb^{3+} in $KGdS_2$ and $KLuS_2$). This points to a highly efficient energy transfer of the excitation energy to the luminescence centre, even when compared to $RbLnS_2$ hosts [18]–[20]. However, emission of the Tb^{3+}-doped samples (see Fig. 3(c)) shows partial superposition with the emission of host lattice, see below. The residual emission around 380 nm in the Pr^{3+}-doped sample is tentatively interpreted as a host-related process, similarly to $RbLuS_2$:Pr [20], though its position is slightly different from the one of undoped $KLuS_2$, see below. For comparison, pure $KPrS_2$ compound was prepared as well but no emission under X-ray excitation was observed, probably due to concentration quenching or some other cross-relaxation processes. Tm^{3+}-doping of $KLnS_2$ results in more complex character of the spectra. In both $KLaS_2$:Tm and $KLuS_2$:Tm RL spectra, at least two emission lines given by Tm^{3+} $4f-4f$ transitions at 373 nm ($^1D_2 - {}^3H_6$) and 483 nm ($^1D_2 - {}^3F_4$) can be found. They are, however, combined with the host emission in the visible part of the spectra. The presence of Tm^{2+} ions in the structure that might alter the emission properties, is also not excluded, taking into account strongly reducing conditions during the sample preparation. RL spectrum of $KGdS_2$:Tm is even dominated by the host emission (see below) and only a weak trace of Tm^{3+} $4f-4f$ emission is present at around 480 nm. The RL spectra of the undoped $KLaS_2$, $KGdS_2$ and $KLuS_2$ in Fig. 3(e) are formed by the broad bands in the green and red part of the spectrum whose intensity is comparable to or exceeding that of BGO and they are partially contaminated by Sm^{3+} and Pr^{3+} emission lines. The mentioned emission bands are probably related to some unknown structural defect. However, more experimental work is needed to characterize in detail the optical properties of these new hosts.

Normalized RT PLE spectra of undoped, Sm^{3+}-doped and Pr^{3+}-doped $KLnS_2$ (Ln = La, Gd, Lu) are presented in Fig. 4. Band edge of the host is clearly visible in all the undoped samples, in particular at 304 nm ($KLuS_2$), 330 nm ($KGdS_2$) and 326 nm ($KLaS_2$), wavelengths almost identical to those in $RbLnS_2$ hosts [18]–[20]. In the Pr and Sm-doped samples, other bands adjacent to or overlapping the band edge are present in the 300 – 400 nm region. We tentatively ascribe them to the CT transitions from S^{2-} to RE^{3+}, based on our previous work [18]–[20], although Sm^{3+} transition could be expected at somewhat lower energies, taking into account the RE^{2+} energy level position in [24]. Furthermore, an analogous ligand-to-Pr^{3+} CT transition was ascribed to the 240 and 320 nm excitation bands in Pr-doped $LuCl_3$ and LuI_3, respectively [25], [26]. Both band edge and CT S^{2-} – Pr^{3+} are also clearly observable in the

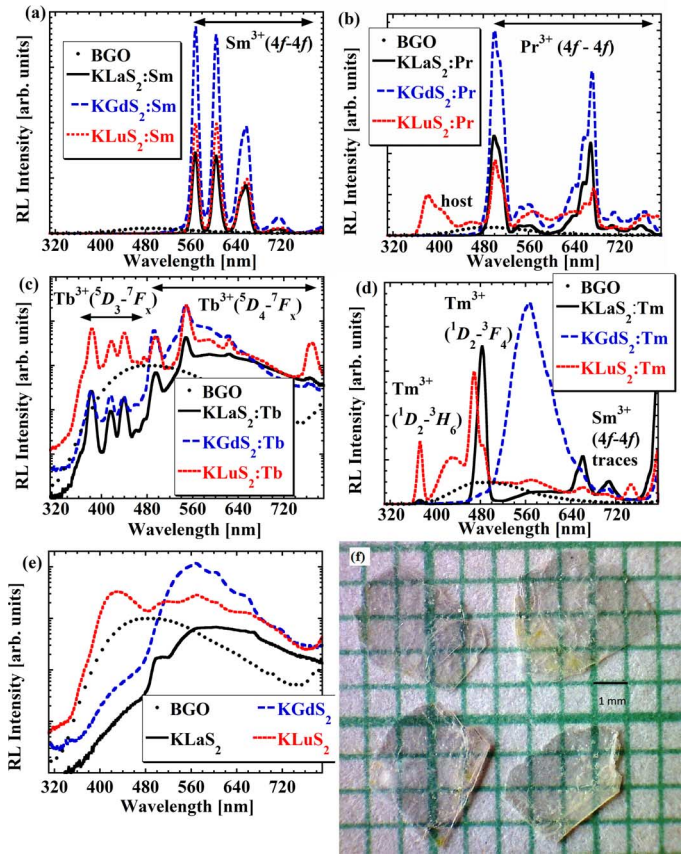

Fig. 3. RT X-ray excited emission spectra of RE^{3+}-doped $KLnS_2$ (Ln = La – black solid lines, Ln = Gd – blue dashed lines, Ln = Lu – red dotted lines; RE = Sm (a), Pr (b), Tb (c) , Tm (d), undoped (e) ; (f) a photo of the Pr^{3+}-doped $KLaS_2$ crystal.

absorption spectra, see Fig. 4(d), in accordance with the PLE spectra. The above-mentioned charge transfer transitions and the posibility of altering their spectral position by altering chemical composition, offer an interesting way of eficient excitation in the near-UV region, which can give rise to a novel principle for a white LED source with cold–warm white light tunability and circadian source development. In the blue part of all the PLE spectra, other bands, probably connected to a host lattice, are present as well.

RT PL spectra of Sm^{3+}-doped, Pr^{3+}-doped, Tb^{3+}-doped and undoped $KLnS_2$ compounds (Ln = La, Gd, Lu) under the specific excitation wavelengths are given in Fig. 5. Excitation wavelengths are taken from the excitation maxima observed in Fig. 4. Sm^{3+} doping under near UV excitation leads to the presence of well-resolved intensive emission lines given by Sm^{3+} $4f-4f$ transitions and PL spectra well coincide with the RL ones for all Ln^{3+} cations. PL spectra of Pr^{3+} in $KLaS_2$ and $KGdS_2$ matrices are composed of characteristic well-resolved intensive emission lines of Pr^{3+} $4f-4f$ transitions while in that of Pr^{3+} in $KLuS_2$ the underlying host emission has comparable intensity, similarly to that in the RL spectra (see Fig. 3(b)). As the Tb^{3+} emission is concerned, the characteristic emission lines within the 370 – 630 nm region are present, which can be ascribed to Tb^{3+} transitions from $^5D_3$ (in the region of 370–480 nm) and $^5D_4$ (480 – 630 nm) levels

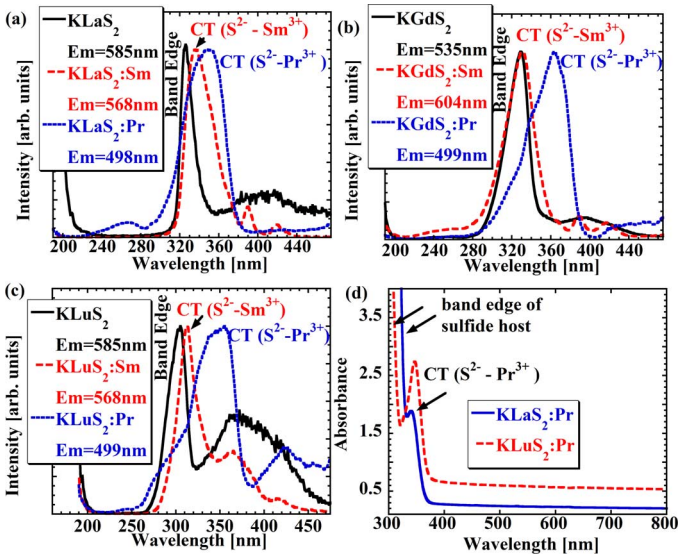

Fig. 4. RT PLE spectra of undoped (black solid lines), Pr^{3+}-doped (blue dotted lines) and Sm^{3+}-doped (red dashed lines) $KLaS_2$ (a), $KGdS_2$ (b) and $KLuS_2$ (c); absorption spectra of Pr^{3+}-doped $KLaS_2$ (blue solid line) and $KLuS_2$ (red dashed line) (d).

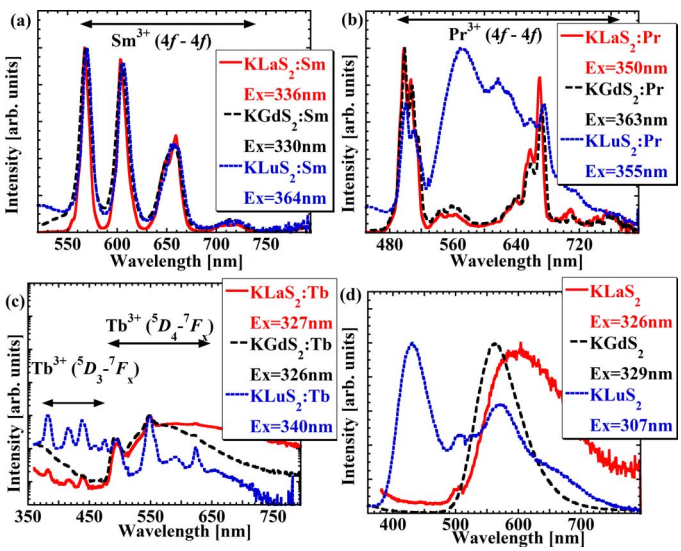

Fig. 5. RT PL spectra of Sm^{3+}-doped (a), Pr^{3+}-doped (b), Tb^{3+}-doped (c) and undoped (d) $KLnS_2$ (Ln = La– red solid lines, Ln = Gd – black dashed lines, Ln = Lu – blue dotted lines) under excitations displayed in the legend.

to the ^7F_x ground state of this luminescence centre. Emission lines within the 500 – 750 nm region, however, are not well resolved, since Tb^{3+} emission is competing with that of the host $KLnS_2$, which may also indicate less efficient energy transfer to the Tb^{3+} centre in these hosts, which is again in a good agreement with the RL spectra behaviour. Similar results were obtained also for the Tb^{3+}-doped $RbLaS_2$ [18]. RT PL spectra of undoped $KLnS_2$ samples consist of broad emission bands in the visible part of the spectrum, in accordance with the RL spectra. The $4f - 4f$ emission traces are, however, almost missing. The above emission bands are due to unknown structural defect, as already mentioned above.

RT photoluminescence decays of RE^{3+}-doped $KLnS_2$ (RE = Pr, Sm, Tb, Tm; Ln = La, Gd, Lu) were recorded in order to determine decay times related to characteristic $4f - 4f$ transition, see Table I. Excitation and emission wavelengths were taken from the PL and PLE spectra maxima, some of which are shown in Figs. 2, 3. RT decay times related to the $^3P_0 - {}^3H_4$ transition of Pr^{3+} are 60 – 70 μs, which is in a good agreement with the expected value of partially relaxed parity-forbidden $4f - 4f$ Pr^{3+} transitions. The onset of slow component is to be noted in the case of Pr^{3+}-doped $KLuS_2$, which corresponds to the considerable intensity of overlapping host emission in RL and PL spectra. Single-exponential decay curve related to the $4f - 4f$ transition of Sm^{3+} shows the decay time of about 3.9 – 4.8 ms, matching well the spin and parity-forbidden Sm^{3+} emission transitions. Single exponential decay curve time related to $^5D_4 - {}^7F_x$ of Tb^{3+} center is calculated to be about 2.6 – 3.8 ms, as again expected of spin and parity-forbidden Tb^{3+} emission transitions. However, faster component is found in the case of $KLaS_2$:Tb as well the origin of which is not clear. Decays related to Tm^{3+} emission centre are more complex, composed of two exponential components, one of which is around 30 – 120 μs and the other around 760 μs, which is probably caused by the presence of the host emission. Due to such reason, no decay curve was obtained for Tm^{3+} in $KGdS_2$.

TABLE I
PHOTOLUMINESCENCE DECAY TIMES OF Pr^{3+}, Sm^{3+}, Tb^{3+} AND Tm^{3+}-DOPED $KLnS_2$ COMPOUNDS (Ln = La, GD, LU).

	RT Pr^{3+} ($^3P_0$ - $^3H_4$) decay time [μs]	RT Sm^{3+} (from $^4G_{5/2}$) decay time [ms]	RT Tb^{3+} ($^5D_4$ - ^7F_x) decay time [ms]	RT Tm^{3+} ($^1D_2$ - $^3F_4$) decay time [μs]
$KLaS_2$	69.4	4.0	2.6 and 0.50	202 and 758
$KGdS_2$	63.1	3.9	2.9	no emission found
$KLuS_2$	59.7 and 464.4	4.8	3.8	37 and 789

IV. CONCLUSIONS

In this study the RE^{3+}-doped (RE = Sm, Pr, Tb, Tm) $KLnS_2$ (Ln = La, Gd, Lu) compounds are presented as novel, potentially interesting "white LED" and X-ray phosphor materials. Single-crystalline samples with a surface area up to a few square millimeters and a thickness of 0.1 mm were prepared by a chemical reaction and annealing technique in an electric resistance furnace. Their structures were studied by XRPD and that of rhombohedral $KLnS_2$ is present as a single crystalline phase in all the samples. X-ray-excited emission of the Pr^{3+}, Sm^{3+} and Tb^{3+} doped hosts features the characteristic $4f - 4f$ line emissions of the dopants within the 480–800 nm (Pr^{3+}), 540–750 nm (Sm^{3+}) and 340–800 nm (Tb^{3+}) spectral regions and their radioluminescence intensities well exceeded those of the BGO powder standard scintillator. The RL spectra of the undoped sample are formed by broad bands in the green and red part of the spectrum. The excitation spectra include the peaks related to the host band edge (300 – 330 nm), and charge transfer transitions within 330–370 nm in the case of Pr and Sm dopants. The charge transfer transitions offer an interesting way of eficient excitation in the near UV region. Related decay times of Sm^{3+}, Pr^{3+}, Tb^{3+} and Tm^{3+} $4f - 4f$ emission lines are in order of units of ms, tens of μs, units of ms and hundreds

of μs, respectively. All samples show reasonable long-term stability.

Elevated effective atomic number ($Zeff(KLuS_2) = 63.3$), eficient energy transfer from the $KLnS_2$ host and the band gap lower than that of oxide-based materials are intrinsic advantages of the RE^{3+}-doped $KLnS_2$ with respect to existing X-ray phosphors. They all provide obvious reasons for further study of this family of materials.

REFERENCES

[1] K. Maeda, N. Kawaida, R. Tsudome, K. Sakai, and T. Ikari, "X-ray and photoluminescence properties of Sm^{3+} doped barium sulfide," *Phys. Stat. Sol. (c)*, vol. 9, no. 12, pp. 8169–8173, 2012.

[2] S. Christoulakis, M. Suchea, N. Katsarakis, and E. Koudoumas, "Europium and samarium doped calcium sulfide thin films grown by PLD," *Appl. Surface Sci.*, vol. 243, no. 19, pp. 8169–8173, 2007.

[3] L. Lu, X. Zhang, Z. Bai, X. Wang, X. Mi, and Q. Liu, "Synthesis of infrared up-conversion material SrS: Eu, Sm," *Adv. Powder Technol.*, vol. 17, no. 2, pp. 181–187, 2006.

[4] D. R. Rao, M. S. R. Rao, and S. A. K. Reddy, "Thermally stimulated luminescence of alkaline earth sulphide phosphors doped with cerium nad samarium impurities," *Mater. Sci. Technol.*, vol. 3, no. 8, pp. 616–620, 1987.

[5] T. P. Tang, M. R. Yang, and K. S. Chen, "Photoluminescence of ZnS:Sm phosphor prepared in a reductive atmosphere," *Ceramics Int.*, vol. 26, no. 2, pp. 153–158, 2000.

[6] Y. Lv, J. Zhang, W. Cao, L. Song, and Z. Xu, "Enhanced luminescence of rare-earth complexes $Tb_{1-x}Eu_x(m\text{-}NBA)_3Phen$ in ZnS," *Spectrochimica Acta. – Part A: Mol. Biomolecular Spectrosc.*, vol. 70, no. 2, pp. 253–257, 2008.

[7] S. Bhushan and S. Pillai, "Photoconductivity and photoluminescence in chemically deposited (Cd-Zn)S:$CdCl_2$,Tb films," *Cryst. Res. Technol.*, vol. 43, no. 7, pp. 762–768, 2008.

[8] D. Adachi, K. Takei, T. Toyama, and H. Okamoto, "Excitation mechanism of luminescence centers in nanostructured ZnS:Tb thin-film electroluminescent devices," in *Proc. 13th Int. Display Workshops*, 2006, vol. 1, pp. 401–404.

[9] C. L. Deng and K. H. Qiu, "Synthesis and luminescence properties of sulfide photoluminescence materials activated by Ce^{3+} and Tb^{3+}," *J. Chengdu Inst. Technol.*, vol. 30, no. 4, pp. 409–412, 2003.

[10] O. Kanehisa, M. Shiiki, T. Suzuki, and K. Uenae, "Effects of crystallinity on the luminescence of ZnS:Tb,P powder and film," *J. Alloys Compounds*, vol. 223, no. 1, pp. 154–159, 1995.

[11] M. Tammenmaa, M. Leskela, T. Koskinen, and L. Niinisto, "Zinc sulphide thin films doped with rare earth ions," *J. Less-Common Metals*, vol. 126, no. c, pp. 209–214, 1986.

[12] V. V. Bakhmet'ev, V. G. Korsakov, M. M. Sychev, H. Tamamura, and I. Nakanishi, "Synthesizing white-luminescence SrS:Pr powder phosphor," *J. Opt. Technol.*, vol. 78, no. 7, pp. 449–451, 2011.

[13] Y. F. Lin, Y. H. Chang, Y. S. Chang, B. S. Tsai, and Y. C. Li, "Luminescent properties of trivalent praseodymium-doped barium zinc sulfide," *J. Electrochem. Soc.*, vol. 153, no. 6, pp. G543–G547, 2006.

[14] B. G. Tagiev, O. B. Tagiev, R. B. Dzhabbarov, N. N. Musaeva, and U. F. Kasumov, "Photoluminescence of $Ca_4Ga_2S_7$:Ce^{3+} and $Ca_4Ga_2S_7$:Pr^{3+}," *Inorganic Mater.*, vol. 36, no. 1, pp. 3–5, 2000.

[15] H. Yanbing, H. Yulin, and X. Xurong, "Electroluminescence of Pr ions in ZnS thin films," *J. Lumin.*, vol. 60–61, pp. 916–918, 1994.

[16] V. K. Tikhomirov, K. Iakoubovskii, P. W. Hertogen, and G. J. Adriaenssens, "Visible luminescence from Pr-doped sulfide glasses," *Appl. Phys. Lett.*, vol. 71, no. 19, pp. 2740–2742, 1997.

[17] J. Apperson, W. E. Lamb, and B. Lunn, "Infra-red luminescence of thulium doped cadmium sulphide," *Infrared Phys.*, vol. 8, no. 3, pp. 241–245, 1968.

[18] L. Havlak, V. Jary, M. Nikl, P. Bohacek, and J. Barta, "Preparation, luminescence and structural properties of RE-doped $RbLaS_2$ compounds," *Acta. Materialia*, vol. 59, no. 16, pp. 6219–6227, 2011.

[19] V. Jary, L. Havlak, J. Barta, E. Mihokova, and M. Nikl, "Luminescence and structural properties of $RbGdS_2$ compounds doped by rare earth elements," *Opt. Mater.*, vol. 35, no. 6, pp. 1226–1229, 2013.

[20] V. Jary, L. Havlak, J. Barta, and M. Nikl, "Preparation, luminiscence and structural properties of rare-earth-doped $RbLuS_2$ compounds," *Phys. Status Solidi RRL*, vol. 6, no. 2, pp. 95–97, 2012.

[21] R. Ballestracci, "Étude cristallographique de nouveaux sulfures de terres rares et de métaux alcalins M = Li, K," *Bull. Soc. Franc. Miner. Crist.*, vol. 88, pp. 207–210, 1965.

[22] V. Jary, L. Havlak, J. Barta, E. Mihokova, and M. Nikl, "Optical properties of Eu^{2+}-doped $KLuS_2$ phosphor," *Chem. Phys. Lett.*, vol. 574, pp. 61–65, 2013.

[23] V. Jary, "Fast Luminescence Phosphors Based on the Pb and Ce-Doped $SrHfO_3$ and Ternary Sulphides," M. S., CTU, Dept. Nucl. Chem., Prague, 2010.

[24] P. Dorenbos, "Systematic behaviour in trivalent lanthanide charge transfer energies," *J. Phys. Condens. Matter*, vol. 15, no. 49, pp. 8417–8434, 2003.

[25] A. M. Srivastava, U. Happek, and P. Schmidt, "Luminescence of $LuCl_3$:Pr^{3+} under interconfigurational ($4f_2 - 4f_15d_1$) and band gap excitations," *Opt. Mater.*, vol. 31, no. 2, pp. 213–217, 2008.

[26] A. M. Srivastava, "Identification of the $I^- \rightarrow Pr^{3+}$ charge transfer transition in the excitation spectrum of LuI_3:Pr^{3+}," *Opt. Mater.*, vol. 30, no. 10, pp. 1567–1570, 2008.

Journal of Luminescence 147 (2014) 196–201

Contents lists available at ScienceDirect

Journal of Luminescence

journal homepage: www.elsevier.com/locate/jlumin

Optical properties of Ce^{3+}-doped $KLuS_2$ phosphor

V. Jarý [a,b,*], L. Havlák [a], J. Bárta [b], E. Mihóková [a], P. Průša [a,b], M. Nikl [a]

[a] Institute of Physics, Academy of Sciences of the Czech Republic, Na Slovance 1999/2, Praha 8, Prague 18221, Czech Republic
[b] Faculty of Nuclear Sciences and Physical Engineering, Czech Technical University in Prague, Brehova 7, Praha 1, Prague 11519, Czech Republic

ARTICLE INFO

Article history:
Received 13 August 2013
Accepted 2 November 2013
Available online 11 November 2013

Keywords:
Inorganic scintillator
Ternary sulfide
Excited state dynamics
Thermally induced ionisation

ABSTRACT

$KLuS_2$ single crystals doped with trivalent cerium were synthesized in the form of crystalline hexagonal platelets. VUV/UV/VIS absorption and luminescence characteristics were measured in the broad temperature and concentration intervals. The band edge of $KLuS_2$ is found at 303 nm, Ce^{3+} 4f–5d excitation band at 490 nm and Ce^{3+} emission at 580 nm with the 35 ns decay time. Both thermal and concentration quenching of the Ce^{3+} emission are investigated. Phenomenological modeling and delayed recombination decays measurement are employed to understand the Ce^{3+} excited state dynamics. The application potential in X-ray phosphors is discussed.

1. Introduction

There are numerous works describing the optical properties of the Ce^{3+}-doped binary sulfides in the literature. $Lu_2S_3:Ce^{3+}$, very dense scintillator, shows the light yield of 25 000–30 000 ph/MeV, the decay time is rather short, i.e. 32 ns and the emission spectrum is peaking at 592 nm [1]. Luminescence properties of the CdS:Ce^{3+} nanoparticles have been investigated in detail [2], and the effect of dopant concentration on the photoluminescence (PL) intensity has also been studied. Analogously, there are numerous papers dealing with the luminescence features of the CaS:Ce^{3+} nanoparticles as well [3,4]. CaS:Eu^{2+}, Mn^{2+} and CaS:Ce^{3+}, Tb^{3+} synthesized by the flux method [5] were aimed to be used for cathode-ray tube display. It was also showed that CaS:Eu^{2+}, Tm^{3+}, Ce^{3+} can be used as an enhanced long persistent red phosphor [6] with a strong energy transfer from Ce^{3+} to Eu^{2+} found at a low doping concentration. A double insulated CaS:Ce thin-film electroluminescent (EL) device emitting a bright green EL due to the Ce^{3+} luminescent centre has been reported [7]. SrS doped by Ce^{3+} and co-doped by Pb^{2+} or Cl^-, Na^+ also gained attention mainly due to possibility of being used as thin films in electroluminescence devices [8–10]. Codoping of SrS:Ce by other RE^{3+} ions and their impact on the transient emission processes are discussed in [11]. The luminescence efficiency of SrS:Ce powders in the doping range from 0.01 at% to 1.0 at% was investigated by photoluminescence decay studies [12]. ZnS as a host for the Ce^{3+} emission centre was introduced [13] and the emission and excitation spectra of ZnS:Ce^{3+},Tb^{3+} indicate that the Ce^{3+} sensitizes Tb^{3+}. Thin films of ZnS:Ce, which may be used in the electroluminescence devices, were also described [14,15] and novel Ce-doped $Zn_xSr_{1-x}S$ solid solutions were prepared as blue–green emitting phosphor thin films [16]. Luminescence spectra of Ce^{3+}-ion in $Ca_{1-x}Sr_xS$ solid solutions have been investigated as well [17]. A study of the photoluminescence of the undoped γ-La_2S_3 and γ-Ce_2S_3 and doped γ-[Na]Ce_2S_3 rare earth sulfides, performed comparatively under steady state and time resolved excitation and detection conditions, has also been reported [18].

Ce^{3+}-doped ternary sulfide designated for scintillation purposes are known as well, mainly those of the general formula $MeGa_2S_4$ (*Me*=Ca, Sr). Ce^{3+}-doped $CaGa_2S_4$ single crystals have been grown under various conditions by the horizontal Bridgman method using a travelling temperature gradient [19]. Ce^{3+} absorption band was observed at 3.2 eV. A novel monoclinic phase of impurity-doped $CaGa_2S_4$ was introduced as a high emission intensity phosphor [20]. $SrGa_2S_4$ provides a deep blue and saturated green emission when doped with Ce^{3+} and Eu^{2+}, respectively [21]. The behaviour and performances of respective electroluminescence devices are discussed in detail. Polarized photoluminescence (PL) spectra of $SrGa_2S_4$:Ce prepared by chemical vapor transport technique were measured and discussed in the framework of the crystal-field theory [22]. The Ce-doped $SrGa_2S_4$ films exhibit the characteristic photoluminescent emission occuring in the 445 nm region [23]. Green to yellowish green light emitting Ce^{3+}-doped barium zinc sulfide (Ba_2ZnS_3) phosphor powders have been synthesized by a double-crucible method [24]. The photoluminescence (PL) spectra show that the emission peaks located in the 502–532 nm range (under excitation at 422 nm) and in the 530–560 nm range (under excitation at 358 nm) depend on the Ce^{3+} concentration. $Ba_2ZnS_3:Ce^{3+}$ co-doped by Ag^+ ions emitting bluish to yellowish-green light [25]. Photoluminescence emission spectra and diffuse

* Corresponding author. Tel.: +420 220 318 510; fax: +420 233 343 184.
E-mail address: jary@fzu.cz (V. Jarý).

0022-2313/$ - see front matter © 2013 Elsevier B.V. All rights reserved.
http://dx.doi.org/10.1016/j.jlumin.2013.11.013

reflectance absorption spectra of phosphors composed of ternary sulfide hosts with the Th_3P_4, calcium ferrite, spinel, and thiogallate structure types each activated by Eu^{2+}, Ce^{3+}, Ho^{3+}, and Mn^{2+} were investigated [26]. Various sulfidic hosts potentially interesting for white LEDs phosphors were recently reviewed [27]. In particular, alkali earth sulfide phosphors doped with Eu^{2+} and Ce^{3+} gained attention in this field [28]. A review on the wavelengths of all five 4f–5d transitions of Ce^{3+} and systematic trends regarding the emission wavelength, maximum obtainable scintillation light output, gamma-ray energy resolution, and scintillation decay time of Ce^{3+} in about 150 different inorganic compounds, including sulfides, is presented in [29,30].

In addition to the recent activities in complex oxides [31] and lanthanide ions-activated orthoborate research [32] we started to study unexplored family of ternary sulfides. Optical properties of the Ce^{3+}-doped ternary sulfide of general formula $RbLnS_2$ (Ln=La, Gd, Lu) have been published for the first time only recently [33–35]. However, in such matrices, Ce^{3+} emission at room temperature is thermally heavily quenched. In this paper we report the luminescence characteristics of the Ce^{3+} center in $KLuS_2$ matrix which, to our best knowledge, have never been reported in the literature.

2. Experimental setup

$KLuS_2$:Ce crystals were prepared in an electric resistance furnace by the reaction of H_2S with a mixture of Lu_2O_3, x% Ce_2O_3 and excess of K_2CO_3. The reaction temperature reached 1000 °C and the hydrogen sulfide flow was applied for 90 min. Further technological details are reported in Ref. [33]. Structural properties of $KLuS_2$ compounds have been recently discussed [36].

Absorption spectra were measured using the UV/VIS Spectrophotometer Shimadzu UV-1601. Photoluminescence (PL) spectra and decay curves were measured by the custom made Spectrofluorometer 5000M, Horiba Jobin Yvon, using the steady state deuterium lamp (photoluminescence excitation (PLE) and emission (PL) spectra in the 190–500 nm and 200–800 nm spectral regions, respectively), Seifert X-ray tube (radioluminescence (RL) spectra within 200–800 nm), microsecond xenon-filled lamp and nanosecond pulsed LED diodes (PL decay curves) as the excitation sources. Spectra were corrected for instrumental effects and a convolution procedure was applied to the decay curves to determine true decay times (SpectraSolve software package, Ames Photonics). Room-temperature (RT) luminescence properties of $KLuS_2$:Ce crystalline platelets were studied without powdering of the samples. The Oxford Instruments liquid nitrogen bath cryostat was used to control the sample temperature in the 80–500 K temperature range. PLE spectra in VUV–UV region were measured at Superlumi station, HASYLAB, DESY, Hamburg.

Light yield and energy resolution were determined by the pulse height spectroscopy of scintillation response [37], using the HPMT (Hybrid Photomultiplier) [38] model DEP PPO 475B, spectroscopy amplifier ORTEC model 672 (shaping time t=1 μs) and multichannel buffer ORTEC 927TM. Low energy γ-ray from ^{57}Co (122 keV) and ^{241}Am (59.5 keV) were used for excitation. The sample was optically coupled to HPMT using a silicon grease. Higher γ-ray energies could not be used, since samples were very thin (approximately 0.1 mm). All measurements were performed at room temperature. Energy resolution and photoelectron yield were obtained from the Gaussian fit of the photopeak in the pulse-height spectra.

3. Results and discussion

X-ray excited emission spectra of $KLuS_2$ doped by different concentrations of trivalent cerium are shown in Fig. 1a. They all feature a broad band with a maximum at about 580–620 nm which we assign to the Ce^{3+} 5d–4f fully allowed transition, based also upon similarity to $RbLuS_2$:Ce [35]. Extended low energy part of the spectrum might be shaped by unspecified perturbed Ce^{3+} centers. With increasing Ce^{3+} concentration above 0.5%, the spectra are getting broader and low energy shifted. There is another band peaking at around 450 nm whose origin remains unclear. It might be connected to the $KLuS_2$ host [39]. A spectrum of the 0.05% sample recorded at 77 K, see the inset of Fig. 1b, shows the characteristic well-resolved doublet of the Ce^{3+} ground state ($5d_1 \rightarrow {}^2F_{5/2}$ at 580 nm and $5d_1 \rightarrow {}^2F_{7/2}$ at 664 nm). The energy separation of two emissions of about 2180 cm^{-1}, matches the value of about 2000 cm^{-1} known from many other hosts. With increasing temperature the doublet becomes unresolved due to thermalization of ground state levels. The integral of each spectrum (in the eV–W/eV coordinates) was related to that of the BGO ($Bi_4Ge_3O_{12}$) powder standard sample obtained under identical experimental conditions. The results are displayed in Fig. 1b. Starting from very low Ce concentration, the Ce 0.002% sample still shows 350% of the BGO integral. Between 0.002% and 2.5%, 350–590% of BGO intensity is obtained. For a heavily doped 6% sample, the RL intensity sharply decreases, but still shows 290% of the BGO integral. Observed decrease for the highest concentration is probably due to the onset of concentration quenching also evidenced in the photoluminescence decay in Fig. 4. In comparison, the Eu^{2+} emission in the $KLuS_2$ is completely quenched for Eu 2% concentration at RT [36]. There is a correlation between the RL intensity and reduction of the decay curve integrals for the highest Ce concentration (cf. Fig. 1b). For above-mentioned applications, the interval of Ce concentrations between 0.1% and 2% appears to be the most suitable.

RT absorption (2.5% sample), PL and PLE spectra (0.05% and 0.5% samples) of the Ce^{3+}-doped $KLuS_2$ are presented in Fig. 2a and b, details are listed in the legends. Both absorption and PLE spectra feature the $KLuS_2$ band edge situated at about 300–310 nm at RT (Fig. 2a) and 290–300 nm at 10 K (Fig. 2b). These values are high-energy shifted with respect to $RbLnS_2$ [33–35] and in a good agreement with Ref. [36]. Another band at around 496 nm is ascribed to the Ce^{3+} 4f–$5d_1$ transition. PLE spectra in the 440–500 nm region (see Fig. 2a) are, however, partially distorted due to a very weak excitation source (deuterium steady state lamp) and strong correction curve influence. Ce^{3+} 4f–$5d_1$ transition is fully allowed and offers an efficient excitation in the blue spectral region. The hint of another excitation band at around 400 nm (see Fig. 2a) in the PLE spectra is noted and could be connected to a host lattice defect [39]. PLE spectra in the VUV spectral part (see Fig. 2b) are dominated by a broad band in the 160–240 nm region, which might reflect the density of states in the valence band, and the onset of the multiplication of electronic excitation ($>2E_g$) below 150 nm [40]. PL spectra, under excitation in both the band edge and Ce^{3+} 4f–5d band regions, and RL spectra coincide (for given temperatures) and exhibit broad intense Ce^{3+} $5d_1$–4f emission peaking at 580 nm. From the position of the lowest 4f–$5d_1$ absorption band (at 496 nm, see Fig. 2a) and emission maximum (580 nm) one can estimate the Stokes Shift of 360 meV.

Experimental determination of the $KLuS_2$:Ce scintillation light yield (LY) was quite difficult due to small size, especially the thickness, of the sample which makes its wrapping difficult. Consequently, the light collection efficiency is questionable and obtained values surely underestimate true LY. Given the relatively low energy of gamma sources, its value can be further influenced by non-proportionality effect [41]. Under gamma excitation of ^{57}Co and ^{241}Am, the measured LY value of the 0.5% Ce sample is 23 800 ph/MeV and 22 300 ph/MeV, respectively, see Fig. 3. For the sample 0.05% Ce, LY value of 20 300 ph/MeV was measured. Despite values for the 0.5% Ce sample, it is premature to make statements on non-proportionality having light yield values only

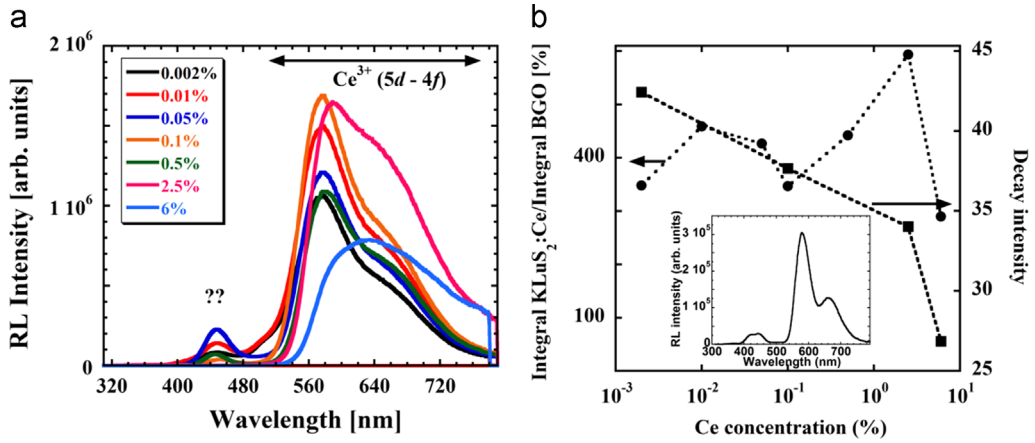

Fig. 1. In (a), X-ray excited emission spectra (40 kV, 15 mA) of the $KLuS_2:Ce^{3+}$ with different concentrations of Ce^{3+} at RT. The spectrum at 77 K for the Ce^{3+}concentration 0.05% is shown in the inset of (b). In (b), concentration dependence of the Ce^{3+} radioluminescence intensity in $KLuS_2$ (full circles) and concentration dependence of the normalized decay curves integrals (full squares).

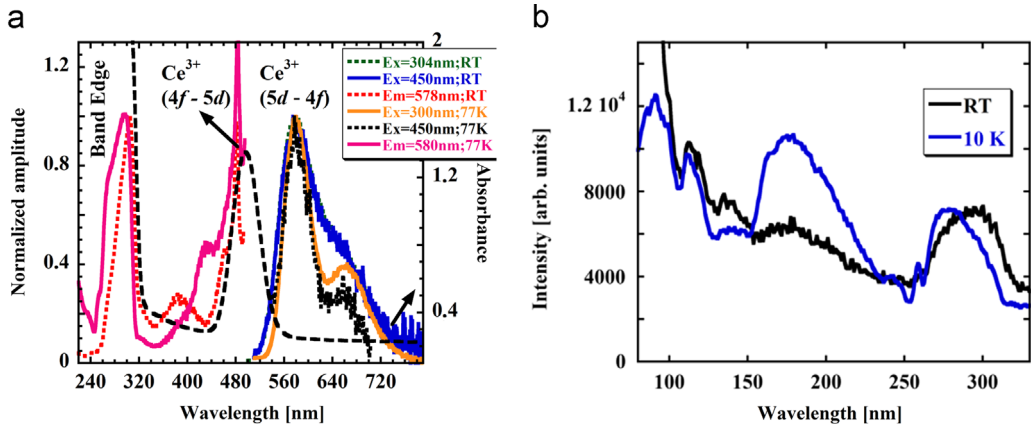

Fig. 2. (a) RT Absorption (black dashed line, 2.5% Ce), PLE (red dotted line for 578 nm emission at RT, 0.05% Ce; pink solid line for 580 nm emission at 77 K, 0.05% Ce) and PL (blue solid line under 450 nm excitation at RT, 0.05% Ce; orange solid line under 300 nm excitation at 77 K, 0.05%; green dotted line under 304 nm excitation at RT; black dotted line under 450 nm excitation at 77 K) spectra of $KLuS_2:Ce$; (b) PLE spectra of $KLuS_2:Ce$ (0.5%) for the 570 nm emission recorded at 10 K and RT using synchrotron radiation. (For interpretation of the references to color in this figure legend, the reader is referred to the web version of this article.)

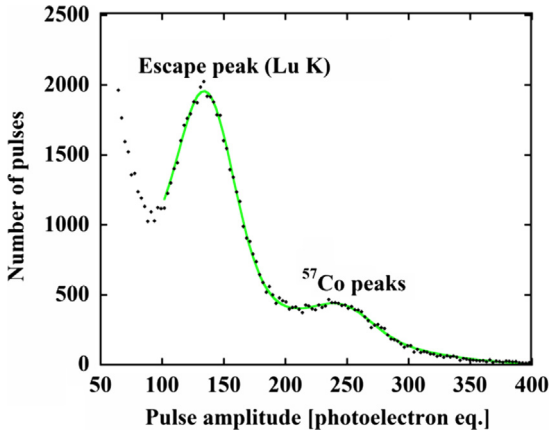

Fig. 3. Pulse height spectrum of ^{57}Co (0.5% sample) measured by $KLuS_2:Ce$. Gaussians with the second order polynomial background was fit to a part of the spectrum. 247 photoelectrons were collected at energy 122 keV, i.e. (PhY) photoelectron yield=2025 phels/MeV. Quantum efficiency (QE) is 8.52%, LY=PhY/QE=23 800 ph/MeV.

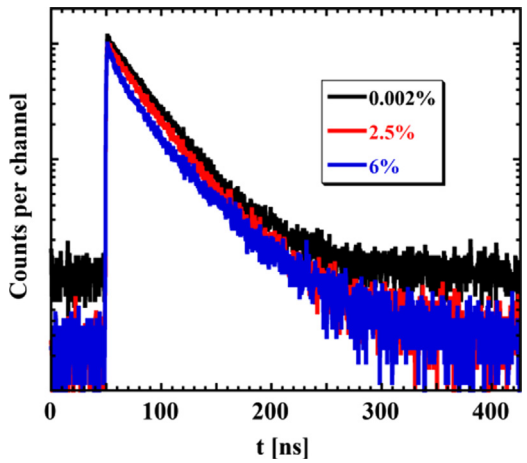

Fig. 4. Normalized RT PL decay curves related to the Ce^{3+} 5d–4f transition (λ_{ex}=490 nm, λ_{em}=580 nm) in $KLuS_2$ for various Ce^{3+} content.

for two different energies measured with precision of approximately 5–10%.

Measured LY is only slightly dependent on the amplifier shaping time, i.e. LY (t=10 μs)/LY (t=0.5 μs)=1.05 which is much less than e.g. in LuAG:Ce where this value is typically 1.7 [42]. Therefore, slow components in the scintillation response of $KLuS_2$:Ce with decay times on the order of units to tens of μs are very weak. However, this measurement is insensitive to much slower (hundreds of μs or more) components in the scintillation response.

Energy resolution for the peak with energy 122 keV (^{57}Co) and 59.5 keV (^{241}Am) is 20 ± 4% and 29 ± 4%, respectively. The value is negatively affected by combination of the low HPMT quantum efficiency, low excitation energy and moderate LY. However, there is a space for improvement by using semiconductor photon detector that is more sensitive for longer wavelength photons.

RT PL decay curves related to the Ce^{3+} 5d–4f transition (λ_{ex}=490 nm, λ_{em}=580 nm) in $KLuS_2$ for different Ce^{3+} content were recorded (Fig. 4) in order to investigate the occurrence of concentration quenching. Decay curve for the Ce 0.002% is strictly single-exponential with the RT decay times of 34.9 ns which is in a good agreement with the expected value of fully-allowed Ce^{3+} 5d–4f transitions. In contrast, the decay of Ce2.5% sample becomes distorted. It can be approximated by a double-exponential function with decay times of about 30.1 ns and 88.5 ns, where the shorter component indicates the onset of concentration quenching. Slower tail may indicate the presence of excited state ionization, see below. Finally, the decay curve of the Ce6% sample is even more distorted. Interestingly, its signal-to-background ratio improves which may be related to processes of the excited state ionization of Ce^{3+} centers as well. Furthermore, the decay curves shown in Fig. 4 were normalized and integrated. The obtained integrated values were plotted as a function of the Ce^{3+} concentration in Fig. 1b and were discussed above.

To further study a thermal stability of the Ce^{3+} emission centre in this ternary sulfide host, the temperature dependence of the Ce^{3+} 5d–4f decay times for two different Ce^{3+} concentrations (0.05% and 0.5%) was investigated between 77 K and 497 K. Decay curves are single exponentials within 77–347 K and 77–257 K for the 0.05%Ce and 0.5%Ce concentrations, respectively. Above these temperatures, a slower tail appears in the decay curve. The decay must be then approximated by the sum of two exponential terms $I(t)=A_1\exp[-t/T_1]+A_2\exp[-t/T_2]+$background. The relative weight (lightsum) of both fast and slow components is calculated as $I_i=A_iT_i/(A_1T_1+A_2T_2)$, i=1,2 and displayed in Fig. 5. The slow decay component (T_2) is probably due to thermally induced ionisation of the Ce^{3+} excited state (see below). It can be concluded that the onset of the ns decay time shortening (concerning the fast component) is at about 320 K for the 0.05% sample and 280 K for the 0.5% sample and decay times change from 41.4 ns at 77 K to 0.29 ns at 497 K (for the 0.05% sample) and from 40.8 ns at 77 K to 6.0 ns at 490 K (for the 0.5% sample). We note that the radiative decay time at 77 K is equal for both Ce^{3+} concentrations. However, the decay time decrease is much more dramatic for the 0.05% sample (more than two orders of magnitude) compared to the 0.5% sample. Taking into account this discrepancy and the presence of the slower component at higher temperatures, one can conclude that another dynamic process is possibly at work, most probably thermally induced ionization of the Ce^{3+} 5d excited state (see below). We also mention that the relative light sum of the slow component is increasing significantly with increasing temperature while that of the fast component is, at the same time, decreasing for both Ce concentrations. It means that the amount of the emission light released in slower component is increasing with increasing temperature.

We approximated the temperature dependence of the fast component decay time for both the 0.05% and 0.5% samples by a simple barrier model described by Eq. (1),

$$(\tau_{\text{observed}})^{-1}=(\tau_{\text{radiative}})^{-1}+K_x\times\exp(-E_x/kT) \quad (1)$$

where τ_{observed}, $\tau_{\text{radiative}}$, K_x, E_x, k, and T represent the PL decay time measured at temperature T, the low temperature limit of the PL decay time, frequency factor, energy barrier height, Boltzmann constant and absolute temperature, respectively. The parameters of the best fit of Eq. (1) to experimental data are $K_x=9\times10^{13}$ s^{-1}, E_x=480 meV for the 0.05% sample and $K_x=1.7\times10^{11}$ s^{-1}, E_x=280 meV for the 0.5% sample. Such different values of the energy barrier and frequency factor again indicate that the decay time shortening is maybe not only due to classical temperature quenching to the ground state but there can be a contribution of another process. In case of mentioned Ce^{3+} excited state thermal ionization, higher Ce^{3+} concentration can enable more effective and fast return of electrons thermally promoted to the conduction band back to an ionized Ce^{4+} centre. Such a trend can effectively slow down the decay in submicrosecond time scale at the highest temperatures.

To further investigate the nature of decay times shortening at higher temperatures we performed the measurement of the temperature dependence of the delayed recombination (DR) decays integrated in the extended time window. This measurement consists in the decay monitoring under the same excitation and emission wavelengths as in Figs. 4 and 5, but using the xenon-filled microsecond flashlamp excitation and multichannel scaling mode detection in the extended time window (44 ms). Under such conditions a prompt nanosecond Ce^{3+} decay is accumulated in the first few channels and the delayed recombination decay (produced by charge carriers that were thermally ionized and later returned back to the emission centre) can be easily investigated (for details concerning the method, see Ref. [43]).

Fig. 6 illustrates the temperature dependence of the normalized (at the lowest temperature) DR integrals related to Ce^{3+} centre in $KLuS_2$ host, for two different Ce^{3+} concentrations (0.05% and 0.5%). Before integrating the decay curves a few data points with the highest intensity at the very beginning of the decay (containing

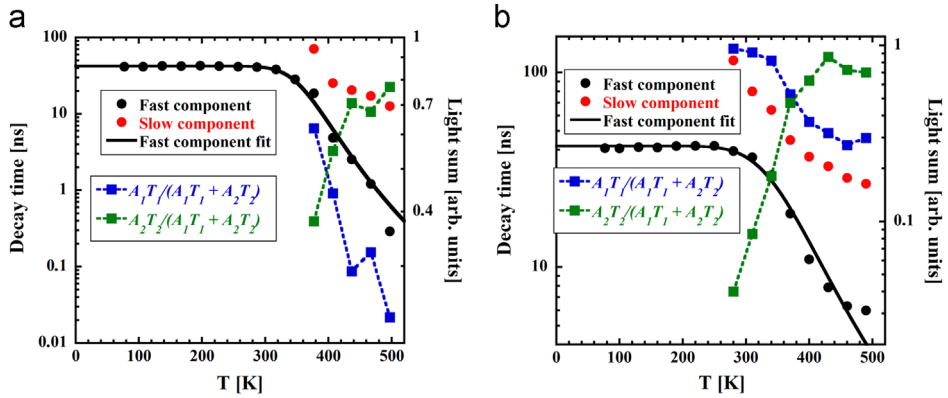

Fig. 5. Temperature dependence of the ns decay time for the (a) $KLuS_2$:Ce 0.05% sample (λ_{ex}=490 nm, λ_{em}=580 nm) and (b) $KLuS_2$:Ce 0.5% (λ_{ex}=490 nm, λ_{em}=600 nm); black full circles are the fast component data, red full circles are the slow component data, blue full squares stand for the light sum of the fast component and green full squares the light sum of the slow component, black solid line is the fit of the phenomenological model (see the text) to the ns decay time data. (For interpretation of the references to color in this figure legend, the reader is referred to the web version of this article.)

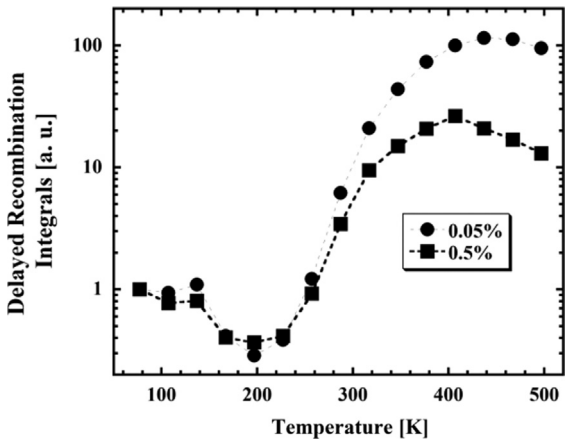

Fig. 6. Temperature dependence of normalized (at the lowest temperature) delayed recombination integrals (ex=490 nm, em=580 nm) for $KLuS_2$:Ce (0.05% – full circles, 0.5% – full squares).

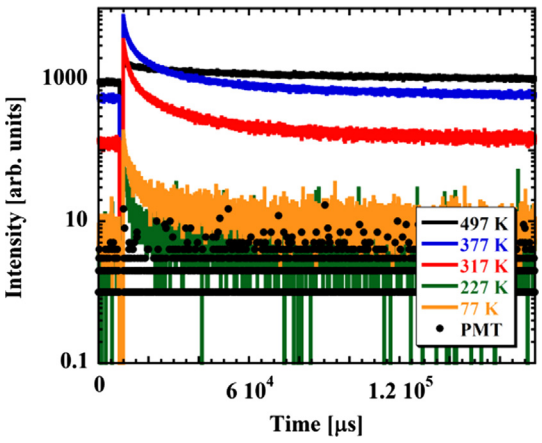

Fig. 7. Examples of delayed recombination decays connected to $KLuS_2$:Ce (0.05%), (λ_{ex}=490 nm, λ_{em}=580 nm) at different temperatures.

prompt nanosecond Ce^{3+} luminescence) were omitted. As demonstrated in Fig. 6 there is, indeed, a rapid increase of the DR integrals between 200 K and 400 K (0.5%), 450 K (0.05%). We ascribe it to a process in which electron escapes from the Ce^{3+} $5d_1$ excited state to the conduction band from where it can return at later times and radiatively recombine with the hole, giving rise to the delayed recombination luminescence. The behavior of the delayed recombination integrals between 400 K and 500 K can be due to shaping of the DR temperature dependence by the presence of traps [44,45]. Interestingly, the relative maximum value of the DR integrals for the 0.05% sample (at around 450 K) is by one order of magnitude higher than that of the 0.5% sample (at around 400 K). As the experimental conditions were identical and both dependences are normalized, it means that more delayed light is produced in the measurement window (44 ms) in the sample containing lower Ce^{3+} concentration. This observation is consistent with the hypothesis given above that at higher Ce concentration there is enhanced return of electrons from conduction band/traps towards ionized Ce^{4+} centers in the submicrosecond time scale. Consequently, the evaluated decay times become longer and evaluated quenching barrier obtained from the decays in Fig. 5 can be altered in the sample with the higher concentration of Ce. On the other hand combined results reported in Figs. 4 and 5 clearly indicate that shortening of the nanosecond decay times between 300 K and 500 K is due to thermal ionization rather than the classical thermal quenching. We also note that delayed recombination integrals show a non-zero value even at the lowest temperatures, which has been explained by quantum tunneling between luminescence center and a nearby defect state [46].

As an example, several delayed decay curves, recorded at different temperatures, are shown in Fig. 7 (λ_{ex}=490 nm, λ_{em}=580 nm). Because of minimized dead-times between the 44 ms long measurement windows, even delayed recombination processes of much longer decay times (up to the time of measurement which is typically 10 min) provide the signal which is visible in the "background" of the decay curve before the rising edge of the ms decay, i.e. the actual measurement window in this experiment is extremely extended, from a few tens of μs up to about 10 min. Ns decay time values, however, begin to shorten at higher temperatures compared to delayed recombination integrals increase. This seeming discrepancy might be due to the difference in monitoring the onset of decay times shortening and the onset of delayed recombination increase. While the former is monitored as the change with respect to its maximum value, the latter is monitored as the change with respect to its minimum value. As a result, the latter can become more sensitive in the overall dynamic range. Better understanding of the DR behavior would require an independent study of characteristics of the traps involved in the delayed recombination process as mentioned above.

4. Conclusions

In this study we present the Ce^{3+}-doped $KLuS_2$ single crystalline material as novel, potentially interesting X-ray phosphor. By the inorganic reaction in an electric resistance furnace we prepared the optically transparent single crystal samples about 0.1 mm thick with a cross-section area up to a few square mm, consisting of the single $KLuS_2$ phase. The absorption and PLE spectra show the $KLuS_2$ band edge at 303 nm and Ce^{3+} $4f–5d_1$ absorption band peaking at 490 nm. Both X-ray and PL excitation provide the broad Ce^{3+} emission peaking at 580 nm with the shoulder at 660 nm due to Ce^{3+} 5d–4f transition. At room temperature, the photoluminescence decay time of the Ce^{3+} center is about 35 ns. The Stokes shift value of 360 meV is evaluated. Concentration dependence study reveals the onset of concentration quenching around 0.5 mol% of Ce^{3+} and the highest emission intensity under X-ray excitation is reached for the sample containing 0.1% of cerium.

Moderate light yield value of the $KLuS_2$:Ce0.5% was measured (under gamma excitation) of about 23 800 ph/MeV and almost no slower components were found in scintillation response within 0.5–10 μs shaping time interval.

A phenomenological model is employed to describe the Ce^{3+} excited state dynamics and explain ns decay times reduction with increasing temperature. The parameters of the best fit of Eq. (1) to experimental data are $K_x=9\times10^{13}$ s^{-1}, E_x=480 meV for the 0.05% sample and $K_x=1.7\times10^{11}$ s^{-1}, E_x=280 meV for the 0.5% sample. The former value set is probably more relevant in the quantitative description of the processes occurring in the $5d_1$ excited state of Ce^{3+} in $KLuS_2$ host where the dominant influence is due to thermally induced ionization of the Ce^{3+} excited state. It is supported by additional measurements and evaluation of the delayed recombination decay curves.

Elevated effective atomic number (Z_{eff}=59), efficient energy transfer from the host to Ce^{3+} centers and lower band gap, relative to oxide-based materials, are intrinsic advantages of the Ce^{3+}-doped $KLuS_2$ and make this material prospective for applications for fast X-ray phosphors, especially when semiconductor detectors would be used. All studied samples also show reasonable long-term stability and negligible moisture sensitivity.

Acknowledgment

Financial support of Czech TACR TA01011017 project and RVO: 68407700 are gratefully acknowledged.

References

[1] J.C. Van´t Spijker, P. Dorenbos, C.P. Allier, C.W.E. Van Eijk, A.R.H.F. Ettema, G. Huber, Nucl. Instrum. Methods Phys. Res., Sect. B 134 (1998) 304.
[2] L. Saravanan, A. Pandurangan, R. Jayavel, Mater. Lett. 66 (2012) 343.
[3] G. Sharma, P. Chawla, S.P. Lochab, N. Singh, Radiat. Eff. Defects Solids 164 (2009) 763.
[4] V. Kumar, S.S. Pitale, V. Mishra, I.M. Nagpure, M.M. Biggs, O.M. Ntwaeaborwa, H.C. Swart, J. Alloys Compd. 492 (2010) L8.
[5] M. Pham-Thi, J. Alloys Compd. 225 (1995) 547.
[6] D. Jia, ECS Trans. 2 (2007) 1.
[7] V. Shanker, S. Tanaka, M. Shiiki, H. Deguchi, H. Kobayashi, H. Sasakura, Appl. Phys. Lett. 45 (1984) 960.
[8] T.A. Oberacker, G. Schlotterbeck, G. Bilger, H.W.D. Braunger; Schock, J. Appl. Phys. 80 (1996) 3526.
[9] S. Tanaka, J. Lumin. 40–41 (1988) 20.
[10] B. Huettl, U. Troppenz, K.O. Velthaus, C.R. Ronda, R.H. Mauch, J. Appl. Phys. 78 (1995) 7282.
[11] S. Okamoto, E. Nakazawa, Jpn. J. Appl. Phys. 34 (1995) 521.
[12] B. Huttl, G.O. Muller, R. Mach, C. Fouassier, P. Benalloul, Adv. Mater. Opt. Electron. 3 (1994) 131.
[13] C.L. Deng, K.H. Qiu, J. Chengdu Inst. Technol. 30 (2003) 409.
[14] S. Tanaka, H. Kobayashi, M. Shiiki, T. Kunou, V. Shanker, H. Sasakura, J. Lumin. 31–32 (1984) 945.
[15] M. Tammenmaa, M. Leskelä, T. Koskinen, L. Niinistö, J. Less-Common Met. 126 (1986) 209.
[16] S.T. Lee, M. Kitagawa, K. Ichino, H. Kobayashi, Appl. Surf. Sci. 100–101 (1996) 656.
[17] O. Krachni, L. Guerbous, L. Louail, Mod. Phys. Lett. B 20 (2006) 1405.
[18] R. Mauricot, J. Dexpert-Ghys, M. Evain, J. Lumin. 69 (1996) 41.
[19] C. Hidaka, T.. Takizawa, J. Cryst. Growth 237–239 (2002) 2009.
[20] A. Suzuki, T. Takizawa, C. Hidaka, N. Shigetaka, I. Kitajima, Acta Crystallogr., Sect. E: Struct. Rep. Online 68 (2012) i42.
[21] P. Bénalloul, C. Barthou, J. Benoit, J. Alloys Compd. 275–277 (1998) 709.
[22] K. Tanaka, T. Ohgoh, K. Kimura, H. Yamamoto, K. Shinagawa, K. Sato, Jpn. J. Appl. Phys. 34 (1995) L1651.
[23] O.N. Djazovski, T. Mikami, K. Ohmi, S. Tanaka, H. Kobayashi, J. Electrochem. Soc. 144 (1997) 2159.
[24] Y.F. Lin, Y.H. Chang, B.S. Tsai, J. Alloys Compd. 377 (2004) 277.
[25] Y.F. Lin, Y.H. Chang, B.S. Tsai, J. Electrochem. Soc. 152 (2005) G698.
[26] M.M. Yuta, W.B. White, J. Electrochem. Soc. 139 (1992) 2347.
[27] P.F. Smet, A.B. Parmentier, D. Poelman, J. Electrochem. Soc. 158 (2011) R37.
[28] D. Jia, X.J. Wang, Opt. Mater. 30 (2007) 375.
[29] P. Dorenbos, J. Lumin. 135 (2013) 93.
[30] P. Dorenbos, Nucl. Instrum. Methods Phys. Res., Sect. A 486 (2002) 208.
[31] J.M. Ogieglo, A. Katelnikovas, A. Zych, T. Jűstel, A. Meijerink, C.R. Ronda, J. Phys. Chem. A 117 (2013) 2479.
[32] Y. Wu, G. Ren, M. Nikl, D. Ding, J. Wang, S. Shang, F. Yang, S. Pan, J. Phys. Chem. A 115 (2011) 13821.
[33] L. Havlák, V. Jarý, M. Nikl, P. Boháček, J. Bárta, Acta Mater. 59 (2011) 6219.
[34] V. Jarý, L. Havlák, J. Bárta, E. Mihóková, M. Nikl, Opt. Mater. 35 (2013) 1226.
[35] V. Jarý, L. Havlák, J. Bárta, M. Nikl, Phys. Status Solidi RRL 6 (2012) 95.
[36] V. Jarý, L. Havlák, J. Bárta, E. Mihóková, M. Nikl, Chem. Phys. Lett. 574 (2013) 61.
[37] M. Moszynski, M. Kapusta, M. Mayhugh, D. Wolski, S.O. Flyck, IEEE Trans. Nucl. Sci. 44 (1997) 1052.
[38] C. D'Ambrosio, H. Leutz, Nucl. Inst. Meth. A 501 (2003) 463.
[39] V. Jarý, L. Havlák, J. Bárta, E. Mihóková, M. Nikl, IEEE Trans. Nucl. Sci. (2013).
[40] J. Becker, J.Y. Gesland, N.Yu. Kirikova, J.C. Krupa, V.N. Makhov, M. Runne, M. Queffelec, T.V. Uvarova, G. Zimmerer, J. Alloys Compd. 275–277 (1998) 205.
[41] G. Bizarri, W.W. Moses, J. Singh, A.N. Vasil´ev, R.T. Williams, J. Appl. Phys. 105 (2009) 044507.
[42] P. Průša, T. Čechák, J.A. Mareš, M. Nikl, A. Beitlerová, N. Solovieva, Yu.V. Zorenko, V.I. Gorbenko, J. Touš, K. Blažek, Appl. Phys. Lett. 92 (2008) 041903.
[43] J. Pejchal, M. Nikl, E. Mihóková, J.A. Mareš, A Yoshikawa, H. Ogino, K.M. Schillemat, A. Krasnikov, A. Vedda, K. Nejezchleb, V. Múčka, J. Phys. D: Appl. Phys. 42 (2009) 055117.
[44] M. Fasoli, A. Vedda, E. Mihókova, M. Nikl, Phys. Rev. B: Condens. Matter 85 (2012) 085127.
[45] E. Mihóková, M. Nikl, L.S. Schulman, V. Jarý, Phys. Status Solidi RRL 7 (2013) 228.
[46] E. Mihóková, L.S. Schulman, V. Jarý, Z. Dočekalová, M. Nikl, Chem. Phys. Lett. 578 (2013) 66.

Phys. Status Solidi RRL **7**, No. 3, 228–231 (2013) / **DOI** 10.1002/pssr.201206499

pss +++rapid research letters+++
www.pss-rapid.com

Delayed recombination and excited state ionization of the Ce^{3+} activator in the $SrHfO_3$ host

Eva Mihóková[*,1], Vítězslav Jarý[1], Lawrence S. Schulman[2], and Martin Nikl[1]

[1] Institute of Physics, AS CR v.v.i., Cukrovarnická 10, 162 53 Prague, Czech Republic
[2] Physics Department, Clarkson University, Potsdam, New York, 13699-5820, USA

Received 26 November 2012, revised 6 December 2012, accepted 11 December 2012
Published online 17 December 2012

Keywords scintillators, thermal ionization, oxides, tunneling, $SrHfO_3$

[*] Corresponding author: e-mail mihokova@fzu.cz, Phone: +420 220 318 539, Fax: +420 233 343 184

We determine the thermal ionization energy of the excited state of Ce^{3+} in a $SrHfO_3$ host by a contactless optical method based on the measurement and analysis of delayed recombination decay following UV excitation. We show the applicability of the method for microcrystalline powder samples. The method provides a consistent value of thermal ionization energy of about 0.25 eV, as previously determined by a thermally stimulated luminescence (TSL) study after UV illumination. We reveal a low temperature contribution to the delayed recombination signal and address its origin. This contribution indicates a complex interaction of the luminescence center with the host lattice neighborhood and the presence of temperature independent losses of fast scintillation light.

1 Introduction The energy of thermal ionization of the excited state of a luminescent center in a host is an important characteristic affecting the figure of merit of a scintillating material and the temperature range of its practical use. For single crystal bulk materials this energy can be determined by photoconductivity measurements, although making ohmic contacts on wide band-gap dielectric materials is a challenging task [1]. "Contactless" techniques that one can also apply to materials in powder form involve the microwave resonator technique [2, 3] which is a relatively complex and demanding experiment. Recently, using routine luminescence techniques, two independent experiments enabling detection of thermal ionization and determination of the ionization energy by contactless optical means, were introduced and tested on the $Lu_2Si_2O_7:Pr^{3+}$ single crystal [4].

Thermal ionization of the excited state of Ce^{3+} in Ce^{3+}-doped $SrHfO_3$ (SHO) was first reported in [5]. Recently, the value 0.25 eV for the ionization energy was determined [6] by a TSL study of SHO:Ce microcrystalline powder after UV illumination.

In this work, we study the thermal ionization of the Ce^{3+} excited state in the SHO host by a method applying the experimental technique and analysis of delayed recombination decay introduced in [4]. We both test the validity of the method for the material in powder form and determine the energy of thermal ionization. Furthermore, we address a low temperature contribution to the delayed recombination signal. This contribution may indicate the existence of so far unexplored processes and phenomena occurring in the relaxation and decay of the excited state of a luminescence center.

2 Experimental details Ce^{3+}-doped SHO powders were prepared by acetate and citrate combustion with a dopant concentration of 0.1 mol% (for details, see [7]).

Photoluminescence (PL) measurements were performed by a custom made 5000M Horiba Jobin Yvon spectrofluorometer. PL delayed recombination decays were excited by a microsecond xenon flashlamp and measured using the multichannel scaling method. An Oxford Instruments liquid nitrogen bath optical cryostat allowed temperature regulation from about 150 to 500 K.

3 Study of ionization of the Ce^{3+} excited state by delayed recombination decay When, after the PL

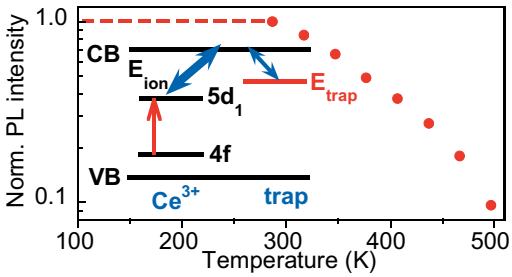

Figure 1 (online colour at: www.pss-rapid.com) Temperature dependence of the normalized (at RT) PL intensity of $SrHfO_3:Ce^{3+}$ excited at 200 nm integrated in the range 350–540 nm of the 5d–4f Ce^{3+} emission (after [6]). The inset shows a sketch of the processes of excited state ionization, electron trapping and detrapping in the Ce^{3+} luminescence center in SHO host. For simplicity only one trapping state is shown.

excitation, the excited state of the luminescent center is thermally ionized, charge carriers that do not decay promptly can migrate through the conduction (or valence) band. During that process they can be trapped and therefore delayed in their recapture at the luminescent center (see the inset of Fig. 1). The time spent by the charge carrier in the trap causes the observed slow tail in the PL decay.

Thus the intensity of delayed recombination light can be, in general, expressed as

$$I_{\mathrm{DR}}(T) = w\,\mathrm{e}^{-\frac{E_{\mathrm{ion}}}{kT}} \int_0^{\infty} \mathrm{d}E\; p(E) \int_{t_{\mathrm{b}}}^{t_{\mathrm{e}}} \mathrm{d}t\; \frac{1}{\tau(E)}\,\mathrm{e}^{-\frac{t}{\tau(E)}}, \qquad (1)$$

where the Boltzmann factor represents the fraction of charge carriers thermally ionized. The quantities T, w, E_{ion} and k are the temperature, pre-exponential factor, ionization energy, and Boltzmann constant, respectively. The rest of the formula expresses the fact, that not all the thermally ionized carriers will contribute to the overall detected delayed recombination signal. In particular, only those that are trapped and subsequently released from the traps (with a distribution function $p(E)$ and trap depth E) whose detrapping time $\tau(E)$ falls into the time interval of delayed recombination signal recording (t_{b}, t_{e}) will contribute. In Eq. (1), the expression integrated with respect to time represents the probability that the charge carrier escapes from a trap of depth E, in the time interval (t, $t + \mathrm{d}t$). Thus, if the time integration limits were from 0 to ∞, then the integral would yield unity, since each trapped charge carrier eventually escapes. Performing the time integral one obtains

$$I_{\mathrm{DR}}(T) = w\,\mathrm{e}^{-\frac{E_{\mathrm{ion}}}{kT}} \int_0^{\infty} \mathrm{d}E\; p(E) \left[\mathrm{e}^{-\frac{t_{\mathrm{b}}}{\tau(E)}} - \mathrm{e}^{-\frac{t_{\mathrm{e}}}{\tau(E)}}\right]. \qquad (2)$$

Equation (2) is general, valid in any class of materials characterized by a trap distribution function $p(E)$. In the case of discrete traps, as in the crystalline hosts, Eq. (2) reduces to [4]

$$I_{\mathrm{DR}}(T) = w\,\mathrm{e}^{-\frac{E_{\mathrm{ion}}}{\mathrm{kT}}} \sum_{k=1}^{n} A_k \left[\mathrm{e}^{-\frac{t_{\mathrm{b}}}{\tau(E_k)}} - \mathrm{e}^{-\frac{t_{\mathrm{e}}}{\tau(E_k)}}\right], \qquad (3)$$

with A_k being the amplitude of the trap with depth E_k and detrapping time $\tau(E_k)$, n the number of traps of various kinds participating in the process. The amplitude A_k is proportional to the number of traps of the same kind contributing to the delayed recombination signal. For more details on delayed recombination theory in crystalline hosts, see Ref. [4].

One should keep in mind that Eq. (3) does not take into account the possible reduction of PL efficiency of the luminescence center with temperature. Therefore, before applying Eq. (3), experimental data $I_{\mathrm{DR}}(T)$ must be corrected for this phenomenon. The correction factor can be determined from the measurement of the temperature dependence of PL steady state intensity. Should the luminescence center not be quenched, the PL intensity as a function of temperature would remain constant. Normalized steady-state intensity of $SHO:Ce^{3+}$ is reported in Fig. 1. The experimental data (solid circles) were measured in [6] under host lattice excitation at 200 nm. The host excitation, instead of the excitation into the 4f–$5d_1$ absorption band of Ce^{3+}, was chosen due to the fact, that PL intensity under host excitation (200 nm) is less affected by experimental distortions connected with the powder form of the sample (detailed explanation is given in [6]). The dashed line represents our assumption (see [6]) that the Ce^{3+} emission below RT is constant. The curve was used to correct the delayed recombination data (below) for the temperature quenching of the Ce^{3+} emission.

The delayed recombination decay of $SHO:Ce^{3+}$ was measured under microsecond xenon flashlamp excitation from 160 to 500 K. At each temperature the sample was excited by 200 nm light, for the same reasons as above. The decay of the emitted light was recorded in a 0–5 ms time window. The entire measurement, with repetitive ex-

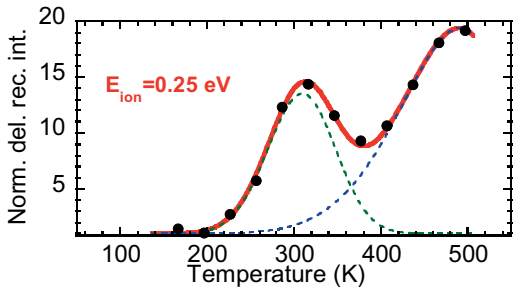

Figure 2 (online colour at: www.pss-rapid.com) Normalized (to minimum) delayed recombination intensity of $SrHfO_3:Ce^{3+}$ as a function of temperature. Solid circles are experimental data. Solid line is the fit of Eq. (3) to the data, dashed lines are contributions of each single trap to the overall signal. The parameters used in the fit are: $A_1 = 1$; $E_1 = 0.18$ eV; $s_1 = 1.2 \times 10^8$ s^{-1}; $A_2 = 0.02$; $E_2 = 0.45$ eV; $s_2 = 2.4 \times 10^9$ s^{-1}; $E_{\mathrm{ion}} = 0.25$ eV.

Table 1 Trap parameters obtained by the initial rise technique. T_M, E, s and τ are temperature of the TSL peak maximum, trap depth, frequency factor and detrapping time, respectively.

irr. at 10 K	T_m [K]	E [eV]	s [s^{-1}]	τ [s] at 160 K	τ [s] at 500 K
	78	0.12 ± 0.01	$\sim 10^{6}$	$\sim 10^{-2}$	$\sim 10^{-5}$
	100	0.19 ± 0.01	$\sim 10^{8}$	$\sim 10^{-2}$	$\sim 10^{-6}$
	205	0.48 ± 0.01	$\sim 10^{10}$	$\sim 10^{5}$	$\sim 10^{-5}$
	230	0.46 ± 0.01	$\sim 10^{8}$	$\sim 10^{6}$	$\sim 10^{-4}$
	255	0.60 ± 0.01	$\sim 10^{10}$	$\sim 10^{9}$	$\sim 10^{-4}$
	290	0.76 ± 0.01	$\sim 10^{11}$	$\sim 10^{12}$	$\sim 10^{-4}$
irr. at RT	320	0.90 ± 0.1	$\sim 10^{13}$	$\sim 10^{15}$	$\sim 10^{-3}$
	413	0.97 ± 0.01	$\sim 10^{10}$	$\sim 10^{20}$	$\sim 10^{-3}$
	473	1.15 ± 0.04	$\sim 10^{11}$	$\sim 10^{25}$	$\sim 10^{1}$
	583	1.60 ± 0.04	$\sim 10^{12}$	$\sim 10^{38}$	$\sim 10^{4}$

citation and signal accumulation, lasted 10 minutes. Each data point (solid circles in Fig. 2) was obtained by integrating the recorded signal in a time interval 10 µs to 5 ms (for more details on experimental procedure, see [4]) and then corrected for temperature quenching of Ce^{3+} emission. Equation (3) was fit to the experimental data.

Most of the parameters entering Eq. (3), namely the trap depths E and frequency factors s (related to detrapping times), were determined from an independent experiment using the TSL technique [6]. Their values corresponding to traps associated with the TSL peaks observed in [6] are reported in Table 1. The detrapping time is expected to have the form

$$\tau(E) = s^{-1} \exp(E/kT). \quad (4)$$

Detrapping times at 160 K and 500 K, temperatures that correspond to the temperature limits of the experiment described above, are also listed in Table 1. In principle, all traps except the deepest one (TSL peak at 583 K) can contribute to the delayed recombination signal, since their detrapping time at 500 K falls in the time window of the measurement from 10^{-5} to 6×10^{2} s. A satisfactory fit of the delayed recombination data in the considered temperature interval (solid line in Fig. 2) was obtained by taking into account the role of two traps. The first is associated with the TSL peak around 100 K and the second is associated with the peak at 205 or 230 K or some combination of both. Consideration of other traps with weak amplitude does not change the quality of the fit. Those traps might be rather distant from the Ce^{3+} center and therefore have a negligible effect on the delayed recombination signal. The best fit of delayed recombination data provides an ionization energy value 0.25 ± 0.02 eV, consistent with that found from the TSL study [6]. The uncertainty 0.02 eV corresponds to the range of E_{ion} within which a satisfactory fit is obtained.

4 Low temperature contribution to the delayed recombination decay The low temperature limit of Eq. (3) is zero. Therefore at low enough temperatures one would not expect to obtain a detectable delayed recombination signal due to thermal ionization of the luminescence center. This is, however, *not* the case. In Fig. 3 we show an example of the measured delayed recombination decay of $SHO:Ce^{3+}$ at 167 K. An intense, easily measurable decay is approximated by a sum of three exponentials (see the function $I(t)$ in the figure) pointing to a rather complex decay process, which has no straightforward explanation. Consequently, the successful fit in Fig. 2 involves an additive constant in Eq. (3) to fit the low temperature region. This presence of a low temperature signal not covered by Eq. (3) suggests that besides the temperature dependent contribution, there is also a temperature independent part that *is not* due to thermal ionization of the luminescence center. There must be another mechanism at work responsible for the low temperature signal. One should point out that such a low temperature signal is not restricted to a certain class of materials or specific recombination center, since such remnants were already observed by us in several different types of oxides doped either by Ce^{3+} (current work, [8]) or Pr^{3+} [4, 9] or even in the undoped ones [10]. It has been obtained even for $Y_3Al_5O_{12}:Pr$ and $Lu_3Al_5O_{12}:Pr$ where thermally induced ionization was not detected below 500 K. Since this is evidently a kind of sub-gap process which does not involve the conduction band of the host, one candidate to explain such a phenomenon could be quantum tunneling between the recombination center and a nearby trap. Space correlation (aggregation) of emission centers and charge carrier traps seem to be a rather frequent event in luminescent materials [11]. Furthermore, tunneling-driven radiative recombination has already been considered in the description of classical phosphors some time ago [12] and systematically applied to explain recently studied photo-, radio- and thermo-luminescence characteristics in doped aluminum perovskites, garnets and silicates as well [13].

Should the low temperature delayed recombination decay be single exponential, it would indicate tunneling between single traps (traps of one kind) and recombination centers occurring at a constant distance in all the ensemble of trap–center pairs. Decay with a more complex course (such as that reported in Fig. 3) indicates either (i) participation of more than one kind of trap, (ii) single traps with different neighborhoods, i.e. single traps differently perturbed, or (iii) single traps with different distances from recombination centers.

A preliminary, simple one-dimensional model of such a process showed that with realistic parameters (such as strengths of potentials of an electron within the trap or recombination center, or the distance between the trap and recombination center) the quantum tunneling can slow down the luminescence decay by several orders of magnitude [14] as observed in the delayed recombination experiment. The presence of the low temperature contribution to the delayed recombination signal shows that even at very low temperatures there can be a definite loss of the

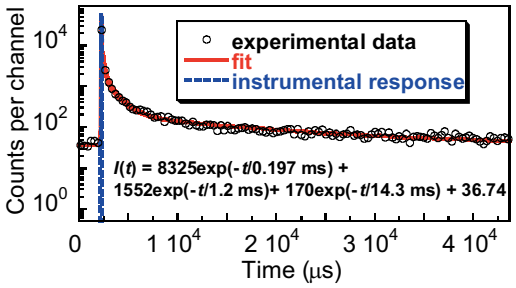

Figure 3 (online colour at: www.pss-rapid.com) Delayed recombination decay of $SrHfO_3:Ce^{3+}$ at 167 K, $\lambda_{exc} = 200$ nm, $\lambda_{em} = 400$ nm. Empty circles are experimental data, solid line is the fit to the data of the function sketched in the figure.

fast scintillation light from the excited luminescence center that is not due to thermal ionization. This escape of excitation energy may happen either during the initial relaxation or after the fully relaxed state of the center has been reached.

5 Conclusion In the present work we determined the energy of thermal ionization of the excited state of the Ce^{3+} ion in a SHO host by a purely optical, contactless method independent of that used previously [6]. The current method yielded a consistent value of the thermal ionization energy of about 0.25 eV.

The validity of the method, first introduced and tested for a $Lu_2Si_2O_7:Pr^{3+}$ single crystal [4], has now been confirmed for a microcrystalline powder of $SrHfO_3:Ce^{3+}$. This is an important step by which the applicability of the method was experimentally established for a class of materials where both an experimental detection of thermal ionization process and the determination of thermal ionization energy are either not feasible by conventional methods [1] or the underlying experiment is too complex and demanding [2, 3]. Besides, such a method is of crucial importance in the fast screening of new scintillating materials which are frequently prepared in a powder form using quick and inexpensive technologies, such as solid state sintering.

We also revealed a low temperature contribution to the delayed recombination processes in $SHO:Ce^{3+}$ and several other materials that is not due to thermal ionization of the luminescent center. Such a result may indicate the presence of unknown relaxation processes leading to temporary displacement of a charge carrier from the excited state of luminescence center to the host lattice neighborhood. Consequently, the delayed recombination decay measurement can also be a tool to assess and evaluate the temperature independent losses of fast scintillation light.

Acknowledgements This work was supported by the Czech GA AV KAN300100802 and M100101212 projects and II-20100033 EC project of DESY Hamburg. Thanks are expressed to A. Vedda and her group for supplying the sample and for discussions. L. S. Schulman thanks the Max Planck Institute for the Physics of Complex Systems for its kind hospitality.

References

[1] E. van der Kolk, S. A. Basun, G. F. Imbusch, and W. M. Yen, Appl. Phys. Lett. **83**, 1740 (2003).
[2] M. F. Joubert, S. A. Kazanski, Y. Guyot, J. C. Gâcon, and C. Pedrini, Phys. Rev. B **69**, 165217 (2004).
[3] H. Loudyi, Y. Guyot, J. C. Gâcon, C. Pedrini, and M. F. Joubert, J. Lumin. **127**, 171 (2007).
[4] M. Fasoli, A. Vedda, E. Mihóková, and M. Nikl, Phys. Rev. B **85**, 085127 (2012).
[5] V. Jarý, E. Mihóková, M. Nikl, P. Boháček, A. Lauria, and A. Vedda, Opt. Mater. **33**, 149 (2010).
[6] E. Mihóková, V. Jarý, M. Fasoli, A. Lauria, F. Moretti, M. Nikl, and A. Vedda, Chem. Phys. Lett., in press; DOI: 10.1016/j.cplett.2012.11.039 (2012).
[7] E. Mihóková, F. Moretti, N. Chiodini, A. Lauria, M. Fasoli, A. Vedda, A. Nale, M. Nikl, and P. Boháček, IEEE Trans. Nucl. Sci. **57**, 1245 (2010).
[8] H. Feng, V. Jarý, E. Mihóková, D. Ding, M. Nikl, G. Ren, H. Li, S. Pan, A. Beitlerova, and R. Kucerkova, J. Appl. Phys. **108**, 033519 (2010).
[9] M. Nikl, G. Ren, D. Ding, E. Mihóková, V. Jarý, and H. Feng, Chem. Phys. Lett. **493**, 72 (2010).
[10] M. Nikl, P. Bohacek, B. Trunda, V. Jarý, P. Fabeni, V. Studnicka, R. Kucerkova, and A. Beitlerova, Opt. Mater. **34**, 433 (2011).
[11] F. Clabau, X. Rocquefelte, T. Le Mercier, P. Deniard, S. Jobic, and M.-H. Whangbo, Chem. Mater. **18**, 3212 (2006).
[12] P. Avouris and T. N. Morgan, J. Chem. Phys. **74**, 4347 (1981).
[13] M. Nikl, E. Mihóková, J. Pejchal, A. Vedda, M. Fasoli, I. Fontana, V. V. Laguta, V. Babin, K. Nejezchleb, A. Yoshikawa, H. Ogino, and G. Ren, IEEE Trans. Nucl. Sci. **55**, 1035 (2008).
[14] E. Mihóková, L. S. Schulman, M. Nikl, and V. Jarý, Low temperature contribution to delayed recombination in scintillating materials, presentation I-45, ICDIM 2012, Santa Fe, NM, USA, June 24–29.

Optical Materials 34 (2012) 872–877

Contents lists available at SciVerse ScienceDirect

Optical Materials

journal homepage: www.elsevier.com/locate/optmat

Defect states in Pr^{3+} doped lutetium pyrosilicate

E. Mihóková [a,b,*], M. Fasoli [a], F. Moretti [a], M. Nikl [b], V. Jarý [b], G. Ren [c], A. Vedda [a]

[a] Dip. di Scienza dei Materiali, Università di Milano-Bicocca, via Cozzi 53, 20125 Milano, Italy
[b] Institute of Physics, AS CR v.v.i., Cukrovarnická 10, 16253 Prague, Czech Republic
[c] Shanghai Institute of Ceramics, Chinese Academy of Sciences, 215 Chengbei Road, Jiading, Shanghai 201800, People's Republic of China

ARTICLE INFO

Article history:
Received 19 October 2011
Accepted 28 November 2011
Available online 20 December 2011

Keywords:
Oxide materials
Optical properties
Tunneling
Luminescence

ABSTRACT

We study defect states in Pr^{3+}-doped $Lu_2Si_2O_7$ crystal by wavelength resolved thermally stimulated luminescence both below and above room temperature. We identify the TSL peaks, analyze them by the initial rise technique and calculate the characteristic parameters of the corresponding traps. The role of tunnelling of charge carriers between traps and recombination centers up to RT is observed and discussed. The TSL spectra show that the charge carrier recombination predominantly occurs at Pr^{3+} centers. We also provide some comparison with the LPS:Ce^{3+} crystal prepared by the same method.

1. Introduction

In the quest for new inorganic scintillators with a fast response, Ce^{3+}-doped lutetium oxyorthosilicate Lu_2SiO_5 (LSO) became a promising material for positron emission tomography (PET) application [1,2]. In recent years lutetium pyrosilicate $Lu_2Si_2O_7$ (LPS) was also introduced as a potentially interesting scintillator host [3]. EPR study of Ce^{3+}-doped LSO and LPS showed that the Ce ion in LPS:Ce substitutes for Lu in its single crystallographic site while in LSO:Ce it is found in both Lu crystallographic sites [4]. The light yield of LPS:Ce single crystals synthesized by the melting zone technique is always high, comparable to that of LSO:Ce, and the cerium scintillation decay time is around 37 ns, with no observable afterglow [5]. On the other hand, the lack of light yield reproducibility for the LPS:Ce^{3+} crystals grown by the Czochralski process was correlated with Ir impurities due to the crystal growth from Ir crucibles [6]. Furthermore, post-growth annealing in air at elevated temperatures was found efficient in increasing the scintillation efficiency [7]. The lack of afterglow in LPS:Ce in contrast to its observation in LSO:Ce was correlated with the significantly higher temperature maxima of thermoluminescence (TSL) glow peaks above room temperature [8]. Recently, a procedure of synthesis of nanocrystalline LPS:Ce [9] allowed much higher concentration of Ce (5%) comparing to monocrystal prepared by Czochralski technique (up to 0.5%).

Due to the expected faster response of 5d–4f transition of Pr^{3+} ion, LPS:Pr^{3+} also became studied as a perspective scintillating material. LPS:Pr crystals grown by Czochralski or floating zone techniques studied in [10] presented much lower light yield than the crystals of LPS:Ce. The fact was explained as due to intense slow 4f–4f emission resulting from efficient energy transfer between self-trapped exciton (STE) state and 4f states of Pr^{3+} ion [10,11]. However, radioluminescence of LPS:Pr powder prepared by sol–gel method [12] did not show any significant contribution of 4f–4f Pr^{3+} emission at room temperature (RT) and the onset of thermal quenching of the 5d–4f emission only appeared above 300 K. Similarly, the study of LPS:Pr crystal prepared by Czochralski technique [13] demonstrated the radioluminescence (RL) amplitude of 5d–4f emission of Pr^{3+} being five times higher than that of $Bi_4Ge_3O_{12}$ (BGO) standard scintillator. Furthermore, the investigation of the temperature dependence of photoluminescence of decay times showed a negligible thermal ionization as well as thermal quenching of Pr^{3+} emission center around RT.

The TSL glow curve in LPS:Pr above RT is presented in [11]. Its similarity to that of LPS:Ce is shown. An effect of Sm^{3+} that can serve as an electron trap demonstrates that the observed TSL peaks in LPS:Ce and LPS:Pr also correspond to electron traps, most likely oxygen vacancies which is also supported by annealing experiments in [7]. However, any detailed analysis of trapping states in LPS:Pr^{3+} is lacking and the reason for dramatic difference in light yield in Ce- and Pr-doped LPS is not clear as well. Therefore, in this work we study the defect states in LPS:Pr by wavelength resolved TSL both below and above RT. Using initial rise technique we evaluate the characteristic parameters of traps corresponding to observed TSL peaks. We also provide comparison of TSL glow curve with that of LPS:Ce^{3+}.

* Corresponding author at: Institute of Physics, AS CR v.v.i., Cukrovarnická 10, 16253 Prague, Czech Republic. Tel.: +420 220 318 539; fax: +420 233 343 184.
E-mail address: mihokova@fzu.cz (E. Mihóková).

0925-3467/$ - see front matter © 2011 Elsevier B.V. All rights reserved.
doi:10.1016/j.optmat.2011.11.029

2. Experimental details

The LPS:Pr^{3+} single crystal of the dimensions $\varnothing 20 \times 40$ mm were grown in SIC CAS, Shanghai, China by the Czochralski method using an Ir crucible [7]. The Pr^{3+} concentration in the melt was 0.5 at.%. A plate of about $7 \times 7 \times 1$ mm was cut from the top of the parent boule and polished to an optical grade. A similar sample cut from an LPS:Ce^{3+} single crystal grown by the Czochralski method by the same producer was used for comparison. The Ce^{3+} concentration in the melt was 0.5%.

Thermally stimulated luminescence (TSL) measurements in the 10–310 K temperature range were performed with a heating rate of 0.1 K/s after irradiation at 10 K. Radioluminescence (RL) measurements as a function of time were performed at 10 K. X-ray irradiation in both cases was realized with a Philips 2274 tube operated at 20 kV. The detection system featured a CCD detector (Jobin-Yvon Spectrum One 3000) coupled to a monochromator (Jobin-Yvon Triax 180) with 100 grooves/mm gratings operating in the range 200–1100 nm.

TSL measurements were also performed from 20 up to 460 °C with a linear heating rate of 1 °C/s after irradiation at RT (X-ray tube operating at 30 kV) using two different apparatuses. The first apparatus was a homemade high sensitivity TSL spectrometer measuring TSL intensity as a function of both temperature and emission wavelength. The detector was a double stage microchannel plate followed by a 512 diode array, the dispersive element was a 140 lines/mm holographic grating, the detection range being 200–800 nm. In the second TSL apparatus the total emitted light was detected as a function of temperature by photon counting using a photomultiplier EMI 9635QB.

Photoluminescence (PL) measurements were performed by a custom made 5000 M Horiba Jobin Yvon spectrofluorometer. Excitation by deuterium steady-state lamp was used. An Oxford Instruments liquid nitrogen bath optical cryostat allowed the temperature regulation from about 150 to 500 K.

3. Results and discussion

3.1. TSL below room temperature

The TSL glow curve of the LPS:Pr^{3+} in the temperature interval 10–310 K is displayed in Fig. 1a. The tail of the glow curve seen in the low temperature region 10–65 K suggests the presence of an athermal tunneling of the charge carriers from the trapping states to recombination centers similarly as evidenced in aluminum garnets [14] or perovskites [15]. Above 80 K the glow curve contains three well resolved peaks at about 100 K, 210 K and 265 K (there is a weak peak at about 75 K). The TSL spectra displayed in Fig. 1b and c contain broad bands corresponding to d → f transitions of Pr^{3+} ion (final f states are indicated in the figure). Up to 150 K there is a defect and/or impurity (possibly Ce^{3+}) emission around 3 eV. Above 150 K this emission vanishes. Therefore it seems that in the temperature region 10–150 K these states are competing in a carrier capture. Sharp lines corresponding to f → f transitions of Pr^{3+} ion (and possibly some impurities) appear below 2.15 eV.

To evaluate the characteristic parameters of traps (trap depths, frequency factors and RT detrapping times) associated with glow peaks we applied the *initial rise* technique [16]. For each peak we performed two partial cleaning measurements with different temperatures T_{stop} close to the temperature of the peak maximum. After any partial cleaning the initial part of the "cleaned" glow curve always contained the tail due to tunneling recombination that needed to be considered in the numerical analysis of the data. The signal due to athermal tunneling is proportional to an inverse

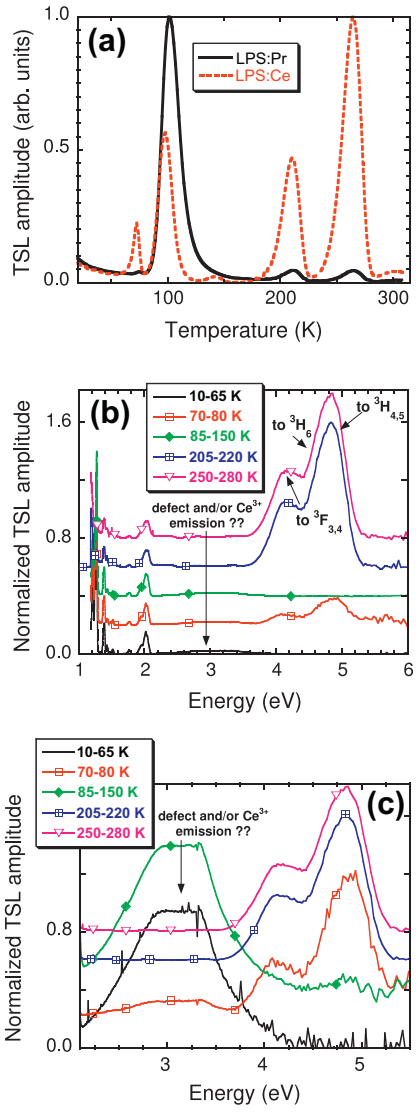

Fig. 1. (a) TSL glow curves of LPS:Pr^{3+} and LPS:Ce^{3+} (for comparison) after X-ray irradiation at 10 K obtained from wavelength resolved measurements integrated in the interval 200–1200 nm and 200–700 nm, respectively. (b) TSL emission spectra of LPS:Pr^{3+} obtained by integration of wavelength resolved TSL measurements in the temperature regions indicated in the figure. Final states of d → f emissions are also indicated in the figure. (c) The detail of the spectra in (b).

power low (IPL) function of time $a/(t + t_0)$, with a and t_0 being constants [17]. Since the heating rate of our experiment is a linear function of temperature T, we can approximate the tunneling tail by the function A/T, where A stands for a constant. The initial part of the glow peak can be approximated by an exponential function [16]. To summarize, the function $Amp(T)$ was fit to the TSL amplitude containing the tunneling tail and initial part of the "cleaned" glow peak:

$$Amp(T) = b + w \times e^{-E/kT} + \frac{A}{T}, \quad (1)$$

where b and A are constants, E is the trap depth, w is a preexponential factor, k is the Boltzmann constant and T is the absolute temperature. An example of the fit of the glow curve after partial cleaning with T_{stop} = 90 K is shown in Fig. 2.

The dominant TSL peak at about 100 K manifests the tail in the high temperature region suggesting that the peak might not correspond to the first order recombination kinetics. Therefore we checked the dependence of the glow curve on the irradiation dose.

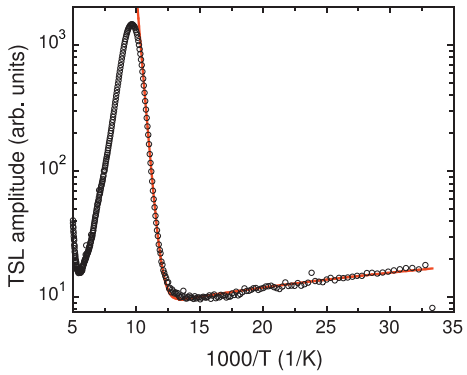

Fig. 2. Arrhenius plot of the TSL glow curve of LPS:Pr^{3+} after partial cleaning with the temperature T_{stop} = 90 K. Empty circles are experimental data, solid line is the fit of the function (1) to the data. Parameters of the fit are: $b = 5$, $w = 3.93 \times 10^{15}$, A = 373 K, E = 0.24 eV.

The irradiation dose in the experiment was varied by two orders of magnitude. The normalized glow curves are displayed in Fig. 3a. The maxima of the TSL peaks at 210 K and 265 K (see the detail in the inset of Fig. 3a) are stable with increasing dose indicating that they obey the first order recombination kinetics. On the other hand, the behavior of the 100 K peak is not consistent with either first or general order kinetics, but rather indicates a composite character of the peak as confirmed by its partial cleaning, in particular that with T_{stop} = 120 K (see Fig. 3b). Fig. 3b demonstrates that the 100 K peak is composed of at least three peaks. Due to close proximity of these peaks we could reliably determine only the parameters associated with the first component at the low temperature side.

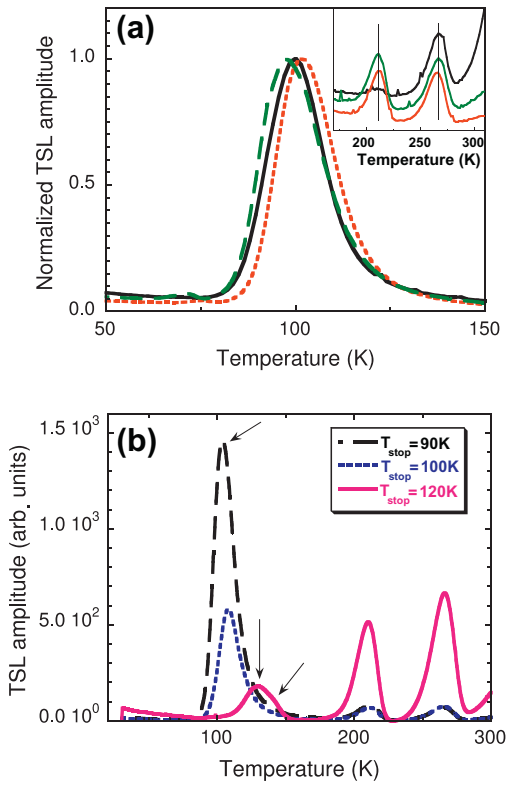

Fig. 3. (a) Normalized TSL glow curves of LPS:Pr^{3+} after X-ray irradiation at 10 K with various irradiation doses. The solid line corresponds to the lowest dose, short dashed line to 10 times higher dose and long dashed line to 70 times higher dose. The inset displays the high temperature detail of the TSL glow curve and (b) TSL glow curve after partial cleaning for three different temperatures T_{stop} indicated in the figure. Arrows indicate the composite character of the TSL peak.

It is worth noting another interesting feature observed during the partial cleaning measurements. In the case of the full glow curve as well as the glow curve after partial cleaning with $T_{stop} \leqslant 120$ K, the spectrum of the tunneling tail contains both defect (3 eV) and Pr^{3+} f → f emissions. (cf. Fig. 1b, integration range 10–65 K). In contrast, in the case of the glow curve after partial cleaning with $T_{stop} \geqslant 200$ K the spectrum of the tail contains only f → f emissions (cf. Fig. 4), consistently with the defect emission vanishing at 150 K (as mentioned above). This observation suggests some comments.

First, there are probably two trap levels with different depths participating in the tunneling recombination process. From the shallower trap level an electron tunnels to the defect state while from the deeper one it tunnels to the f state of Pr^{3+}. Since the defect emission vanishes at 150 K, the trap active in the tunneling process to the defect state is one from the collection giving rise to the 100 K TSL peak. On the other hand the tunneling to the f state of Pr^{3+} ion is observed also for partial cleaning with T_{stop} = 300 K. This observation indicates that the trap active in the tunneling process to an f state of Pr^{3+} is none of those associated with the 210 K or 265 K peaks but rather a deeper one observable above RT.

Second, the numerical analysis of the data after partial cleaning with $T_{stop} \geqslant 200$ K becomes easier and probably more reliable, since there is one less parameter to fit. If we consider the glow curve obtained by integrating the TSL signal only in the d–f Pr^{3+} emissions, the tunneling tail is cut off and the TSL amplitude of the initial rise of the glow peak can be approximated by a simple single-exponential function:

$$Amp(T) = b + w \times e^{-E/kT}, \tag{2}$$

where significance of particular quantities is the same as in (1).

Keeping in mind the above written, the function (1) was fit to the data obtained after partial cleaning with $T_{stop} \leqslant 100$ K, while both (1) and (2) were fit to the data obtained after partial cleaning with $T_{stop} \geqslant 200$ K. Arrhenius plots of data and fits corresponding to various temperatures T_{stop} are displayed in Fig. 5 with T_{stop} indicated in the figure. For $T_{stop} \geqslant 200$ K we only display fits of the function (2) to the data. Corresponding average trap depths resulting from fits and partial cleanings corresponding to the same TSL peak are listed in Table 1.

Based on the assumption that the three studied glow peaks correspond to the first order recombination kinetics (for the 210 K and 265 K peaks confirmed by the dose dependence measurement, cf. inset of Fig. 3a) we calculated the frequency factors associated with corresponding traps using the formula relating the frequency

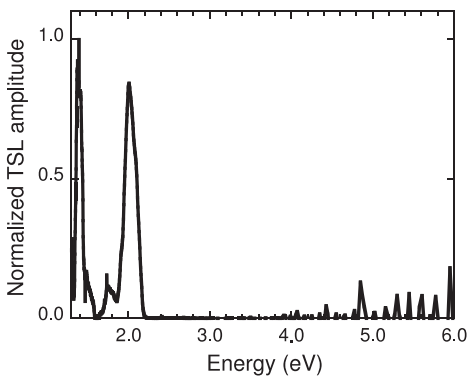

Fig. 4. Normalized TSL spectrum of the tunneling tail obtained by integration of wavelength resolved TSL measurement of LPS:Pr^{3+} after partial cleaning with the temperature T_{stop} = 205 K. The temperature region of integration was 30–150 K.

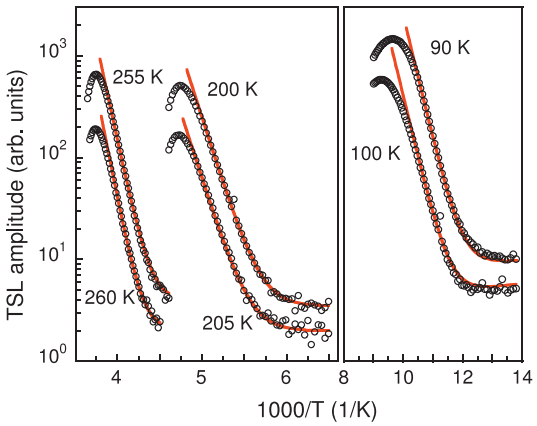

Fig. 5. Arrhenius plot of initial rise of TSL peaks after partial cleaning of the glow curve of LPS:Pr^{3+} with various temperatures T_{stop} indicated in the figure. Empty circles are experimental data, solid lines are fits of function (1) or (2) to the data.

Table 1
Characteristic parameters of traps associated with TSL peaks below RT.

T_m (K)	E (eV) average	s (s^{-1})	τ (s) at RT
102	0.24 ± 0.01	$\sim 10^{10}$	$\sim 10^{-6}$
211	0.51 ± 0.01	$\sim 10^{10}$	$\sim 10^{-2}$
265	0.74 ± 0.06	$\sim 10^{13}$	$\sim 10^{0}$

factor s, the heating rate β (0.1 K/s) and the temperature maximum of the TSL peak T_m [16]:

$$\beta E/kT_m^2 = s \times e^{-E/kT_m}, \quad (3)$$

The trap depth E is taken from the initial rise evaluation, reported in Table 1.

The detrapping time of the trap τ at the temperature T can be calculated as [16]:

$$\tau = s \times e^{E/kT}, \quad (4)$$

The values of frequency factors s and detrapping times τ at room temperature are also listed in Table 1. It is worth noting that even if the trap associated with the dominant TSL peak around 100 K is very shallow and its RT detrapping time is on the order of microseconds (see Table 1), the charge carriers released from this trap do not contribute to the fast Pr^{3+} d → f scintillation light. They almost exclusively recombine at either the defect center or f levels of Pr^{3+} as can be seen from the spectra in Fig. 1b and c (integration range 85–150 K).

Shallow traps are delaying the transport of charge carriers to the recombination centers and consequently may play a significant role in the deterioration of light yield (LY) of the scintillation material. Despite the same host lattice, LY of Pr-doped LPS is substantially different from that of Ce-doped. As reported in Ref. [10], high quality large single crystals of LPS:Ce manifested the light yield value up to 26,300 photons/meV, while Pr-doped LPS in the same study showed the LY of only 5000 photons/MeV. Since the intrinsic quantum efficiency of the Pr^{3+} and Ce^{3+} emission centers in LPS host is up to RT similar and close to 1 (as can be deduced from the temperature dependence of PL decay times [8,12,13]) such a big difference must be due to some trapping and/or energy transfer effects in the transport stage of scintillation mechanism. That is why we also studied TSL glow curve of LPS:Ce crystal.

The glow curve manifests very similar shape as that of LPS:Pr^{3+} (see Fig. 1a), in other words there are similar shallow traps present in both crystals. The tail of the glow curve seen in the low temperature region 10–65 K is also due to athermal tunneling from the trapping states to recombination centers. Above 80 K the glow curve contains five well resolved peaks at about 70 K, 100 K, 140 K, 210 K and 265 K. In the case of LPS:Pr^{3+} it was shown that the TSL peak around 100 K is composed of several peaks. It seems that in LPS:Ce^{3+} some peaks of this collection are missing. While in LPS:Pr^{3+} the principal peak is that around 100 K, in LPS:Ce^{3+} the dominant peak is that around 265 K. Similarity of shallow trapping states in both crystals does not by itself indicate any big differences in scintillation mechanism. Therefore we performed complementary experiment to shed more light on the issue.

During the X-ray irradiation at 10 K we monitored the "prompt" emission as a function of both time and emission wavelength. After the irradiation was stopped, for several minutes we continued to monitor the afterglow at 10 K.

Unlike in LPS:Ce for which the RL amplitude slightly decreases as a function of irradiation time, the prompt RL light of LPS:Pr increases (cf. Fig. 6a and b). The feature is observed for both d → f and f → f emissions. Similar behavior was observed in some rare-earth doped glasses and explained in terms of competition in the charge carrier capture between the traps and rare-earth recombination centers [21]. As the traps are getting filled the competition becomes less important. Such mechanism may also apply in LPS:Pr. We note that in principle such an effect might be caused by both the electron or hole traps.

The results presented above definitely manifest a difference in scintillation characteristics of LPS:Ce and LPS:Pr crystals. This

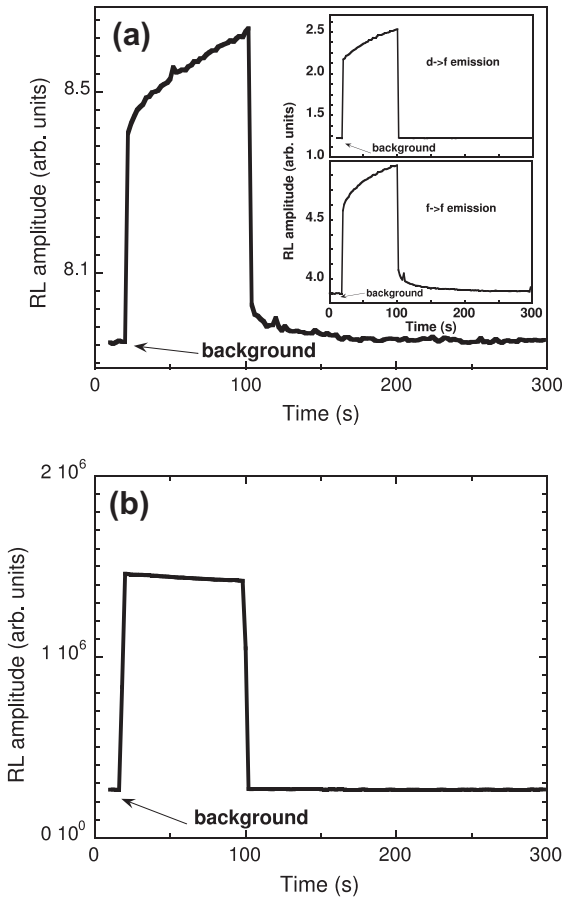

Fig. 6. Prompt RL and afterglow monitored at 10 K during 90 s and up to 300 s after irradiation by X-rays. In (a) LPS:Pr; the wavelength resolved signal is integrated in the entire interval 200–1100 nm. In the inset the signal integrated in the interval 250–350 nm and 590–1030 nm corresponding to d–f and f–f emissions of Pr^{3+} center, respectively. In (b) LPS:Ce; the afterglow signal is absent. The wavelength resolved signal is integrated in the interval 300–600 nm corresponding to the d–f emission of Ce^{3+} center.

difference could be related to the transport stage of the scintillation and result in their significantly different light yield reported in the literature. However, further study is needed to understand the true origin of this difference.

3.2. TSL above room temperature

The TSL glow curve of LPS:Pr^{3+} crystal after irradiation at RT is displayed in Fig. 7a. Corresponding TSL spectra obtained from wavelength resolved measurement by integration in the temperature interval 20–470 °C are displayed in Fig. 7b. TSL spectra show that the charge carriers predominantly recombine at Pr^{3+} centers.

To evaluate the depths of traps associated with glow peaks above room temperature we again applied the *initial rise* technique. However, as manifested by the temperature dependence of integrated PL intensity in Fig. 8, Pr^{3+} recombination center is quenched above RT. Consequently, before analysis the glow curves need to be corrected for this temperature quenching of recombination center (as in the inset of Fig. 8). Numerical analysis of the data was performed by fitting the function (2) to the data obtained after partial cleaning of the glow curve and corrected for the temperature quenching of recombination center.

As seen from Fig. 7a the glow peaks are broad and overlapping which makes impossible to determine the characteristics of all of them. We succeeded to analyze three glow peaks at about 60, 210 and 340 °C. There are also peaks at about 160 and 280 °C which become evident only after partial cleaning procedure that could not be analyzed due to strong overlap with neighboring peaks. For each peak we performed two to three partial cleaning

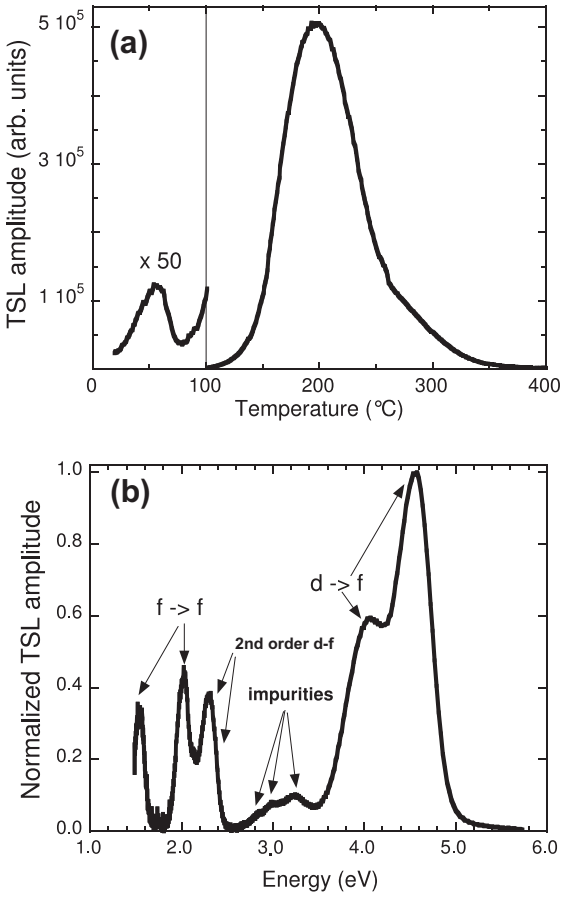

Fig. 7. (a) TSL glow curve of LPS:Pr^{3+} after X-ray irradiation at RT and (b) TSL emission spectra obtained by integration of wavelength resolved measurement between 40 and 310 °C.

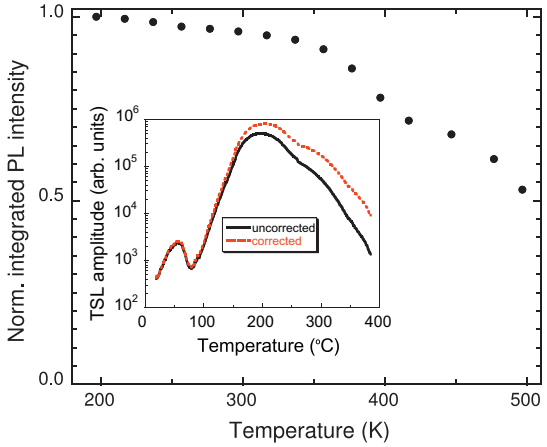

Fig. 8. Normalized integrated PL intensity of LPS:Pr^{3+} as a function of temperature. Emission spectra were excited at 240 nm and integrated in the range 250–420 nm. In the inset TSL glow curves after X-ray irradiation at RT uncorrected and corrected for temperature quenching of the recombination center.

measurements with different temperatures T_{stop}. Arrhenius plots of data and fits corresponding to selected temperatures T_{stop} are displayed in Fig. 9 with T_{stop} indicated in the figure. The low temperature part of the glow curves after partial cleaning below 100 °C started with the hint of the tail probably due to athermal tunneling observed in measurements described in the previous subsection. For glow curves after partial cleaning at higher temperatures (above 100 °C) any definite statement about the presence or absence of tunneling tail cannot be made due to the low signal level.

Variation of the irradiation dose by about two orders of magnitude did not change the TSL peak positions, therefore we may again assume that the traps associated with the glow peaks follow the first order recombination kinetics. We calculated corresponding frequency factors and room-temperature detrapping times associated with each trap using formulas (3) and (4). In this case the heating rate β is 1 °C/s. All trap characteristics are listed in Table 2.

TSL glow curve of LPS:Pr^{3+} above RT has already been presented in [11]. The shape of the glow curve was similar to that of LPS:Ce^{3+}. The main TSL peaks were identified at about 460 and 530 K. The glow curve presented in this work appears more complex. Comparing to [10] we observe three additional peaks at about 60, 160 and 340 °C. The peaks at 210 °C (483 K) and 280 °C (553 K) correspond

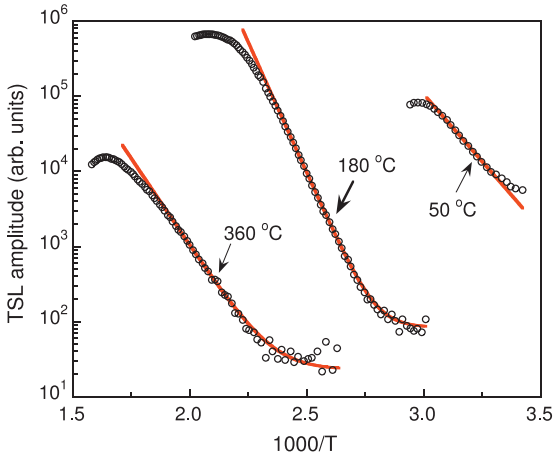

Fig. 9. Arrhenius plot of initial rise of TSL peaks after partial cleaning of the glow curve of LPS:Pr^{3+} with selected temperatures T_{stop} indicated in the figure. Empty circles are experimental data, solid lines are fits of function (2) to the data.

Table 2
Characteristic parameters of traps associated with TSL peaks above RT.

T_m (°C)	T_m (K)	E (eV) average	s (s^{-1})	τ (hours) at RT
61	334	0.74 ± 0.1	$\sim 10^9$	$\sim 10^{-1}$
210	483	1.46 ± 0.01	$\sim 10^{14}$	$\sim 10^7$
340	613	1.03 ± 0.01	$\sim 10^7$	$\sim 10^7$

to those observed in [11] at 460 K and 530 K, respectively. The high temperature shift is most probably due to higher heating rate (1 K/s) used in the present work with respect to that in [11] (0.5 K/s). Additional TSL peaks observed by us are either due to additional traps present in the studied crystal or due to their lower concentration and masking by more intense TSL peaks in the previous work.

The traps monitored by TSL in LPS:Pr^{3+} most likely correspond to electron traps since Pr^{3+} similarly as Ce^{3+} are stable hole traps. As mentioned, this hypothesis, at least above RT, was confirmed by adding Sm^{3+} into LPS:Ce^{3+} sample [11]. Oxygen vacancies could be considered as strong candidates for electron traps in LPS:Pr^{3+}, since they are frequently present in silicates as well as other oxides [18–20].

4. Conclusion

Our TSL study demonstrates that several shallow and deep trapping states are present in LPS:Pr^{3+} crystal. Since similar deep traps were observed for both LPS:Pr^{3+} and LPS:Ce^{3+} prepared by different methods [11] we suggest that defects responsible for at least those traps have intrinsic origin.

The participation of athermal tunneling of charge carriers between the traps and recombination centers in charge carrier recombination was manifested up to RT. The persistence of tunneling process up to such high temperature can, in principle, give rise to intense slow components in scintillation decay and explain a low light yield observed in previous work referred in the literature even if radioluminescence efficiency in LPS:Pr is quite high. However, a similar process we also observed in the LPS:Ce crystal studied for comparison. Previous observation of tunneling-driven radiative recombination in garnets or perovskites indicates that the phenomenon is rather frequently encountered in oxide materials with various structures.

Despite our effort to shed the light on the difference in reported light yield in LPS:Pr and LPS:Ce, further study is needed to understand the difference in the transport stage of scintillation mechanism that lies behind it.

Acknowledgments

This work was supported by the CARIPLO Foundation project "Energy transfer and trapping phenomena in nano-structured scintillator materials" (2008–2011) and also by the Czech MSMT KONTAKT ME10084 project.

References

[1] H. Suzuki, T.A. Tombrello, C.L. Melcher, J.S. Schweizer, Nucl. Instrum. Methods Phys. Res. A 320 (1992) 263–272.
[2] C.L. Melcher, R.A. Manente, C.A. Peterson, J.S. Schweizer, J. Cryst. Growth 128 (1993) 1001–1005.
[3] L. Pidol, A. Kahn-Harari, B. Viana, E. Virey, B. Ferrand, P. Dorenbos, J.T.M. De Haas, C.W.E. Van Eijk, IEEE Trans. Nucl. Sci. 51 (2004) 1084–1087.
[4] L. Pidol, O. Guillot-Noël, A. Kahn-Harari, B. Viana, D. Pelenc, D. Gourier, J. Phys. Chem. Solids 67 (2006) 643–650.
[5] D. Pauwels, N. Le Masson, B. Viana, A. Kahn-Harari, E.V.D. van Loef, P. Dorenbos, C.W.E. van Eijk, IEEE Trans. Nucl. Sci. 47 (2000) 1787–1790.
[6] L. Pidol, O. Guillot-Noël, M. Jourdier, A. Kahn-Harari, B. Ferrand, P. Dorenbos, D. Gourier, J. Phys.: Condens. Matter 15 (2003) 7815–7821.
[7] H. Feng, D. Ding, H. Li, S. Lu, S. Pan, X. Chen, G. Ren, J. Appl. Phys. 103 (2008) 083109-1–083109-7.
[8] L. Pidol, A. Kahn-Harari, B. Viana, B. Ferrand, P. Dorenbos, J.T.M. de Haas, C.W.E. van Eijk, E. Virey, J. Phys.: Condens. Matter 15 (2003) 2091–2102.
[9] J. Sokolnicki, M. Guzik, Opt. Mater. 31 (2009) 826–830.
[10] L. Pidol, B. Viana, A. Kahn-Harrari, A. Bessiere, P. Dorenbos, Nucl. Instrum. Methods Phys. Res. A 537 (2005) 125–129.
[11] L. Pidol, B. Viana, A. Galtayries, P. Dorenbos, Phys. Rev. B 72 (2005) 125110-1–125110-9.
[12] M. Nikl, A.M. Begnamini, V. Jary, D. Niznansky, E. Mihóková, Phys. Stat. Sol. RRL 3 (2009) 293–295.
[13] M. Nikl, G. Ren, D. Ding, E. Mihóková, V. Jary, H. Feng, Chem. Phys. Lett. 493 (2010) 72–75.
[14] M. Nikl, A. Vedda, M. Fasoli, I. Fontana, V.V. Laguta, E. Mihóková, J. Pejchal, J. Rosa, K. Nejezchleb, Phys. Rev. B 76 (2007) 195121-1–195121-8.
[15] A. Vedda, M. Fasoli, M. Nikl, V.V. Laguta, E. Mihóková, J. Pejchal, A. Yoshikawa, M. Zhuravleva, Phys. Rev. B 80 (2009) 045113-1–045113-9.
[16] S.W.S. Mc Keever, Thermoluminescence of Solids, Cambridge University Press, Cambridge, 1985.
[17] D.J. Robbins, B. Cockayne, J.L. Glasper, B. Lent, J. Electrochem. Soc. 126 (1979) 1213–1220.
[18] A. Meijerink, W.J. Schipper, G. Blasse, J. Phys. D 24 (1991) 997–1002.
[19] D.W. Cooke, B.L. Bennett, R.E. Muenchaussen, K.J. McClellan, J.M. Roper, M.T. Whittaker, J. Appl. Phys. 86 (1999) 5308–5310.
[20] R. Visser, C.L. Melcher, J.S. Schweitzer, H. Suzuki, T.A. Tombrello, IEEE Trans. Nucl. Sci. 41 (1994) 689–693.
[21] M. Fasoli, N. Chiodini, F. Moretti, A. Vedda, Phys. Stat. Sol. (c) 4 (2007) 1056–1059.

Journal of Luminescence 190 (2017) 309–313

Contents lists available at ScienceDirect

Journal of Luminescence

journal homepage: www.elsevier.com/locate/jlumin

Defect states and temperature stability of Eu^{2+} center in Eu-doped yttrium aluminum garnet

E. Mihóková*, V. Babin, V. Jarý, L. Havlák, M. Buryi, M. Nikl

Institute of Physics, AS CR v. v. i., Na Slovance 2, 18221 Prague 8, Czech Republic

ARTICLE INFO

Keywords:
Oxide materials
Optical properties
Tunneling
Luminescence

ABSTRACT

We study defect states in Eu-doped $Y_3Al_5O_{12}$ powder by thermally stimulated luminescence (TSL) in the temperature range 77–500 K. We identify the main TSL peaks, analyze them by the initial rise technique and calculate the characteristic parameters of the corresponding traps. Tunneling of charge carriers between traps and recombination centers up to about 265 K is observed and discussed. Recent study established the presence of both Eu^{2+} and Eu^{3+} centers in the studied $Y_3Al_5O_{12}$ powder. The TSL spectra show that Eu^{2+} and Eu^{3+} centers compete in the charge carrier capture. We show that previously observed Eu^{2+} luminescence quenching is due to both classical thermal quenching and thermal ionization of the Eu^{2+} excited state. We model the temperature dependence of the delayed recombination intensity.

1. Introduction

Yttrium-aluminum garnet, $Y_3Al_5O_{12}$ (YAG), is one of the most widely studied inorganic hosts due to its high application potential when doped by rare-earth (RE) ions. Single crystals of YAG had already been grown in the 1960s [1] and soon after the potential of Ce^{3+}-doped YAG single crystals for fast scintillators was reported [2,3]. The first comprehensive description of YAG:Ce scintillator characteristics was carried out by Moszynski et al. [4], details can be found in a recent review paper [5]. YAG:Ce, however, has lately been given a lot of attention as most frequently used yellow phosphor for white light solid state lighting [6–13] while coupled to a blue excitation diode.

Recent study [14] employing a powerful combination of the optical and electron paramagnetic resonance techniques, provided a definite proof of the existence of stable Eu^{2+} emission center in the YAG host. Basic optical, scintillation and electron paramagnetic features of this Eu^{2+} center were reported as well. Strong blue emission peaking at 440 nm is due to the Eu^{2+} 5d → 4 f transition and can be effectively excited in a broad UV band peaking at 300 nm with corresponding decay times of about 450–500 ns around room temperature.

In the field of solid state lighting the current search for RGB phosphor excitable by near UV LED diode is sparking an interest in new material compositions [15–18]. YAG:Eu in the mixed powder or ceramic form can also be a suitable candidate. As reported in [14], its efficient blue photoluminescence provides a feature enabling to manufacture the all-in-one host RGB phosphor under near UV LED excitation.

In this work we study the defect states in YAG:Eu by thermally stimulated luminescence (TSL) measurements in the temperature range 77–500 K. Using initial rise technique we evaluate the characteristic parameters of traps corresponding to observed TSL peaks. We also study and discuss temperature stability of Eu^{2+} center present in the material.

2. Experimental details

Eu-doped $Y_3Al_5O_{12}$ (YAG) phosphor in the powder form with a hypothetical formula $Y_{2.97}Eu_{0.03}Al_5O_{11.955}S_{0.03}$ was synthesized by three-step solid-state reaction (1 × 1350 °C/20 h, 2 × 1450 °C/20 h) under the reducing Ar:5%H_2 atmosphere (5 N Ar, 5 N H_2) from starting materials 0.5612 g of Y_2O_3 (5 N), 0.4266 g of Al_2O_3 (5 N) and 0.0092 g of EuS (prepared from 4 N Eu_2O_3 under 2N5 H_2S atmosphere). The phase purity of prepared Eu-doped YAG phosphor was confirmed by XRD analysis. The details of the preparation are described elsewhere [14]. Based on previously reported data [14] the Eu^{3+} to Eu^{2+} concentration ratio can be roughly estimated to be 70.

Thermally stimulated luminescence (TSL) measurements in the 77–500 K temperature range were performed with a heating rate 5 K/min after irradiation at 77 K. The temperature was controlled by the Oxford cryostat. X-ray irradiation was realized with a Seifert X-ray tube operated at 40 kV and 15 mA. The detection system featured a TBX-04 detector (IBH, UK) coupled to a monochromator (Horiba Jobin Yvon). In the case of spectrally unresolved TSL measurements the glow curves were registered by a monochromator at the zero order. Spectrally resolved TSL curves were obtained with Ocean Optics QE65000 spectrometer equipped with a cooled CCD sensor.

Photoluminescence (PL) and radioluminescence (RL) spectra were

* Corresponding author.

http://dx.doi.org/10.1016/j.jlumin.2017.05.065
Received 6 January 2017; Received in revised form 3 May 2017; Accepted 20 May 2017
Available online 26 May 2017

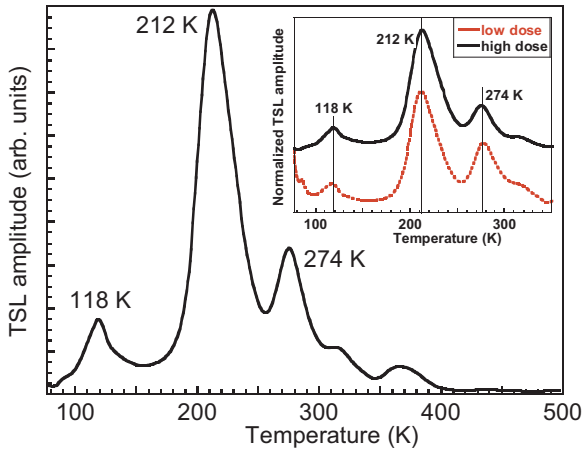

Fig. 1. TSL glow curve of YAG:Eu after X-ray irradiation at 77 K. In the inset the detail of the TSL curve after irradiation by two different irradiation doses. Vertical lines indicate stability of TSL peak positions under variation of irradiation dose by about two orders of magnitude.

measured by a custom made 5000 M Horiba Jobin Yvon spectrofluorometer. Excitation was realized with a deuterium steady state lamp (PL spectra) and X-ray tube (RL spectra). Temperature between 8 and 800 K was controlled by Janis Instruments cryostats. PL delayed recombination decays were excited by a microsecond xenon flashlamp and measured using the multichannel scaling method. The decay data were fit by exponential function using the Spectra-Solve program package. From the fit delayed decay times were determined.

3. Results and discussion

3.1. Thermally stimulated luminescence

The TSL glow curve of the YAG:Eu in the temperature interval 77–500 K is displayed in Fig. 1. The glow curve contains three well resolved peaks at about 118 K, 212 K and 274 K. Some minor peaks are observed also above 300 K. The TSL spectra are displayed in Fig. 2a,b. The spectra were recorded at 77 K during irradiation (black long dashed line) and at temperatures (indicated in the figure) near maxima of the TSL glow peaks. Each spectrum in Fig. 2a was recorded by the scan of emission monochromator using TBX detector. The spectra are corrected for the spectral dependence of the dectector's efficiency and for the reduction of the luminescence intensity during the scan. The spectra in Fig. 2b are uncorrected spectrally resolved TSL curves obtained by the Ocean Optics QE65000 spectrometer equipped with a cooled CCD sensor.

The TSL spectra in Fig. 2a,b contain broad band on the high energy spectral side corresponding to d→f transitions of Eu^{2+} ion together with sharp lines on the low energy side characteristic of the Eu^{3+} ion f→f transitions. Measured TSL spectra suggest that in the temperature region of the principal TSL glow peaks there is a competition of Eu^{2+} and Eu^{3+} recombination centers for a carrier capture. In the simple recombination scheme the transfer mechanism of charge carriers from the host lattice to the Eu^{3+} center can be interpreted as the sequential capture of an electron (during irradiation) and then the hole released from the hole trap (during the heating). In other words Eu^{3+} center is known as a stable electron trap [19]. Recombination of the charge carriers gives rise to the Eu^{3+} emission in the TSL spectra. In contrast, the transfer from the host to the Eu^{2+} center follows the sequence hole-electron capture [20], where the electron would be released from an electron trap during the TSL process. In this case the recombination of charge carriers would produce the Eu^{2+} emission in the TSL spectra. Consequently, participation of both Eu^{2+} and Eu^{3+} emission centers in the charge carrier recombination means, that TSL peaks that we observe in the glow curve can correspond to both electron and hole traps. In

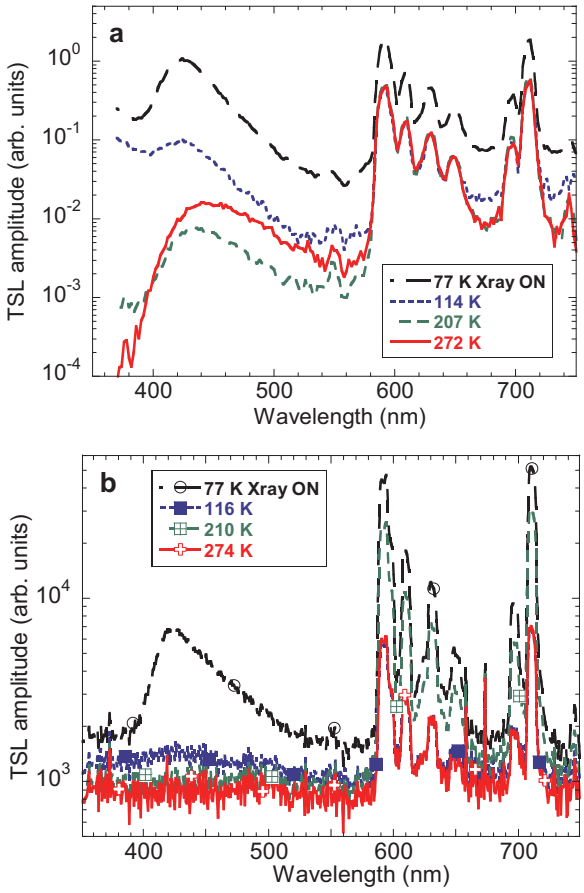

Fig. 2. TSL emission spectra of YAG:Eu recorded at 77 K during irradiation (black long dashed line) and at temperatures (indicated in the figure) near maxima of the TSL glow peaks. In a) each spectrum was recorded by the scan of emission monochromator using TBX detector and corrected; in b) uncorrected spectrally resolved TSL curves were obtained by the Ocean Optics QE65000 spectrometer equipped with a cooled CCD sensor.

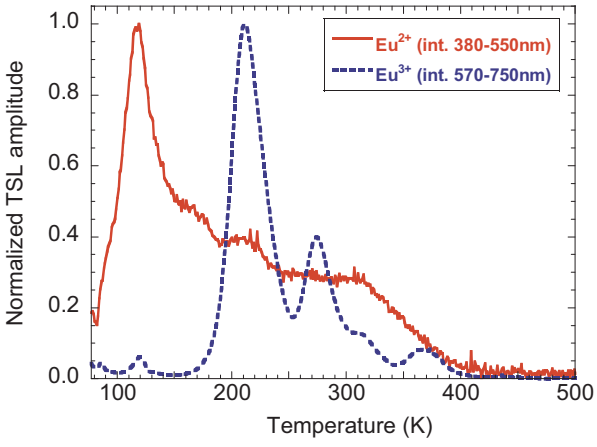

Fig. 3. Normalized TSL glow curves obtained from uncorrected spectrally resolved TSL measurements. The solid and dashed lines were obtained by integration of the TSL spectra within 380–550 nm (region of Eu^{2+} emission) and 570–750 nm (region of Eu^{3+} emission), respectively.

Fig. 3 we display normalized TSL glow curves obtained from spectrally resolved TSL measurements by integration in two regions of emission. One region corresponds to d→f emission of Eu^{2+} center and the other to f→f emissions of Eu^{3+} center. One can see that the 118 K TSL peak corresponds to recombination of charge carriers predominantly at Eu^{2+} centers while two higher TSL peaks represents recombination of charge carriers predominantly at Eu^{3+} centers. Therefore the 118 K peak is

expected to be associated with an electron trap, while the 212 and 274 K peaks with hole traps. We tried to check this assessment also by comparison with the TSL measurements performed for YAG:Ce single crystal.

TSL glow curve of single crystal YAG:Ce was monitored in [21]. Ce^{3+} ions act as recombination centers and the transfer from the host to Ce^{3+} ions follows the sequence hole-electron capture, similarly to Eu^{2+}. Therefore the YAG:Ce glow curve monitors the thermal release of electrons from electron traps. TSL glow curve features the principal TSL peak at 93 K followed by weaker structures at 121 and 176 K. If one compares the result with currently observed glow curve of YAG:Eu in Fig. 1 with peaks at 118, 212 and 274 K, there can be a correlation between the peaks at 121 and 118 K in YAG:Ce and YAG: Eu, respectively. In other peaks one does not see any particular correlation between YAG:Ce and YAG: Eu. This observation supports the conclusion made above, that the TSL peak at 118 K corresponds to an electron trap. In contrast, principal peaks at 212 and 274 K in YAG:Eu *mainly* correspond to the hole traps. However, TSL spectra in the temperature region of these two peaks (cf. Figs. 2,3) show, that besides dominant recombination of charge carriers at Eu^{3+} centers, there is a fraction of charge carriers recombining at Eu^{2+} centers. Such feature suggests that there have to be TSL structures corresponding to *electron* traps (active in recombination at Eu^{2+}) that are masked by dominant TSL peaks at 212 and 274 K that are due to hole traps.

To determine the order of recombination kinetics corresponding to the observed TSL peaks we checked the dependence of the glow curve on the irradiation dose. The irradiation dose in two experiments was subject to variation of about two orders of magnitude (irradiation in two experiments lasting 1 and 120 min, respectively). The glow curves for low and high doses are displayed in the inset of Fig. 1. The maxima of all TSL peaks (see the detail in the inset of Fig. 1) are stable with increasing dose indicating that they obey the first order recombination kinetics.

To evaluate the characteristic parameters of traps (trap depths, frequency factors and RT detrapping times) associated with principal glow peaks we applied the *initial rise* technique [22]. For each peak we performed several partial cleaning measurements with different temperatures T_{stop} close to the temperature of the peak maximum. After any partial cleaning the initial part of the "cleaned" glow curve up to 265 K contained the tail that is attributed to quantum tunneling of the charge carriers between the trapping states to recombination centers similarly as confirmed in a variety of complex oxides, such as aluminum garnets with different dopants [23,24], perovskites [25] or silicates [26,27]. Such tunneling recombination needed to be considered in the numerical analysis of the data. The signal due to temperature independent quantum tunneling is proportional to an inverse power law (IPL) function of time $a/(t+t_0)$, with a and t_0 being constants [28]. Since the heating rate of our experiment is a linear function of temperature T, we can approximate the tunneling tail by the function A/T, where A stands for a constant. The initial part of the glow peak can be approximated by an exponential function [22]. To summarize, the function *Amp (T)* was fit to the TSL amplitude containing the tunneling tail and initial part of the "cleaned" glow peak:

$$Amp(T) = b + w \times e^{-E/kT} + \frac{A}{T}, \quad (1)$$

where b and A are constants, E is the trap depth, w is a preexponential factor, k is the Boltzmann constant and T is the absolute temperature. An example of the fit of the glow curve after partial cleaning with $T_{stop} = 219$ K is shown in Fig. 4.

As mentioned above, the tunneling tail was observed after partial cleaning performed up to 265 K. For partial cleaning of the 274 K peak with $T_{stop} \geq 265$ the tail was no longer observable. This feature indicates that the trap involved in the tunneling process is the one associated with the TSL peak at 209 K and possibly (but not necessarily) also the one associated with the 116 K peak. Furthermore, the

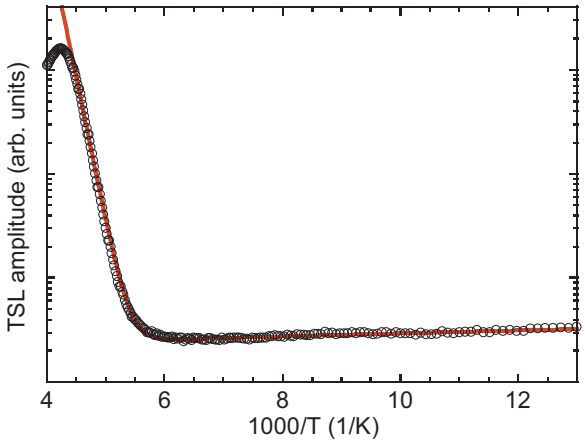

Fig. 4. Arrhenius plot of the TSL glow curve of YAG:Eu after partial cleaning with the temperature $T_{stop} = 219$ K. Empty circles are experimental data, solid line is the fit of the function (1) to the data. Parameters of the fit are: b = 200, w = 2.8×10^{17}, A = 9.5×10^3 K, E = 0.552 eV.

numerical analysis of the data after partial cleaning with $T_{stop} \geq 265$ K does not require the fit of the tunneling tail. The TSL amplitude of the initial rise of the glow peak can be approximated by a simple single-exponential function

$$Amp(T) = b + w \times e^{-E/kT}, \quad (2)$$

where the significance of particular quantities is the same as in (1).

To summarize, the function (1) was fit to the data obtained after partial cleaning with $T_{stop} \leq 265$ K, while (2) was fit to the data obtained after partial cleaning with $T_{stop} \geq 265$ K. Arrhenius plots of data and fits corresponding to selected temperatures T_{stop} are displayed in Fig. 5 with T_{stop} indicated in the figure. Corresponding average trap depths resulting from fits and partial cleanings corresponding to the same TSL peak are listed in Table 1.

Based on the assumption that the three studied glow peaks correspond to the first order recombination kinetics (confirmed by the dose dependence measurement, cf. inset of Fig. 1a) we calculated the frequency factors associated with corresponding traps using the formula relating the frequency factor s, the heating rate β (0.1 K/s) and the temperature maximum of the TSL peak T_m [22]:

$$\beta E/kT_m^2 = s \times e^{-E/kT_m}, \quad (3)$$

The trap depth E is taken from the initial rise evaluation, reported in

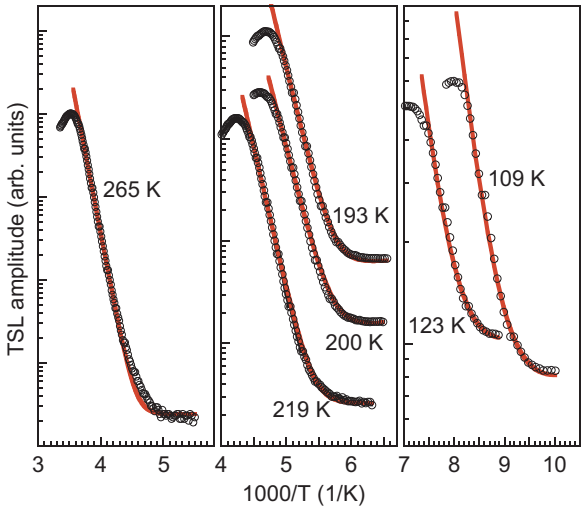

Fig. 5. Arrhenius plot of initial rise of TSL peaks after partial cleaning of the glow curve of YAG:Eu with various temperatures T_{stop} indicated in the figure. Empty circles are experimental data, solid lines are fits of function (1) to the data.

Table 1
Characteristic parameters of traps associated with TSL peaks in the temperature range 77–500 K.

T_m [K]	E (eV)	s (s^{-1})	τ (s) at RT
118	0.25 ± 0.01	$\sim 10^{10}$	10^{-6}
212	0.55 ± 0.01	$\sim 10^{12}$	10^{-3}
274	0.81 ± 0.01	$\sim 10^{14}$	0.7

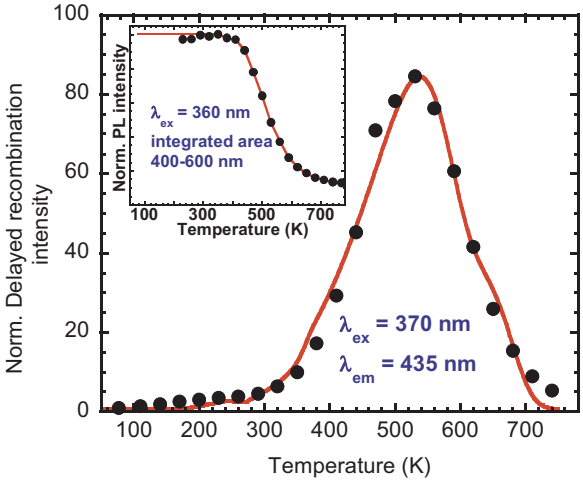

Fig. 6. Delayed recombination decay intensity as a function of temperature. Solid circles are experimental data corrected for the reduction of the Eu^{2+} emission center efficiency with temperature. Solid curve is the fit of function (5) (in the text) to the data. The parameters of the fit are: $A_1 = 1$; $E_1 = 0.25$ eV; $s_1 = 1 \times 10^{10}$ s^{-1}; $A_2 = 0.25$; $E_2 = 0.82$ eV; $s_2 = 1.5 \times 10^{12}$ s^{-1}; $A_3 = 0.08$; $E_2 = 1.2$ eV; $s_3 = 1 \times 10^{14}$ s^{-1}; $E_{ion} = 0.17$ eV. In the inset normalized PL intensity of the Eu^{2+} emission as a function of temperature.

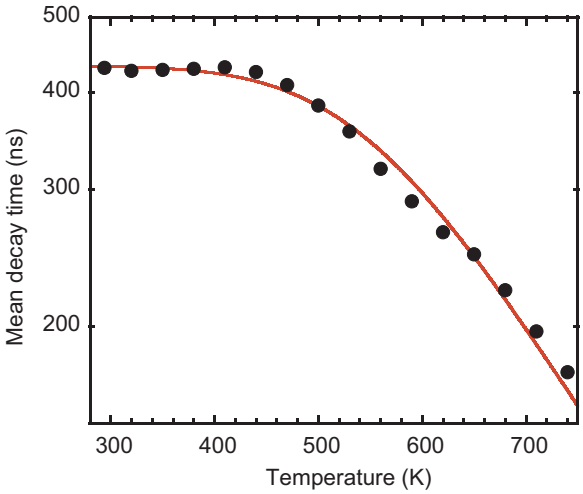

Fig. 7. Temperature dependence of PL nanosecond decay times. Solid circles are experimental data $\tau_{observed}$ reported in Ref 14. Solid line is the fit of the function $1/\tau_{observed} = 1/\tau_{rad} + K_1 \times \exp(-E_1/kT) + K_2 \times \exp(-E_2/kT)$ to the data, where k and T are the Boltzmann factor and absolute temperature, respectively, and $1/\tau_{rad} = 2.31 \times 10^6$ s^{-1}, $K_1 = 3 \times 10^6$ s^{-1}, $E_1 = 0.17$ eV, $K_2 = 1 \times 10^9$ s^{-1}, $E_2 = 0.36$ eV.

Table 1.

The detrapping time of the trap τ at the temperature T can be calculated as [22]:

$$\tau = s \times e^{E/kT}, \quad (4)$$

The values of frequency factors s and detrapping times τ at room temperature are also listed in Table 1. It is worth noting that the trap associated with the dominant TSL peak around 118 K is very shallow,

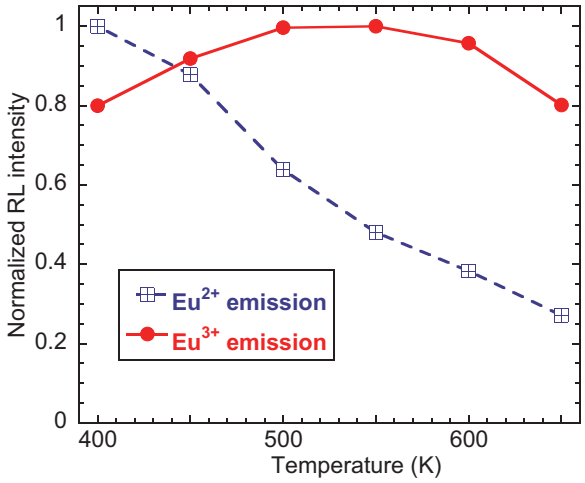

Fig. 8. Temperature dependence of RL intensity (for each center normalized to the maximum value). The intensity of Eu^{2+} and Eu^{3+}-related emissions was obtained by integration of RL spectra within 370–540 nm an 540–760 nm, respectively. Symbols are experimental data. Solid and dashed lines are only to guide the eye.

its RT detrapping time is on the order of microseconds (see Table 1), and the charge carriers released from this trap do contribute to the fast Eu^{2+} d→f light as seen from the TSL spectra in Fig. 2.

4. Study of thermal stability of the Eu^{2+} emission center

In the previous work on YAG:Eu powder [14] where various PL characteristics were reported, the temperature dependence of nanosecond decay of Eu^{2+} center manifested a speed-up with an onset at temperatures above 400 K. Such speed-up can be either due to classical thermal quenching or the thermal ionization of the emission center excited state or the participation of both. Simple barrier model provided the energy of the barrier process of 0.355 eV.

Thermal quenching or reduction of PL efficiency of the emission center with temperature can be monitored by the measurement of the temperature dependence of the steady state PL intensity. In the absence of thermal quenching the intensity would remain constant. As the data in the inset of Fig. 6 show, the steady state Eu^{2+} PL intensity starts to be quenched at about 400 K.

To determine whether thermal ionization of the Eu^{2+} center excited state might also play a role in a thermal stability of the center we performed the delayed recombination decay measurement. The technique consists in monitoring the slow tails in the PL decay due to thermal ionization of the emission center resulting in the release of the charge carrier into conduction or valence bands, its trapping at the localized trap state present in the band gap and returning back to emitting center at later times. The observation of temperature dependent delayed recombination signal confirms the presence of the thermal ionization of the emission center excited state. The technique is described in detail in [29,30]. The delayed recombination decay of YAG:Eu was measured under microsecond xenon flashlamp excitation from 77 to 740 K. At each temperature the sample was excited by the 370 nm light. The decay of the emitted light was recorded in a 0–5 ms time window. The entire measurement with repetitive excitation and signal accumulation lasted 10 min. Each data point (solid circles in Fig. 6) was obtained by integrating the recorded signal in a time interval of 10 μs to 5 ms and corrected for thermal quenching of the Eu^{2+} emission center (see below).

Temperature dependence of the delayed recombination intensity can be expressed by a formula introduced in [31] where the thermal escape of the charge carriers into the conduction or valence bands given by a Boltzmann factor is modulated by a function representing the role of traps involved in the process of retrapping the carrier by an emission

center:

$$I_{DR}(T) = we^{-\frac{E_{ion}}{kT}} \sum_{k=1}^{n} A_k \left[e^{-\frac{t_b}{\tau(E_k)}} - e^{-\frac{t_e}{\tau(E_k)}} \right], \quad (5)$$

where T, w, E_{ion} and k are the temperature, pre-exponential factor, ionization energy, and Boltzmann constant, respectively. In addition, A_k is the amplitude of the trap with depth E_k and detrapping time τ (E_k), n the number of traps of various kinds participating in the process. The amplitude A_k is proportional to the number of traps of the same kind contributing to the delayed recombination signal.

The model (5) was successfully applied to experimental data of $Lu_2Si_2O_7:Pr^{3+}$ single crystal [31] as well as the $SrHfO_3:Ce^{3+}$ powder [32]. Since the model does not take into account possible reduction of PL efficiency of the luminescence center, the measured data of the delayed recombination intensity needed to be corrected accordingly. The correction factor is determined from the measurement of the temperature dependence of the steady state intensity reported in the inset of Fig. 6.

Some trap parameters entering the formula (5) were determined by TSL analysis in the previous section. One has to bear in mind though what was pointed out above. The observed principal TSL peaks (besides that at 118 K) and corresponding traps more likely correspond to the hole traps associated with recombination at Eu^{3+} centers. The TSL peaks corresponding to electron traps with associated recombination at Eu^{2+} center might be somewhat masked and therefore their parameters might differ from those reported in Table 1 for T above 200 K.

We succeeded to obtain a satisfactory fit of the temperature dependence of delayed recombination intensity (solid line in Fig. 6) by consideration of the role of three traps and ionization energy of about 0.17 eV. The first trap corresponds to the 118 K peak, the second to the peak located in the region above 200 K masked by dominant 212 K and 274 K peaks due to hole traps and the third deeper trap would correspond to the peak falling in the region where due to low TSL signal the parameters of the traps could not be determined.

Activation energy of thermal ionization process is different from that found by considering the single barrier quenching process in Ref. [14]. This finding indicates, that thermal stability of the Eu^{2+} emission center is affected by both classical thermal quenching and thermal ionization of the Eu^{2+} excited state. We revisited the fit of temperature dependence of nanosecond decay times reported in [14]. It turns out that the same quality of the fit (see Fig. 7) is obtained by considering two barrier processes with activation energies 0.17 eV (thermal ionization) and 0.36 eV (classical thermal quenching).

Thermal ionization of the excited state of the Eu^{2+} centers is accompanied by formation of Eu^{3+} centers. This is manifested by the increase of Eu^{3+} emission intensity between 400 and 550 K at the expense of Eu^{2+} emission intensity in the RL spectra (see Fig. 8). The reduction of the Eu^{3+} RL intensity above 550 K is possibly due to thermal quenching of Eu^{3+} center itself.

5. Conclusion

Our TSL study demonstrates that several trapping states are present in YAG:Eu. They give rise to three principal TSL peaks at 118, 212 and 274 K. The peak at the lowest temperature corresponds to an electron trap and released charge carriers recombine at Eu^{2+} centers. Two higher temperature peaks correspond to hole traps and released charge carriers recombine at Eu^{3+} centers. By the initial rise technique we determined characteristic parameters of these tarps. The participation of quantum tunneling of charge carriers between the traps and recombination centers in charge carrier recombination was manifested up to about 265 K.

Study of thermal stability of Eu^{2+} emission center demonstrates that the onset of thermal quenching at about 400 K is due to both classical thermal quenching and thermal ionization of the Eu^{2+} excited state. The latter was monitored by delayed recombination decay measurements. Temperature dependence of the delayed recombination intensity was satisfactorily modeled by previously determined formula that takes into account the role of traps participating in the delayed recombination process.

Acknowledgements

Financial support of the Czech Science Foundation projects no. 15-18300Y and 17-06479S are gratefully acknowledged.

References

[1] C.D. Brandle, J. Cryst. Growth 264 (2004) 593.
[2] M.J. Weber, Solid State Commun. 12 (1973) 741.
[3] R. Autrata, P. Schauer, Jos Kvapil, J. Kvapil, J. Phys. E 11 (1978) 707.
[4] M. Moszynski, T. Ludziewski, D. Wolski, W. Klamra, L.O. Norlin, Nucl. Instrum. Methods Phys. Res. A 345 (1994) 461.
[5] M. Nikl, A. Yoshikawa, Adv. Opt. Mater. 3 (2015) 463.
[6] A.A. Setlur, W.J. Heward, M.E. Hannah, U. Happek, Chem. Mater. 20 (2008) 6277.
[7] V. Bachmann, C. Ronda, A. Meijerink, Chem. Mater. 21 (2009) 2077.
[8] V. Tucureanu, A. Matei, A.M. Avram, Opto-Electron. Rev. 23 (2015) 239.
[9] M.J. Lee, S.H. Park, Y.H. Song, E.K. Ji, U.B. Humayoun, D.B. Lee, D.H. Yoon, Mater. Lett. 161 (2015) 708.
[10] X. Shen, D.F. Zhang, X.W. Fan, G.S. Hu, X.B. Bian, L. Yang, J. Mater. Sci. -Mater. El. 27 (2016) 976.
[11] J. Huang, X.L. Hu, J.J. Shen, D.L. Wu, C.F. Yin, R. Xiang, C. Yang, X.J. Liang, W.D. Xiang, CrystEngComm 17 (2015) 7079.
[12] Y. Jia, Y. Huang, Y. Zheng, N. Guo, H. Qiao, Z. Qi, W. Lv, H. You, J. Mater. Chem. 22 (2012) 15146.
[13] Y. Qiang, Y. Yu, G. Chen, J. Fang, J. Lumin. 172 (2016) 105.
[14] L. Havlak, J. Bárta, M. Buryi, V. Jarý, E. Mihóková, V. Laguta, P. Boháček, M. Nikl, J. Phys. Chem. C 120 (2016) 21751.
[15] S. Ye, F. Xiao, Y.X. Pan, Y.Y. Ma, Q.Y. Zhang, Mater. Sci. Eng.: Rep. 71 (2010) 1.
[16] Y.-C. Lin, M. Karlsson, M. Bettinelli, Top Curr. Chem. (Z) 374 (2016) 21.
[17] V. Jarý, L. Havlák, J. Bárta, M. Buryi, E. Mihóková, M. Rejman, V. Laguta, M. Nikl, Materials 8 (2015) 6978.
[18] L. Havlak, V. Jary, J. Barta, M. Buryi, M. Rejman, V. Laguta, M. Nikl, Mater. Des. 106 (2016) 363.
[19] R. Yokota, J. Phys. Soc. Jpn. 23 (1967) 129.
[20] D.J. Lowers, T. Takizawa, C. Hidaka, E. van der Kolk, J. Appl. Phys. 111 (2012) 093709.
[21] E. Mihóková, M. Nikl, J.A. Mareš, A. Beitlerová, A. Vedda, K. Nejezchleb, K. Blažek, C. D'Ambrosio, J. Lumin. 126 (2007) 77.
[22] S.W.S. Mc Keever, Thermoluminescence of Solids, Cambridge University Press, Cambridge, 1985.
[23] M. Nikl, A. Vedda, M. Fasoli, I. Fontana, V.V. Laguta, E. Mihóková, J. Pejchal, J. Rosa, K. Nejezchleb, Phys. Rev. B 76 (2007) 195121.
[24] E. Mihóková, V. Babin, K. Bartosiewicz, L.S. Schulman, V. Čuba, M. Kučera, M. Nikl, Opt. Mater. 40 (2015) 127.
[25] A. Vedda, M. Fasoli, M. Nikl, V.V. Laguta, E. Mihóková, J. Pejchal, A. Yoshikawa, M. Zhuravleva, Phys. Rev. B 80 (2009) 045113.
[26] E. Mihóková, M. Fasoli, F. Moretti, M. Nikl, V. Jarý, G. Ren, A. Vedda, Opt. Mater. 34 (2012) 872.
[27] E. Mihóková, V. Jarý, L.S. Schulman, M. Nikl, IEEE Trans. Nucl. Sci. 61 (2014) 257.
[28] D.J. Robbins, B. Cockayne, J.L. Glasper, B. Lent, J. Electrochem. Soc. 126 (1979) 1213.
[29] J. Pejchal, M. Nikl, E. Mihóková, J.A. Mareš, A. Yoshikawa, H. Ogino, K.M. Schillemat, A. Krasnikov, A. Vedda, K. Nejezchleb, V. Múčka, Pr^{3+} -doped complex oxide single crystal scintillators, J. Phys. D: Appl. Phys. 42 (2009) 055117.
[30] E. Mihóková, M. Nikl, Meas. Sci. Technol. 26 (2015) 012001.
[31] M. Fasoli, A. Vedda, E. Mihóková, M. Nikl, Phys. Rev. B 85 (2012) 085127.
[32] E. Mihóková, V. Jarý, L.S. Schulman, M. Nikl, Phys. Status Solidi RRL 7 (2013) 228.

Chemical Physics Letters 578 (2013) 66–69

Contents lists available at SciVerse ScienceDirect

Chemical Physics Letters

journal homepage: www.elsevier.com/locate/cplett

Quantum tunneling and low temperature delayed recombination in scintillating materials

E. Mihóková [a,*], L.S. Schulman [b], V. Jarý [a], Z. Dočekalová [c], M. Nikl [a]

[a] Institute of Physics, Acad. of Sciences of the Czech Rep., Cukrovarnická 10, 162 53 Prague 6, Czech Republic
[b] Physics Department, Clarkson University, Potsdam, NY 13699-5820, USA
[c] Czech Technical University, Trojanova 13, 120 00 Prague 2, Czech Republic

ARTICLE INFO

Article history:
Received 11 April 2013
In final form 31 May 2013
Available online 13 June 2013

ABSTRACT

We study the origin of the low temperature contribution to delayed recombination decay in scintillating materials. This contribution represents the loss of fast scintillation light even at the lowest temperatures. The possible role of quantum effects, as previously suggested, is tested both experimentally and theoretically. The experiments were performed on $Lu_2Si_2O_7:Pr^{3+}$ crystals. The results suggest that quantum tunneling between the luminescence center and a nearby defect is a good candidate for explaining the observed phenomena.

1. Introduction

An important factor that can significantly deteriorate scintillator performance or at least reduce the temperature range of its practical use is the thermal ionization of the luminescence center. There are several experimental techniques that enable the study of the thermal ionization of the excited state of a luminescence center and the determination of the activation energy of the process. Conventional photoconductivity measurements can only be applied for single crystalline bulk materials. 'Contactless' methods that one can also apply to materials in powder form include the microwave resonator technique [1,2], or two independent techniques, recently developed, using purely optical means. The first consists of the study of thermally stimulated luminescence (TSL) after UV illumination [4,5]. The second lies in the analysis of the delayed recombination decay.

The delayed recombination decay method is based on the fact that when the luminescent center is thermally ionized after excitation, charge carriers that do not decay promptly can migrate through the conduction (or valence) band, be recaptured by the center, and recombine there at later times. Before recapture by the center, the charge carrier can be trapped by defects in the host material which delay its recombination at the luminescence center. Delayed recombination can be observed as a slow tail in the decay after the direct excitation of the luminescence center. The experimental implementation of the method is described in detail in [3]. A theoretical model of the temperature dependence of the time-integrated delayed recombination decay intensity due to thermal ionization based on the role of traps was given in [4]. It assumed a discrete trap distribution that is usually considered in single crystal materials and successfully fit experimental data obtained for $Lu_2Si_2O_7:Pr^{3+}$ (LPS:Pr^{3+}) single crystals. Generalization of the model for any kind of trap distribution function was made in [6]. Applicability of the model to powder materials has been successfully tested for $SrHfO_3$ [6].

Several issues were addressed in [6]. The theoretical formula describing the temperature dependence of the time-integrated delayed recombination decay intensity (due to thermal ionization of the excited state luminescence center) has a zero low temperature limit. However, experimental results indicate that at temperatures around 150 K, where one no longer expects a significant delayed recombination signal (due to the absence of thermal ionization at such low temperatures), there is still an easily detectable contribution [4,6–8]. Furthermore, a successful fit of the model mentioned above to the low temperature delayed recombination data included an unspecified additive constant. All this points to the fact that there is a temperature-independent contribution to delayed recombination decay that is not due to thermal ionization. One candidate for explaining this independent mechanism is quantum tunneling between the luminescence center and a nearby trap. A quantum or thermally-assisted tunneling process is a phenomenon that seems to be rather frequently applied to explain certain other characteristics of luminescence and scintillating materials [9–13].

In this letter we provide support for the trap-tunneling hypothesis, both experimental and theoretical. First, for the LPS:Pr^{3+} single crystal, where, in the range 200–500 K, the delayed recombination intensity was successfully fit by a theoretical formula [4,6], we measure contributions to the delayed recombination in the low temperature limit. These are lower temperatures than had previously been measured, and indeed we find that the delayed

* Corresponding author. Fax: +420 2 312 3184.
E-mail address: mihokova@fzu.cz (E. Mihóková).

0009-2614/$ - see front matter © 2013 Elsevier B.V. All rights reserved.
http://dx.doi.org/10.1016/j.cplett.2013.05.070

recombination is non zero and practically constant. Second, we set-up a simple one-dimensional model of quantum tunneling between the luminescence center and a nearby defect to show that it can produce a delay in the luminescence decay of several orders of magnitude, as experimentally seen.

2. Experimental results

An LPS:Pr^{3+} single crystal of dimensions ø 20×40 mm was grown in SIC CAS, Shanghai, China by the Czochralski method using an Ir crucible [14]. The Pr^{3+} concentration in the melt was 0.5 at.%. A plate of about $7 \times 7 \times 1$ mm was cut from the top of a parent boule and polished to optical grade. Photoluminescence (PL) measurements were performed by a custom made 5000 M Horiba Jobin Yvon spectrofluorometer. PL delayed recombination decays were excited by a microsecond xenon flashlamp and measured using the multichannel scaling method. Temperature between 8 and 217 K was controlled by a Janis Instruments closed cycle refrigerator.

In Figure 1 we display new data on the delayed recombination intensity of an LPS:Pr^{3+} single crystal in the temperature range 8–217 K. To complete the picture, in the inset we reproduce the data and the fit to the theoretical model from [4]. In the fitting procedure an additive constant was included (as well as in [6]) so as to reproduce the data around 200 K. Our new low temperature data confirm that a significant, detectable delayed recombination signal survives down to 8 K, where undoubtedly there cannot be any contribution from thermal ionization. Furthermore, within the observed interval 8–217 K this delayed signal can be, to a good approximation, considered constant. In particular the slight variation is to be compared to the intensity changes of several orders of magnitude in the interval 200–500 K (cf. the inset in Figure 1). Preliminary low temperature data in other materials confirm this conclusion in that even less variation is observed. In other words, a steady, non-thermal, level has been reached. These characteristics support the hypothesis [6] that the low temperature contribution to delayed recombination signal is due to quantum tunneling.

3. The model

In this section we investigate whether quantum effects could indeed be responsible for the low temperature delayed recombination observed above. We also consider whether this could explain

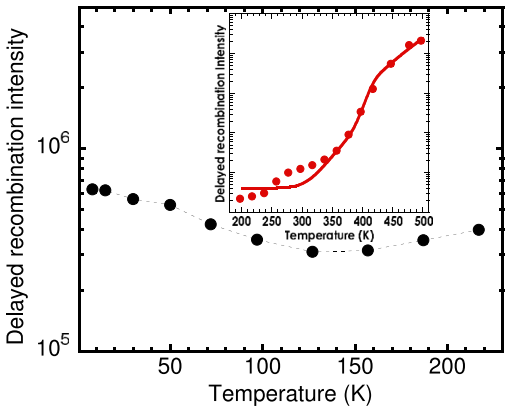

Figure 1. Temperature dependence of the delayed recombination intensity of LPS:Pr^{3+} emission; λ_{exc} = 240 nm, λ_{em} = 305 nm. Luminescence decay was integrated in the range from 50 μs to 600 s. (The dashed line is only to guide the eye.) In the inset, for comparison, we reproduce part of Fig. 8 from [4] where the data were obtained under identical experimental conditions. The solid circles are the experimental data and the fit is the solid line.

similar observations in the other materials we have mentioned, where some indication of such a low temperature signal has already been experimentally noted. These materials would have a luminescence center, an activator, (typically Ce^{3+} or Pr^{3+} ion) embedded in some oxide (perovskite, silicate or garnet) matrix. The temperature would be low enough that the probability of thermal ionization of the excited state of the luminescence center is negligible. Therefore electrons in the excited state of the luminescence center cannot reach the conduction band; they can however, be caught in nearby traps.

The presumed scenario is as follows: The emitting center, activator, begins in its ground state and is excited by a flash of light that drives it to its excited state. One can think of Ce^{3+} as the activator and its 4f and 5d states as the ground and excited states. Most electrons immediately decay on a time scale of tens of nanoseconds. Some, however, meander into the trapping states within the material band gap. There they remain for a period considerably longer than tens of ns; when they return to the Ce^{3+} they lead to delayed recombination. The pattern of this late-luminescence is sometimes exponential, sometimes more complicated, perhaps resembling a power law, depending on the matrix and the emitting center. We note that we cannot determine experimentally the relative number of fast (ns) photons to slow (delayed) photons, since these two-fast and slow light—are monitored by very different experimental techniques.

In our scenario (see the scheme in Figure 2a), the electron tunnels from the activator into a nearby trap. In principle the trap energy can be higher or lower than that of the excited activator state. However, we deem it more likely that it be lower. For long-term processes energy conservation would prevent the trapping, a problem that can be avoided for lower energies through non-radiative decay. Once in the trap, the electron can tunnel back. As we show below this—in principle—time dependent process, will be handled using time-independent wave functions, in particular through the extent that the idealized trap eigenstate spills into the activator region. But not all amplitude in the activator can lead to decay, because of selection rules. Note also that with a trap energy that differs from that of the activator excited state, the photon that is ultimately emitted will not have precisely the same energy as if it came from the activator excited state. In practice though, if the energy difference is small, our apparatus would not note the change.

We show that this model can quantitatively lead to the observed phenomena. The one-dimensional model is of the form $H = p^2/2m + V(x)$, with m the electron mass and $V(x)$ a potential with the following qualitative form: The trap is a region of attraction some distance (a few Å) from the activator. The activator itself

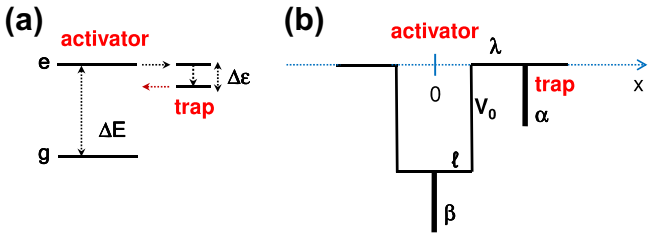

Figure 2. (a) Simple scheme for a tunneling process between the activator, with the ground state g and excited state e, and the trap located nearby. The energy separation between the ground and excited state of the activator is ΔE while that of the excited state of the activator and the trap state is $\Delta\varepsilon$. (b) The one-dimensional potential used in our numerical calculations (Section 5). The activator is placed at the origin (0) and V_0, ℓ, β, are the depth and half-width of the square as well as the strength of delta function representing the region of attraction of the activator, while α is the strength of delta function representing the region of attraction of the trap; $\lambda + \ell$ is thus the distance of the trap from the center of the activator.

has a region of attraction set up in such a way that the energy separation between its ground state and first excited state approximate that known for Ce^{3+} or Pr^{3+} ions in oxide hosts. The form of potential (cf. Section 5) together with the definition of parameters that we considered in this work is shown in Figure 2b. However, whatever potential one takes, the one-dimensional model exaggerates the tunneling effect because, unlike 3 dimensions, the wave function does not spread. Partly we will compensate for this effect by use of a geometrical factor, but a more accurate calculation will demand full dimensionality.

The amplitude of the electron 'in the trap' that enters the region of the activator is like any electron amplitude there and is subject to a (quantized) electromagnetic field that can drive it to the ground state. However, as indicated it must satisfy selection rules, which in one dimension we take to be the requirement of a parity change. We therefore calculate the probability of finding the trap electron actually in the activator region and having its parity opposite to that of the ground state. We further multiply this probability by a geometrical factor that accounts for the use of a one dimensional model for a three-dimensional situation. Finally, the three-dimensional probability is multiplied by the usual decay rate for excited-to-ground state decay to get an effective decay rate for the electron from this trap. The use of this rate is justified by the fact that the trap energy is not much below the excited state of the activator, so that electromagnetic transition matrix elements should be about the same.

In general there may be several traps near the activator. If all are about the same distance and depth relative to the activator, there will be a single exponential decay, albeit with an exponential slower than the direct recombination rate. If there is a variety of distances and depths the different decays will be incoherent with one another and the overall decay profile will be a sum of many exponentials, leading, as shown by Huntley [13], to the possibility of apparent power law decay.

The parameters determine the trap energy, the ground and excited states of the activator and the distance between trap and activator. We pick these values so that the trap energy is a bit below the excited state of the activator. The distance is varied and is on the scale of a few Angstroms, reflecting the dimensions in the relevant substances.

4. Theory

The electron without an electromagnetic field follows the time-independent Schrödinger equation:

$$-\eta\partial_x^2\psi + V\psi = E\psi, \tag{1}$$

where $\eta = \frac{\hbar^2}{2m}, \partial_x = \frac{\partial}{\partial x}$, and we will eventually define $v = V/\eta$. This will be solved numerically. The general form of V has two regions of attraction, one for the activator, one for the trap. The activator has a ground state and an excited state of opposite parity.

This was solved by discretizing on the line. The eigenvalues and eigenvectors are found by numerical diagonalization of the discretized matrix for H. We look only at the 3 lowest eigenfunctions. Depending on the parameters used, it can be difficult to distinguish the wave function located in the trap from those associated with the ion. Our selection looked for that wave function with the largest value of $\langle\psi|x|\psi\rangle$ and called this the trap state, ψ_T, since we are taking the trap to the right of (relatively positive with respect to) the activator. After that the lowest energy state was the state of even parity, ψ_E, and finally the third, nominally odd, state ψ_O. For all parameter sets reported below there were only 3 bound states.

In the physical Hamiltonian there appears the quantized electromagnetic field whose effect is to allow transitions to the ground state with the emission of a photon. Such transitions however obey selection rules and to lowest order require changes in angular momentum by 1, hence a change of parity. Furthermore these transitions will only take place in the vicinity of the activator, where there is a ground state to go to. Therefore our calculation of the amplitude for transition looks at the antisymmetric component of ψ_T in the vicinity of the activator.

The usual decay rate from the excited state of the activator has the following form:

$$\Gamma_0 = C\cdot\left|\langle\psi_{\text{ground}}\psi_\gamma|a^\dagger x|\psi_{\text{excited}}\rangle\right|^2, \tag{2}$$

where 'C' is a number that includes factors of π, density of states, energy denominators and the like, and ψ_γ is the created photon.

An electron that is principally in the trap will nevertheless have a wave function with a non-zero tail that extends into the region of the activator. The odd parity portion of this piece of wave function will allow a transition to the activator ground state with the emission of a photon. We assume that since the energy of the trap state is not very different from that of the excited state, transition amplitudes should be about the same. Comparing to Eq. (2), the difference would be the replacement of ψ_O by the odd portion of ψ_T. There will also be small difference in energy denominators, but we ignore this. Within the ion, the odd portion of ψ_T should resemble ψ_O. As a consequence, the reduction R in decay rate should be simply the norm of the odd component of ψ_T, namely

$$R = \int_{\text{region of ion}}\left|\frac{1}{2}(\psi_T(x)-\psi_T(-x))\right|^2 dx \tag{3}$$

In one dimension all amplitude from the trap must go either left or right. In three dimensions the wave function tends to spread, so that the one-dimensional model tends to enhance the likelihood of returning to the activator. We introduce a geometrical factor G that will partially compensate for this effect.

The simplest way to deal with this is to imagine that the activator is actually 3-dimensional and spherically symmetric. Then one can calculate the solid angle subtended by the activator as seen from the center of the trap. We then take the ratio of this to *all* solid angles. This ratio, G, is

$$G = \frac{\pi\ell^2}{4\pi(\ell+\lambda)^2}. \tag{4}$$

The decay rate is calculated by combining the pieces.

Eq. (2) applies in one dimension. As discussed above, in 3 dimensions the amplitude spreads out and to use the one-dimensional result one should take this fact into account. The final result is therefore

$$\begin{aligned}\Gamma &= G\times R\times\Gamma_0\\ &= \frac{\pi\ell^2}{4\pi(\ell+\lambda)^2}\times\int_{\text{region of ion}}\left|\frac{1}{2}(\psi_T(x)-\psi_T(-x))\right|^2 dx\times\Gamma_0.\end{aligned} \tag{5}$$

5. Numerical results

The form of the Hamiltonian used in our numerical work is a discretized version of

$$H = -\eta\,\partial_x^2 - \beta\delta(x) - V_0\theta(\ell-|x|) - \alpha\delta(x-\ell-\lambda), \tag{6}$$

with $V_0, \alpha, \beta, \lambda$ constants.

Figure 3 presents the wave functions for the following parameter values: $\lambda = 20$ Å, $\ell = 2.2$ Å, $\beta = 3.9$ eV, $\alpha = 1.6$ eV and $V_0 = 2.5$ eV. The range of x is $[-50, 50]$, in steps of 0.001. For these values, the energies are $\Delta E = 3$ eV, $\Delta\varepsilon = 70$ meV. The reduction in decay rate is about 3×10^{-6}. This rate reduction implies a lifetime

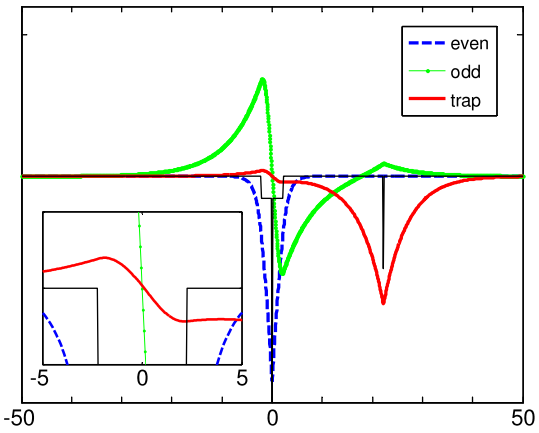

Figure 3. Wave functions. A rescaled version of the potential is also shown. The solid (red) is the trap wave function, the dashed (blue) the even state and the dotted (green), the odd. The parameter values are given in the text. In the inset is the detail of the trap wave function in the region of the activator. (For interpretation of the references to colour in this figure legend, the reader is referred to the web version of this article.)

on the order of 10 ms (provided that the prompt lifetime is on the order of tens of ns, which is typical for Ce^{3+} and Pr^{3+} in oxide hosts). This delayed lifetime extends the usual lifetime by six orders of magnitude.

We find these results encouraging in that our initial expectation was that tunneling would be much too small. The contrary seems to be the case and the times we get are consistent with the delayed recombination seen experimentally. Nevertheless, we view the one-dimensional calculation only as a proof of principle and expect greater reliability, as well as insights, for a full 3 dimensional calculation (which may be reduced to two, using azimuthal symmetry).

6. Conclusion

In the present work we exhibited experimental results showing residual delayed recombination even at the lowest of temperatures. We then showed that quantum tunneling is a likely source of that low temperature signal. Such a signal has been observed in the delayed recombination decay of several scintillating materials. Our work is thus both experimental and theoretical. In particular, the experimental data showed delayed recombination at low temperature for LPS:Pr, a signal that was well within the range of detectability and is practically constant as a function of (low) temperature. This is consistent with the temperature independence of the quantum tunneling process. Numerical calculations using a simple one-dimensional model of quantum tunneling between the trap and luminescence (recombination) center showed a delay of the decay by several orders of magnitude, which is the delay observed in experiment.

Our results help understand the origin of temperature independent losses of fast scintillation light. Since such losses do not seem to be infrequent, this finding may serve as the first step in future technological attempts to prevent them.

Acknowledgement

This work was supported by the project M100101212 of the Academy of Sciences of the Czech republic.

References

[1] M.F. Joubert, S.A. Kazanski, Y. Guyot, J.C. Gâcon, C. Pedrini, Phys. Rev. B 69 (2004) 165217.
[2] H. Loudyi, Y. Guyot, J.C. Gâcon, C. Pedrini, M.F. Joubert, J. Lumin. 127 (2007) 171.
[3] J. Pejchal et al., J. Phys. D: Appl. Phys. 42 (2009) 055117.
[4] M. Fasoli, A. Vedda, E. Mihóková, M. Nikl, Phys. Rev. B 85 (2012) 085127.
[5] E. Mihóková, V. Jarý, M. Fasoli, A. Lauria, F. Moretti, M. Nikl, A. Vedda, Chem. Phys. Lett. 556 (2013) 89.
[6] E. Mihóková, V. Jarý, L.S. Schulman, M. Nikl, Phys. Status Solidi RRL 7 (2013) 228.
[7] H. Feng et al., J. Appl. Phys. 108 (2010) 033519.
[8] M. Nikl, G. Ren, D. Ding, E. Mihóková, V. Jarý, H. Feng, Chem. Phys. Lett. 493 (2010) 72.
[9] P. Avouris, T.N. Morgan, J. Chem. Phys. 74 (1981) 4347.
[10] M. Nikl et al., IEEE Trans. Nucl. Sci. 55 (2008) 1035.
[11] A. Vedda et al., Phys. Rev. B 78 (2008) 195123.
[12] E. Mihóková et al., Opt. Mater. 34 (2011) 228.
[13] D.J. Huntley, J. Phys. Condens. Matter 18 (2006) 1359.
[14] H. Feng, D. Ding, H. Li, S. Lu, S. Pan, X. Chen, G. Ren, J. Appl. Phys. 103 (2008) 083109.

Low Temperature Delayed Recombination Decay in Complex Oxide Scintillating Crystals

E. Mihóková, V. Jarý, L. S. Schulman, and M. Nikl

***Abstract*—We study the low temperature contribution to delayed recombination decay in several complex oxide scintillating crystals. We experimentally test the previously suggested hypothesis that the losses of fast scintillation light even at the lowest temperatures can be due to quantum effects. The results obtained for several material systems confirm that quantum tunneling between the luminescence center and a nearby defect is a good candidate for the origin of the observed phenomena.**

***Index Terms*—Luminescence, oxides, scintillator, tunneling.**

I. Introduction

SOME applications of scintillating materials require their fast response. Loss of fast scintillation light is a highly undesired phenomenon that deteriorates a scintillator's performance. One of the factors responsible for such a loss is thermal ionization of the luminescence center excited state. Temperature independent losses of fast scintillation light are less intuitive. Nevertheless, according to observations provided by the experimental technique of delayed recombination decay they do not seem infrequent and have recently been addressed [1].

Delayed recombination decay measurement was developed [2] as an alternative experimental technique enabling observation and quantitative evaluation of thermal ionization of the luminescence center [1], [3]. As opposed to conventional photoconductivity using blocking electrodes [4] or the microwave resonator technique [5], [6], it is a purely optical method. It is based on the observation of slow tails in the luminescence decay under UV excitation. When the luminescence center is thermally ionized, charge carriers that do not decay promptly can migrate through conduction or valence bands and after being trapped and released they return to the luminescence center and recombine producing delayed (slow) light.

Experimental results together with theoretical evaluation [1] indicated that at low enough temperatures where one no longer expects a detectable delayed recombination signal (due to the absence of thermal ionization) there is still a contribution that seems temperature independent. It was hypothesized as due to quantum tunneling between the luminescence center and a nearby trap [1]. The charge carrier, as in scheme in Fig. 1, would tunnel from an activator to a nearby trap and back. Recently we set up a simple one-dimensional model of quantum tunneling following the scheme in Fig. 1 and showed that it indeed can produce a delay in the luminescence decay of several orders of magnitude, as experimentally seen [7].

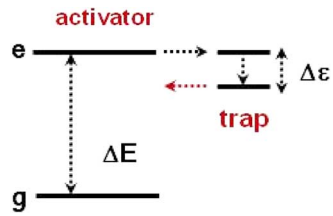

Fig. 1. Simple scheme for a tunneling process between the activator, with ground state g and excited state e, and the trap located nearby. The energy separation of the ground and excited state of the activator is ΔE while that of the excited state of the activator and the trap is $\Delta\varepsilon$.

In this work we provide extensive experimental support for the quantum tunneling hypothesis. We study delayed recombination decay in several complex oxide scintillating crystals. We observe practically constant delayed recombination decay intensity in an extended low temperature interval. These results are consistent with the temperature independence of the quantum tunneling process.

II. Samples and Experimental Details

The orthosilicate $Lu_2SiO_5 : Pr^{3+}$ and $Y_2SiO_5 : Pr^{3+}$ single crystals were grown by the micro-pulling down method using an Ir crucible [8]. The concentration of Pr^{3+} in the melt was 0.25 at%. $Lu_2SiO_5 : Ce^{3+}$ single crystal was grown by the Czochralski method in SIC CAS, Shanghai, China [9]. The concentration of Ce was 0.5 mol%. A plate of about $6 \times 8 \times 1$ mm was polished to an optical grade.

The pyrosilicate $Lu_2Si_2O_7 : Pr^{3+}$ and $Lu_2Si_2O_7 : Ce^{3+}$ single crystals were grown in SIC CAS, Shanghai, China by the Czochralski method using an Ir crucible [10]. The dopant concentration in the melt was 0.5 at%. Plates of about $7 \times 7 \times 1$ and $5 \times 5 \times 1$ mm, respectively, were cut from the top of parent boules and polished to optical grade.

$Gd_3Ga_3Al_2O_{12} : Ce^{3+}$ was grown by the Czochralski method [11]. Concentration of Ce was 1% in the melt. A plate with dimensions about $5 \times 5 \times 1$ mm was polished to an optical grade.

Photoluminescence emission (PL) and excitation (PLE) spectra were performed by a custom made 5000M Horiba Jobin

Manuscript received May 16, 2013; accepted July 15, 2013. Date of publication August 21, 2013; date of current version February 06, 2014. This work was supported by the Czech M100101212, LH12150, and LH12185 projects.

E. Mihóková, V. Jarý, and M. Nikl are with the Institute of Physics, ASCR, 162 53 Prague 6, Czech Republic (e-mail: mihokova@fzu.cz; jary@fzu.cz; nikl@fzu.cz).

L. S. Schulman is with the Physics Department, Clarkson University, Potsdam, NY 13699-5820 USA (e-mail: schulman@clarkson.edu).

Color versions of one or more of the figures in this paper are available online at http://ieeexplore.ieee.org.

Digital Object Identifier 10.1109/TNS.2013.2273974

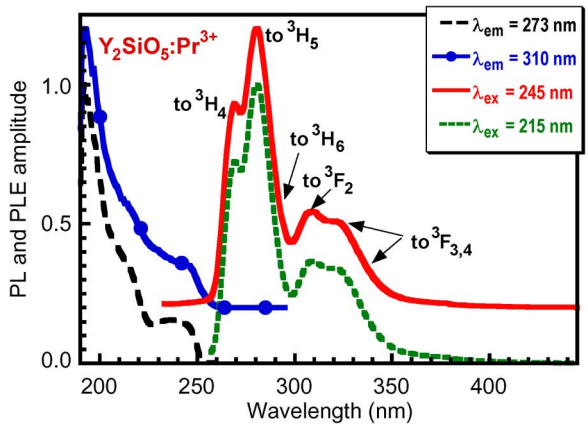

Fig. 2. Normalized PL and PLE spectra of $Y_2SiO_5 : Pr^{3+}$ at 8 K. Excitation and emission wavelengths are displayed in the legend. Excitation (emission) spectra monitored at different wavelengths are vertically shifted by 0.2.

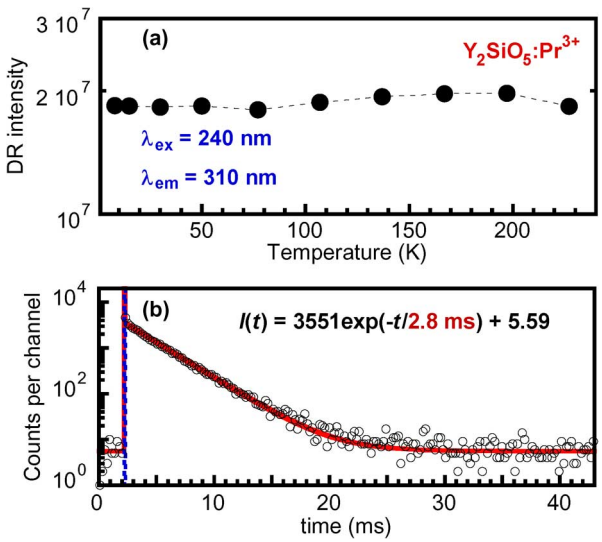

Fig. 3. In (a) delayed recombination intensity of $Y_2SiO_5 : Pr^{3+}$ as a function of temperature. Excitation and emission wavelengths are displayed in the figure. In (b) delayed recombination decay at 8 K. Empty circles are experimental data, solid line is the fit of function I(t), given in the figure, to the data.

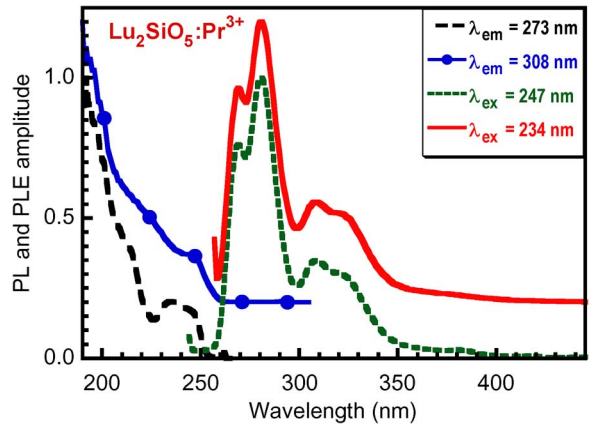

Fig. 4. Normalized PL and PLE spectra of $Lu_2SiO_5 : Pr^{3+}$ at 8 K. Excitation and emission wavelengths are displayed in the legend. Excitation (emission) spectra monitored at different wavelengths are vertically shifted by 0.2.

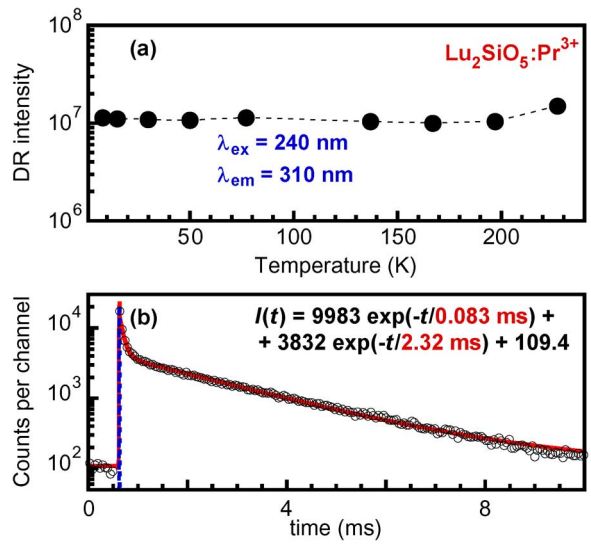

Fig. 5. In (a) delayed recombination intensity of $Lu_2SiO_5 : Pr^{3+}$ as a function of temperature. Excitation and emission wavelengths are displayed in the figure. In (b) delayed recombination decay at 8 K. Empty circles are experimental data, solid line is the fit of function I(t), given in the figure, to the data.

Yvon spectrofluorometer. Excitation was realized with a deuterium steady state lamp. PL delayed recombination decays were excited by a microsecond xenon flashlamp and measured using the multichannel scaling method. Temperature between 8–217 K was controlled by the Janis Instruments closed cycle refrigerator.

III. Results and Discussion

A. Pr^{3+}—Doped Complex Oxides

PL excitation and emission spectra of $Y_2SiO_5 : Pr^{3+}$ (YSO:Pr) measured at 8 K are displayed in Fig. 2. The PL emission between 250–350 nm contains several bands corresponding to 5d-4f transitions of Pr^{3+} (final ^3H_x and ^3F_x multiplet 4f states are well resolved as shown in Fig. 2). The lowest excitation peak at about 247 nm corresponds to a transition from the $^3H_4$ ground state to the lowest $^5d_1$ state of Pr^{3+} [2], [12].

In Fig. 3(a) we display the delayed recombination intensity of $Y_2SiO_5 : Pr^{3+}$ measured under UV excitation into the 4f-5d transition of the Pr ion within the 8–230 K temperature interval. A practically constant signal is observed in the whole temperature range. Such temperature independence of the delayed recombination intensity supports the hypothesis that quantum tunneling between the activator and nearby trap(s) would be at work in this temperature range. Fig. 4 shows an example of delayed recombination decay at 8 K. The decay is perfectly approximated by a single exponential function indicated in the figure. This result represents a nice example of a host and an activator where there is quantum tunneling between a *single* trap (or a trap of one kind) and an activator.

The results for Pr-doped lutetium oxyorthosilicate are displayed in Figs. 4 and 5. PL and PLE spectra at 8 K (Fig. 4) are similar to those of YSO:Pr. The delayed recombination intensity under UV excitation into the 4f-5d transition of Pr^{3+} ion is again constant up to 200 K (Fig. 5(a)). The delayed recombination decay at 8 K is now approximated by a double exponential. This more complex decay indicates participation of more than a single trap in the quantum tunneling process mentioned above. There is either more than one kind of trap or at least two traps of

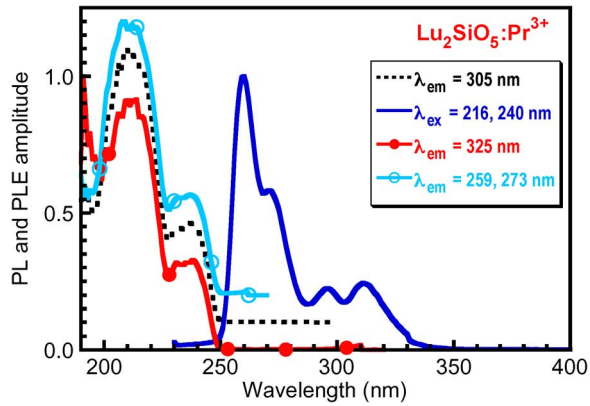

Fig. 6. Normalized PL and PLE spectra of $Lu_2Si_2O_7 : Pr^{3+}$ at 8 K. Excitation and emission wavelengths are displayed in the legend. Excitation spectra at $\lambda_{em} = 305$ nm and 259 (273) nm are vertically shifted by 0.1 and 0.2, respectively.

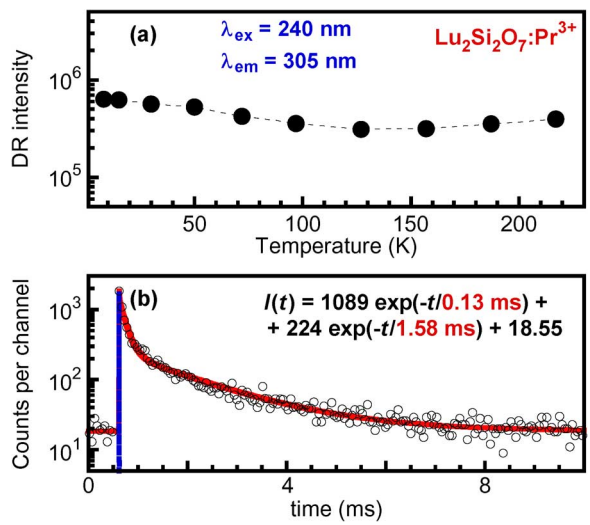

Fig. 7. In (a) delayed recombination intensity of $Lu_2Si_2O_7 : Pr^{3+}$ as a function of temperature. Excitation and emission wavelengths are displayed in the figure. In (b) delayed recombination decay at 8 K. Empty circles are experimental data, solid line is the fit of function I(t), given in the figure, to the data.

the same kind at different distances from the activator (recombination center).

PL emission spectrum of Pr-doped lutetium pyrosilicate (Fig. 6) has similar band positions to that of the above reported orthosilicates. However, the distribution of emission intensity corresponding to transitions into different final f states has changed. The delayed recombination intensity under UV excitation into 4f-5d transitions of Pr^{3+} has a practically constant signal up to about 220 K, as already reported in [7]. Here we also show an example of the delayed recombination decay at 8 K. It is more complex, similar to the above example for LSO:Pr. Namely, more traps are participating in the quantum tunneling process. It is worth noting that the participation of quantum tunneling of charge carriers between traps and Pr recombination centers in charge carrier recombination was, in this material, already manifested up to room temperature by an independent study of thermally stimulated luminescence (TSL) [13].

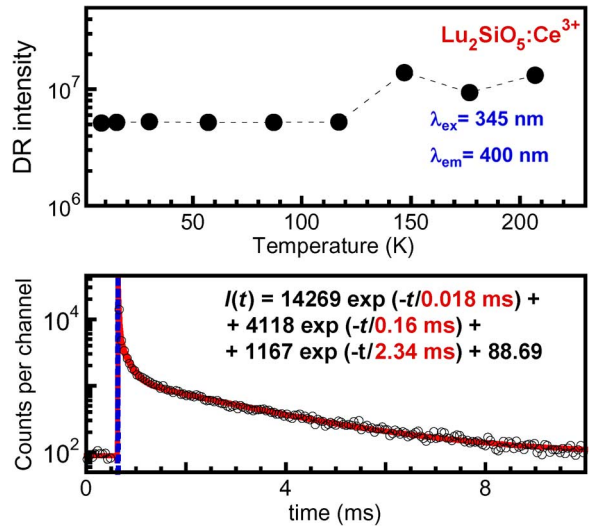

Fig. 8. In (a) delayed recombination intensity of $Lu_2SiO_5 : Ce^{3+}$ as a function of temperature. Excitation and emission wavelengths are displayed in the figure. In (b) delayed recombination decay at 8 K. Empty circles are experimental data, solid line is the fit of function I(t), given in the figure, to the data.

B. Ce^{3+}—Doped Complex Oxides

Excitation and emission spectra of $LSO : Ce^{3+}$ at 11 K for both Ce1 and Ce2 sites have been reported in [14]. We monitored delayed recombination intensity at Ce1 sites under UV excitation at the $4f - 5d_1$ transition of Ce1 ions in the temperature interval 8–220 K (Fig. 8(a)). The delayed recombination intensity is constant up to about 120 K. Again, this is likely to be due to quantum tunneling between the Ce1 ions and nearby traps. An example of delayed recombination decay measured at 8 K (Fig. 8(b)) shows even more complex decay than above, indicating participation of several traps in the quantum tunneling process.

Note that the role of thermally assisted tunneling between oxygen vacancies (electron traps) and Ce recombination centers was in this material already suggested as a mechanism explaining particular TSL features [15].

Ce-doped lutetium pyrosilicate is displayed in Figs. 9 and 10. The delayed recombination intensity under excitation to the $4f - 5d_1$ transition of Ce^{3+} (cf. Fig. 9) is constant within the whole monitored temperature range 8–230 K (Fig. 10(a)). The delayed recombination decay at 8 K shows participation of more than one trap in the quantum tunneling process.

Recently, remarkably high light yield was reported for tailored compositions of Ce-doped $(Lu, Gd)_3(Ga, Al)_5O_{12}$ single crystals grown by the micro-pulling down technique [16], [17]. This result was achieved thanks to a combination of band gap engineering and strategies for favorable $^5d_1$ Ce^{3+} level positioning by admixing Ga and Gd into the LuAG structure [18]. Optical properties of an analogous set grown by the Czochralski technique was also studied and $Gd_3Ga_3Al_2O_{12}$ (GGAG) composition showed the most favourable characteristics [19], [20]. The luminescence and scintillation mechanisms of those crystals were addressed in [21]. We measured the low temperature delayed recombination decay in this novel promising material as well. The delayed recombination decay of Ce^{3+} was measured under excitation in the $4f - 5d_1$ transition of Ce^{3+} (cf.

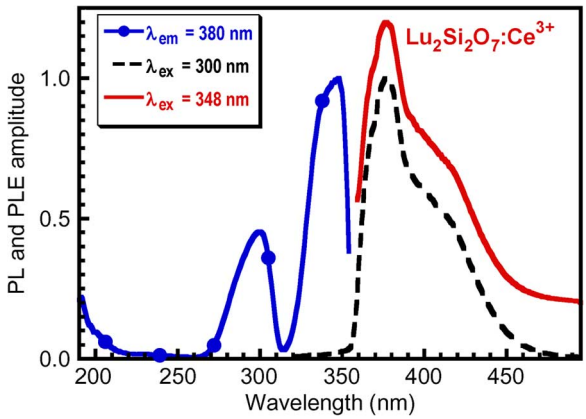

Fig. 9. Normalized PL and PLE spectra of $Lu_2Si_2O_7 : Ce^{3+}$ at 8 K. Excitation and emission wavelengths are displayed in the legend. Emission spectra monitored at different wavelengths are vertically shifted by 0.2.

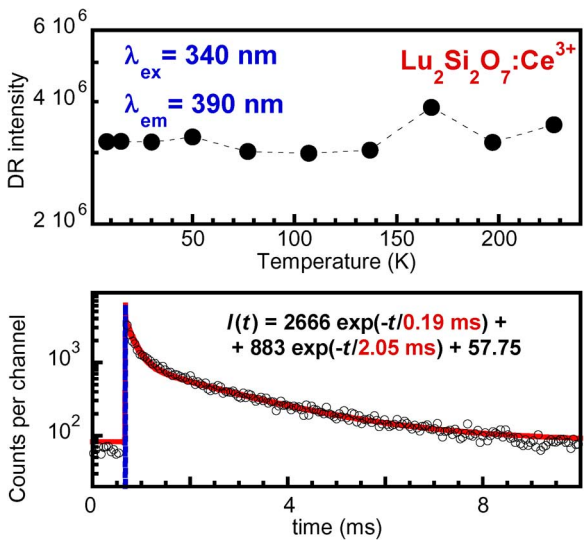

Fig. 10. In (a) delayed recombination intensity of $Lu_2Si_2O_7 : Ce^{3+}$ as a function of temperature. Excitation and emission wavelengths are displayed in the figure. In (b) delayed recombination decay at 8 K. Empty circles are experimental data, solid line is the fit of function I(t), given in the figure, to the data.

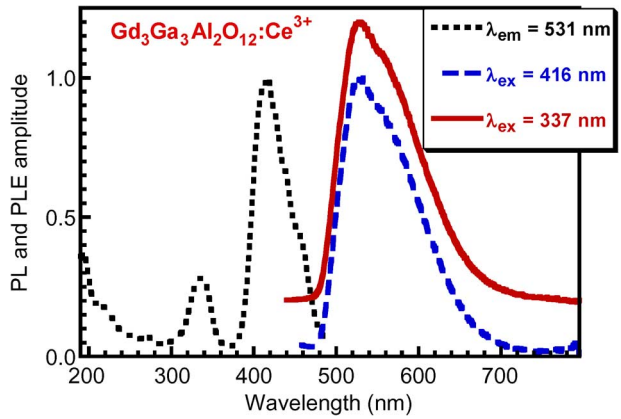

Fig. 11. Normalized PL and PLE spectra of $Gd_3Ga_3Al_2O_{12} : Ce^{3+}$ at 8 K. Excitation and emission wavelengths are displayed in the legend. Emission spectra monitored at different wavelengths are vertically shifted by 0.2.

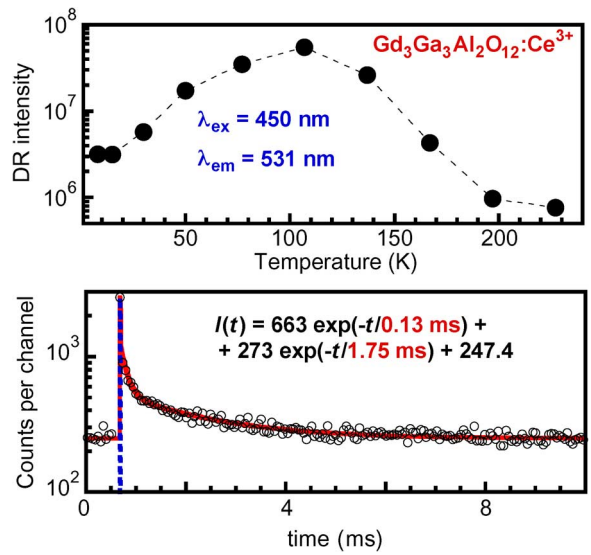

Fig. 12. In (a) delayed recombination intensity of $Gd_3Ga_3Al_2O_{12} : Ce^{3+}$ as a function of temperature. Excitation and emission wavelengths are displayed in the figure. In (b) delayed recombination decay at 8 K. Empty circles are experimental data, solid line is the fit of function I(t), given in the figure, to the data.

Fig. 11). The delayed recombination intensity was monitored within 8–230 K (see Fig. 12). The material definitely features an intense low temperature signal that does not exclude participation of quantum tunneling process as above. However, unlike in all the above materials, the signal is not constant. There is an intense peak that, at the present state of knowledge, is difficult to explain. Before hypothesizing on the origin of this particular behavior of this Ce-doped multicomponent garnet it would first be helpful to study simpler scintillating garnets like $Lu_3Al_5O_{12}$ or $Y_3Al_5O_{12}$. We note that delayed recombination decay in 5d-4f luminescence of Pr-doped $Lu_3Al_5O_{12}$ or $Y_3Al_5O_{12}$ was already studied within 77–500 K and showed practically constant intensity below room temperature [2].

IV. Conclusion

A hypothesis on the origin of the low temperature contribution to the delayed recombination decay in scintillating materials has been extensively experimentally tested. We measured delayed recombination intensity in the temperature interval from 8 to 230 K in various complex oxide crystals. Selected crystals had different lattice structures, were grown by different techniques and doped with different activators, either Ce^{3+} or Pr^{3+}, mostly used in fast scintillating materials. In all the materials studied, with the exception of GGAG:Ce, the intensity of the delayed recombination intensity was practically constant up to at least 120 K. Such temperature independence of the delayed recombination intensity correlates well with the temperature independence of quantum tunneling between the activator and nearby trap(s) that was suggested as the culprit for observed phenomena.

Single exponential delayed recombination decay of YSO:Pr proved to be a nice example of a simple process of quantum tunneling between the Pr activator and a single trap. All other materials shoving more complex delayed recombination decay correspond to a case of quantum tunneling between the activator and several traps—either more than one kind, or the traps of one

kind located at various distances from the activator. The latter could ultimately produce inverse power-law decay [22].

ACKNOWLEDGMENT

The authors would like to thank G. Ren from the Shanghai Institute of Ceramics, and A. Yoshikawa and K. Kamada from the Institute of Materials Research, Tohoku University, for providing samples for this study.

REFERENCES

[1] E. Mihóková, V. Jarý, L. S. Schulman, and M. Nikl, "Delayed recombination and excited state ionization of the Ce^{3+} activator in the $SrHfO_3$ host," *Phys. Status Solidi RRL*, vol. 7, pp. 228–231, 2013.

[2] J. Pejchal, M. Nikl, E. Mihóková, J. A. Mareš, A. Yoshikawa, H. Ogino, K. M. Schillemat, A. Krasnikov, A. Vedda, K. Nejezchleb, and V. Múčka, " Pr^{3+}-doped complex oxide single crystal scintillators," *J. Phys. D, Appl. Phys.*, vol. 42, pp. 055117(1)–055117(10), 2009.

[3] M. Fasoli, A. Vedda, E. Mihóková, and M. Nikl, "Optical methods for the evaluation of the thermal ionization barrier of lanthanide excited states in luminescent materials," *Phys. Rev. B*, vol. 85, pp. 085127(1)–085127(8), 2012.

[4] C. Pedrini, D. S. McClure, and C. H. Anderson, "Photoionization thresholds of divalent rare earth ions in alkaline earth fluorides," *J. Chem. Phys.*, vol. 70, pp. 4959–4962, 1979.

[5] M. F. Joubert, S. A. Kazanski, Y. Guyot, J. C. Gâcon, and C. Pedrini, "Microwave study of photoconductivity induced by laser pulses in rare-earth-doped dielectric crystals," *Phys. Rev. B*, vol. 69, pp. 165217(1)–165217(13), 2004.

[6] H. Loudyi, Y. Guyot, J. C. Gâcon, C. Pedrini, and M. F. Joubert, "First photoconductivity measurement following photoionization of rare-earth dopant in dielectric powder," *J. Lumin.*, vol. 127, pp. 171–175, 2007.

[7] E. Mihóková, L. S. Schulman, V. Jarý, Z. Dočekalová, and M. Nikl, "Low temperature contribution to delayed recombination in scintillating materials," *Chem. Phys. Lett.*, vol. 578, pp. 66–69, 2013.

[8] A. Novoselov, H. Ogino, A. Yoshikawa, M. Nikl, J. Pejchal, J. A. Mares, A. Beitlerova, C. D'Ambrosio, and T. Fukuda, "Study on crystal growth and luminescence properties of Pr-doped RE_2SiO_5 ($RE = Y$, Lu)," *J. Cryst. Growth*, vol. 287, pp. 309–312, 2006.

[9] L. Qin, H. Li, S. Lu, D. Ding, and G. Ren, "Growth and characteristics of LYSO ($Lu_{2(1-x-y)}Y_{2x}SiO_5 : Ce$) scintillation crystals," *J. Cryst. Growth*, vol. 281, pp. 518–524, 2005.

[10] G. H. Ren, H. Y. Li, S. Lu, D. Z. Ding, H. Feng, and G. D. Wang, "Growth and luminescence properties of lutetium pyrosilicate ($Lu_2Si_2O_7 : Ce$) scintillation crystals," *J. Synth. Cryst.*, vol. 36, pp. 967–970, 2007.

[11] K. Kamada, T. Yanagida, T. Endo, K. Tsutumi, Y. Usuki, M. Nikl, Y. Fujimoto, A. Fukabori, and A. Yoshikawa, "2 inch diameter single crystal growth and scintillation properties of $Ce : Gd_3Al_2Ga_3O_{12}$," *J. Cryst. Growth*, vol. 352, pp. 88–90, 2012.

[12] M. Nikl, H. Ogino, A. Yoshikawa, E. Mihokova, J. Pejchal, A. Beitlerova, A. Novoselov, and T. Fukuda, "Fast 5d-4f luminescence of Pr^{3+} in Lu_2SiO_5 single crystal host," *Chem. Phys. Lett.*, vol. 410, pp. 218–221, 2005.

[13] E. Mihóková, M. Fasoli, F. Moretti, M. Nikl, V. Jarý, G. Ren, and A. Vedda, "Defect states in Pr^{3+} doped lutetium pyrosilicate," *Opt. Mater.*, vol. 34, pp. 872–877, 2012.

[14] H. Suzuki, T. A. Tombrello, C. L. Melcher, and J. S. Schweitzer, "UV and gamma-ray excited luminescence of cerium-doped rare-earth oxyorthosilicates," *Nucl. Instrum. Methods Phys. Res. A*, vol. 320, pp. 263–272, 1992.

[15] A. Vedda, M. Nikl, M. Fasoli, E. Mihokova, J. Pejchal, M. Dusek, G. Ren, C. R. Stanek, K. J. McClellan, and D. D. Byler, "Thermally stimulated tunneling in rare-earth-doped oxyorthosilicates," *Phys. Rev. B*, vol. 78, pp. 195123(1)–195123(8), 2008.

[16] K. Kamada, T. Endo, K. Tsutumi, T. Yanagida, Y. Fujimoto, A. Fukabori, A. Yoshikawa, J. Pejchal, and M. Nikl, "Composition engineering in cerium-doped $(Lu, Gd)_3(Ga, Al)_5O_{12}$ single crystal scintillators," *Cryst. Growth Des.*, vol. 11, pp. 4484–4490, 2011.

[17] K. Kamada, T. Yanagida, J. Pejchal, M. Nikl, T. Endo, K. Tsutumi, Y. Fujimoto, A. Fukabori, and A. Yoshikawa, "Scintillator-oriented combinatorial search in the Ce-doped $(Y, Gd)_3(Ga, Al)_5O_{12}$ multicomponent garnet compounds," *J. Phys. D, Appl. Phys.*, vol. 11, pp. 4484–4490, 2011.

[18] M. Fasoli, A. Vedda, M. Nikl, C. Jiang, B. P. Uberuaga, D. A. Anderson, K. J. McClellan, and C. R. Stanek, "Band-gap engineering for removing shallow traps in rare-earth $Lu_3Al_5O_{12}$ garnet scintillators using Ga_{3+} doping," *Phys. Rev. B*, vol. 84, pp. 081102(1)–081102(4), 2011.

[19] P. Prusa, K. Kamada, J. A. Mares, A. Yoshikawa, and M. Nikl, "Light yield of $(Lu, Y, Gd)_3(Ga, Al)_5O_{12} : Ce$ garnets," *Radiat. Meas.* 2013 [Online]. Available: http://dx.doi.org/10.1016/j.radmeas.2013.01.055

[20] E. Mihóková, K. Vávrů, K. Kamada, V. Babin, A. Yoshikawa, and M. Nikl, "Deep trapping state in cerium doped $(Lu, Y, Gd)_3(Ga, Al)_5O_{12}$ single crystal scintillators," *Radiat. Meas.* 2013 [Online]. Available: http://dx.doi.org/10.1016/j.radmeas.2012.12.018

[21] M. Nikl, K. Kamada, S. Kurosawa, Y. Yokota, A. Yoshikawa, J. Pejchal, and V. Babin, "Luminescence and scintillation mechanism in Ce^{3+} and Pr^{3+} doped $(Lu, Y, Gd)_3(Ga, Al)_5O_{12}$ single crystal scintillators," *Phys. Status Solidi C*, vol. 10, pp. 172–175, 2013.

[22] D. J. Huntley, "An explanation of the power-law decay of luminescence," *J. Phys., Condens. Matter*, vol. 18, pp. 1359–1365, 2006.

Optical Materials 40 (2015) 127–131

Contents lists available at ScienceDirect

Optical Materials

journal homepage: www.elsevier.com/locate/optmat

Low temperature delayed recombination decay in scintillating garnets

E. Mihóková [a,*], V. Babin [a], K. Bartosiewicz [a], L.S. Schulman [b], V. Čuba [c], M. Kučera [d], M. Nikl [a]

[a] Institute of Physics, ASCR, v.v.i., Cukrovarnická 10, 162 53 Prague, Czech Republic
[b] Physics Department, Clarkson University, Potsdam, NY 13699-5820, United States
[c] Czech Technical University, FNSPE, Břehová 7, 115 19 Prague, Czech Republic
[d] Charles University, Faculty of Math. and Physics, Ke Karlovu 5, 121 16 Prague, Czech Republic

ARTICLE INFO

Article history:
Received 15 September 2014
Received in revised form 25 November 2014
Accepted 14 December 2014
Available online 5 January 2015

Keywords:
Luminescence
Garnets
Scintillator
Tunneling

ABSTRACT

We study the temperature dependence of delayed recombination decay intensity in a variety of scintillating crystals based on garnet hosts in a wide temperature range 8–500 K. Previous work on several scintillating materials based on silicate hosts showed nonzero constant signal from very low temperatures up to about 120 K. This observation supported a previously suggested hypothesis on low temperature losses of fast scintillation light due to quantum tunneling between the activator and nearby traps. In garnets, the subject of the present article, we observe practically constant signal in the entire monitored temperature range. We thus further test and confirm the quantum tunneling hypothesis in a different class of scintillating materials. We also show that there is no thermal ionization of the activator's excited state in all materials studied, well above room temperature.

1. Introduction

In applications of scintillators where fast response is required any losses of fast scintillation light are highly undesired and need to be prevented. They are usually associated with thermal effects such as classical thermal quenching of the activator's luminescence or thermal ionization of its excited state. Recently, however, using the delayed recombination decay technique, it has been observed that the losses of fast scintillation light can occur at very low temperatures where none of the above thermal effects apply [1].

Delayed recombination measurement has been developed to study thermal ionization of the luminescence center excited state [2] as an alternative to other techniques, such as photoconductivity using blocking electrodes [3], the microwave resonator technique [4] or thermoluminescence after UV excitation [5–7]. It consists in the observation of slow tails in luminescence decay under UV excitation. When the luminescence center is thermally ionized, charge carriers that do not decay promptly can migrate through conduction or valence bands. After being trapped and released they return to the luminescence center and recombine producing delayed (slow) light.

As addressed above, a nonzero delayed recombination signal was also observed at very low temperatures. These low temperature losses of fast scintillation light have been associated with quantum tunneling from the activator to a nearby trap and back, as in the scheme in Fig. 1. A similar mechanism of excitation energy or electron transfer is in the usual donor–acceptor situation also referred to as Dexter transfer, or transfer due to the exchange interaction depending on the overlap between the wave functions of the activator and the trap.

The hypothesis was supported both experimentally and theoretically. Experimentally, in a variety of Ce and Pr-doped scintillating silicates, constant delayed recombination decay intensity was measured at least up to about 120 K, a result consistent with the temperature independence of quantum tunneling [8]. Theoretical support was first provided by a simple one-dimensional model [9] that attained several orders of magnitude delay of the activator's luminescence decay due to quantum tunneling. Extending the numerical calculation to two dimensions allowed a finer check of the tunneling hypothesis, and indeed the correct orders of magnitude were again obtained. Furthermore, analytic estimates on a relation between a trap's depth and its distance from the activator have also been made [10] and are expected to allow estimates of significant properties of the traps. Unlike many calculations based on tunneling between traps and recombination centers in various materials [11–17] this approach is independent of any assumptions about "attempt frequency".

In this work we study the temperature dependence of delayed recombination decay intensity in a variety of scintillating Ce^{3+} and Pr^{3+}-doped simple garnets. These materials are considered to have significant potential in the family of fast and high light yield oxide scintillators. For this reason, experimental and theoretical aspects have been addressed by many groups in last two decades

* Corresponding author.

http://dx.doi.org/10.1016/j.optmat.2014.12.011
0925-3467/

[18–27]. The present work is intended to help understand unexplained features previously observed in a novel, more complex material, multicomponent garnet $Gd_3Ga_3Al_2O_{12}:Ce^{3+}$ (GGAG:Ce) [8]. Ultraefficient GGAG:Ce single crystal scintillator was discovered in 2011 [28] and immediately became a hot topic in the scintillator community [28–32]. We now monitor simple garnets in a broad temperature region 8–500 K and observe practically constant signal throughout. These results show that quantum tunneling between activator and nearby trap(s) is at work in another wide class of scintillating materials. Previously observed features in GGAG:Ce delayed decay are discussed in the light of results currently obtained for simple garnets.

2. Samples and experimental details

Pr^{3+}-doped $Lu_3Al_5O_{12}$ (LuAG) and $Y_3Al_5O_{12}$ (YAG) single crystals with Pr concentration in the crystal of 0.19 wt% and 0.16 wt%, respectively, were grown by the Czochralski technique from 5*N* Lu_2O_3 and 5*N* Pr_2O_3 raw powders by CRYTUR, Ltd. (Turnov, Czech Republic).

Two LuAG:Ce single crystals were grown by the Czochralski technique in a molybdenum crucible under a reducing atmosphere by CRYTUR, Ltd. (Turnov, Czech Republic). The samples with Ce concentration 0.03, and 0.12 wt% were grown from 5*N* Lu_2O_3 and 4*N* Al_2O_3 raw powders.

LuAG:Ce nanopowder was prepared by UV-irradiation of aqueous solutions containing soluble metal salts. The details of preparation can be found in [33]. Ce(III) nitrate hexahydrate was added to the solutions according to the stoichiometry $Lu_{3-x}Ce_xAl_5O_{12}$, where $x = 0.5\%$. Photochemically prepared powder was calcined at 1200 °C.

Single crystalline LuAG:Ce thin film was grown by liquid phase epitaxy from a $BaO–Ba_2O_3–BaF_2$ flux on (1 1 1) oriented LuAG substrate; the growth process is described elsewhere [34,35]. The thickness of the film was 12.3 μm and the Ce concentration 0.28%.

Two single crystals of YAG:Ce were grown by the Czochralski technique from 6*N* Y_2O_3 and 5*N* Al_2O_3 raw powders in a molybdenum crucible by CRYTUR, Ltd. (Turnov, Czech Republic). The Ce concentration in these crystals was about 0.32 wt% of CeO_2 in the melt (later designated as low Ce) and 1000 ppm of Ce in the high quality industrial single crystal (later designated as high Ce).

Absorption spectra were measured by the Shimadzu 3101PC spectrometer in the 190–1200 nm range. Photoluminescence emission (PL) and excitation (PLE) spectra were measured by using a custom made 5000M Horiba Jobin Yvon spectrofluorometer. Excitation was realized with a deuterium steady state lamp. Temperature between 8 and 497 K was controlled by a Janis Instruments closed cycle refrigerator. PL delayed recombination decays were excited by a microsecond xenon flashlamp and measured using the multichannel scaling method. The decay data were fit by three-exponential function used the *Spectra-Solve* program package. From the fit three delayed decay times were determined.

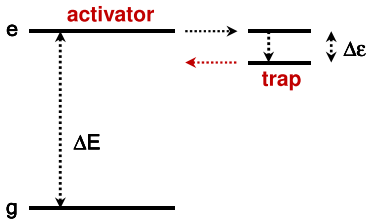

Fig. 1. Simple scheme for a tunneling process between the activator, with ground state *g* and excited state *e*, and the trap located nearby. The energy separation of the ground and excited state of the activator is ΔE while that of the excited state of the activator and the trap is $\Delta\varepsilon$.

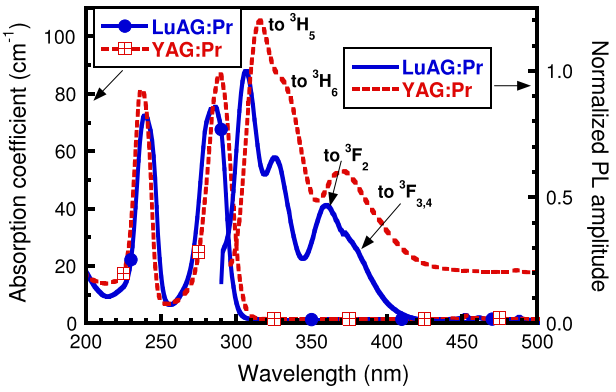

Fig. 2. Absorption spectra at RT and normalized PL spectra at 8 K of LuAG:Pr^{3+} and YAG: Pr^{3+} single crystals, excitation wavelength is 285 nm. Emission spectrum of YAG:Pr^{3+} is vertically shifted by 0.2.

The errors on decay times from the shortest to the longest were estimated from statistical error of the number of counts in each channel to be up to 1%, 2–3% and 4–5%, respectively. Based on these estimates the error on delayed recombination intensities obtained by integration of the decay curves is estimated to be up to 5%.

3. Results and discussion

3.1. Pr^{3+}-doped aluminum garnets

Absorption spectra at room temperature (RT) and PL emission spectra of LuAG:Pr^{3+} and YAG:Pr^{3+} measured at 8 K are displayed in Fig. 2. The lowest absorption band, at about 280 nm, corresponds to a transition from the $^3H_4$ ground state to the lowest $^5d_1$ state of Pr^{3+}, while the band at about 240 nm corresponds to a $^3H_4 \rightarrow 5d_2$ transition [36]. The PL emission between 280 and 420 nm contains several bands corresponding to $5d_1 \rightarrow 4f$ transitions of Pr^{3+} (final ^3H_x and ^3F_x multiplet 4f states are well resolved as shown in Fig. 2). The same transitions in a YAG host are shifted to lower energies with respect to the LuAG host.

In Fig. 3a we display the delayed recombination intensity of LuAG:Pr^{3+} and YAG:Pr^{3+} measured under UV excitation into the $4f \rightarrow 5d$ transition of the Pr ion within the 8–500 K temperature interval. An almost perfectly constant signal is observed in the whole temperature range. Such temperature independence of the delayed recombination intensity manifests two important features. First, it supports the hypothesis of quantum tunneling between the activator and nearby trap(s) as suggested in [1,9]. Second, it also shows no signs of thermally induced ionization of the Pr^{3+} excited state and therefore confirms the known temperature stability of Pr^{3+}-doped aluminum garnets well above RT [2]. Fig. 3b shows an example of delayed recombination decay at 8 K for both Pr^{3+}-doped LuAG and YAG. The decay is approximated by a three-exponential function indicated in the figure. Such complex decay represents a tunneling between an activator and several traps: either traps of a different kind or traps of the same kind distributed at various distances from the activator.

3.2. Ce^{3+}-doped lutetium aluminum garnet

The results for two Ce^{3+}-doped LuAG single crystals are displayed in Figs. 4 and 5. We compare two samples with different concentrations of Ce^{3+} in the crystal, *low* and *high* (cf. Section 2). The Ce concentration difference can be assessed from absorption spectra shown in Fig. 4, namely from the Ce^{3+} absorption band

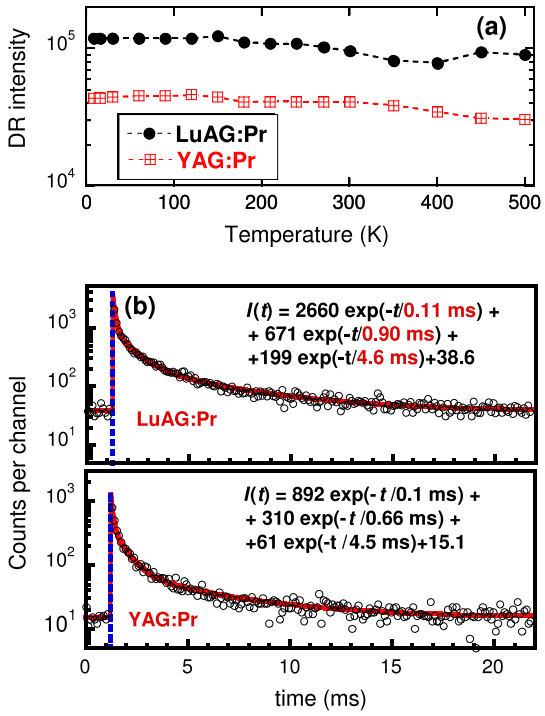

Fig. 3. In (a) delayed recombination intensity of LuAG:Pr^{3+} (λ_{ex} = 285 nm, λ_{em} = 310 nm) and YAG: Pr^{3+} (λ_{ex} = 285 nm, λ_{em} = 325 nm) single crystals as a function of temperature. In (b) delayed recombination decays at 8 K. Empty circles are experimental data, solid line is the fit of function $I(t)$, given in the figure, to the data.

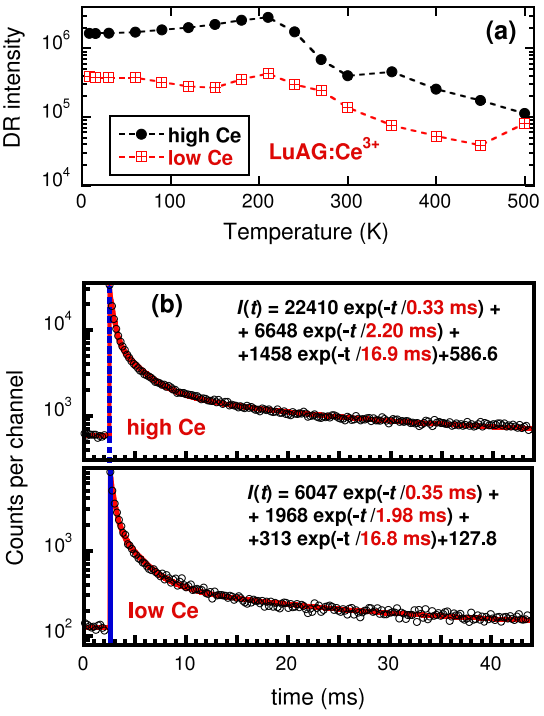

Fig. 5. In (a) delayed recombination intensity of two crystals of LuAG:Ce^{3+} (λ_{ex} = 450 nm, λ_{em} = 530 nm) with the Ce concentration of 0.03 wt% (*low Ce*) and 0.12 wt% (*high Ce*) as a function of temperature. In (b) delayed recombination decays at 8 K. Empty circles are experimental data, solid line is the fit of function $I(t)$, given in the figure, to the data.

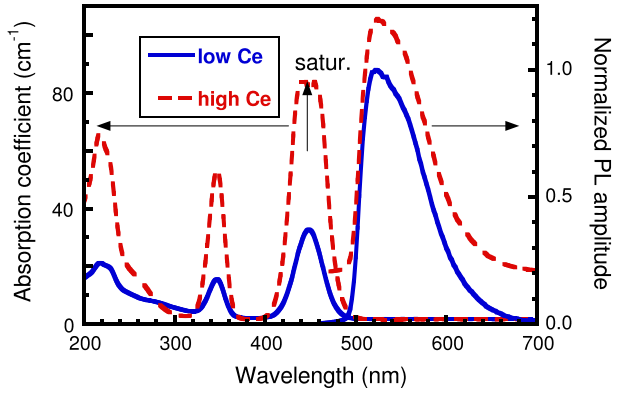

Fig. 4. Absorption spectra and normalized PL spectra at RT of LuAG:Ce^{3+} single crystals. Ce concentration is 0.03 and 0.12 wt%, designated as *low Ce* and *high Ce*, respectively. PL spectra are excited at 450 nm. PL spectrum of the *high Ce* sample is vertically shifted by 0.2.

$4f \rightarrow 5d_2$, peaking at about 350 nm. The lowest Ce^{3+} absorption band $4f \rightarrow 5d_1$, peaking at about 450 nm is saturated for the sample with a high concentration of Ce.

In both samples, the delayed recombination intensity under UV excitation of the $4f \rightarrow 5d_1$ transition of Ce^{3+} ion is practically constant up to 200 K (Fig. 5a). There is a slight decrease of intensity in the temperature interval 200–500 K. This drop in intensity for Ce^{3+}-doped LuAG compared to Pr^{3+}-doped LuAG above may be due to decreasing amplitude of absorption into $5d_1$ band in favor of increasing amplitude of absorption into the $5d_2$ band with increasing temperature [37]. Alternatively, with increasing temperature the activator can get out of resonance with some of the previously (at lower temperatures) participating traps ($\Delta\varepsilon$ is too big– cf. Fig. 1) due to which the total number of traps contributing to the overall delayed recombination signal would drop. In any case, as for the Pr^{3+}-doped LuAG above, there is no indication of thermal ionization of the Ce^{3+} excited state which also gives a confirmation of high thermal stability of Ce-doped LuAG. The delayed recombination decays at 8 K (Fig. 5b) are complex, as above, approximated by a three-exponential curve.

In Figs. 6 and 7 we present data for LuAG:Ce^{3+} in the form of a single crystalline thin film prepared by liquid phase epitaxy and nanopowder prepared by radiation synthesis. Room temperature PLE and PL spectra show two lowest excitation bands of Ce^{3+} and broad emission due to Ce^{3+}, respectively. Correspondingly, delayed recombination intensities as a function of temperature are displayed in Fig. 7b. The intensity of the thin film sample is perfectly constant up to 200 K and as above, shows a similar drop above 200 K. The intensity course of a nanopowder sample presents

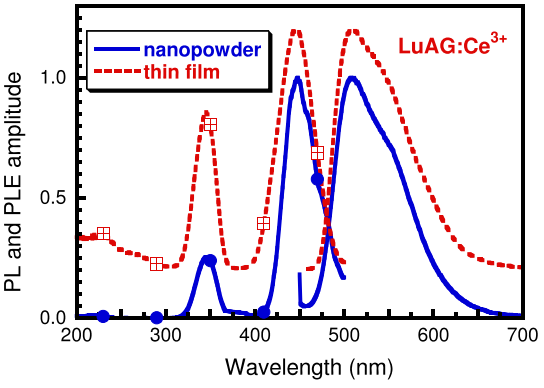

Fig. 6. Normalized PLE and PL spectra of the LuAG:Ce^{3+} compacted nanopowder (λ_{ex} = 430 nm, λ_{em} = 510 nm) calcined at 1400 °C and thin film λ_{ex} = 445 nm, λ_{em} = 510 nm) at RT.

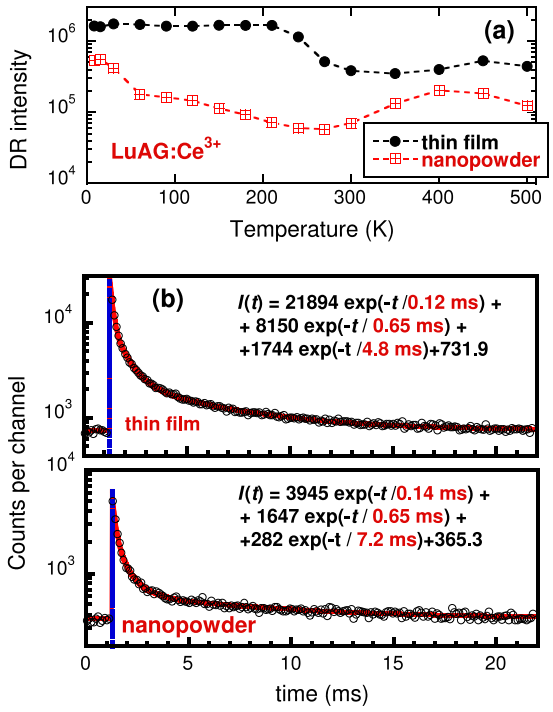

Fig. 7. In (a) delayed recombination intensity of LuAG:Ce^{3+} thin film (λ_{ex} = 435 nm, λ_{em} = 530 nm) and nanopowder (λ_{ex} = 435 nm, λ_{em} = 525 nm) as a function of temperature. In (b) delayed recombination decays at 8 K. Empty circles are experimental data, solid line is the fit of function $I(t)$, given in the figure, to the data.

somewhat irregular variations. However, intensity changes do not exceed an order of magnitude and may possibly be due to distortions caused by light scattering on the powder grains. On the average, taking into account the possible distortions mentioned earlier one may consider the signal almost constant. The delayed recombination decays at 8 K (Fig. 7b) are again complex, approximated by a triple exponential. The results on this variety of LuAG:Ce samples confirm the plausibility of the quantum tunneling hypothesis.

3.3. Ce^{3+}-doped yttrium aluminum garnet

The results for two Ce^{3+}-doped YAG single crystals are displayed in Figs. 8 and 9. As in the case of a LuAG host, we compare two samples with different concentration of Ce^{3+} in the crystal, low and high. As in LuAG, the Ce concentration difference can again be assessed from the Ce^{3+} absorption band $4f \rightarrow 5d_2$ peaking at about 350 nm (see Fig. 8). The lowest Ce^{3+} absorption band $4f \rightarrow 5d_1$ peaking at about 450 nm is also saturated for the sample with high concentration of Ce.

In both samples the delayed recombination intensity under UV excitation into the $4f \rightarrow 5d_1$ transition of Ce^{3+} ion is practically constant up to 200 K (Fig. 9a). The drop of intensity above 200 K observed in LuAG is found for the YAG host as well. The drop is more significant in the low Ce sample. This may be connected with the quality of the sample. While high Ce crystal is designated by the producer as a *high quality* industrial sample, the quality of the low Ce sample is supposedly lower, which suggests a higher number of traps compared to the high Ce crystal. This could lead to a reduction in participating traps in the tunneling process as the temperature increases when the activator's excited state gets out of resonance with the trap level (as suggested above). Nevertheless, as in LuAG host, no signs of thermally induced ionization are present and thermal stability of YAG:Ce crystals is confirmed up to 500 K. The delayed recombination decays at 8 K (Fig. 9b)

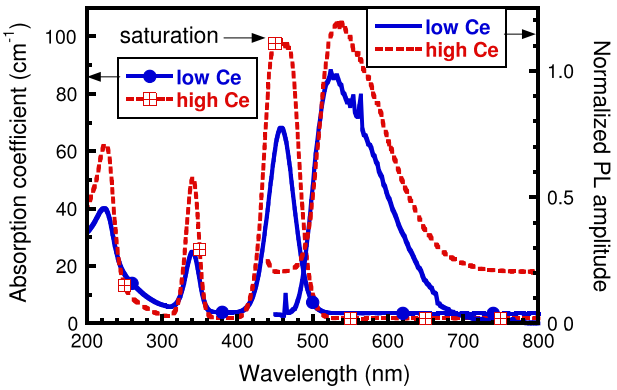

Fig. 8. Absorption spectra and normalized PL spectra at RT of YAG:Ce^{3+} single crystals. The concentration was 0.32 wt% of CeO_2 in the melt and 1000 ppm of Ce^{3+} in the crystal, designated as *low Ce* and *high Ce*, respectively. PL spectra are excited at 430 nm. PL spectrum of the *high Ce* sample is vertically shifted by 0.2.

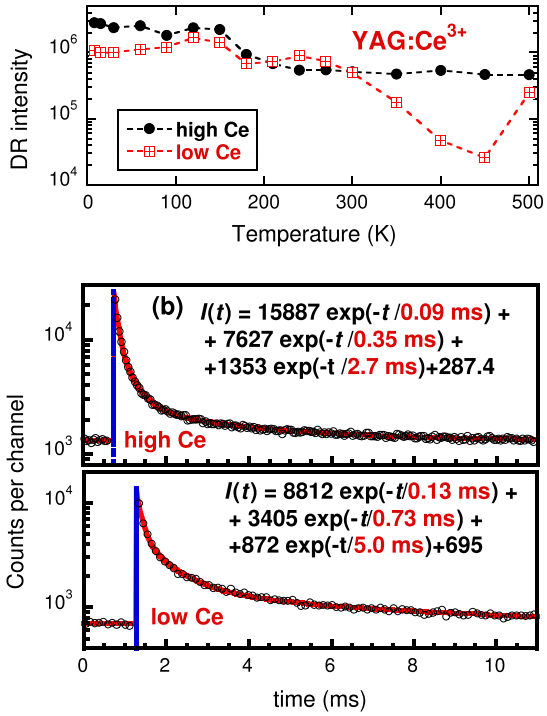

Fig. 9. In (a) delayed recombination intensity of two single crystals of YAG:Ce^{3+} (λ_{ex} = 430 nm, λ_{em} = 535 nm) with the different Ce concentration of 0.32 wt% of CeO_2 in the melt (*low Ce*) and 1000 ppm of Ce^{3+} in the crystal (*high Ce*) as a function of temperature. In (b) delayed recombination decays at 8 K. Empty circles are experimental data, solid line is the fit of function $I(t)$, given in the figure, to the data.

are complex, as in all cases studied, and are approximated by a three-exponential curve. Therefore participation of several traps in the tunneling process is expected.

3.4. GGAG:Ce^{3+} versus simple garnets

The delayed recombination decay intensity of a GGAG:Ce^{3+} crystal was monitored in the 8–230 K temperature range in [8]. For convenience, the results are reproduced in Fig. 10.

Unlike all other silicates studied in the same work, the signal is not constant and there is an intense peak around 100 K. Before hypothesizing on the origin of the peak in [8] we first wanted to test the simple garnets to see whether such a feature might be universal in garnet hosts. None of simple garnets studied in the pres-

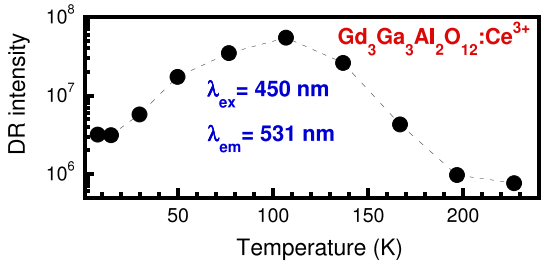

Fig. 10. Delayed recombination decay intensity of GGAG:Ce^{3+} as a function of temperature. Excitation and emission wavelengths are displayed in the figure from [8].

ent work have manifested such a peak. Therefore, the peak is uniquely present in GGAG:Ce and would be associated with particular features of this host. The band structure calculations of this multicomponent garnet host have not yet been reported. However, compared to LuAG and YAG, due to the presence of Gd^{3+} and Ga^{3+} cations, its band gap shrinks and a composition of the bottom of the conduction band profoundly changes [38–40]. These changes would also affect the positioning of the Ce^{3+} excited states together with that of electron traps below the conduction band. Recently it has been shown that the shallow trap levels in GGAG:Ce are quasi-continuously distributed rather than being discrete [41]. Such feature might explain the peak around 100 K in question. With increasing temperature the number of participating kinds of traps (from the distribution) would be increasing up to the point when they start to get out of resonance with the activator's excited state and the signal would start decreasing. Besides the presence of the peak around 100 K, there is a slight drop of the DR signal around 200 K compared to values at the low temperature limit in GGAG:Ce (cf. Fig. 10). In contrast to the peak around 100 K, such a drop was consistently observed in all the studied Ce-doped simple garnets (see above).

4. Conclusion

Quantum tunneling between traps and activator centers had previously been shown to play a decisive role in low temperature delayed recombination [8–10]. In this article we confirmed similar behavior for another wide class of scintillating materials, namely simple garnets. Compared to the silicates previously studied, tunneling in garnets involves deeper trap(s). This follows from the position of the activator's excited state with respect to the conduction band. For example, the $5d_1$ state of Ce^{3+} in $Y_3Al_5O_{12}$ is situated about 1.2 eV below the conduction band [42], while that of Pr^{3+} in $Lu_2Si_2O_7$ is about 0.5 eV [7] and that of Ce^{3+} in Lu_2SiO_5 is about 0.45 eV [43]. We studied various forms of garnets, in particular Czochralski grown single crystals, LPE thin film and a nanopowder prepared by a radiation synthesis. Different activators, Ce^{3+} or Pr^{3+}, have been used. The change due to the activator's concentration between the low and high level within the same sample batch was checked. For all samples studied we obtained consistent results showing practically constant delayed recombination intensity within the entire temperature range 8–500 K. Such results confirm first, the presence of quantum tunneling between the activator and nearby traps and second, the absence of thermal ionization of the activator's excited state well above room temperature.

Acknowledgements

This work was supported by the Czech AS project M100101212 and Czech National Science Foundation Project 13-09876S. Partial support of EC Marie Curie Initial Training Network LUMINET, No. 316906 is also gratefully acknowledged.

References

[1] E. Mihóková, V. Jarý, L.S. Schulman, M. Nikl, Phys. Status Solidi RRL 7 (2013) 228–231.
[2] J. Pejchal, M. Nikl, E. Mihóková, J.A. Mareš, A. Yoshikawa, H. Ogino, K.M. Schillemat, A. Krasnikov, A. Vedda, K. Nejezchleb, V. Múčka, J. Phys. D: Appl. Phys. 42 (2009) 055117.
[3] C. Pedrini, D.S. McClure, C.H. Anderson, J. Chem. Phys. 70 (1979) 4959–4962.
[4] M.F. Joubert, S.A. Kazanskii, Y. Guyot, J.C. Gâcon, C. Pedrini, Phys. Rev. B 69 (2004) 165217.
[5] H. Arbell, A. Halperin, Phys. Rev. 117 (1960) 45–52.
[6] A.J.J. Bos, R.M. van Duijvenvoorde, E. van der Kolk, W. Drozdowski, P. Dorenbos, J. Lumin. 131 (2011) 1465–1471.
[7] M. Fasoli, A. Vedda, E. Mihóková, M. Nikl, Phys. Rev. B 85 (2012) 085127.
[8] E. Mihóková, V. Jarý, L.S. Schulman, M. Nikl, IEEE Trans. Nucl. Sci. 61 (2014) 257–261.
[9] E. Mihóková, L.S. Schulman, V. Jarý, Z. Dočekalová, M. Nikl, Chem. Phys. Lett. 377 (2013) 66–69.
[10] E. Mihóková, L.S. Schulman, J. Phys. Condensed Matter (submitted for publication).
[11] D.G. Thomas, J.J. Hopfield, W.M. Augustyniak, Phys. Rev. 140 (1965) A202–A220.
[12] N. Riehl, J. Lumin. 1 (2) (1970) 1–16.
[13] C.J. Delbecq, Y. Toyozawa, P.H. Yuster, Phys. Rev. B 9 (1974) 4497–4505.
[14] P. Avouris, T.N. Morgan, J. Chem. Phys. 74 (1981) 4347–4355.
[15] M. Tachyia, A. Mozumder, Chem. Phys. Lett. 28 (1974) 87–89.
[16] M. Tachyia, A. Mozumder, Chem. Phys. Lett. 34 (1975) 77–79.
[17] D.J. Huntley, J. Phys.: Condens. Matter 18 (2006) 1359–1365.
[18] R. Autrata, P. Schauer, Jos. Kvapil, J. Kvapil, J. Phys. E 11 (1978) 707–708.
[19] M. Moszynski, T. Ludziewski, D. Wolski, W. Klamra, L.O. Norlin, Nucl. Instrum. Methods Phys. Res. A 345 (1994) 461–467.
[20] C.R. Stanek, K.J. McClellan, M.R. Levy, C. Milanese, R.W. Grimes, Nucl. Instrum. Methods Phys. Res. A 579 (2007) 27–30.
[21] M. Kuklja, J. Phys.: Condens. Matter 12 (2000) 2953–2967.
[22] C. Dujardin, C. Mancini, D. Amans, G. Ledoux, D. Abler, E. Auffray, P. Lecoq, D. Perrodin, A. Petrosyan, K.L. Ovanesyan, J. Appl. Phys. 108 (2010) 013510.
[23] H. Ogino, A. Yoshikawa, M. Nikl, A. Krasnikov, K. Kamada, T. Fukuda, J.Cryst. Growth 287 (2006) 335;
, J. Cryst. Growth 292 (2006) 239–242.
[24] L. Swiderski, M. Moszynski, A. Nassalski, A. Syntfeld-Kazuch, T. Szczesniak, K. Kamada, K. Tsutsumi, Y. Usuki, T. Yanagida, A. Yoshikawa, IEEE Trans. Nucl. Sci. 56 (2009) 934–938.
[25] I.V. Khodyuk, J.T.M. de Haas, P. Dorenbos, IEEE Trans. Nucl. Sci. 57 (2010) 1175–1181.
[26] W. Drozdowski, P. Dorenbos, J.T.M. De Haas, R. Drozdowska, A. Owens, K. Kamada, K. Tsutsumi, Y. Usuki, T. Yanagida, A. Yoshikawa, IEEE Trans. Nucl. Sci. 55 (2008) 2420–2424.
[27] M. Nikl, A. Yoshikawa, K. Kamada, K. Nejezchleb, C.R. Stanek, J.A. Mares, K. Blazek, Prog. Cryst. Growth Charact. Mater. 59 (2013) 47–72.
[28] K. Kamada, T. Yanagida, T. Endo, K. Tsutumi, Y. Fujimoto, A. Fukabori, A. Yoshikawa, J. Pejchal, M. Nikl, Cryst. Growth Des. 11 (2011) 4484–4490.
[29] J.M. Ogiegło, A. Katelnikovas, A. Zych, T. Jüstel, A. Meijerink, C.R. Ronda, J. Phys. Chem. A 117 (2013) 2479–2484.
[30] J. Ueda, K. Aishima, S. Tanabe, Opt. Mater. 35 (2013) 1952–1957.
[31] P. Dorenbos, J. Lumin. 134 (2013) 310–318.
[32] Y. Wu, G. Ren, Opt. Mater. 35 (2013) 2146–2154.
[33] J. Bárta, V. Čuba, M. Pospíšil, V. Jarý, M. Nikl, J. Mater. Chem. 22 (2012) 16590–16597.
[34] M. Kucera, K. Nitsch, M. Kubova, N. Solovieva, M. Nikl, J.A. Mares, IEEE Trans. Nucl. Sci. 55 (2008) 1201–1205.
[35] M. Kucera, K. Nitsch, M. Nikl, M. Hanuš, S. Daniš, J. Cryst. Growth 312 (2010) 1538–1545.
[36] M. Nikl, J. Pejchal, E. Mihokova, J.A. Mares, H. Ogino, A. Yoshikawa, T. Fukuda, A. Vedda, C. D'Ambrosio, Appl. Phys. Lett. 88 (2006) 141916.
[37] D.J. Robbins, J. Electrochem. Soc. 126 (1979) 1550–1555.
[38] Y.-N. Xu, W.Y. Ching, B.K. Brickeen, Phys. Rev. B 61 (2000) 1817–1824.
[39] A.B. Muñoz-García, L. Seijo, Phys. Rev. B 82 (2010) 184118.
[40] M. Fasoli, A. Vedda, M. Nikl, C. Jiang, B.P. Uberuaga, D.A. Andersson, K.L. McClellan, C.R. Stanek, Phys. Rev. B 84 (2011) 081102(R).
[41] K. Brylew, W. Drozdowski, A.J. Wojtowicz, K. Kamada, A. Yoshikawa, J. Lumin. 154 (2014) 452–457.
[42] D.S. Hamilton, S.K. Gayen, G.J. Pogatshnik, R.D. Ghen, W.J. Miniscalco, Phys. Rev. B 39 (1989) 8807–8815.
[43] E. van der Kolk, S.A. Basun, G.F. Imbusch, W.M. Yen, Appl. Phys. Lett. 83 (2003) 1740–1742.

IOP Publishing Journal of Physics: Condensed Matter
J. Phys.: Condens. Matter **27** (2015) 075501 (8pp) doi:10.1088/0953-8984/27/7/075501

Low temperature delayed recombination and trap tunneling

E Mihóková[1] **and L S Schulman**[2,3]

[1] Institute of Physics, Academy of Sciences of the Czech Republic, Cukrovarnická 10, 162 53 Prague 6, Czech Republic
[2] Physics Department, Clarkson University, Potsdam, NY 13699-5820, USA
[3] Max Planck Institute for the Physics of Complex Systems, Nöthnitzer Street 38, 01187 Dresden, Germany

E-mail: mihokova@fzu.cz and schulman@clarkson.edu

Received 19 October 2014, revised 19 December 2014
Accepted for publication 5 January 2015
Published 28 January 2015

Abstract

Delayed recombination of charge carriers at an activator is a significant problem for fast scintillators and is usually associated with thermal effects. However, experimental results have shown that this phenomenon can occur even at the lowest temperatures. We here provide evidence in support of the idea that this is due to quantum tunneling between activator and nearby traps, and provide analytic estimates relating the energy levels and locations of those traps to the observed delayed recombination. Several calculations are devoted to showing that deviations from the simplest estimates in fact do not occur. Moreover, these estimates are consistent with lower dimensional numerical calculations for a physically significant range of trap distances. In two examples involving the activator Pr, the formulas developed are used to give the locations of traps based on likely values of trap energy depth.

Keywords: scintillator, tunneling, traps

(Some figures may appear in colour only in the online journal)

1. Introduction

Loss of fast scintillation light is an undesirable phenomenon causing deterioration of scintillator performance in many applications where such fast response is vital. The usual culprit is the thermal ionization of the excited state of the activator in the scintillating host material. This phenomenon can be effectively observed and quantitatively evaluated by various techniques, such as conventional photoconductivity using blocking electrodes [1], the microwave resonator technique [2] or purely optical techniques based on the measurement of thermoluminescence after UV excitation [3, 4]. Yet another possibility is a delayed recombination decay measurement [5]. The last method consists in the observation of slow tails in the luminescence decay under UV excitation. When the luminescence center is thermally ionized, charge carriers that do not decay promptly can migrate through conduction or valence bands. After being trapped and released they return to the luminescence center and recombine producing delayed (slow) light.

Applying the delayed recombination technique, it has recently been learned that the loss of fast scintillation light can also occur at temperatures below those associated with the thermal ionization described above [6–8]. Our tentative explanation has been that this reflects quantum tunneling of the charge carrier from an activator to a nearby trap and back, as in the scheme in figure 1. An order of magnitude confirmation is obtained based on one-dimensional tunneling calculations [7]. Furthermore, in several complex oxide scintillating crystals we observe practically constant delayed recombination decay intensity over an extended low temperature range [8]. These results are consistent with the temperature-independence of the quantum tunneling process.

In this article we show that analytic estimates are possible (section 2) and we provide 2D verification that these estimates are reasonable (section 3). But we have *not* provided an *ab initio* calculation of decay rates. What we have done is begin with a straightforward analytic expression and bound or estimate several factors that might affect this expression. These factors are part of the theoretical calculation and the purpose

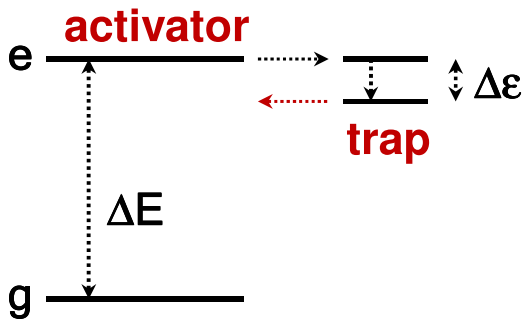

Figure 1. Scheme for a tunneling process between an activator, with ground state g and excited state e, and a trap located nearby. The energy separation of the ground and excited state of the activator is ΔE while that of the excited state of the activator and the trap is $\Delta\varepsilon$.

in calculating them is to show that they are *not* important. Having done this, we confirm and extend the arguments for the plausibility of the tunneling explanation of the low temperature recombination decay.

Moreover, under some circumstances, our calculations give information on physical quantities associated with the traps (section 4). In particular, when a single exponential delayed recombination decay is observed (as, for example, in the case of Y_2SiO_5:Pr^{3+} [8]), one can get a relation between a trap's depth and its distance from the atom. Since significant tunneling should only occur if the trap depth is close to the energy of the excited activator level we expect these two energies to be about the same, although as suggested by figure 1, there can be a small energy loss, $\Delta\varepsilon$, in the trap. This information is sufficient to get an excellent handle on trap distance, hence on the structural features of the scintillator. As the number of nearby traps increases (experimentally, one sometimes gets an exponential, sometimes a more complicated curve) less direct, but still potentially useful, information would be available. For this we will provide another example, $Lu_2Si_2O_7$:Pr^{3+}. With the reasonable assumption that both traps are of about the same depth (and therefore probably of the same sort), distances can be obtained.

There have been many calculations based on tunneling between traps and recombination centers [9–15]. All these assume that the traps are initially filled by incident ionizing radiation, yielding, complex luminescence decays that can be expressed as a sum of many exponentials. For the case of traps at randomly distributed distances from recombination centers one can get an inverse power-law decay [14, 15].

Our approach has the further benefit of being independent of any assumptions about 'attempt frequency'. This quantity, often denoted s, is used as a prefactor to the exponential in decay calculations. However, considerable variability and judgement is involved in its use and in some contexts it can be quite misleading (see, e.g. [16] for further discussion). We have a time-independent way of calculating decay rates (see below) that does not use this quantity.

2. Wave function estimates

Let the distance between the centers of the activator (recombination center) and the trap be λ (distances measured in Å). If the activator has effective radius r_A and the trap r_T, we assume that λ is somewhat larger than both r_T and r_A.

We focus on three states. First there is the ground state of the activator, which we call 'ψ_G'. If the activator is thrice ionized Ce, this is a $4f$ state. Then there is its excited state, ψ_E, which (again for Ce^{3+}) is a $5d_1$ state. And finally there is the trap state, ψ_T. This is likely to be an oxygen vacancy at some distance from the activator. The exact form of this state near the oxygen vacancy does not influence our calculation strongly because the decay takes place near the activator. (As we calculate below, its effect, through what one might consider normalization, is extremely small.) The trap state near the activator will have approximately the same form as ψ_E, since they satisfy the same partial differential equation, with nearly the same energy parameter, E. Under these circumstances, what matters for the decay rate is the size of the trap wave function in the vicinity of the activator. As indicated, in that vicinity ψ_T will have the shape of ψ_E but will be scaled down by the reduction in amplitude relative to the neighborhood of the trap. That amplitude is not the same as the amplitude as if the activator were not there. Typically, the activator presents an attractive potential, so that there is a tendency for the trap wave function to be larger in this region. This effect can be further enhanced by resonance phenomena, for example near equality of trap and excited state energy. We have studied this phenomenon in one-dimensional models and found that the probability enhancement is typically about two or three (although it can be larger). For this reason we include in our estimates a factor, η, to allow for this effect.

To estimate the dropoff of the wave function (apart from η) we take the trap to be an attractive point potential. In three dimensions the wave function is $\sqrt{\kappa/2\pi}\exp(-\kappa r)/r$ where r is the distance from the trap center and $\kappa = \sqrt{-2mE_T}/\hbar$. (This is normalized to square-integral unity.) For later use, we indicate the lower dimensional forms. In two dimensions the corresponding wave function is a Bessel function (H_0 of imaginary argument) with asymptotic (large-r) form $A\sqrt{\kappa/r}\exp(-\kappa r)$, while in one dimension it is simply $\sqrt{\kappa}\exp(-\kappa r)$. The value of A depends on the normalization, which allows for the small-r features of the Bessel function. See appendix A for details.

Using these estimates the decay rate can be calculated. For prompt emission, what governs the decay rate is the absolute value of the square of the matrix element $\langle\psi_E|r|\psi_G\rangle$. If, in the region of the activator the trap wave function resembles the activator's excited state, than the only reduction in decay rate would come from the smaller amplitude associated with the trap state. As a result

$$\Gamma = R\Gamma_0\,, \tag{1}$$

where Γ_0 is the activator's usual and rapid decay rate, Γ the rate for decay from the trap, and R the reduction factor, which by our reasoning is

$$R = \frac{\eta\int_{\text{activator}}\left|\sqrt{\frac{\kappa}{2\pi}}\frac{\exp(-\kappa r)}{r}\right|^2 \mathrm{d}^3 r_{\text{activator}}}{\langle\psi_T|\psi_T\rangle}\,. \tag{2}$$

Note that the r, sans subscript, in equation (2) is the coordinate centered on the trap. The physical picture behind equation (2) is that, with the excitation, some of the electron's amplitude gets to the trap. In some instances, according to the probabilistic rules of quantum mechanics, it gets caught in the trap. However, the eigenstate of the full Hamiltonian associated with the trap, although mostly located in the trap, extends outward and its tail overlaps the physical location of the activator. Returning to equation (2), it says that the (spatial) amplitude of the trap wave function in the region of the activator resembles that of the activator's excited state, since they have approximately the same energy and therefore satisfy nearly the same partial differential equation (but their phases can be different, consistent with eigenstate orthogonality).

As we shall see, this estimate can prove useful, but should not be expected to produce exact results. Besides the factor η mentioned above, there could be factors working in the opposite direction. In particular, because of the possible energy difference, some of the amplitude near the activator may not resemble the excited state and the assumption of a base decay rate of Γ may not be warranted. However, there is no evidence that the matrix element $\langle\psi_E|r|\psi_G\rangle$ should be strongly affected by such a difference.

Continuing in this vein of approximation we may sometimes assume that the activator is far enough away from the trap that its integral is simply the volume of the activator times $(\kappa/2\pi)\left[\exp(-\kappa r)/r\right]^2$. Taking the effective activator radius to be a, this gives

$$R = \eta\frac{\kappa}{2\pi}\frac{\exp(-2\kappa r)}{r^2}\left(\frac{4\pi}{3}\right)a^3 = \eta\frac{2}{3}\left(\frac{a}{\lambda}\right)^2(\kappa\, a)\exp(-2\kappa\lambda)\,, \tag{3}$$

where in the second equality we recall our use of λ for the activator-trap center-to-center distance. Aside from constants, this justifies the 'geometrical factor' invoked in [7] (the exponential and the $\kappa\, a$ term, here explicit, were there implicit in ψ_T). In the two-dimensional case, of interest for comparison with our numerical work, one lower factor of a/λ appears, recalling the asymptotic form of the two-dimensional wave function mentioned above.

2.1. Comment on the approximation in equation (3)

A 3D estimate of the correction in going from equation (2) to equation (3) will be done numerically in the next subsection, but the essential point can be seen in one dimension. There the wave function is $\psi_T = \sqrt{\kappa}\exp(-\kappa|x|)$, taking the trap to be centered on 0 and the activator, with diameter $2a$, to be at $-\lambda$. The integral in question would then be

$$I \equiv \kappa\int_{-\lambda-a}^{-\lambda+a}\exp(-2\kappa|x|)\mathrm{d}x\,. \tag{4}$$

The approximation (3) would correspond to approximating I by $I_0 = 2\kappa a\exp(-2\kappa\lambda)$. The one-dimensional integral is readily performed, yielding

$$\frac{I}{I_0} = \frac{\sinh(2\kappa a)}{2\kappa a} \approx 1 + \frac{2}{3}(\kappa a)^2 + \ldots\,. \tag{5}$$

In three dimensions the qualitative features are the same, namely the leading correction is *second* order in κa. This is because in the linear approximation (1st order) the tilt due to the exponent and other factors gains as much on the near side of the integral as it loses on the far side.

This justifies the approximation so long as the radius of the activator is not significantly larger than the dropoff rate of the trap wave function. If the trap is 1 eV below the conduction band, $1/\kappa$ is approximately 2 Å (for example, in YAG:Ce^{3+} the $5d_1$ state of Ce^{3+}, is situated about 1.2 eV below the conduction band [17]). For an activator of radius 2 Å (which is greater than that of Ce^{3+}) this implies there will be some correction. However, the overall factor of $\exp(-2\kappa\lambda)$ will dominate since λ should be on the order of 10 Å or more.

2.2. The integral in equation (2)

The integral for the reduction factor is

$$\begin{aligned}\frac{R}{\eta} &= \frac{\int_{\text{activator}}\left|\sqrt{\frac{\kappa}{2\pi}}\frac{\exp(-\kappa r)}{r}\right|^2\mathrm{d}^3r_{\text{activator}}}{\langle\psi_T|\psi_T\rangle}\\ &= \frac{\frac{\kappa}{2\pi}\int_{\text{activator}}\left|\frac{\exp(-2\kappa|-\lambda\hat{z}+\hat{r}_{\text{activator}}|)}{|-\lambda\hat{z}+\hat{r}_{\text{activator}}|^2}\right|\mathrm{d}^3r_{\text{activator}}}{1}\\ &= \kappa\frac{\exp(-2\kappa\lambda)}{\lambda^2}\int_0^a\rho\mathrm{d}\rho\int_{-\sqrt{a^2-\rho^2}}^{\sqrt{a^2-\rho^2}}\mathrm{d}z\\ &\quad\times\frac{\exp\left(-2\kappa\left[\sqrt{(z-\lambda)^2+\rho^2}-\lambda\right]\right)}{\frac{(z-\lambda)^2+\rho^2}{\lambda^2}}\,.\end{aligned} \tag{6}$$

In the above expressions we use cylindrical polar coordinates, with ρ the radial polar coordinate.

R was estimated in equation (3) as $\eta\frac{2}{3}a^3\kappa\frac{\exp(-2\kappa\lambda)}{\lambda^2}$; one can obtain greater analytic accuracy by expanding the integral. But it is simpler to graph the numerical results. See figure 2. It is clear that little is gained by making the analytical calculation more precise.

2.3. Comment on the various decay rates and other approximations

The 'κ' that appears in equation (2) satisfies $\frac{\hbar^2\kappa^2}{2m} = |E_T|$ and is κ_T, the imaginary wave number associated with the trap. Although the assumption of a point trap may be more or less justified, the relation between E_T and κ_T will always hold, provided features of the trap are no longer significant at the location of the activator.

A remaining issue could be called the question of normalization. One could imagine that a larger trap would hold on to more of its amplitude and although the asymptotic value of the wave function was *proportional to* $\exp(-\kappa r)/r\sqrt{\kappa}$ there might be a smaller overall coefficient to this term because of the amplitude held in the trap. We investigated this question in one dimension where the same expectation obtains. As it turns out, for a square well there is actually *less* amplitude caught in the range $[-L/2, L/2]$ than for a point singularity. In figure 3 we show the coefficient, A in $A\sqrt{\kappa}\exp(-\kappa r)$ for the square well wave function outside the well. This result

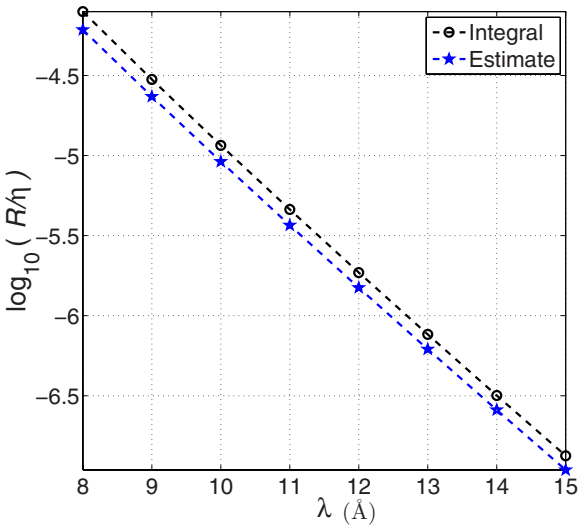

Figure 2. Comparison of a crude estimate for R/η with the numerical evaluation of the integral in equation (6). This is shown on a logarithmic scale. The parameter values are $a = 3.3$ Bohr radii (effective radius of the activator), $\kappa \approx 0.36$ (corresponding to trap energy 1 eV below the conduction band) and λ varying from 8 to 15 Å. From the figure it is clear that the difference of logarithms is approximately constant and the actual numbers give a constant ratio of about 5/4. A smaller value of a would be more physically accurate, and would only improve the comparison.

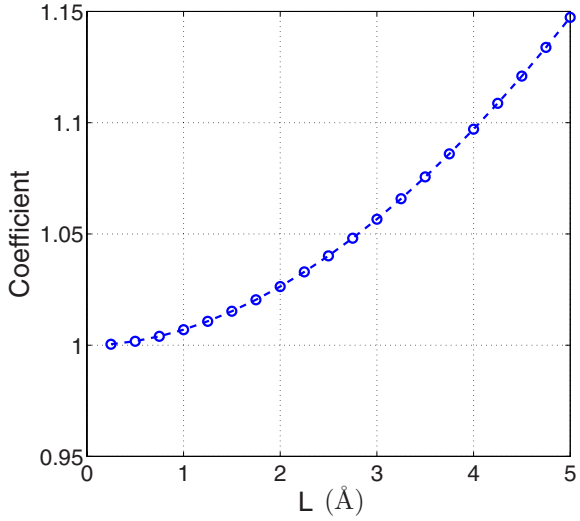

Figure 3. Coefficient of $\sqrt{\kappa}\exp(-\kappa r)$ in the wave function outside a square well of width L centered on 0. The energy of the well, for all L, is $-\hbar^2\kappa^2/2m$. For this figure we take $\kappa = 0.3$, which in our units (inverse Å) is about the value expected for the energy of the trap.

seems unintuitive and comes about because we are holding the well ground state energy fixed and are adjusting the depth of the well as L increases. As a result the well becomes ever more shallow. Of course more and more amplitude is held within the well, since the exponential form of the wave function holds only for $|x| > L/2$. Nevertheless, once it has the exponential form (now at larger x value) the coefficient is actually larger. However, this whole question is pretty much irrelevant. Note that A is very close to unity, even for traps of 2 Å, which is larger than the Ce atom. At one Bohr radius A is about 1.002.

The expectation is that $E_E > E_T$ so that $\kappa_E > \kappa_T$. This means it is easier to get to a trap than to get back and a small non-radiative correction takes place at the trap. This coupled with the large number of initially excited charged particles provides the asymmetry in the number of prompt recombiners and delayed ones.

3. Numerical results

Our models for the activator and the trap are simple, and going from one dimension (in [7]) to two allows a more stringent test of the tunneling hypothesis. Both the trap and the 'activator' are taken to be isotropic, Gaussian wells, the smoothness of the Gaussians reducing the sensitivity of the solution to grid size. Specifically, the potential has the following form:

$$V(\rho, z) = -\alpha e^{-(\rho^2+z^2)/r_A^2} + \beta/2(\rho^2 + z^2) - \gamma e^{-(\rho^2+(z-\lambda)^2)/r_T^2}, \tag{7}$$

where ρ is the 2D polar coordinate (along the line connecting the centers of the trap and activator) and z the orthogonal coordinate whose origin is the activator. The quantities α and γ are the depths of the activator and trap potential wells, respectively, β models the centrifugal potential and r_A and r_T are effective activator and trap radii, respectively. The parameters used in our calculations were chosen so that ΔE was somewhat larger than 2 eV and $\Delta\varepsilon$ was several tens of meV (see figure 1). Solution of the Schrödinger equation was achieved using the program 'WavePacket' [18]. Since both activator and trap were symmetric about the line connecting their centers, there was azimuthal symmetry and we sought only eigenstates having that symmetry. In figure 4 we present an example of the trap wave function obtained from our numerical calculation. The right hand panel illustrates the presence of the trap wave function in the activator region.

To calculate the reduction factor, R, a slightly different procedure is followed from that used in our estimates above. Since the dominant term—the one that fixes the usual decay rate—is the dipole matrix element [19] $\langle\psi_G|\boldsymbol{r}|\psi_E\rangle$ and since all wave functions, trap, excited and ground states, were computed, this could be evaluated. As a result, and following our earlier approach, we calculated a reduction factor relative to the lifetime of the excited state. With the additional information from the numerical calculation, the reduction of the decay rate R_D is

$$R_D = \frac{|\langle\psi_G|\boldsymbol{r}|\psi_T\rangle|^2}{|\langle\psi_G|\boldsymbol{r}|\psi_E\rangle|^2 + |\langle\psi_G|\boldsymbol{r}|\psi'_E\rangle|^2}, \tag{8}$$

where ψ'_E is a second excited state obtained from the computation.

As explained in appendix A, because in lower dimensions the wave function is better focused on the atom, to obtain the total reduction R, one should reduce the factor R_D obtained in the lower-dimensional calculations by a geometrical factor. From that appendix we quote those factors:

$$G_{3\text{ to }1} = \frac{1}{3}\left(\frac{r_A}{\lambda}\right)^2, \tag{9}$$

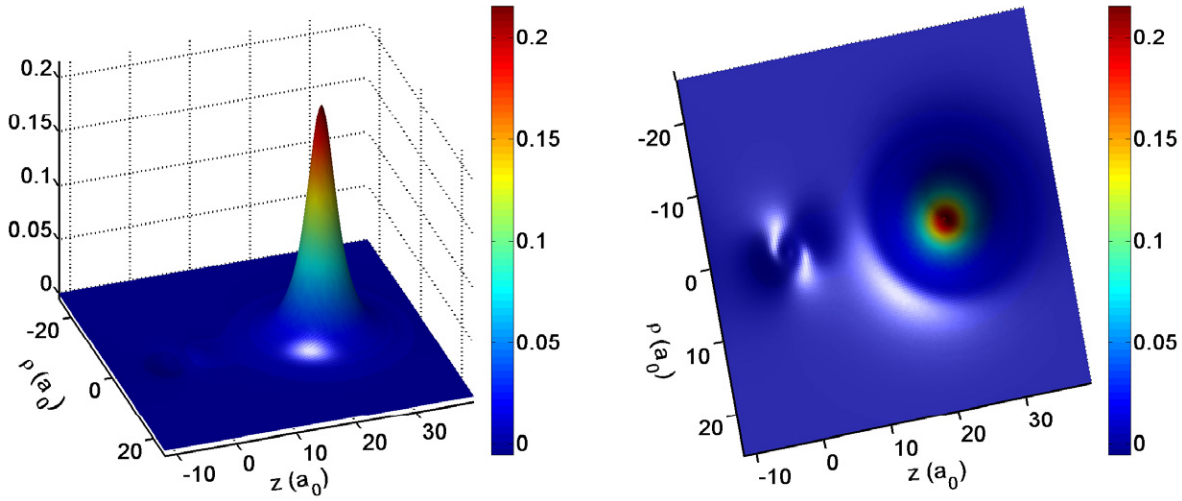

Figure 4. Example of a calculated trap wave function shown from two different perspectives. The trap-activator distance λ is 23 Bohr radii (about 12 Å). The view in the second panel better displays the portion of the wave function in the area of the activator. The small asymmetry that can be seen as white spots on the dark background is an artifact of the solution method.

$$G_{3\text{ to }2} = \frac{4}{3\pi}\left(\frac{r_A}{\lambda}\right). \tag{10}$$

In figure 5 we show the results of numerical calculations (squares, red in color), analytic calculations doing (circles, black) and not doing (stars, blue in color) the integral in equation (2). Many features are evident from this graph. First, there is considerable disagreement between analytic and numerical values at the smallest distances. Here our assumptions (in the analytic calculation) about the large distance between the trap and activator (i.e. $\lambda/r_A \gg 1$) are simply false and it is seen in the numerical calculations that there is considerable overlap of trap and activator wave functions. Thus for close-by traps the numerical work is more reliable. However, as the distance grows the analytic result improves and might be more reliable than numerical calculations. The problems of the numerics at these distances are also illustrated in the figure: at the largest distance values there is a dependence on mesh size that creates considerable uncertainty. Since our objective is not a precise calculation of decay rates, but rather a way to get semi-quantitative information about the traps, the figure gives confidence in the simpler form of estimate for traps from about 12 Å and further.

Finally we mention that although improvements in the mesh size (and better computers) could improve results at the largest distances, we see little point in this, since our numerical model is not a precise version of the underlying physical system, nor is our intent an *ab initio* calculation.

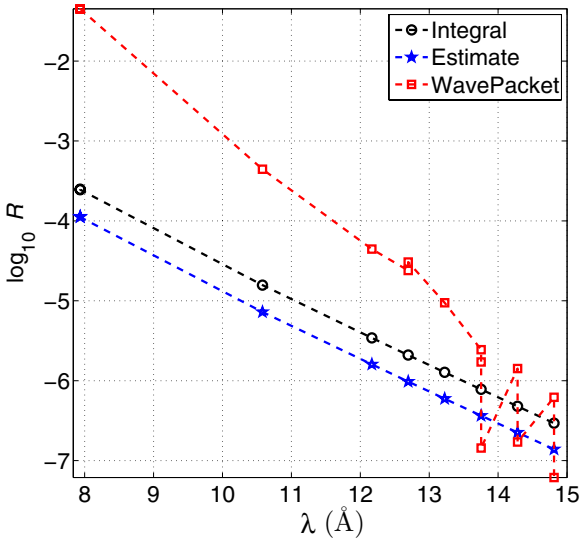

Figure 5. Reductions of the decay rates for various trap distances. Trap energies are typically about negative 1.2 or 1.3 eV. Where several results are given for the same distance, different mesh sizes have been used.

4. Application

The formulas developed, in particular equation (3), can be used to determine trap properties. Those factors over which we have less control, can, in effect, provide theoretical error bounds on the quantities we give.

We begin with the most straightforward example, Y_2SiO_5:Pr^{3+} [8] whose decay curve is shown in figure 6. Details on the sample and experiment can be found in [8]. There is a single exponential with time constant (inverse decay rate) of 2.8 ms. The prompt decay for this scintillator has a lifetime of 18 ns [5]. Thus the reduction factor is 8.2×10^{-6}. The best estimate for the trap binding energy is the energy separation of the activator excited state from the conduction band, which was estimated to be 0.4 eV [5]. Finally, for the radius of the Pr^{3+} ion we use the value 1.13 Å [20]. Using these values, and based on equation (3), we show in figure 7 the reduction factor as a function of λ (distance) and for η (attraction enhancement) equal 1 (lowest curve), 2 (middle) and 3. As can be seen in the figure, for $\eta = 2$ (the most conservative value), the trap distance is about 13 Å from the activator. The (theoretical) spread, based on the plausible range of η is from 12 to 14 Å. It is suggestive that these distances are about the lattice distance in the Y_2SiO_5 [21] host.

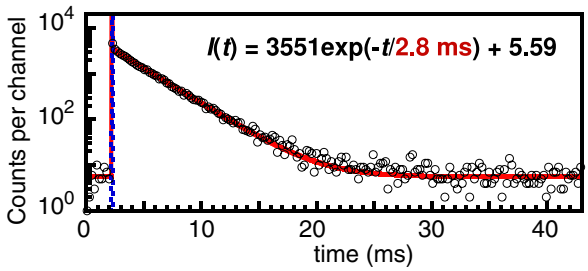

Figure 6. Y_2SiO_5:Pr^{3+} delayed recombination decay at 8 K [8]. Empty circles are the experimental data, solid line is the function, I(t), given in the figure.

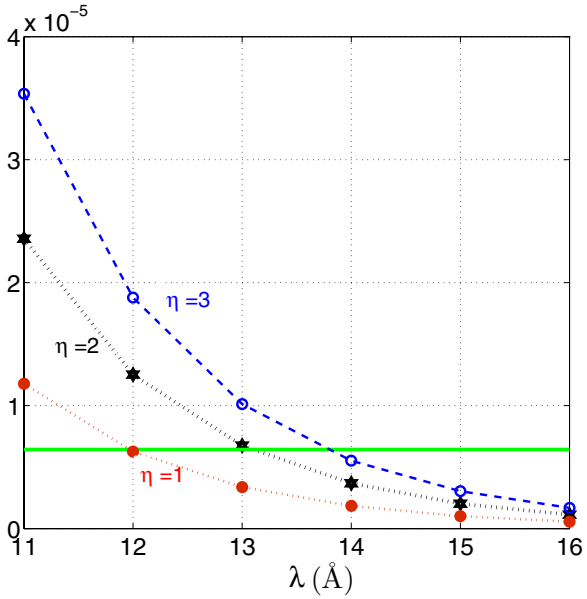

Figure 7. Reduction factor versus distance for $\eta = 1, 2$ and 3. The solid horizontal line is the reduction factor for Y_2SiO_5:Pr^{3+}. See the text for deductions based on this figure.

A second example is $Lu_2Si_2O_7$:Pr^{3+} (LPS:Pr) whose decay curve is shown in figure 8. Details on the sample and experiment can be found in [8]. Now the story is a bit more complicated as there are two lifetimes and two reduction factors. The lifetimes are, respectively, 0.13 and 1.6 ms. The lifetime for prompt decay is 19 ns [22]. This gives reduction factors of 1.5×10^{-4} and 1.3×10^{-5}, respectively. As above, the best guess for the trap binding energy is that of the activator excited state. With that assumption the binding energy is roughly the same for both of them, so that if they actually differ, it does not matter. The location of the Pr^{3+} excited state below the conduction band was determined to be [4] 0.54 eV. In figure 9 we show reduction factor as a function of λ for various plausible η's. For the short lifetime and $\eta = 2$, we have a trap distance value of about 7.7 Å; with $\eta = 1$ the distance would be 6.7 Å and $\eta = 3$ yields about 8.2 Å . For the longer lifetime we get an $\eta = 2$ value of about 11 Å, and a range of 10 Å to about 11.5 Å .

As observed earlier, for quantum tunneling to occur there should be a trap whose energy is nearly resonant with the excited state of the activator. For Pr^{3+} in LPS:Pr the excited state energy separation from the conduction band is 0.54 ± 0.05 eV [4]. There is independent evidence that such a

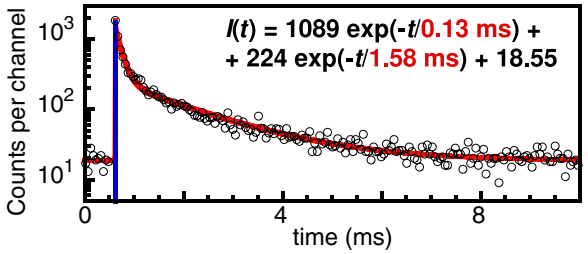

Figure 8. $Lu_2Si_2O_7$:Pr^{3+} delayed recombination decay at 8 K [8]. Empty circles are the experimental data, solid line is the function, I(t), given in the figure.

trap with nearly resonant energy is indeed present. Thermally stimulated measurements (TSL) were performed in LPS:Pr to determine the trap parameters [23]. There are three intense TSL peaks observed below room temperature and associated trap depths were determined to be about 0.24, 0.51 and 0.74 eV. The depth 0.51 ± 0.01 eV associated with the TSL peak at 211 K is within experimental error in excellent agreement with the separation of the Pr^{3+} excited state from the conduction band.

Combined information on LPS:Pr material properties confirm that the observed delay in the decay in figure 8 is most likely due to quantum tunneling between the trap associated with the 211 K peak and the Pr^{3+} activator. Our calculation shows that this trap is located at distances of about 8 and 11 Å. The trap is most likely an oxygen vacancy. The mean distance of Lu-O in LPS:Pr is about 2.23 Å [24] which makes the closer trap a vacancy located at the third or fourth nearest oxygen site with respect to the Pr ion. Since there is no need for charge compensation when substituting Pr^{3+} for Lu^{3+} or Y^{3+} (above), the vacancy is not necessarily expected to be located at the closest oxygen sites.

5. Conclusion

We have employed a time-independent method for the calculation of lifetimes associated with delayed recombination radiation at low temperatures. It is based on the importance of quantum tunneling at low temperatures. With this method we focus on the trap wave function. The formula for the decay probability is based on a straightforward estimate of that wave function, and this is verified in two ways. First there are a number of theoretical issues that could spoil the wave function implications and these are estimated and found to be small. Moreover, they appear in the logarithm of formulas used for actual physical estimates. Second, numerical calculations are performed which, when allowance is made for a change in dimension, give agreement with the theory.

The actual result depends on a number of physical factors, principally the trap depth and the distance of the trap from the activator. Because trap depth can be estimated, we get a handle on trap-activator distances that can aid in the identification of the nature of the trap. Examples of such calculations are provided in section 4 for the cases of Y_2SiO_5:Pr^{3+} and $Lu_2Si_2O_7$:Pr^{3+}.

In summary, combined information from independent experiments and our theoretical estimates provides solid evidence that quantum tunneling is responsible for the slow tails in the delayed recombination decay observed in

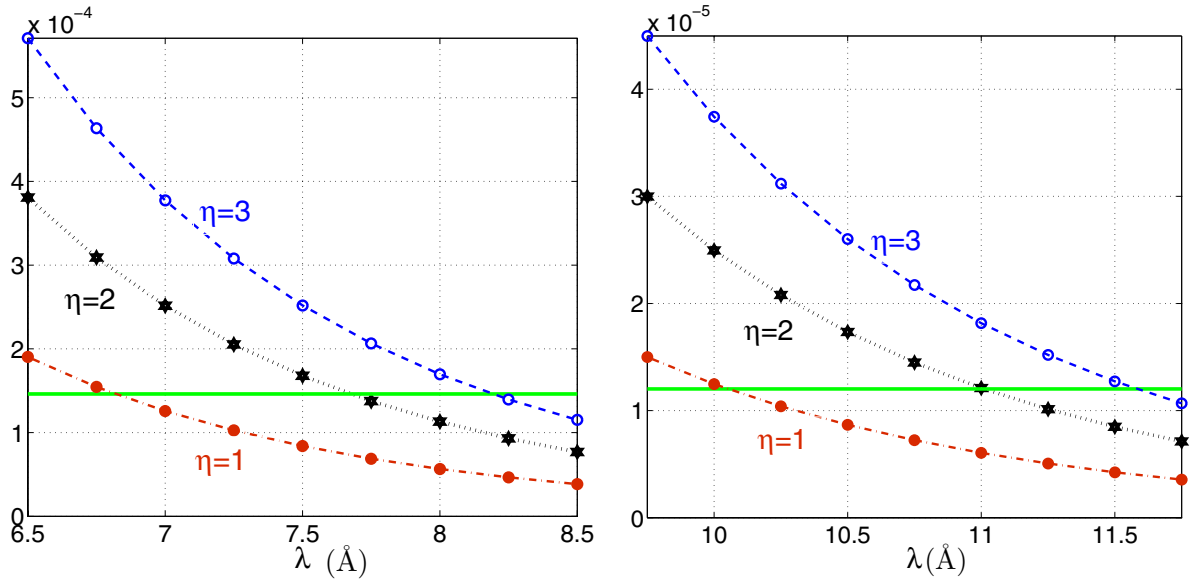

Figure 9. Reduction factor versus distance for $\eta = 1, 2$ and 3. The solid horizontal lines are the reduction factors for the two (delayed) lifetimes of $Lu_2Si_2O_7:Pr^{3+}$. See the text for deductions based on this figure.

scintillating materials. Moreover, the verification technique itself yields information on trap location.

Acknowledgments

We are grateful to the creators of WavePacket [18] and in particular to Ulf Lorenz for his kind assistance in the use of that program. We also thank the Czech Academy of Sciences for support in connection with ASCR project M100101212.

Appendix A. The geometrical factor

When comparing results in different dimensions it should be recalled that the lower the dimension, the easier it is to tunnel. For example, in one dimension half the wave function amplitude is confined to one side of the trap, whereas in three dimensions a much smaller fraction of the wave function's amplitude reaches the location of the atom (or attractive potential) to which the particle tunnels. This issue arises when comparing results in different dimensions, as it did in our previous estimates based on one-dimensional information [7] and as it does when comparing our two-dimensional numerical results to experimental data. It should be noted though that the geometrical factor plays a qualitative role, and a certain amount of leeway, perhaps a factor two (for reasons explained elsewhere in this article) should be allowed for in its use.

We obtain the geometrical factor by comparing the wave functions of point singularities in various dimensions, insofar as they overlap with distant objects. The normalized asymptotic wave functions are as follows

$$\psi_T(r) = \begin{cases} \sqrt{\kappa}\, \mathrm{e}^{-\kappa r} & \text{1 dimension,} \\ \sqrt{\dfrac{\kappa}{2r}}\, \mathrm{e}^{-\kappa r} & \text{2 dimensions,} \\ \sqrt{\dfrac{\kappa}{2\pi}}\, \dfrac{1}{r}\, \mathrm{e}^{-\kappa r} & \text{3 dimensions,} \end{cases} \tag{A.1}$$

where in all cases r is the distance from the trap center and $\kappa = \sqrt{-2mE_T}/\hbar$. For one and three dimensions these are exact. For two dimensions the asymptotic (large r) form is given. The exact wave function is the Hankel function (Bessel function of the third kind), const$\cdot H_0^1(\mathrm{i}\kappa r)$, with r the two-dimensional polar coordinate. The usual form of this function (see [25]) is normalized to $\int_0^\infty \mathrm{d}x |H_0^1(\mathrm{i}\kappa x)|^2 = 1/\kappa$. We require 2D normalization and based on the fact that $\int_0^\infty \mathrm{d}r 2\pi r |H_0^1(\mathrm{i}\kappa r)|^2 = 4/(\pi\kappa^2)$, we deduce that the physical wave function is

$$\psi(r) = \frac{\kappa\sqrt{\pi}}{2} H_0^1(\mathrm{i}\kappa r)\,. \tag{A.2}$$

The asymptotic form of the Hankel function for a pure imaginary argument is given by [25]

$$H_0^1(\mathrm{i}\kappa r) \sim \sqrt{\frac{2}{\pi\kappa r}} \mathrm{e}^{-\kappa r}\,, \quad \kappa r \to \infty\,, \quad \kappa, r \text{ real.} \tag{A.3}$$

Combining the information in equations (A.2) and (A.3) one arrives at equation (A.1).

To get the geometrical factors, $G_{3\,\mathrm{to}\,1}$ and $G_{3\,\mathrm{to}\,2}$, we compare the overlap of the atomic region with the wave function in various dimensions. Call the region of the atom Ω, then in one dimension the overlap is

$$I_1 \equiv \int_\Omega \mathrm{d}r |\sqrt{\kappa}\, \mathrm{e}^{-\kappa r}|^2 \approx \kappa\, \mathrm{e}^{-2\kappa\lambda} \int_\Omega \mathrm{d}r = \kappa\, \mathrm{e}^{-2\kappa\lambda} 2r_A\,. \tag{A.4}$$

In two dimensions we assume the asymptotic form is valid and find that

$$I_2 \equiv \int_\Omega \mathrm{d}^2 r \left|\sqrt{\frac{\kappa}{2r}}\, \mathrm{e}^{-\kappa r}\right|^2 \approx \frac{\kappa}{2\lambda}\, \mathrm{e}^{-2\kappa\lambda} \int_\Omega \mathrm{d}^2 r = \frac{\kappa}{2\lambda}\, \mathrm{e}^{-2\kappa\lambda} \pi {r_A}^2\,. \tag{A.5}$$

Finally,

$$I_3 \equiv \int_\Omega \mathrm{d}^3 r \left|\sqrt{\frac{\kappa}{2\pi}}\, \frac{1}{r}\, \mathrm{e}^{-\kappa r}\right|^2 \approx \frac{\kappa}{2\pi\lambda^2}\, \mathrm{e}^{-2\kappa\lambda} \int_\Omega \mathrm{d}^3 r$$
$$= \frac{\kappa}{2\pi\lambda^2}\, \mathrm{e}^{-2\kappa\lambda} \frac{4}{3}\pi {r_A}^3 = \frac{2}{3}\frac{\kappa {r_A}^3}{\lambda^2}\, \mathrm{e}^{-2\kappa\lambda}\,. \tag{A.6}$$

This immediately gives the geometric factors

$$G_{3\text{ to }1} \equiv I_3/I_1 = \frac{2{r_A}^3/3\lambda^2}{2r_A} = \frac{1}{3}\left(\frac{r_A}{\lambda}\right)^2, \qquad \text{(A.7)}$$

$$G_{3\text{ to }2} \equiv I_3/I_2 = \frac{2{r_A}^3/3\lambda^2}{\pi {r_A}^2/2\lambda} = \frac{4}{3\pi}\left(\frac{r_A}{\lambda}\right). \qquad \text{(A.8)}$$

References

[1] Pedrini C, McClure D S and Anderson C H 1979 Photoionization thresholds of divalent rare earth ions in alkaline earth fluorides *J. Chem. Phys.* **70** 4959

[2] Joubert M F, Kazanskii S A, Guyot Y, Gâcon J C and Pedrini C 2004 Microwave study of photoconductivity induced by laser pulses in rare-earth-doped dielectric crystals *Phys. Rev.* B **69** 165217

[3] Fleniken J, Wang J, Grimm J, Weber M and Happek U 2001 Thermally stimulated luminescence excitation spectroscopy (TSLES): a versatile technique to study electron transfer processes in solids *J. Lumin.* **94–95** 465–9

[4] Fasoli M, Vedda A, Mihóková E and Nikl M 2012 Optical methods for the evaluation of the thermal ionization barrier of lanthanide excited states in luminescent materials *Phys. Rev.* B **85** 085127

[5] Pejchal J *et al* 2009 *J. Phys. D: Appl. Phys.* **42** 055117

[6] Mihóková E, Jarý V, Schulman L S and Nikl M 2013 Delayed recombination and excited state ionization of the Ce^{3+} activator in the $SrHfO_3$ host *Phys. Status Solidi: Rapid Res. Lett.* **7** 228–31

[7] Mihóková E, Schulman L S, Jarý V, Dočekalová Z and Nikl M 2013 Quantum tunneling and low temperature delayed recombination in scintillating materials *Chem. Phys. Lett.* **578** 66–9

[8] Mihóková E, Jarý V, Schulman L S and Nikl M 2014 Low temperature delayed recombination decay in complex oxide scintillating crystals *IEEE Trans. Nucl. Sci.* **61** 257–61

[9] Thomas D G, Hopfield J J and Augustyniak W M 1965 Kinetics of radiative recombination at randomly distributed donors and acceptors *Phys. Rev.* **140** A202–20

[10] Riehl N 1970 Tunnel luminescence and infrared stimulation *J. Lumin.* **1, 2** 1–16

[11] Delbecq C J, Toyozawa Y and Yuster P H 1974 Tunneling recombination of trapped electrons and holes in KCl:AgCl and KCl:TlCl *Phys. Rev.* B **9** 4497–505

[12] Avouris P and Morgan T N 1981 A tunnneling model for the decay of luminescence in inorganic phosphors: the case of Zn2SiO4:Mn *J. Chem. Phys.* **74** 4347–55

[13] Tachyia M and Mozumder A 1974 Decay of trapped electrons by tunneling to scavenger molecules in low-temperature glasses *Chem. Phys. Lett.* **28** 87–9

[14] Tachyia M and Mozumder A 1975 Kinetics of geminate-ion recombination by electron tunneling *Chem. Phys. Lett.* **34** 77–9

[15] Huntley D J 2006 An explanation of the power-law decay of luminescence *J. Phys.: Condens. Matter* **18** 1359–65

[16] Langer J S 1969 Statistical theory of the decay of metastable states *Ann. Phys.* **54** 258–75

[17] Hamilton D S, Gayen S K, Pogatshnik G J, Ghen R D and Miniscalco W J 1989 Optical absorption and photoionization measurements from the excited states of Ce^{3+}:$Y_3Al_5O_{12}$ *Phys. Rev.* B **39** 8807–15

[18] Lorenz U and Schmidt B 2009 WavePacket-simulations in quantum dynamics (http://sourceforge.net/projects/wavepacket)

[19] Lyu L-J and Hamilton D S 1991 Radiative and nonradiative relaxation measurements in Ce^{3+} doped crystals *J. Lumin.* **48, 49** 251–4

[20] Shannon R D 1976 Revised effective ionic radii and systematic studies of interatomie distances in Halides and Chaleogenides *Acta Cryst.* A **32** 751–67

[21] Santos C, Ribeiro S, Strecker K, Suzuki P A, Kycia S and Silva C R M 2009 Crystallographic characterization of silicon nitride ceramics sintered with Y_2O_3–Al_2O_3 or E_2O_3–Al_2O_3 additions *Ceram. Int.* **35** 289–93

[22] Nikl M, Ren G, Ding D, Mihóková E, Jarý V and Feng H 2010 Luminescence and scintillation kinetics of the Pr^{3+} doped $Lu_2Si_2O_7$ single crystal *Chem. Phys. Lett.* **493** 72–5

[23] Mihóková E, Fasoli M, Moretti F, Nikl M, Jarý V, Ren G and Vedda A 2012 Defect states in Pr^{3+} doped lutetium pyrosilicate *Opt. Mater.* **34** 872–7

[24] Soetebier F and Urland W 2002 Crystal structure of lutetium disilicate $Lu_2Si_2O_7$ *Z. Kristallogr. NCS* **217** 22

[25] Abramowitz M and Stegun I A 1965 *Handbook of Mathemtical Functions* (New York: Dover)

Physics Letters A 380 (2016) 3430–3433

Contents lists available at ScienceDirect

Physics Letters A

www.elsevier.com/locate/pla

Energy bands and gaps near an impurity

E. Mihóková [a,*], L.S. Schulman [b]

[a] Institute of Physics, Acad. of Sciences of the Czech Rep., Cukrovarnická 10, 162 53 Prague 6, Czech Republic
[b] Physics Department, Clarkson University, Potsdam, NY 13699-5820, USA

ARTICLE INFO

Article history:
Received 11 April 2016
Received in revised form 9 August 2016
Accepted 11 August 2016
Available online 18 August 2016
Communicated by V.A. Markel

Keywords:
Crystal structure
Impurity
Modeling
Energy bands

ABSTRACT

It has been suggested that in the neighborhood of a certain kind of defect in a crystal there is a bend in the electronic band. We confirm that this is indeed possible using the Kronig–Penney model. Our calculations also have implications for photonic crystals.

Band gaps occur for waves in any non-trivial periodic structure. Current interest, however, focuses on two particular manifestations: electrons and photons. The present work, although focused on electrons, does have material relevant to photonic crystals.

In Baran et al. [1] the authors deal with electron states in crystals and explain the luminescence spectra of β-Ca_2SiO_4:Eu^{2+}, Eu^{3+}. They have the interesting suggestion that in the neighborhood of an impurity there is a bend in the conduction band; namely in that region there are fewer electron states and they are of higher energy.

There are other experimental observations that could be explained by considering local changes in the conduction or valence bands. As an example, consider irregularities that have been seen in the low temperature dependence of scintillator delayed-recombination signals. For many substances this signal is approximately temperature independent. This phenomenon has been explained as due to quantum tunneling between a recombination center and a nearby trap, and has been seen in a number of scintillating materials [2–6]. In particular, a constant low temperature delayed recombination signal was observed up to at least about 150–200 K. However, there is at least one important case that does not fit this picture. The intense peak in the delayed recombination signal in Ce^{3+}-doped $Gd_3Ga_3Al_2O_{12}$ (GGAG) [4] at around 100 K has so far not been satisfactorily explained. But if the conduction band does bend near the Ce^{3+} impurity things can change dramatically. The Ce^{3+} ion and the nearby resonant trap could then have different energy separations from the conduction band and unlike the Ce^{3+} excited state, the trap can be very shallow. The temperature independent quantum tunneling between Ce^{3+} and the trap would be accompanied by the transfer of excitation energy from the shallow trap to Ce^{3+} via the conduction band at very low temperatures. The latter temperature dependent process would produce the observed bump in the delayed recombination signal.

We have explored this idea of the conduction band bending using the simplest of one-dimensional models, the Kronig–Penney model with δ-functions.

A great deal of work along these lines has already been done, since impurities play an important role in almost-periodic systems. Early literature that employs the Kronig–Penney model includes Stęślicka and Sengupta [7], Kasamanyan [8] and many others. For photonic crystals, where the one-dimensional feature can be directly relevant, the Kronig–Penney model has also provided a framework; see Luna-Acosta et al. [9,10]. The emphasis in these works has been on the impurity state itself or on transmission properties. In many cases the techniques are similar [11], however, our primary concern is electronic states that respond to a single impurity. This seems close to the work of Baran et al. [1].

What we find is that a lone defect has a profound effect on the eigenstates, and besides shifting the location of the gap it can also change the nature of the eigenfunctions throughout the crystal. The Bloch theorem does not apply [12] and many familiar features show radical differences. We cannot be sure of the extent to which these properties persist in three dimensions, although [1] suggests its relevance.

* Corresponding author.
E-mail addresses: mihokova@fzu.cz (E. Mihóková), schulman@clarkson.edu (L.S. Schulman).

http://dx.doi.org/10.1016/j.physleta.2016.08.017
0375-9601/

Without an impurity and in a simple form, the Kronig–Penney model has Hamiltonian

$$H_0 = \frac{p^2}{2m} + \lambda \sum_{n=0}^{N-1} \delta(x - na)\,,$$

where a is the lattice spacing, N the number of cells, m the mass, and λ the strength of the potential. Note that we immediately use a δ function potential, since for the matters of principle that we seek the details of the periodic potential should not matter. In keeping with this viewpoint we also set $m = 1$ and $\hbar = 1$. To make comparisons to physical systems we will derive our energy scale from typical values for crystal systems.

We shall generally take λ to be negative, mimicking the attraction experienced by electrons at atomic locations. And finally, for the electronic case we insist (as is usual in these models) that the state at $x = Na$ differ from that at $x = 0$ *only* by a phase, that phase being Nka with k the wave vector entering the Bloch theorem.

With these assumptions, the wave function in cell n (such that $na < x < (n+1)a$) can be taken to be $\psi_n = A_n e^{iK(x-na)} + B_n e^{-iK(x-na)}$ with energy $E = K^2/2$. The condition at na imposed by the δ-function is $\Delta\psi' = 2\lambda\psi$ with $\Delta\psi'$ being the change in ψ's derivative. Note that the K appearing here is not the k of the Bloch theorem. It follows that

$$\begin{bmatrix} A_n \\ B_n \end{bmatrix} = M \begin{bmatrix} A_{n-1} \\ B_{n-1} \end{bmatrix}, \text{ with } M = \begin{bmatrix} \Omega(1+z) & \Omega^* z \\ -\Omega z & \Omega^*(1-z) \end{bmatrix},$$

$z = \lambda/(2iK)$, and $\Omega = e^{iKa}$ ($\Omega^* = e^{-iKa}$). The requirement that the eigenvalues of M^N be of magnitude 1 fixes the allowable bands and the gaps. Letting $\phi = Ka$, this condition is $|\cos\phi + (\lambda/2K)\sin\phi| < 1$. For bound states one can do an analytic continuation and the spectral condition is $\left|\cosh\bar{\phi} - (|\lambda|/2\overline{K})\sinh\bar{\phi}\right| < 1$, where $\overline{K}$ and $\bar{\phi}$ are the analytic continuations, $E = -\overline{K}^2/2$ and λ is assumed negative. We will later use the numerical value of the top of the "valence band" (the bound states) and the bottom of the conduction band to relate our energy to the physical scales. The matrix M is known as the transfer matrix; it conserves current ($\propto K(|A_n|^2 - |B_n|^2)$) and is an element of the group SU(1, 1) [13].

We assume that our impurity is at site L with $1 \le L \le N$. We do *not* seek a value for the impurity level—as some of the articles cited earlier do. Rather we assume it is there and its associated defect provides a force—different from the usual—on nearby electrons. This is in keeping with the physical situation in [1], where the presence of Eu^{3+} (an impurity) causes an additional charge compensating defect to appear in the vicinity of the europium to maintain the lattice charge neutrality. To keep things simple we assume that in cell-L, as a consequence, there is an additional positive, constant, repulsive potential throughout the interval $La < x < (L+1)a$ [14]. To provide a framework for solution we further assume that this situation repeats, so that, as for the system without impurities, we require that the associated full transfer matrix (presented below) has eigenvalues of magnitude unity. (In this our method could be thought of as involving a supercell. For photons one calculates instead transmission probability.)

In cell L (i.e., $La < x < (L+1)a$) the momentum is reduced and we have $K' = \sqrt{K^2 - 2V}$, with V the value of the potential in that interval. As the wave function in that interval we take $\psi_L = A_L e^{iK'(x-La)} + B_L e^{-iK'(x-La)}$ (with analytic continuation if necessary). There are now two transfer matrices, from $L-1$ to L and from L to $L+1$. These are designated $M_{K\to K'}$ and $M_{K'\to K}$, respectively. A straightforward calculation gives

$$M_{K_1\to K_2} = \begin{bmatrix} \Omega_1\left(\frac{K_1+K_2}{2K_2} + z_2\right) & \Omega_1^*\left(\frac{K_2-K_1}{2K_2} + z_2\right) \\ \Omega_1\left(\frac{K_2-K_1}{2K_2} - z_2\right) & \Omega_1^*\left(\frac{K_1+K_2}{2K_2} - z_2\right) \end{bmatrix},$$

where $z_2 = \frac{\lambda}{2iK_2}$, $\Omega_1 = e^{iK_1 a}$, and K_1 and K_2 are either K and K' or the reverse. With the impurity at L the total transfer matrix for all L cells is $M_{\text{all}} \equiv M^{N-L} M_{K'\to K} M_{K\to K'} M^{L-2}$.

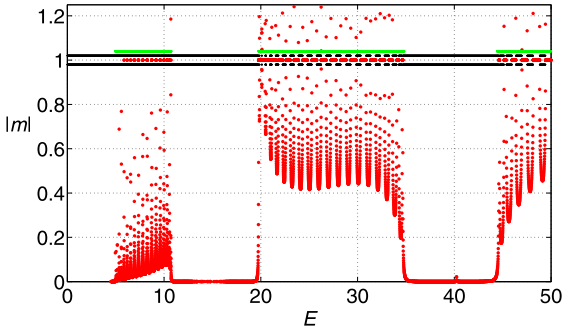

Fig. 1. Absolute values of eigenvalues of M_{all} ($|m|$) are shown as red points (some of which are excluded because of a cutoff in the axes). In addition, when an eigenvalue does not have magnitude 1, a pair of black dots are displayed at 1 ± 0.02. Finally to better judge the effect of the impurity, the normal, i.e., $V = 0$, energy band is shown in green at a height of 1.04 (although these are magnitude unity eigenvalues of M^N) [15]. Parameter values: $\lambda = -10$, $a = 1$, $V = 15$, $N = 20$, $L = 9$. The energy, E, in this figure is roughly twice the actual energy in eV. (For interpretation of the references to color in this figure legend, the reader is referred to the web version of this article. See also [15].)

To see whether the spectrum of M_{all} fulfills the expectations of [1] we display Fig. 1. The red dots, which are slightly larger than the others, are the eigenvalues of M_{all}; when they have magnitude one indefinite ring propagation is possible. Superimposed on this image are green dots at height 1.04, which are located at energy values for which magnitude 1 eigenvalues exist for $V = 0$. These would be the bands (and in their absence, the gaps) without the impurity. To make clear that many energy values *within* the non-defect bands are also eliminated we have put a pair of black dots displaced by 0.02 from 1 for each eigenvalue of M_{all} that is *not* of magnitude 1 [15]. In principle this can also be seen from the red dots at small magnitude values [16]. A number of observations can be made from this image. First, many states that were formerly ($V = 0$) in the conduction band no longer appear there. Moreover, the first conduction band ($5 \lesssim E \lesssim 10$ in our units) has increased its energy, as suggested in [1]. That there is little or no increase for the next band is to be expected since the energies are larger and the potential may be expected to have less influence. And then there is what we do not see. No new states emerge in the gap, although the impurity can increase transmission, a kind of resonance phenomenon in photonic crystals. (Confusion may arise since the red dot at the top of the first conduction band might be taken to be to the right of the green dot above it. But this is an artifact of the dot size, which is larger for the $V \neq 0$ band.) No points appear below about $E = 4.5$ because of issues of numerical accuracy [17]. Even for transmission data, the values of the small-K matrix M_{all} are so large that a cutoff at 10^{-10} in the graph would lose these numbers as well.

It is interesting to focus on the first (left-most) E value in the conduction band. Although it is to the right of the beginning of the $V = 0$ band (confirming the "bend in the band") even this is not the full story. For more information we turn to another graph, shown in Fig. 2. First note that when $V = 0$ the wave functions

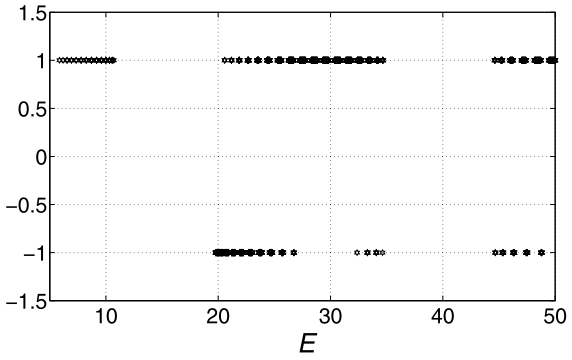

Fig. 2. This graph indicates whether a state is a maximum, minimum or neither *at the impurity point*. The horizontal axis is the energy of the state in question. When the (sum of the) absolute values of the probability amplitudes for that state is a local minimum at the impurity point value on the graph (at the corresponding energy) is $+1$. For a local maximum the value is -1, and if the value is neither a 0 appears. The graph is confined to states for which eigenvalue $|m|$ has magnitude 1, corresponding to conduction band states in the presence of the impurity.

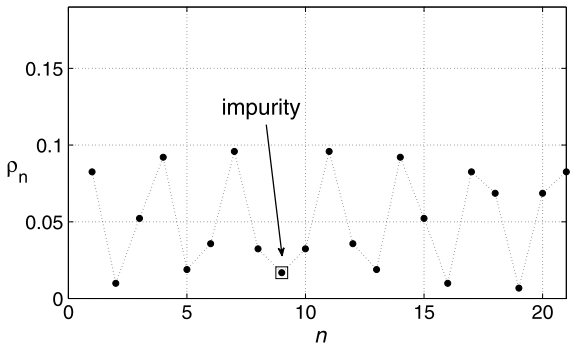

Fig. 3. Magnitude squared of components ($\rho_n \equiv |A_n|^2 + |B_n|^2$) of lowest energy state ($E = 5.862$) in the conduction band. The horizontal axis is the cell number n and the plotted quantity is constant in each cell. The absolute value of the corresponding eigenvalue is 1. Note that this quantity is *not* constant from cell to cell (as for Bloch states), and has a significant minimum at the location of the defect. There are 20 cells with the defect site indicated by a square.

in all cells have the same magnitude ($\propto \rho_n \equiv |A_n|^2 + |B_n|^2$), by virtue of the Bloch theorem. This is not the case for $V \neq 0$. We will later discuss how this imposes structure on the overall state space, but for now we note that the amplitude of the wave function in the cell near the defect may be a (local) minimum or maximum or neither with respect to its probability of occupancy. For the left-most eigenvalue-magnitude-1 state it is seen that this is a minimum. Fig. 2 shows that this is the case for the entire band. So not only does the bottom of the band increase, but even for those states that can have electron occupancy, that occupancy is reduced. In effect, one is much less likely to find an electron in this region.

Regarding the absence of a gap state, one must distinguish between the defect, which has a particular location and induces the potential V, and the electronic states in the vicinity. To say that there is not gap state means that with the potential (V) due to the defect there is no *additional* state, one that would be conducting, in the gap energy range. We remark that in our searches through parameter space, we did not encounter such states.

Although we have used non-dimensional units, it is possible to compare our results to experiment in the following rough way. For the parameter values used above (see Fig. 1) the valence band, i.e., bound states, had as its highest energy level, about -12 units, while the conduction band started at about 5. In the experimental data that concerns us [1] this range is about 7 eV. Therefore we

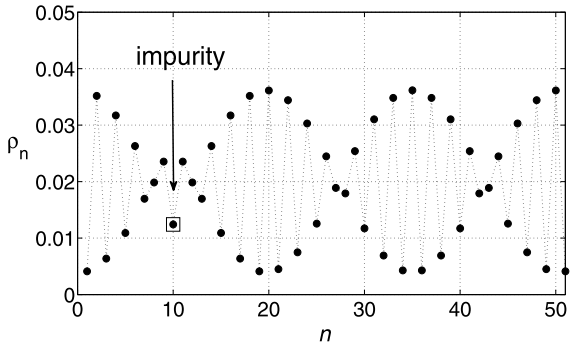

Fig. 4. As in Fig. 3, we show the lowest eigenstate, $E = 6.92$, for parameters $N = 50$, $a = 1$, $\lambda = -10$, $L = 10$, $V = 15$. The horizontal axis is the cell number n and the vertical axis is $\rho_n \equiv |A_n|^2 + |B_n|^2$.

consider 2.4 of our units to represent about 1 eV, so that the shift in the band is a bit under 1/2 eV.

We next turn to the form of the eigenstates. The fact that non-zero V forces one cell to be different causes variation in the probability that an electron at some energy occupies any particular cell. In Fig. 4 we show the lowest eigenstate for a larger array. The placement of the impurity has forced a minimum at its location, causing a beat-like envelope to occur.

For photonic crystals the nature of the "defect" would depend on the wavelength; for example, in the microwave work of [9] there were changes in the index of refraction. Given the variety of potentials that might be used in this case, we consider also negative V in our model. In addition, of greater interest than the eigenvalues is the transmission coefficient. A simple calculation shows that $T = 1/M_{\text{all}}(2,2)$, where T is defined as $|A_N/A_0|^2$, using the wave function notation defined earlier. For this quantity our results are similar to those of [9,10] (and therefore we do not show the graphs). Like them, we find that the impurity can actually enhance transmission. This tends to occur in regions (of energy or frequency) where transmission would be unlikely for the perfect crystal. For some parameter values T can be increased by orders of magnitude, including bringing it to be essentially unity.

Besides this potentially useful observation we note that the effect of the impurity on the wave function can be significant. As examples we show Fig. 5, where it is clear that the defect's presence is felt throughout the system. Interestingly although the potential is attractive, it is only at the largest K value shown that the magnitude at the defect site rises significantly. Apart from that it can be seen that the defect can impose periodic structure (of various periods) or even can act as a node.

Discussion. Even in the face of defects, band structure continues to give insights into electron behavior. In Baran et al. [1] it is suggested that there is a bend in the conduction band in the neighborhood of the defect. Based on a simple model, we have confirmed that this can occur. Besides the parameter values given in this paper we have examined many more and found that band-bending is a general feature. Moreover, even for the states permitted in the bent band, electronic amplitude is down, so not only are there fewer states, but they are less likely to have an electron in the affected region.

In addition, the defect can have a profound affect on wave function structure throughout the system, as we have demonstrated with both electronic and photonic almost-periodic structures. It must be noted though that for this issue the dimensionality plays a role, and while even in 3 dimensions there is a breakdown in the Bloch theorem, unless the defects were themselves symmetrically arranged, the neat periodic behavior observed here would probably not occur.

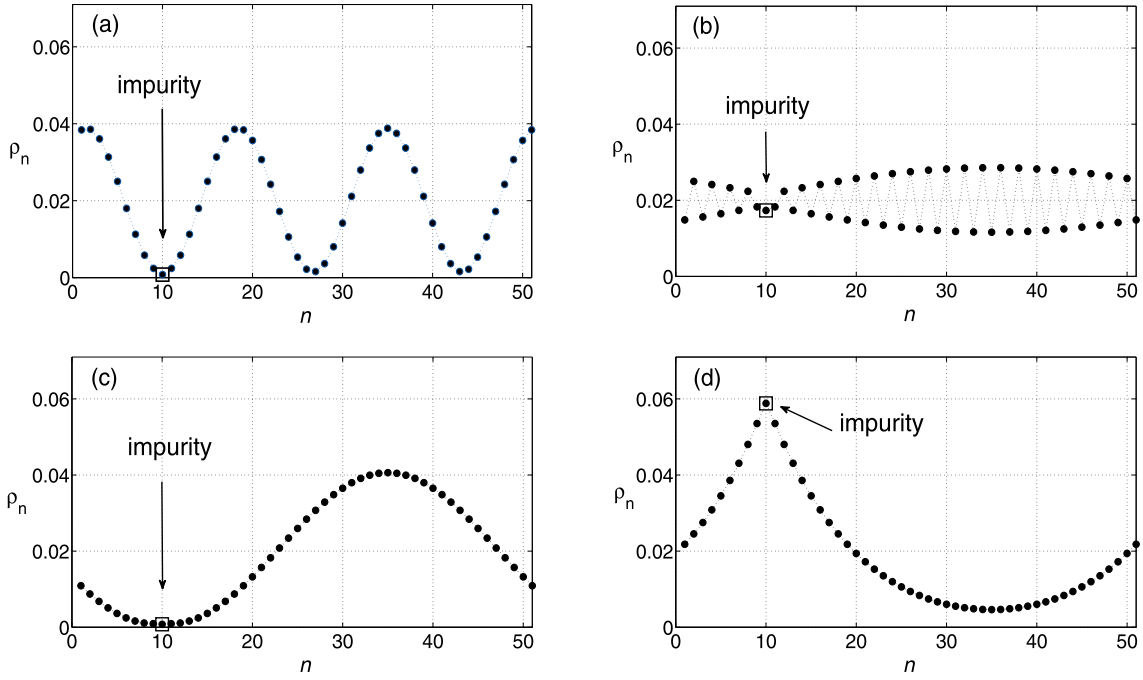

Fig. 5. Various wave functions for parameter values $N = 50$, $a = 1$, $L = 10$, $\lambda = 2$, $V = -5$. The K values are 1.32 (a), 2.05 (b), 3.68 (c) and 9.62 (d). The horizontal axis is the cell number n and the vertical axis is $\rho_n \equiv |A_n|^2 + |B_n|^2$.

Acknowledgements

We are grateful to the Czech Science Foundation for the support of Project GA 13-09876S.

References

[1] A. Baran, J. Barzowska, M. Grinberg, S. Mahlik, K. Szczodrowski, Y. Zorenko, Binding energies of Eu^{2+} and Eu^{3+} ions in β-Ca_2SiO_4 doped with europium, Opt. Mater. 35 (2013) 2107–2114.
[2] E. Mihóková, V. Jarý, L.S. Schulman, M. Nikl, Delayed recombination and excited state ionization of the Ce^{3+} activator in the $SrHfO_3$ host, Phys. Status Solidi RRL 7 (2013) 228–231.
[3] E. Mihóková, L. Schulman, V. Jarý, Z. Dočekalová, M. Nikl, Quantum tunneling and low temperature delayed recombination in scintillating materials, Chem. Phys. Lett. 578 (2013) 66–69.
[4] E. Mihóková, V. Jarý, L.S. Schulman, M. Nikl, Low temperature delayed recombination decay in complex oxide scintillating crystals, IEEE Trans. Nucl. Sci. 61 (2014) 257–261.
[5] E. Mihóková, L.S. Schulman, Low temperature delayed recombination and trap tunneling, J. Phys. Condens. Matter 27 (2015) 075501.
[6] E. Mihóková, V. Babin, K. Bartosiewicz, L. Schulman, V. Čuba, M. Kučera, M. Nikl, Low temperature delayed recombination decay in scintillating garnets, Opt. Mater. 40 (2015) 127–131.
[7] M. Stęślicka, S. Sengupta, Kronig–Penney model for impurity states, Physica 54 (1971) 402–410.
[8] Z.A. Kasamanyan, On the theory of impurity levels, Sov. Phys. JETP 34 (1972) 648–650, in Russian: Ž. Èksp. Teor. Fiz. 61 (1971) 1215–1220.
[9] G.A. Luna-Acosta, H. Schanze, U. Kuhl, H.-J. Stöckmann, Impurity effects on the band structure of one-dimensional photonic crystals: experiment and theory, New J. Phys. 10 (2008) 043005.
[10] G.A. Luna-Acosta, N.M. Makarov, U. Kuhl, H.-J. Stöckmann, One dimensional Kronig–Penney model with positional disorder: theory versus experiment, Phys. Rev. B 80 (2009) 115112.
[11] There is considerable literature on completely random one-dimensional models, also using SU(1, 1) occasionally. However, that is significantly different from what we study here.
[12] When we say the theorem does not hold, we refer to the individual cells, one of which is different from the others. For repetitions of all N of them the Bloch theorem does hold.
[13] A. Peres, M. Revzen, A. Ron, Calculation of localization length in disordered chains, Phys. Rev. B 24 (1981) 7463.
[14] Arguably we could center the potential on La, rather than have it be between there and $(L+1)a$. This would require yet another, matrix $(M_{K'\to K'})$, so that our choice is motivated by simplicity.
[15] To aid viewers who see this figure in monochrome, we note that for values of E between 5 and 10 there are 4 rows of points (dense enough to look like lines) visible in the neighborhood of magnitude 1. The topmost is at 1.04 and indicates the location of the conduction band in the absence of the defect. The one below (at 1.02) is black as is the one at the bottom (at 0.98) and they represent non-unit eigenvalues of M_{all}. Finally the third from the top (at 1), in red, shows the norm-1 eigenvalues of M_{all}.
[16] Because $\det M_{\text{all}} = 1$, the product of its eigenvalues is 1. Therefore for all eigenvalues that are not 1, there will be one red dot above the line at 1 and one below. Thus every dot below the line corresponds to the absence of an eigenvalue 1 on the line at 1. For clarity though we have drawn an additional pair of black dots to indicate each absence.
[17] Despite the numerical errors incurred when the eigenvalues of M_{all} grow, for matrices having eigenvalue of magnitude 1, we do believe our numerical results. As a check on this we looked at the $V = 0$ case, where M^N can also get very much out of hand. For this case we evaluated both M and M^N (for $N = 256$) to see if both gave the same conduction bands, i.e., K values for which the magnitude of the eigenvalue is 1. They did. Our numerical software had 16 digit accuracy. For the parameters we used, the 18th power of M had elements of order 10^{13} for K as large as 2. For $K = 3$, M^{18} still had elements of order 10^6 and the product of the eigenvalues differed from the determinant (which it should equal) by 10^{-3}—large! However, for the points on our graph (for which $N = 20$), beginning at a bit larger than $K = 4.5$, the values of the matrix M became smaller and rounding errors, ceased to be a problem.